

University of Southampton Research Repository ePrints Soton

Copyright © and Moral Rights for this thesis are retained by the author and/or other copyright owners. A copy can be downloaded for personal non-commercial research or study, without prior permission or charge. This thesis cannot be reproduced or quoted extensively from without first obtaining permission in writing from the copyright holder/s. The content must not be changed in any way or sold commercially in any format or medium without the formal permission of the copyright holders.

When referring to this work, full bibliographic details including the author, title, awarding institution and date of the thesis must be given e.g.

AUTHOR (year of submission) "Full thesis title", University of Southampton, name of the University School or Department, PhD Thesis, pagination

UNIVERSITY OF
Southampton
School of Engineering Sciences

Investigation of a Miniature Differential Ion Thruster

Cheryl Collingwood

Thesis submitted in partial fulfilment of the degree of Doctor of Philosophy

July 2011

UNIVERSITY OF SOUTHAMPTON

ABSTRACT

FACULTY OF ENGINEERING SCIENCE & MATHEMATICS
SCHOOL OF ENGINEERING SCIENCES

Doctor of Philosophy

INVESTIGATION OF A MINIATURE DIFFERENTIAL ION THRUSTER

by Cheryl Collingwood

Complex space missions involving formation flying or drag compensation are driving the need for spacecraft propulsion systems capable of providing low but also highly accurate thrust levels. Currently, no single propulsion device exists that is able to provide both precision and coarse thrust capability over the micro-Newton to milli-Newton thrust range required by these missions. A need for a precision, low thrust, miniature electric propulsion device with a wide throttling range therefore exists.

The concept of a differential ion thruster was initially proposed by the Ion Propulsion Group of QinetiQ to address this requirement. It was proposed that an unprecedented throttling range and thrust resolution could be achieved through differential control of opposing ion beams, by which very small net offsets in thrust could be achieved. Single ion beam operation, as for conventional gridded ion thrusters, would permit higher thrust levels to be achieved with high specific impulse. The extraction and independent control of two ion beams from a single gridded ion thruster has never previously been reported.

Prototype and breadboard models of the proposed Miniaturised Differential Gridded Ion Thruster (MiDGIT) were designed and manufactured in collaboration with QinetiQ to provide a proof-of-concept and to demonstrate preliminary performance. Test campaigns were conducted at the QinetiQ Large European Electric Propulsion Facilities and within the EP1 vacuum chamber at the University of Southampton. The work reported in this thesis contributes to the first detailed characterisation of a twin-ended radio frequency gridded ion thruster utilising a common plasma discharge.

Two control methods were identified which permitted independent control of the ion beams extracted from either end of the thruster. These were: variation of the accelerator grid potential in order to induce changes in the plasma sheath geometry upstream of each screen grid leading to variations in the extracted ion currents, and variation of the RF power delivered to each end of the thruster to generate a higher plasma density on one end of the discharge and ultimately a net thrust out of that end of the thruster.

The performance of the MiDGIT thruster has been evaluated with regards to both coarse thrust and fine thrust control requirements. Though the MiDGIT thruster has demonstrated a wide thrust range surpassing competing single-ended miniature ion thrusters, the extraction of two ion beams to achieve very low thrust levels leads to low specific impulse and high specific power for the MiDGIT thruster compared to any other single-ended ion thruster that can achieve the same thrust levels. Recommendations to improve efficiency are made and suggestions for future work and further development of the MiDGIT thruster are given.

Contents

Abstract	I
Contents	III
List of Figures	VII
List of Tables	XIII
Declaration of Authorship.....	XV
Acknowledgements.....	XVII
Nomenclature.....	XIX
List of Acronyms	XXI
1. Introduction.....	1
1.1 Micropropulsion for Formation Flying.....	2
1.1.1 Propulsion Requirements Important to Formation Flying.....	2
1.1.2 Micropropulsion Technologies Suitable for Formation Flying	5
1.2 Motivation for Research	15
1.3 Research Aims and Objectives	19
1.4 Thesis Outline.....	19
2. Radio Frequency Ion Thrusters: Background and Literature Review	21
2.1 Inductively Coupled Plasma Discharges	21
2.1.1 General Plasma Properties of Inductively Coupled Plasma	23
2.1.2 Heating of Electrons and Non-Linear Effects in ICP	27
2.1.3 Transformer Model of Inductive Coupling	28
2.1.4 Discharge Modes in Inductively Coupled Plasma.....	31
2.1.4 Discharge Diagnostics of Inductively Coupled Plasma.....	33
2.2 Radio Frequency Ion Thrusters	34
2.2.1 General Design	34
2.2.2 Thruster Ignition.....	37
2.2.3 Ion Extraction	39
2.2.4 Main Losses for RF Ion Thrusters.....	45
2.2.5 Thruster Performance	46
2.2.6 Advantages of RF Ion Thrusters.....	48
2.2.7 RIT Development	48
2.2.8 Miniature RF Ion Thrusters	50
2.2.9 Numerical Models of Miniature RF Ion Thrusters	53
2.3 Summary	55
3. The MiDGIT Thruster.....	57
3.1 MiDGIT System Concept.....	57
3.1.1 Control Modes	59
3.1.2 Concept Advantages.....	61
3.2 System Considerations	62
3.2.1 Flow Rate Control	62
3.2.2 Beam Supply Control	62
3.2.3 Beam Telemetry	62
3.2.4 Thrust Vector.....	62
3.2.5 Neutralization	62
3.3 General Design Considerations	63

3.3.1	Discharge Chamber Material.....	63
3.3.2	Discharge Chamber Geometry	64
3.3.3	Coil Geometry	65
3.3.4	Gas Distributor	65
3.4	Prototype and Breadboard Thruster Models.....	67
3.4.1	Prototype Configuration	67
3.4.2	Breadboard Configuration	68
4.	Experimental Arrangement and Procedures	71
4.1	Operating Modes and Electrical Configuration.....	71
4.1.1	Single-End Configuration.....	71
4.1.2	Differential Configuration	73
4.2	LEEP-1 Vacuum Facility	75
4.2.1	Vacuum Chamber	75
4.2.2	Thruster Interface	76
4.2.3	Radio Frequency Generator.....	76
4.2.4	Power Supplies and Meters	81
4.2.5	Propellant Feed System	81
4.2.6	Diagnostic Equipment	85
4.2.7	Thruster Operation and Procedures	85
4.3	EP1 Vacuum Facility.....	87
4.3.1	Vacuum Chamber	87
4.3.2	Thruster Interface	87
4.3.3	Radio Frequency Generator.....	88
4.3.4	Propellant Feed System	89
4.3.5	Power Supplies and Meters	91
4.2.6	Diagnostic Equipment	91
4.3.7	Thruster Operation and Procedures	98
5.	Coarse Thrust Control	101
5.1	Thruster Configuration	101
5.2	Discharge Ignition	103
5.3	Operational Envelope	105
5.4	Performance Mapping	108
5.5	Beam Probe Measurements	110
5.6	Performance Analysis.....	118
5.7	Additional Performance Tests by QinetiQ	123
5.7.1	Extended Thrust Capability	123
5.7.2	Thrust Stepping	124
5.8	Summary	126
6.	Differential Thrust Control	129
6.1	Discharge Ignition and Dual Beam Extraction.....	130
6.2	Differential Thrust Control.....	132
6.2.1	Variation of Accelerator Grid Potential.....	132
6.2.2	Variation of RF Power.....	150
5.8	Summary of Differential Thrust Control	184
7.	Conclusion	187
7.1	Preliminary Performance of the MiDGIT Thruster	188
7.1.1	Coarse Thrust Control	188
7.1.2	Fine Thrust Control	189
7.1.3	General Observations	191
7.2	Suitability as a Precision Microthruster.....	192

7.3	Significance of the Work.....	194
7.4	Recommendations and Future Work.....	195
Appendix A		197
A	Triple Langmuir Probe Theory.....	197
A.1	Langmuir Probes.....	197
A.2	Triple Langmuir Probes.....	208
Appendix B		215
B	Discharge Model	215
B.1	General Assumptions.....	215
B.2	General Description	216
B.3	Cross Section Data.....	218
References		221

List of Figures

1.1 Schematic of the T5 gridded ion thruster.....	9
1.2 Schematic of a FEEP Thruster.....	9
1.3 Schematic of a Colloid Thruster.....	11
1.4 Schematic of an Ablative Pulsed Plasma Thruster.....	11
1.5 Plot comparing required thrust range for science and Earth observation missions with the current performance of various thruster technologies.....	15
1.6 The basic configuration of the MiDGIT thruster.....	17
2.1 Diagram to illustrate the presheath and sheath regions in a plasma.....	25
2.2 Equivalent circuit model of an inductive discharge modeled as a transformer.....	29
2.3 Absorbed power against plasma density for an inductive discharge for different values of source current.....	32
2.4 Schematic of the RF ion thruster, RIT-4.....	35
2.5 Minimum pressure required for ignition of an inductive discharge in Xe and Ar as a function of the electron flux undergoing collisions in a skin depth of 1.4 cm.....	39
2.6 Schematic of two grid ion extraction, indicating modified sheath width, l_e , due to curvature of the plasma sheath.....	40
2.7 Ion extraction simulations performed by Zhong et al. indicating (a) over perveance, (b) perveance, (c) under perveance and cross-over.....	43
2.8 Power losses determined via numerical simulation of the BRFIT-7 thruster.....	46
2.9 Scaling laws for the RIT microthrusters.....	51
2.10 Power losses determined via numerical simulation of the BRFIT-3 thruster.....	55
3.1 Schematic of the MiDGIT Architecture.....	58
3.2 Sheath geometry indicated by the ratio of electron density to ion density upstream of the screen grid for different accelerator grid potentials.....	59
3.3 Ion distribution through a two grid extraction system simulated by Zhong et al. displaying over-focussing for $V_{ACC} = -800V$	60
3.4 Plot of (a) neutral number density and (b) neutral velocity for an annulus with eight 1mm diameter injection holes at a flow rate of 0.35 mgs^{-1}	66
3.5 Images of the MiDGIT prototype with earth screen removed.....	67
3.6 Images of the MiDGIT breadboard thruster displaying ceramic shutter plates.....	69
3.7 Images of the MiDGIT breadboard thruster and extraction grids.....	69
4.1 Electrical configuration of the MiDGIT thruster and T5 hollow cathode neutralizer during single-end operation.....	72
4.2 Equivalent circuit of RFG and antenna matching unit.....	73
4.3 Electrical configuration of MiDGIT thruster and T5 hollow cathode neutralizer during differential operation.....	74
4.4 The loadlock of the LEEP-1 vacuum facility at QinetiQ.....	75
4.5 Mounting plate with attached neutralizer and flow pipe showing the MiDGIT prototype thruster.....	76
4.6 Schematic of RFG comprising signal generator, RF amplifier and matching unit.....	77
4.7 Comparison of measured RF forward power determined from signal generator and that displayed by SWR power meter.....	80
4.8 Schematic of flow control system for MiDGIT testing.....	82
4.9 Chamber pressure for a commanded flow rate.....	84
4.10 Comparison of chamber pressure for MFC1 and MFC2 flow controllers.....	84

4.11	Corrected flow rate for MFC1 and MFC2.....	84
4.12	Beam probe system displaying (a) schematic of probe orientation and (b) image of screened faraday cup.....	85
4.13	Typical flow calibration curve for Micro-Trak 101 MFC with xenon	90
4.14	Schematic of Rogowski coil mounting	92
4.15	Configuration of triple Langmuir probes for measuring electron temperature and density.....	94
4.16	Orientation of triple Langmuir probe tips inserted through the extraction grids grids of the MiDGIT prototype thruster	97
5.1	Images of the MiDGIT breadboard thruster operating in single-end mode, with T5 hollow cathode neutralizer shown in (a).	102
5.2	Maximum and minimum beam current measured during initial adjustment of flow rate and RF power ($V_b = 950V$, $V_{ACC} = -95V$).	106
5.3	Accelerator grid currents measured during initial adjustment of flow rate and RF power ($V_b = 950V$, $V_{ACC} = -95V$).	106
5.4	Beam current and accelerator drain current for the SE1 configuration for various flow rates and RF power ($V_b = 950V$, $V_{ACC} = -95V$).	109
5.5	Beam current and accelerator drain current for the SE2 configuration for various flow rates and RF power ($V_b = 950V$, $V_{ACC} = -95V$).	109
5.6	Beam profiles for the SE1 configuration for various flow rates and RF power	111
5.7	Beam profiles for the SE2 configuration for various flow rates and RF power	112
5.8	Example of a Gaussian fit to a beam profile affected by CEX collisions.....	115
5.9	Estimated beam divergence against measured beam current for SE1 and SE2	116
5.10	(a) Ratio of estimated beam current to measured beam current and (b) ratio of accelerator grid current to beam current for SE1 and SE2	116
5.11	Specific impulse against thrust determined for the SE1 and SE2 configurations of the MiDGIT breadboard thruster for the operating points below the observed perveance limit (with $V_b = 950V$, $V_{ACC} = -95V$).	119
5.12	Thrust against specific power determined for the SE1 and SE2 configurations of the MiDGIT breadboard thruster operating with $V_b = 950V$, $V_{ACC} = -95V$	120
5.13	Specific impulse against specific power determined for the SE1 and SE2 configurations of the MiDGIT breadboard thruster.....	120
5.14	Electrical efficiency against mass utilization efficiency determined for the SE1 and SE2 configurations of the MiDGIT breadboard thruster	121
5.15	Total thruster efficiency determined for the SE1 and SE2 configurations of the MiDGIT breadboard thruster ($V_b = 950V$, $V_{ACC} = -95V$).	121
5.16	Discharge loss against mass utilization efficiency for the SE1 and SE2 configurations of the MiDGIT breadboard thruster ($V_b = 950V$, $V_{ACC} = -95V$).	122
5.17	Thrust stepping of the SE2 configuration of the MiDGIT breadboard thruster operated at 0.051 mgs^{-1} with $V_b = 950V$, $V_{ACC} = -250V$	125
6.1	Images of (a) the MiDGIT breadboard thruster operating in differential mode, (b) dual ion beam extraction from the MiDGIT prototype thruster during variation of the accelerator grid potentials on either end	132
6.2	(a) Thrust calculated at perveance for the MiDGIT breadboard grids with a beam voltage of 950V and accelerator grid voltage of -75V for SE2 and varying accelerator grid voltage for SE1, (b) Net thrust due to varying accelerator grid voltage on SE1.....	133
6.3	(a) Measured beam current for SE1 and SE2 during variation of V_{ACC1} (with $V_{ACC2} = -75V$, $V_b = 950V$, $\dot{m} = 0.052 \text{ mgs}^{-1}$, $P_{fw} = 27.6W$) (b) Measured accelerator grid currents for SE1 and SE2 during variation of V_{ACC1}	135

6.4 (a) Measured beam current for SE1 and SE2 during variation of V_{ACC2} (with $V_{ACC1} = -75V$, $V_b = 950V$, $\dot{m} = 0.052\text{mgs}^{-1}$, $P_{fw} = 27.6W$) (b) Measured accelerator grid currents for SE1 and SE2 during variation of V_{ACC2}	136
6.5 Beam profiles of the ion beam extracted from SE2 during variation of the negative accelerator grid potential V_{ACC1} (with $V_{ACC2} = -75V$, $V_b = 950V$, $\dot{m} = 0.052\text{mgs}^{-1}$, $P_{fw} = 27.6W$)	137
6.6 Beam profiles of the ion beam extracted from SE2 during variation of the negative accelerator grid potential V_{ACC2} (with $V_{ACC1} = -75V$, $V_b = 950V$, $\dot{m} = 0.052\text{mgs}^{-1}$, $P_{fw} = 27.6W$)	137
6.7 Accelerator drain ratio (I_{ACC}/I_b) for SE1 and SE2 during V_{ACC1} variation at 0.052mgs^{-1} , $27.6W$	139
6.8 Accelerator drain ratio (I_{ACC}/I_b) for SE1 and SE2 during V_{ACC2} variation at 0.052mgs^{-1} , $27.6W$	139
6.9 Beam current determined from measured grid currents for SE1 (black) and SE2 (red) whilst either V_{ACC1} (solid line) or V_{ACC2} (dashed line) is varied. Also presented is the beam current determined from beam profiles for SE2 during variation of V_{ACC1} (blue circles) or V_{ACC2} (blue squares). Good agreement can be seen during variation of V_{ACC1} but not for V_{ACC2}	141
6.10 Log plots of the beam profiles of SE2 when $V_{ACC2} = -75V$, $-150V$ and $-300V$ (with $V_{ACC1} = -75V$, $V_b = 950V$, $\dot{m} = 0.052\text{mgs}^{-1}$, $P_{fw} = 27.6W$)	141
6.11 Net thrust out of SE1 determined from the measured grid currents for SE1 and SE2 during variation of the accelerator grid potential on either SE1 or SE2 at 0.052mgs^{-1} , $27.6W$	142
6.12 (a) Measured beam current for SE1 and SE2 during variation of V_{ACC1} (with $V_{ACC2} = -75V$, $V_b = 950V$, $\dot{m} = 0.058\text{mgs}^{-1}$, $P_{fw} = 38.1W$) (b) Measured accelerator grid currents for SE1 and SE2 during variation of V_{ACC1}	143
6.13 (a) Measured beam current for SE1 and SE2 during variation of V_{ACC2} (with $V_{ACC1} = -75V$, $V_b = 950V$, $\dot{m} = 0.058\text{mgs}^{-1}$, $P_{fw} = 38.1W$) (b) Measured accelerator grid currents for SE1 and SE2 during variation of V_{ACC2}	144
6.14 Beam profiles of the ion beam extracted from SE2 during variation of the negative accelerator grid potential V_{ACC1} (with $V_{ACC2} = -75V$, $V_b = 950V$, $\dot{m} = 0.058\text{mgs}^{-1}$, $P_{fw} = 38.1W$)	145
6.15 Beam profiles of the ion beam extracted from SE2 during variation of the negative accelerator grid potential V_{ACC2} (with $V_{ACC1} = -75V$, $V_b = 950V$, $\dot{m} = 0.058\text{mgs}^{-1}$, $P_{fw} = 38.1W$)	145
6.16 Accelerator drain ratio (I_{ACC}/I_b) for SE1 and SE2 during V_{ACC1} variation at 0.058mgs^{-1} , $38.1W$	146
6.17 Accelerator drain ratio (I_{ACC}/I_b) for SE1 and SE2 during V_{ACC2} variation at 0.058mgs^{-1} , $38.1W$	146
6.18 Beam current determined from measured grid currents for SE1 (black) and SE2 (red) whilst either V_{ACC1} (solid line) or V_{ACC2} (dashed line) is varied. Also presented is the beam current determined from beam profiles for SE2 during variation of V_{ACC1} (blue circles) or V_{ACC2} (blue squares). For this case at higher plasma density, the beam current determined from the beam profiles is not in agreement with that determined from the grid currents	147
6.19 Log plots of the beam profiles of SE2 when $V_{ACC2} = -75V$, $-150V$ and $-300V$ (with $V_{ACC1} = -75V$, $V_b = 950V$, $\dot{m} = 0.058\text{mgs}^{-1}$, $P_{fw} = 38.1W$)	148
6.20 Net thrust out of SE1 determined from the measured grid currents for SE1 and SE2 during variation of the accelerator grid potential on either SE1 or SE2 at 0.058mgs^{-1} , $38.1W$	149
6.21 Magnetic flux density for two six-turn induction coils separated by 16mm	152
6.22 Electric field distribution for two six-turn induction coils separated by 16mm	153

6.23 Resistive losses indicating power deposition within a Xenon discharge from two induction coils.....	153
6.24 Electron temperature within a cylindrical xenon discharge	154
6.25 Electron density within a cylindrical xenon discharge	155
6.26 Plasma potential within a cylindrical xenon discharge	155
6.27 Ion flux indicating that ions are predominantly lost radially to the walls	156
6.28 Resistive losses indicating power deposition, with a coil spacing of 10mm.....	157
6.29 Electron temperature within a cylindrical xenon discharge	157
6.30 Electron density within a cylindrical xenon discharge	158
6.31 Plasma potential within a cylindrical xenon discharge	158
6.32 Resistive losses indicating power deposition with varying coil currents.....	160
6.33 Electron temperature along discharge axis.....	161
6.34 Plasma density along discharge axis.....	161
6.35 Plasma potential along discharge axis.	162
6.36 Ion flux with varying coil current on one end.....	163
6.37 Comparison of plasma density and electron temperature along the boundary at each end of the discharge with varying coil current.....	164
6.38 Axial estimates of (a) electron temperature and (b) electron density obtained by triple Langmuir probe for the MiDGIT prototype thruster ($\dot{m} = 0.203\text{mgs}^{-1}$, $\nu_{\text{rf}} = 13.56\text{MHz}$)....	167
6.39 RMS coil current in induction coils 1 and 2 against phase difference between I_{C1} and I_{C2} during variation of the transmitter tuning capacitor on AMU1	170
6.40 Beam and accelerator grid against phase difference between I_{C1} and I_{C2} during variation of the transmitter tuning capacitor on AMU1.....	170
6.41 Thrust stepping by variation of the transmitter tuning capacitor on AMU1 ($V_{\text{ACCI}} = -95\text{V}$, $V_{\text{b}} = 950\text{V}$, $\dot{m} = 0.203\text{mgs}^{-1}$, $\nu_{\text{rf}} = 13.56\text{MHz}$).....	172
6.42 Net thrust during variation of the transmitter tuning capacitor on AMU1.....	172
6.43 Beam and accelerator grid currents during differential operation of the MiDGIT breadboard thruster. RF power to each induction coil was varied by adjustment of the antenna matching units. ($V_{\text{ACCI}} = -95\text{V}$, $V_{\text{b}} = 995\text{V}$, $\dot{m} = 0.058\text{mgs}^{-1}$, $\nu_{\text{rf}} = 5.25\text{MHz}$).....	174
6.44 Beam profiles of the ion beam extracted from SE1 during variation of AMU1.....	175
6.45 Beam profiles of the ion beam extracted from SE1 during variation of AMU2.....	175
6.46 Beam current determined from measured grid currents for SE1 (black) and SE2 (red) whilst RF power to the two induction coils is varied via the antenna matching units. Also presented is the beam current determined from beam profiles of SE1 during variation of AMU1 (blue circles) and AMU2 (blue triangles).....	176
6.47 Log plot of beam profiles obtained of SE1 during variation of AMU1. The beam profiles at low power display a two-tier distribution indicating a greater percentage of CEX interactions influencing the beam.....	177
6.48 Thrust determined for SE1 and SE2 during differential operation of the MiDGIT breadboard thruster. RF power to each induction coil was varied by adjustment of the antenna matching units.....	178
6.49 Net thrust during differential operation of the MiDGIT breadboard thruster.....	178
6.50 Specific impulse (determined from net thrust) during differential operation of the MiDGIT breadboard thruster	179
6.51 Resistive losses for a xenon discharge with a grid to coil spacing of (a) 10mm and (b) 15mm	180
6.52 Electron temperature for a xenon discharge with a grid to coil spacing of (a) 10mm and (b) 15mm.....	181
6.53 Ion flux for a xenon discharge with a grid to coil spacing of (a) 10mm and (b) 15mm	181

6.54	Comparison of ion density along grid boundary for a discharge with a 10mm grid-to-coil spacing and a 15mm grid-to-coil spacing	182
6.55	Comparison of electron temperature along grid boundary for a discharge with a 10mm grid-to-coil spacing and a 15mm grid-to-coil spacing	182
6.56	Electron flux for a xenon discharge with a grid to coil spacing of (a) 10mm and (b) 15mm	183
A.1	A typical I-V trace for a Langmuir probe.....	197
A.2	Values for parameter α used to determine Bohm current to a cylindrical Langmuir probe	203
A.3	Instantaneous probe characteristic in a plasma with an oscillating potential	207
A.4	Triple Langmuir probe circuit for direct-display of electron temperature and density.	209
A.5	Function $f(\phi_{12})$ for a cylindrical Langmuir probe for various $(e/K + \phi_f)$	213
B.1	Plot of plasma potential showing geometry of 2D axisymmetric discharge model.....	217
B.2	Plot of electron temperature with time showing convergence	218

List of Tables

1-1	Propulsion requirements for proposed formation flying missions.....	5
1-2	Performance data of thruster technologies considered suitable for formation flying spacecraft.....	13
1-3	Generic propulsion requirements for formation flying and drag compensation.....	18
2-1	Characteristic plasma properties of inductively coupled plasmas	22
2-2	Plasma diagnostic methods and their measurement capability.....	34
2-3	Scheduled performance data for the RIT microthrusters	52
3-1	Properties of ceramics considered for the MiDGIT discharge chamber.....	63
3-2	Summary of the grid geometry for the MiDGIT prototype.....	68
3-3	Electron backstreaming limit and maximum beam current and thrust at perveance predicted for the MiDGIT prototype grids	68
3-4	Summary of the grid geometry for the MiDGIT breadboard.....	70
3-5	Electron backstreaming limit and maximum beam current and thrust at perveance predicted for the MiDGIT breadboard grids.....	70
4-1	Attenuation of RF power between AMU and induction coil at 5.25MHz.	79
4-2	Beam and accelerator grid supplies and meters.....	81
4-3	Conditions for which a collisionless, thin sheath can be assumed for a 0.1mm diameter wire Langmuir probe inserted into a xenon discharge.....	96
5-1	Propulsion requirements specific to coarse thrust control.	101
5-2	Summary of breadboard configuration for single-end operation.....	102
5-3	Grid currents measured during initial variation of flow rate and RF power	107
5-4	Estimated beam current, beam divergence and thrust correction factor determined from the beam profiles of SE1 and SE2.....	113
5-5	Maximum thrust achieved by operating the MiDGIT breadboard thruster at higher .beam potential and lower background pressure.	124
5-6	Minimum thrust step at various flow rates for the SE1 and SE2 configurations of the MiDGIT breadboard thruster due to a 0.1dB change in forward RF power.....	126
5-7	Summary of the performance of the SE1 and SE2 configurations of the MiDGIT breadboard thruster (<i>neglecting neutralizer power and flow rate</i>).....	128
6-1	Propulsion requirements specific to fine thrust control.	129
6-2	Discharge conditions for the MiDGIT prototype for dual ion beam extraction.	131
6-3	Initial performance of the MiDGIT breadboard thruster during dual ion beam extraction, operating with $V_b = 950V$, $V_{ACC} = -95V$	131
6-4	Repeatability of measured forward RF power and rms coil currents during the three ..test cases.....	166
6-5	Beam and accelerator grid currents measured during differential operation of the MiDGIT prototype thruster at $\dot{m} = 0.203mgs^{-1}$, $\nu_{rf} = 13.56MHz$. Also listed are the capacitor and inductor settings of the AMUs and the rms current measured in each induction coil to indicate the effect of varying the transmitter tuning capacitor (C_T) of AMU1	169
6-6	Summary of initial performance demonstrated during differential operation of the MiDGIT breadboard thruster (<i>neglecting neutralizer power and flow rate</i>).	186
7-1	Comparison of the performance of the MiDGIT breadboard thruster against ...competing microthrusters.	193
A-1	Conditions defining four regimes of current collection by Langmuir probes..	203
A-2	Summary of assumptions and validity of the three main theories for ion current collection by Langmuir probes	205

Declaration of Authorship

I, *Cheryl Collingwood*, declare that the thesis entitled:

Investigation of a Miniature Differential Ion Thruster

and the work presented in the thesis are both my own, and have been generated by me as the result of my own original research. I confirm that:

- this work was done wholly or mainly while in candidature for a research degree at this University;
- where any part of this thesis has previously been submitted for a degree or any other qualification at this University or any other institution, this has been clearly stated;
- where I have consulted the published work of others, this is always clearly attributed;
- where I have quoted from the work of others, the source is always given. With the exception of such quotations, this thesis is entirely my own work;
- I have acknowledged all main sources of help;
- where the thesis is based on work done by myself jointly with others, I have made clear exactly what was done by others and what I have contributed myself;
- none of this work has been published before submission.

Acknowledgements

Firstly, I would like to thank Prof. Stephen Gabriel of the University of Southampton and Neil Wallace of QinetiQ for allowing me the opportunity to work on this project. Particular thanks go to Dr Michael Corbett (formally of QinetiQ) with whom I worked closely with during the test campaigns at the QinetiQ LEEP facilities. We both learned a lot about RF ion thrusters during that time! Special thanks also to Pete Jameson for managing the QinetiQ project work for the MiDGIT thruster, Mike Kelly for his skills in manufacturing the MiDGIT prototype and breadboard thrusters, Stephen Clark for assembling the electrical support equipment for the QinetiQ tests and Malcolm Fiddick for general assistance with the QinetiQ LEEP facilities.

At the University of Southampton I would like to thank Simon Klitz for his assistance in manufacturing probe and thruster supports for the EP1 chamber and for his help in getting some large vacuum chambers round some very tight corners! I would also like to thank technicians Clive Stafford and James Rabbetts for the general electrical support that they provided over the years.

On a personal note, I would like to thank my family for their support and understanding, particularly over the final few weeks of writing this thesis.

My sincerest thanks to Angelo for the support and inspiration you have given me – I hope you continue to climb to ever greater heights in your life.

Heartfelt thanks to Christine; good friends are like stars, you don't always see them but you know they are always there.

σ	Cross section, m^2
σ	Electrical conductivity, $\text{Ohms}\cdot\text{m}^{-1}$
ϕ	Potential, V
θ	Rotation angle, $^\circ$ or phase
Γ	Particle flux, $\text{m}^{-2}\text{s}^{-1}$
A	Plasma parameter
μ	mean
μ_0	Permeability of free space, $4\pi\times 10^{-7}\text{N}\cdot\text{A}^{-2}$
ν	Collision frequency, s^{-1} or Hz
ω	Angular frequency, $\text{rads}\cdot\text{s}^{-1}$

Subscripts

0	initial	ie	ion-electron
ACC	Accelerator	ii	ion-ion
b	beam	is	ion saturation
c	cyclotron or coil	Lp	Langmuir probe
e	electron	p	plasma
ebs	electron backstreaming	pe	plasma electron
ee	electron-electron	r	reflected
eff	effective	rf	radio frequency
es	Electron saturation	s	source, sheath or screen
eV	electron volt	T	Total
ex	exhaust		
f	final or floating		
fw	forward		
g	gas or grid		
i	ion		

Units: This thesis uses mks units of the Système International D'unités (SI); occasionally energies may be given in terms of electron volts (eV) but this will be stated.

List of Acronyms

ABR	Allen-Boyd-Reynolds
AMU	Antenna Matching Unit
AC	Alternating Current
BRL	Bernstein-Rabinowitz-Laframboise
BRFIT	Busek Radio Frequency Ion Thruster
CEX	Charge Exchange
CGT	Cold Gas Thruster
DC	Direct Current
DMM	Digital Multi Meter
DSMC	Direct Simulation Monte Carlo
EEDF	Electron Energy Distribution Function
ESA	European Space Agency
FCU	Flow Control Unit
FEA	Finite Element Analysis
FEEP	Field Emission Electric Propulsion
GIT	Gridded Ion Thruster
GPIB	General Purpose Interface Bus
GSTP	General Support Technology Programme
HV	High Voltage
ICP	Inductively Coupled Plasma
LEEP	Large European Electric Propulsion facilities
LISA	Laser Interferometer Space Antenna
LIF	Laser Induced Fluorescence
LV	Low Voltage
MC	Monte Carlo
MFC	Mass Flow Controller
MiDGIT	Miniature Differential Gridded Ion Thruster
OML	Orbital Motion Limited
PIC	Particle-In-Cell
PPT	Pulsed Plasma Thruster
PSCU	Power Supply and Control Unit
RF	Radio Frequency
RFG	Radio Frequency Generator
RIT	Radio-frequency Ion Thruster
SE	Single-end
SEERS	Self Excited Electron Resonance Spectroscopy
SWR	Standing Wave Ratio
TL	Thrust Level
TPF	Terrestrial Planet Finder
TRL	Technology Readiness Level
XEUS	X-ray Expanding Universe Spectroscopy mission

Chapter One

1. Introduction

The concept of flying multiple spacecraft in precise formations is being extensively studied as a means for enabling advanced space science and Earth observation missions [1,2]. The distribution of payloads over several platforms permits not only increased mission flexibility and reduced risk but will also allow significant improvements to the performance of space antennae and telescopes. The resolution and sensitivity of a telescope, for instance, are dependent on the size of the instrument's optics, which are limited for a single platform by launch mass and volume constraints. The ability to control spacecraft in precise formations will allow very large virtual instruments to be simulated by mounting instruments on separate spacecraft but controlling the spacecraft collectively to act as if they were a single, much larger body. A dual spacecraft configuration was suggested for the XEUS (X-ray Evolving Universe Spectroscopy) mission, for example, for achieving a focal length of 35m, improving resolution by 200 times to that of the current XMM-Newton X-ray telescopes [3].

Some of the most challenging formation flying missions currently envisioned involve constellations of spacecraft for interferometry applications, such as ESA's Laser Interferometer Space Antenna (LISA) [2] and NASA's Terrestrial Planet Finder (TPF) [4]. Interferometry provides a technique for very high resolution, narrow angle astrophysical imaging and involves the use of an array of detectors whose signals can be combined to produce interference fringes for image or measurement analysis. Angular resolution is not diffraction limited as for single structure telescopes but dependent on observation frequency and the separation distance (baseline) between detectors. To achieve the levels of resolution and sensitivity required to improve fundamental physics measurements and advance deep space observations, baselines up to several kilometres are desirable, which will only be achievable through spacecraft formation flying. Accurate reconstruction of signals from multiple spacecraft will require precise control of their relative positions so that the signals can be coherently combined. The ability to maintain translational position to within 1cm and

angular position to within 1 arcminute, as typically required by these missions, will impose very strict demands on a spacecraft's attitude control system, and subsequently any propulsion system employed on a spacecraft [5]. Thrusters capable of providing micro-Newton thrust levels, with sub- μN resolution and very low noise, will be essential for enabling precision pointing of spacecraft, particularly for performing optical path difference (OPD) control during scientific observations of interferometry missions. Additionally, higher thrust levels up to several milli-Newton will be required for orbit maintenance, failure recovery and reconfiguration or resizing of spacecraft constellations such as for adjusting resolution when changing target or observation wavelength. Typical durations for proposed formation flying missions range from nine months for technology demonstrator missions, up to several years for full science missions [6]. Any disturbances on the spacecraft, such as that due to solar radiation pressure, must also be offset by the propulsion system during these missions, requiring that thrusters provide constant positioning corrections and therefore be operated over long periods of time. It will be important that thrusters for formation flying applications provide a high ratio of thrust to rate of propellant consumed (i.e. specific impulse) to minimize propellant requirements for a mission. Formation flying missions have therefore been a key driver in the development of micropropulsion technologies that can provide very accurate thrust levels over the μN -mN thrust range at low power which are also able to meet strict mass and volume constraints for small spacecraft.

1.1 MICROPROPULSION FOR FORMATION FLYING

The term *micropropulsion* was initially defined by Micci and Ketsdever as “any propulsion system that is suitable for use on *microspacecraft*” (spacecraft with a mass of 20kg or less) and covers concepts from scaled-down versions of existing thruster technologies to new and innovative propulsion devices [7]. More generally, the term micropropulsion now tends to be used to indicate propulsion systems with μN -mN thrust capability and does not relate to the size of a spacecraft, as micropropulsion devices can also be used onboard larger spacecraft requiring precision attitude control. A comprehensive review of micropropulsion technologies was compiled by Mueller which compares system criteria to determine suitability of different thruster technologies for various mission scenarios [8].

1.1.1 Propulsion Requirements Important to Formation Flying

At the simplest level, a rocket (*or thruster, when referring to spacecraft applications*) generates thrust by expelling mass at high velocity which imparts a reaction force on the

system according to Newton's Third Law. The net force on an object is equivalent to the time rate of change of the (linear) momentum of the object, as stated by Newton's Second Law:

$$F = \frac{dp}{dt} \quad (1.1)$$

Therefore, the magnitude of the thrust imparted on a rocket can be equated to the rate of change of momentum of the expelled propellant:

$$T = \frac{\partial m}{\partial t} v_{ex} = \dot{m} v_{ex} \quad (1.2)$$

where v_{ex} is the effective exhaust velocity of the propellant and \dot{m} is the propellant mass flow rate [15].

The thrust delivered over a given interval is termed *impulse*:

$$I = \int T dt \quad (1.3)$$

The *specific impulse*, defined as the impulse (or conversely thrust) achieved per unit weight of propellant, provides a measure of the efficiency of a thruster. For steady state conditions, it can be related to the effective exhaust velocity of the propellant by:

$$I_{sp} = \frac{T}{\dot{m} g_0} = \frac{v_{ex}}{g_0} \quad (1.4)$$

where g_0 is the standard acceleration due to gravity. It is advantageous for any type of thruster to maximize exhaust velocity to achieve a desired thrust level to avoid a high consumption of propellant.

The two roles for propulsion systems onboard spacecraft are; *primary propulsion*, to impart translational velocity changes to a spacecraft required for orbit insertion, orbit transfer or stationkeeping; and *attitude control*, to impart rotational velocity changes.

Considering the principle of conservation of momentum, the translational velocity change imparted on a spacecraft (neglecting external forces) by an amount of propellant can be shown to be proportional to propellant exhaust velocity, and therefore specific impulse, by:

$$\Delta v = v_{ex} \ln\left(\frac{m_0}{m_f}\right) = (I_{sp} g_0) \ln\left(\frac{m_0}{m_f}\right) \quad (1.5)$$

with m_0 being the initial mass of a spacecraft including its fuel, m_f being the final (dry) mass of the spacecraft without fuel and Δv the velocity change of the spacecraft. This is the *ideal rocket equation* and indicates the importance of high specific impulse propulsion systems for missions of long duration or for performing high delta-v manoeuvres; high I_{sp} systems require lower propellant fractions for a given mission or manoeuvre, thus permitting mass and volume reductions over lower I_{sp} systems [15, 16].

The ability to provide very accurate, low thrust levels in the μN range will be an important criterion for thrusters regarding precision pointing capability. Thrusters for precision attitude control applications must be capable of providing very small *impulse bits* (I_{bit}), defined as the change in momentum applied per firing (or pulse) of a thruster.

The thrust required from each thruster to rotate a spacecraft about a single axis through a given angle θ_m can be given by:

$$T = \frac{4\theta_m I_M}{n L t_m^2} \quad (1.6)$$

where t_m is the manoeuvre time, n is the number of thrusters firing, I_M is the moment of inertia of the spacecraft and L is the moment arm [9]. Using equations 1.4 and 1.6 the total propellant consumption per unit time for performing the rotational manoeuvre in terms of specific impulse and impulse bit can therefore be defined by the following relation [9]:

$$\dot{m}_T = \frac{n^2 L (I_{bit})^2}{4\theta_m I_M I_{sp} g_0} \quad (1.7)$$

It can be seen that minimizing the impulse bit of a thruster has a greater effect on reducing the amount of propellant required for a given rotational manoeuvre over an increase to its specific

impulse. The minimum impulse bit (or resolution) of a thruster is therefore a key parameter that must be considered alongside other performance parameters such as specific impulse and specific power for precision pointing applications.

1.1.2 Micropropulsion Technologies Suitable for Formation Flying

Orbit and attitude control requirements for a number of formation flying missions have previously been analysed by London [10], Mueller [8], and de Groot [11]. Interferometry formation flying missions impose the strictest demands on a spacecraft's propulsion system, typically requiring thrust from 1 μ N up to mN level, impulse bits less than 1 μ Ns, and total impulse up to 10,000 Ns due to the long duration of these missions. Table 1-1 summarizes the propulsion requirements specified for a number of proposed formation flying missions.

	LISA	DARWIN	GAIA
Thrust level (Fine) (Coarse)	1-100 μ N 1N	1-150 μ N <10mN	- 1-500 μ N
Thrust Resolution	0.1 μ N	<3 μ N	1 μ N
Thrust Noise	0.1 μ NHz ^{1/2} (0.1mHz – 1 Hz)	1.65 μ NHz ^{1/2}	1 μ NHz ^{1/2} (1mHz – 1 Hz)
Response time	100 ms	130 ms	250 ms
Total Impulse	5000 Ns	1466 Ns	10,000 Ns
Lifetime	9000 hours @ 75 μ N	21900 hrs	18000 hrs @ 150 μ N

Table 1-1. Propulsion requirements for proposed formation flying missions.

Previous studies into micropropulsion technologies have identified cold gas thrusters (CGTs) as one of the most suitable propulsion options for formation flying missions [8,12]. Cold gas thrusters essentially comprise a pressurized tank containing an inert gas such as nitrogen or helium at high pressure, a valve which regulates the release of the gas and a nozzle which accelerates the gas to generate thrust. Conventional cold gas thrusters provide a very simple, low power, reliable and easily throttleable system capable of achieving the milli-Newton thrust levels required for orbit insertion, orbit maintenance and reconfiguration manoeuvres. Miniature CGTs are also being developed by use of MEMS technologies that are capable of low micro-Newton thrust levels required for precision attitude control, such as the AMPAC-ISP Micro-Newton Proportional Thruster (MPT) [13]. Though cold gas thrusters are a simple device, their performance is fairly poor as the exhaust velocity of the gas is restricted to low speeds; no additional energy is supplied to the gas through heating, and therefore, only pressure energy is available for conversion to kinetic energy. The specific impulse of CGTs is

usually of the order 60-70s. Heating the gas can increase specific impulse up to 100-120s, though performance at even this level would still impose large propellant demands on missions of long duration. Valve leakage rates are also a concern for miniature CGTs at the low thrust levels required for precision pointing applications [10].

All conventional propulsion systems that rely on nozzle expansion of a gas to convert stored energy in the propellant to directed kinetic energy for thrust (i.e. cold gas and chemical propulsion systems) have an associated fundamental limit to the exhaust velocity that they can achieve [9]. Considering 1-D isentropic compressible flow, nozzle theory can be used to provide a simple expression defining the propellant exhaust velocity achieved at the exit plane of a nozzle:

$$v_{ex} = \sqrt{\frac{2\gamma}{\gamma - 1} \frac{R_g T_0}{M} \left[1 - \left(\frac{p_e}{p_0} \right)^{(\gamma-1)/\gamma} \right]}$$

(1.8)

where R_g is the universal gas constant, γ is the ratio of specific heats of a gas, M is the molecular weight of the gas, T_0 is the absolute chamber (stagnation) temperature, and p_0 and p_e are the chamber pressure and the pressure at the exit of the nozzle respectively. A full derivation of this equation can be found in most books covering gas dynamic theory [14]. The specific heat ratio for most propellants is typically of the order 1.2 – 1.6 and therefore does not affect the exhaust velocity significantly [9]. The exhaust velocity, and subsequently the performance of a nozzle, are therefore mainly governed by the molecular weight of the gas, the temperature of the gas and the nozzle pressure ratio, and so, can be increased through the use of low molecular weight propellants, by minimizing (p_e/p_0) or by increasing the gas temperature. Maximizing the pressure difference across the nozzle through use of high chamber pressures however will be restricted due to structural limitations. Also, a theoretical maximum exhaust velocity exists if exhausting into vacuum (when $p_e = 0$) :

$$v_{ex,max} = \sqrt{\frac{2\gamma R_g T_0}{(\gamma - 1)M}}$$

(1.9)

The above value represents the finite thermal energy contained within the flow [15]. The exhaust velocity (for a choice of propellant) is only significantly affected by the temperature of the gas: energy can either be input by heating the gas using an external energy source or

increased via combustion. The maximum exhaust velocity will also be physically limited due to the maximum temperature that structural components can withstand and by the amount of energy stored in chemical bonds. Cold gas and chemical propulsion systems are therefore considered to be *energy limited*, as there is a fundamental limit to the thermal or chemical energy that can be converted to kinetic energy of the gas [15]. Exhaust velocities achieved by cold gas and chemical propulsion systems are restricted to less than 5km/s, with specific impulse less than 500s [16].

To increase performance above that achieved by chemical thrusters, and thus enable more complex and demanding space missions, requires a means of accelerating propellant that does not rely on the energy stored within propellant. Electric propulsion (EP) devices generate thrust by either electrically heating gas which is then expanded through a nozzle or by using electrostatic or electromagnetic fields to extract and accelerate ions from plasma to very high speeds [16]. The energy source for EP devices is independent of the thrust mechanism and the amount of energy that can be supplied is only limited by power available onboard a spacecraft, which can be supplied by solar panels or radio-isotope power sources. Electric propulsion devices can consequently achieve much higher exhaust velocities than conventional chemical thrusters and provide higher propellant efficiencies, though at the expense of higher power requirements. The specific impulse of EP devices can be up to two orders of magnitude greater than that achieved by chemical thrusters meaning they are highly suited for long duration missions or for performing high delta-v maneuvers of low mass spacecraft [16].

The high efficiency, high thrust accuracy and low thrust noise of EP systems have therefore also made them attractive candidates for formation flying missions. Research into electric propulsion technologies for micropropulsion applications has been summarized by London [10], Mueller [8] and Kilter and Karlsson [12]. Out of all the electric micropropulsion technologies currently developed, only a small number are considered suitable for formation flying applications; these are Field Effect Electric Propulsion (FEEP) thrusters, Pulsed Plasma Thrusters (PPT), colloid thrusters and miniature gridded ion thrusters.

1.1.2.1 Miniature Gridded Ion Thrusters

Gridded Ion Thrusters (GITs) are considered to be the most developed EP technology and have a considerable amount of flight heritage having been used for north-south station keeping (NSSK) on telecommunication satellites [17], for primary propulsion on interplanetary missions such as DAWN [18], and recently for precise atmospheric drag compensation of the GOCE spacecraft [19].

The concept of the gridded ion thruster involves the ionization of an inert gas, commonly xenon due to its relatively high mass and low ionization potential, from which ions are extracted and accelerated via electrostatic forces by use of biased multi-aperture grids. A schematic of a DC gridded ion thruster is shown in Figure 1.1. The extracted ions are accelerated to very high velocities, typically of the order of $30,000 \text{ ms}^{-1}$ across potentials of several kV applied between the grids [16, 47]. To maintain the spacecraft's potential, a neutralizer cathode is incorporated alongside the thruster to provide an electron current downstream of the positive ion beam to neutralize the beam. Any negative charge accumulation on the spacecraft would result in reduced thrust levels or, more importantly, back-streaming of ions towards the spacecraft with possible damaging effects through arcing or sputtering. The plasma discharge in GITs can be achieved via a number of different methods such as direct electron bombardment, whereby energetic electrons are emitted from an internal cathode into the discharge which then collide with neutral particles resulting in ionization, or by power coupling via radio frequency energy or microwaves to excite free electrons already present in the gas discharge for ionization [16,47].

Conventional gridded ion thrusters are generally 10cm-30cm in diameter, providing thrust from a few mN up to several 100mN, with high specific impulse of 3000s -10,000s and high efficiency, typically 60% or greater [16, 20-22, 47]. Several scaling-down studies have been conducted in recent decades to develop miniature gridded ion thrusters for μN thrust applications. Miniature gridded ion thrusters with diameters $<5\text{cm}$ have been developed by JPL [23], Busek [24, 25] and Astrium/Giessen [26, 27, 40, 41] which have demonstrated thrust from low μN level to several mN and specific impulse typically of the order 1500s. Ion thrusters however display poor efficiency on scaling down mainly due to high discharge losses; the ratio of surface-area to volume increases with decreasing discharge radius leading to greater ion recombination losses at the walls of the discharge chamber. Miniaturization of thruster components such as the discharge cathode have also proven challenging [23].

1.1.2.2 FEED Thrusters

Field Emission Electric Propulsion is an advanced electrostatic propulsion concept that has been predominantly developed within Europe which can provide very low thrust levels down to $\sim 1\mu\text{N}$, with higher precision and controllability than most other types of electric propulsion device [7]. Thrust is achieved by the extraction and acceleration of a beam of positive ions which have been generated at the surface of a liquid metal by the use of *field emission*; a process where electrons are extracted from a conducting material via quantum tunneling due to the application of an intense electric field [7]. This type of propulsion device avoids the use

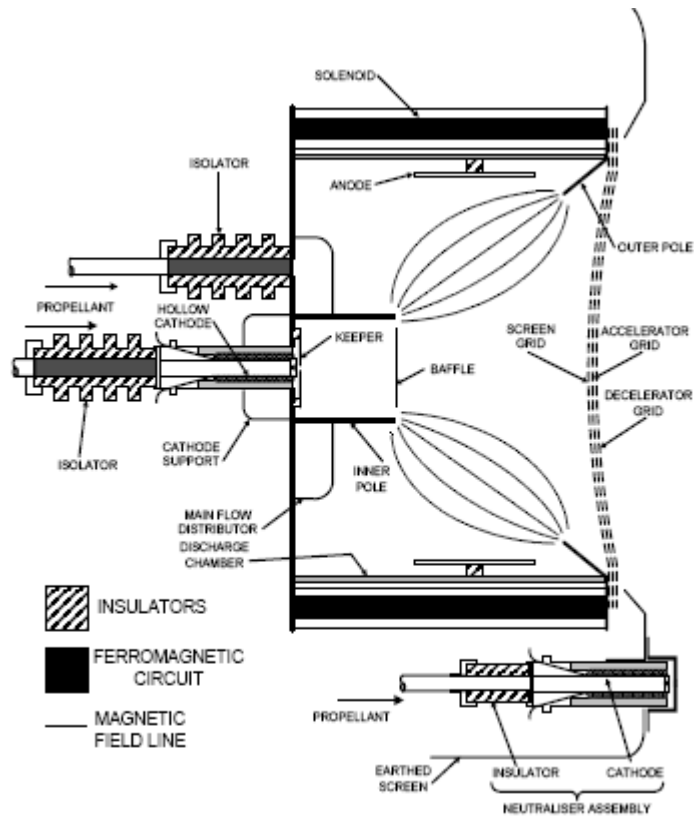


Figure 1.1. Schematic of the T5 gridded ion thruster ^[20].

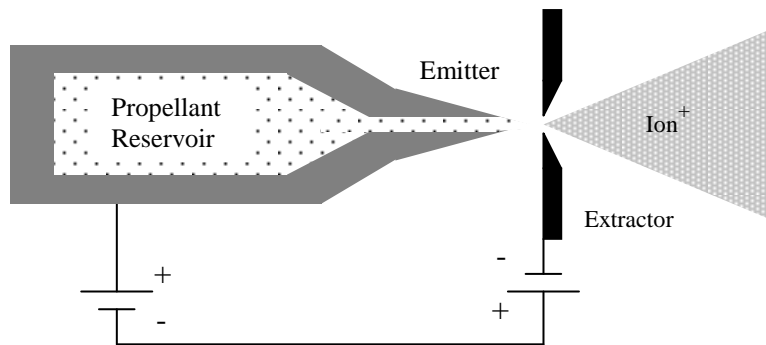


Figure 1.2. Schematic of a FEEP thruster.

of a gaseous discharge to generate ions and therefore FEEP thrusters are easily scalable to small sizes and are manufactured using MEMS techniques.

Two different designs for FEEP thrusters are currently being developed in Europe; one utilizing liquid cesium with slit shaped emitters by ALTA/Centrosazio [28], and one utilizing liquid Indium (a more benign propellant) with needle type emitters by the Austrian Institute of Technology (AIT) [29]. A typical schematic of a FEEP thruster is shown in Figure 1.2. A liquid metal is held within a propellant reservoir and due to capillary forces is forced into a narrow channel at one end. The channel ends in a tip separated from an extractor electrode. A high potential is applied between the tip and extractor electrode generating an intense electric field that deforms the liquid metal surface into cusps or '*Taylor cones*'. The electric field can reach $\sim 10^8 \text{ Vcm}^{-1}$ at the tip of the Taylor cone, permitting electrons to be stripped from metal atoms at the tip. The generated ions are then accelerated away from the liquid metal by the extraction electrode producing a beam of ions for thrust, whilst the free-electrons are collected through the liquid metal bulk by the channel walls.

1.1.2.3 Colloid Thrusters

Colloid thrusters are similar to FEEP thrusters but utilize electrolytic fluids as propellant [30, 31]. Incomplete ionization of the fluid at the tips of the Taylor cones results in charged droplets being extracted from the capillary instead of ions. Colloid thrusters require micro-machined pumps to control the flow of the fluid, thus increasing their complexity compared to FEEP thrusters. The specific impulse for colloid thrusters is lower than that achieved by FEEP thrusters but is still above that achieved by cold gas thrusters for them to be considered suitable for micropropulsion applications. A general schematic of a colloid thruster is shown in Figure 1.3.

1.1.2.4 Pulsed Plasma Thruster

Pulsed Plasma Thrusters (PPTs) are an electromagnetic EP device; the most common type being the ablative PPT which was first flown on the Soviet Zond-2 spacecraft in 1964 [7, 33]. The ablative PPT generally uses solid TeflonTM as propellant. A solid bar of TeflonTM is positioned between two electrodes; a high voltage pulse is initially applied to a spark plug to ablate a small amount of propellant from the front face of the bar. A capacitor then discharges across the electrode gap, ablating more TeflonTM and ionizes a fraction of the vapour. The ions generated are accelerated away via the Lorentz force to provide thrust, reaching high velocities up to several 1000ms^{-1} . A second component of thrust arises due to the thermal

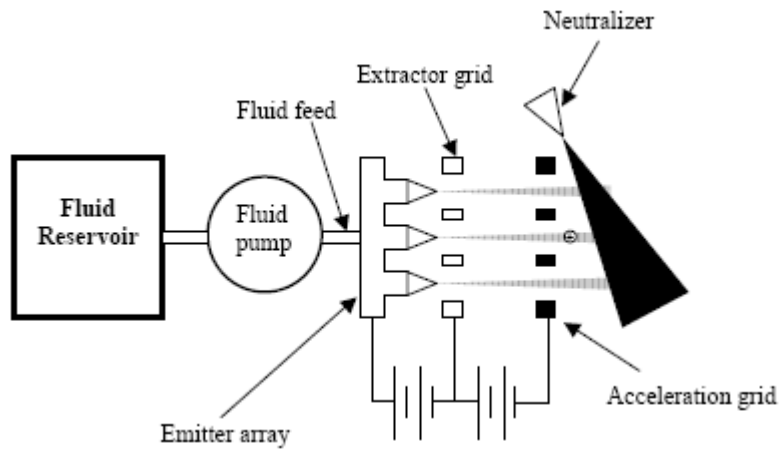


Figure 1.3. Schematic of a colloid thruster ^[30].

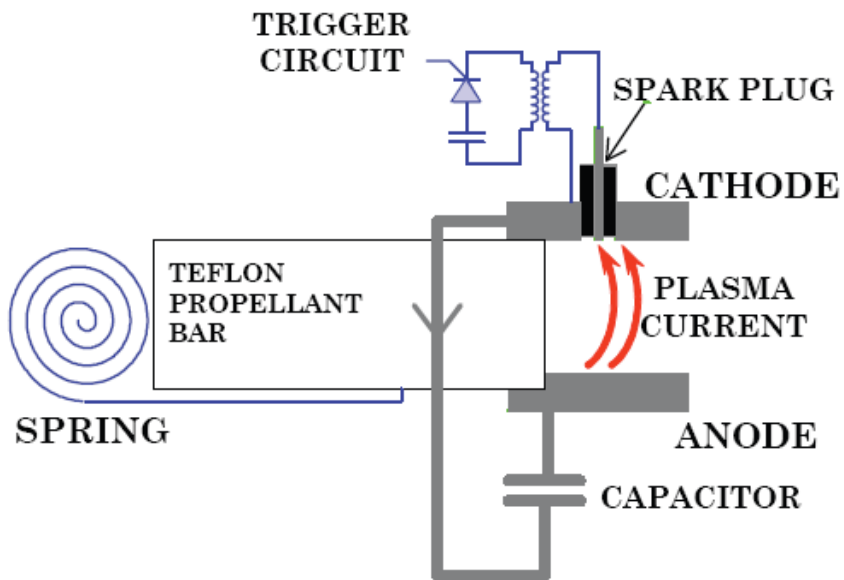


Figure 1.4. Schematic of an ablative pulsed plasma thruster ^[32].

expansion of the non-ionized propellant, but due to its low velocity does not contribute significantly to the total thrust. A spring located at the rear of the Teflon™ block provides a force to push the bar forward for the next firing. The general design of an ablative PPT can be seen in Figure 1.4.

Ablative PPTs can achieve very small, precise impulse bits of the order 100μNs. The minimum impulse bit can be varied by changing the amount of energy stored in the capacitor by varying the charge time. Thrust can therefore be varied by changing the pulse frequency. Conventional ablative PPTs have demonstrated thrust levels between ~50μN and 4.5mN, with specific impulse between 400s – 1700s [34]. A number of miniature pulsed plasma thrusters (μPPT) are under development by AIT [35], Busek [36] and MarsSpace [37] for application on nanosatellite missions. Pulsed plasma thrusters are very compact systems as they do not require propellant tanks or feed lines. The power processing electronics for PPTs, ultimately the energy storage capacitor, currently limit the degree of miniaturization of pulsed plasma thrusters.

Performance data of different cold gas and EP thrusters which have been considered for formation flying applications are summarised in Table 1-2. FEEP thrusters, colloid thrusters and μPPTs are each capable of providing very small impulse bits at μN thrust levels and thus are considered well suited for precision attitude control applications. Due to a low thrust-to-power ratio however, they are not appropriate for mN thrust applications. Contamination effects on optical payloads and other spacecraft subsystems also raise concern over the use of these particular EP devices. The sensitivity of cesium (and to a lesser degree, indium) to atomic oxygen has also raised concern over the use of FEEP thrusters on low Earth orbiting missions; oxidation of the liquid cesium can lead to clogging of the emitters [38]. Gridded ion thrusters however operate on inert gases such as argon and xenon and have higher thrust-to-power ratios. They are also capable of achieving significantly higher specific impulse than other EP devices making them attractive for long duration missions. Though μPPT are considered for precision attitude control applications, the pulse-mode operation of μPPTs may lead to low level vibrations being induced in structural components of a spacecraft. Therefore, μPPTs may not be able to meet the strict noise and stability requirements of the most demanding formation flying missions, such as those for interferometry. They also do not have the total impulse capability for these missions. Any disturbance torques acting on a spacecraft must also be compensated by the propulsion system; only proportional thrusters, such as cold gas, miniature gridded ion and FEEP thrusters, which are able to provide continuous and variable thrust levels and which also have a fast response time, are therefore suitable for high precision formation flying missions [39]

Thruster	Propellant	Thrust range		I_{bit}	I_{sp}	Thruster efficiency	Power (W)	Specific Power (W/mN)	Mass	TRL
		Min	Max							
Cold Gas	He, Xe, N ₂	1 μN	10mN	1 μNs-10mNs	60-120	>95%	<5	<3	<0.3kg	5-9
MOOG 58X125A	N ₂	-	4.4	-	65	-	2.4	-	7.3g	9
AMPAC-ISP SV14-002	N ₂ , Xe	0	10mN	-	70	-	<3.5	0.0875	75g	8
AMPAC-ISP VP03-001	He, Xe, N ₂	0	1mN	-	>70	-	-	-	<300g	-
Bradford Proportional Micro Thruster	He, Xe, N ₂	1 μN	2mN	-	65-76	-	<4.5	2.25	175g	5/6
FEFP	Cs, In	0.25 μN	500 μN	0.01 μNs	1000-10,000	60-95%	10-150	60-90	<3kg	4/5
ALTA/Centraspazio FT-150	Cs	0.3 μN	200 μN	-	4500	-	-	60	1.41kg	-
AIT needle	In	1 μN	100 μN	5nNs	1600-8000	90%	13	75 40-55	2.5kg	-
AIT porous tungsten	In	0.25 μN	>450 μN	-	4000-8000	-	-	80 60-85	-	-

Table 1-2. Performance data of thruster technologies considered suitable for formation flying spacecraft (continued over page).

Thruster	Propellant	Thrust range		I_{bit}	I_{sp}	Thruster efficiency	Power (W)	Specific Power (W/mN)	Mass	TRL
		Min	Max							
Colloid		0.5 μ N	500 μ N		400-1500	75%	10	10-50	<3kg	
Busek	Formamide	20 μ N	190 μ N	-	400	-	6	-	2.5kg	-
Queen Mary	EMI-BF ₄	5 μ N	500 μ N	-	-	-	-	50	-	-
Stanford	Glycerol	0.5 μ N	4.0 μ N	-	200	-	6		0.5kg	-
Ablative PPT	Teflon	61 μ N	1mN	70 μ Ns	200-1500	10%	2-75	60	7kg	
NOVA	Teflon	-	378 μ N	378 μ Ns	300	3%	30	80	6.35kg	-
LES 8/9	Teflon	-	600 μ N	300 μ Ns	1075	7%	26	43	7.33kg	-
AFRL XPPT-48	Teflon	-	1mN	1mNs	1125	7%	75	75	10.5kg	-
AFRL μ PPT	Teflon	-	150 μ N	15 μ Ns	800	6%	10	67	<1kg	-
Busek/AFRL two-stage μ PPT	Teflon	-	171 μ N	-	1066	-	4.5	94	-	-
Aerojet Dawgstar μ PPT	Teflon	61 μ N	264 μ N	60 μ Ns	266	-	15	57	4.20kg	-
AIT μ PPT	Teflon	-	-	10-30 μ Ns	>500s	-	<2	-	<0.1kg	-
Ion Thrusters	Xe	10 μ N	3.5mN		3000	50%	<150	40		4
MIXI	Xe	0.5mN	3mN	-	3100	-	<100	-	-	4
μ RIT	Xe	10 μ N 150 μ N	200 μ N 3.5mN	-	3700	50%	-	40	-	4

Table 1-2 (continued). Performance data of thruster technologies considered suitable for formation flying spacecraft.

1.2 MOTIVATION FOR RESEARCH

Propulsion systems capable of providing low but highly accurate thrust levels in the sub- μN to mN throttling range will be an enabling technology for complex formation flying missions. It is evident however, by comparison of propulsion requirements specified for formation flying missions and the performance of current thruster technologies, that different propulsive tasks cannot currently be performed by a single device. Figure 1.5 highlights that no single thruster developed to date has demonstrated the full thrust range from $<1\mu\text{N}$ up to several mN typically required by formation flying spacecraft. Propulsion systems baselined for formation flying missions have therefore often comprised either a complete cold-gas system utilizing both conventional and miniature CGTs (provided that propellant mass and volume requirements can be accommodated) or systems combining cold gas thrusters for coarse attitude control and miniature EP thrusters for precision attitude control [12].

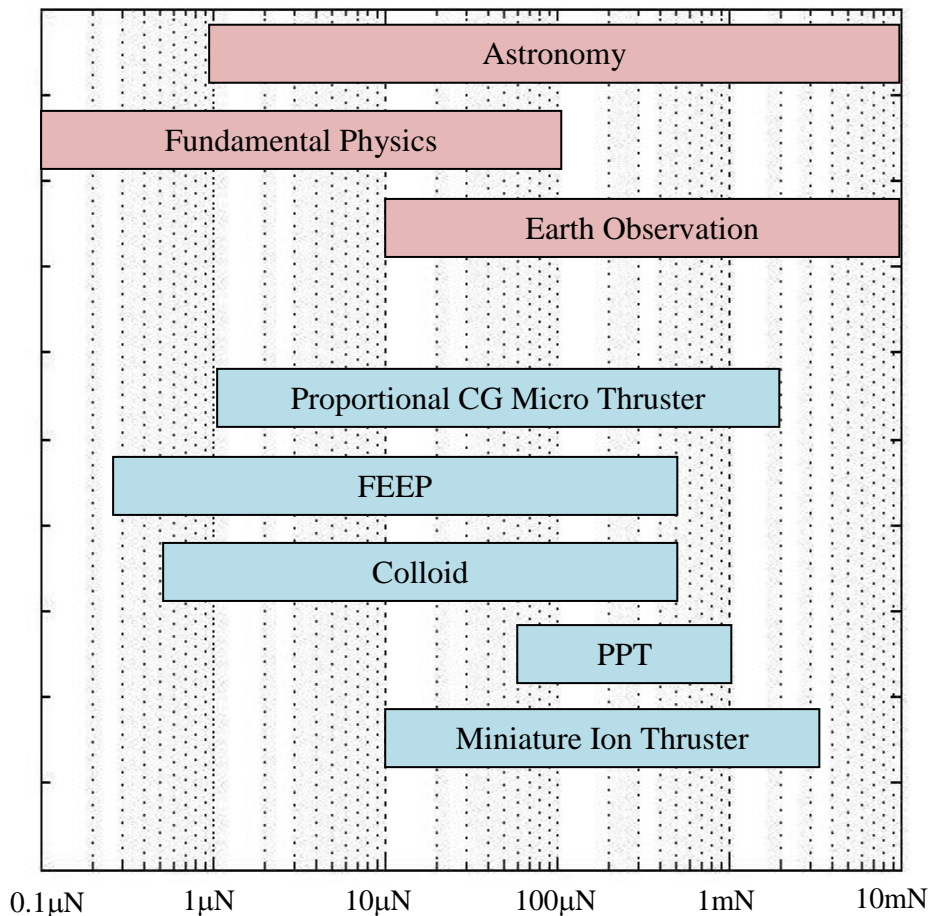


Figure 1.5. Plot comparing required thrust range for science and Earth observation missions with the current performance of various thruster technologies.¹

¹ Figure adapted from [116].

A fully redundant propulsion system for 3-axis (6 degrees-of-freedom) control of a spacecraft could require up to 24 thrusters depending on the configuration options for thruster accommodation. If two different types of thruster are needed to meet the orbit and attitude control requirements for a given mission, up to 48 thrusters might therefore be required. The total mass of the propulsion system would be even greater for a system utilizing thrusters operating on different types of propellant, as separate propellant storage tanks and flow control components would be needed.

The benefits provided by electric propulsion over chemical propulsion would make an all-electric propulsion system more attractive than a complete cold gas system for a large number of mission scenarios. The RIT- μ X propulsion system, utilizing miniature radio frequency ion thrusters developed by the University of Giessen, has recently been proposed as an all-electric μ N-mN propulsion system for formation flying spacecraft [40]. A thrust range of less than 1μ N to several mN is inherently difficult to achieve from a single gridded ion thruster however (as will be outlined in Chapter 2). The RIT- μ X system is therefore designed around a set of different sized thrusters with interchangeable grids that can be selected in combination to meet specific requirements for a mission. The minimum thrust level currently demonstrated by one configuration of thruster is $\sim 10\mu$ N, with a thrust range up to 200μ N [41]. Thrust levels less than 1μ N have not yet been reported. An all-electric propulsion system utilizing just a *single* type of thruster with both coarse and precision control capabilities would provide a more optimal solution. A need for a precision, low thrust, miniature electric propulsion device with a wide throttling range therefore exists.

The concept of a *differential* gridded ion thruster was proposed by Wallace [43] of the Ion Propulsion Group of QinetiQ to address this requirement. It was proposed that an unprecedented throttling range and thrust resolution could be achieved through differential control of opposing ion beams, enabling very small net offsets in thrust to be achieved (as shown schematically in Figure 1.6). The proposed Miniaturised Differential Gridded Ion Thruster (MiDGIT) would be sized to achieve μ N thrust levels through differential ion beam control but would also have the capability of single ion beam operation, as for conventional gridded ion thrusters, for achieving mN thrust levels with high specific impulse required for orbit control manoeuvres.

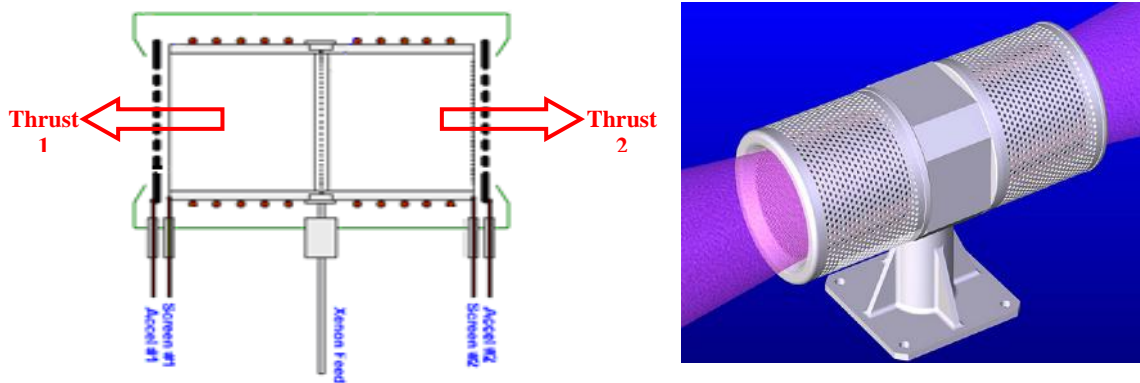


Figure 1.6. The basic configuration of the MiDGIT thruster.

A contract was awarded to QinetiQ by the European Space Agency (ESA) under the General Support Technology Programme (GSTP) to develop a breadboard model of the MiDGIT thruster. Orbit and attitude control requirements for a number of ESA proposed drag compensation and formation flying missions were analyzed by Jameson [42] to provide a basis for the design and evaluation of the thruster. The set of generic propulsion requirements derived from this assessment are provided in Table 1-3.

Essentially two design options exist for a differential ion thruster; one comprising two individual single-ended ion thrusters firing in opposite directions, and one comprising a twin-ended ion thruster utilizing a common discharge chamber. Differential control of two individual thrusters would require accurate matching of the discharge conditions in each thruster, which would be technically challenging and would lead to relatively complex thruster control algorithms. The use of a twin-ended thruster would provide system benefits, such as reduced system complexity and mass through the use of shared components, and would also allow a greater level of redundancy but would require considerable development.

A trade-off was conducted by QinetiQ of the two configuration options for the MiDGIT thruster, following which the twin-ended thruster configuration was selected. As mentioned, the use of a common discharge chamber would reduce system complexity and mass through shared components but would also impose less strict demands on power conditioning and flow control systems compared to the use of two single-ended thrusters (these points will be briefly outlined in Chapter 3).

	Fine	Coarse
Thrust range	1 – 150 μ N	150 μ N to >1mN
Thrust resolution	<0.5 μ N	<0.5 μ N
Thrust repeatability	0.5 μ N	0.5mN
Thrust linearity and bias	0.5 μ N	0.5 μ N
Specific impulse	>90s @ 12 μ N	>1500s @ 1mN
Specific power	<50W/mN	
Thrust noise (1mHz – 1Hz)	1.65 μ N/ $\sqrt{\text{Hz}}$ up to 100 μ N	
Thrust response time	60ms	
Thrust actuation frequency	100Hz	
Total impulse	40kNs	
Lifetime	21900hrs	
Thrust direction stability	0.2°	
Beam divergence	<25°	
Mass	<44kg for 3 axis system	
Volume	< 294dm ³ for redundant 3 axis system	
Thermal	50/+100°C (non operating) -20/+70°C (operating)	
Radiation	>10krad	

Table 1-3. Generic propulsion requirements for formation flying and drag compensation ^[42].

Consideration was also given to the type of thruster that would be suitable for a miniature differential ion thruster. Differential control of multiple ion beams extracted from a common plasma discharge will require the individual beam currents to be resolved. This would not be possible for a single-anode design of a DC gridded ion thruster, as only the total combined beam current could be monitored. Also, miniaturization of the discharge cathode and optimization of the magnetic field configuration was considered to require significant effort (these have been identified to be important by Wirz [23]). The beam current in radio frequency (RF) ion thrusters however can typically be monitored by the electron current to the screen grid of the thruster, which effectively acts as an anode. Provided the individual screen grid currents of separate grid sets can be monitored, an RF ion thruster provides the simplest thruster design to enable differential ion beam control. An inductive plasma discharge was therefore selected as the ionization mechanism for the MiDGIT thruster.

1.3 RESEARCH AIMS AND OBJECTIVES

The primary objective of the collaborative project with QinetiQ was "*to design, manufacture and test a breadboard mini ion engine that is capable of providing both micro and milli-Newton level thrust, and consequently be able to perform both orbit control and attitude control for a wide variety of future drag compensation and formation flying missions*" [43].

A differential ion thruster utilizing a radio frequency inductive plasma discharge was selected by QinetiQ to meet this objective. The extraction of two independent ion beams from a gridded ion thruster has never previously been reported. The key aim of the work presented in this thesis was to provide a proof-of-concept for the proposed MiDGIT thruster involving verification of the following:

- 1 The feasibility of extracting two ion beams simultaneously from a common plasma discharge.
- 2 The feasibility of individually controlling the ion beams to produce a net offset in thrust.
- 3 The feasibility of switching to a single ion beam mode for achieving higher thrust and specific impulse levels.

Prototype and breadboard models of the thruster were manufactured in order to investigate design issues and identify engineering constraints of a differential ion thruster. Characterisation of the breadboard thruster was then performed to demonstrate preliminary performance and evaluate the concept of the MiDGIT thruster for formation flying applications. The work presented in this thesis contributes to the first detailed characterisation of a twin-ended radio frequency gridded ion thruster; the particular significance of the work is detailed in Chapter 7.

1.4 THESIS OUTLINE

The baseline design of the MiDGIT thruster was selected to comprise an inductive plasma discharge from which multiple ion beams could be extracted. A review of RF ion thrusters was therefore conducted by the author to aid the design of the MiDGIT thruster; this is presented in Chapter 2. The review begins by introducing theory relevant to the discharge mechanism of RF ion thrusters and then provides an overview of RF ion thruster design and operation.

A description of the MiDGIT concept is provided in Chapter 3, including a summary of design and operational issues of a *differential* RF ion thruster. The design and geometry of prototype and breadboard models manufactured of the MiDGIT thruster are also included.

Test campaigns were performed on the prototype and breadboard thrusters to provide a proof-of-concept for the MiDGIT thruster. The experimental arrangement and procedures employed during these tests are described in Chapter 4. A detailed characterisation of the MiDGIT breadboard thruster was performed in collaboration between the author and QinetiQ to determine baseline performance. The performance of the MiDGIT breadboard thruster operating in single-end mode is presented in Chapter 5. Investigations into differential ion beam control by the author and differential performance tests on the MiDGIT breadboard thruster by the author and QinetiQ are presented in Chapter 6.

Principle conclusions are summarised in Chapter 7 including a brief assessment of the MiDGIT thruster with regards to suitability for missions requiring precision attitude control. The significance of the research and recommendations for future work are also given in Chapter 7.

Chapter Two

2. Radio Frequency Ion Thrusters: Background and Literature Review

The concept of the radio frequency ion thruster was first developed by Prof Loeb of Giessen University in the 1960's utilizing the principle of an inductive plasma discharge [44]. RF ion thrusters are attractive for scaling down for micropropulsion applications as the discharge mechanism does not require electrodes in direct contact with plasma. This chapter will begin by providing a summary of inductively coupled plasmas to give an insight into the discharge processes occurring in radio frequency ion thrusters. The general design and operation of RF ion thrusters will then be discussed and a review of research into miniature RF ion thrusters will be provided.

2.1 INDUCTIVELY COUPLED PLASMA DISCHARGES

An electric discharge in a rarefied gas by induction from an external coil was first observed by Hittorf in 1884 [45]. Over the past century this type of discharge has been extensively studied and is often referred to today as an inductively coupled plasma discharge (ICP), radio frequency inductive discharge (RFI) or H-type discharge. ICP discharges generate plasmas with high electron density at low neutral pressures without the need of internal electrodes. They are therefore attractive for the applications of materials processing and spectroscopy and are also found in the fusion community as ion sources for the production of high-energy neutral beams [46]. Characteristic properties of ICPs are given in Table 2-1. The collision rate between electrons and neutral gas molecules in low pressure ICPs is relatively low and therefore ICPs are generally weakly ionized, non-equilibrium plasma. The electron temperature is considerably higher than that of the ions and neutral gas molecules, whose temperatures approximate that of a gas at room temperature. The electron energy distribution function (EEDF) is typically non-Maxwellian in ICPs, though at relatively high densities electron coulomb collisions can drive the EEDF towards a Maxwellian [46].

Plasma parameter	Typical value
Pressure, p	<10 mTorr
Operating frequency, ν_{rf}	1 - 30 MHz
Plasma density, n_e	$10^{16} \leq n_e \leq 10^{19} \text{ m}^{-3}$
Electron Temperature, T_e	$1 \leq T_e \leq 10 \text{ eV}$
Electron Debye length, λ_d	$6 \leq \lambda_d \leq 150 \text{ }\mu\text{m}$
Ion-neutral mean free path, λ_{in}	$4 \text{ mm} \leq \lambda_{in} \leq 1 \text{ m}$
Electron-neutral mean free path, λ_{en}	$2 \text{ cm} \leq \lambda_{en} \leq 1 \text{ m}$
Electron-neutral collision frequency, ν_{en}	$1 \leq \nu_{en} \leq 50 \text{ MHz}$

Table 2-1. Characteristic plasma properties of inductively coupled plasmas ^[46].

A common configuration for an ICP source consists of a cylindrical, dielectric vessel containing plasma surrounded by a conducting coil to which an oscillating current is applied to generate an RF field. The time-varying axial magnetic field within the coil is proportional to the RF current and is given by:

$$B_z = \mu_0 \frac{N}{l} I_{RF} e^{i\omega t} \quad (2.1)$$

where N/l is the number of coil turns per unit length of the coil and ω is the RF cyclic frequency ($\omega_{rf} = 2\pi\nu_{rf}$).

The magnetic field of the induction coil penetrates the vessel inducing an azimuthal electric field in the plasma according to Faraday's Law.

$$\nabla \times \vec{E} = -\frac{\partial \vec{B}}{\partial t} \quad (2.2)$$

The azimuthal electric field can be approximated by:

$$E_\theta = -\frac{i\omega r}{2} B_{z0} e^{i\omega t} \quad (2.3)$$

where B_{z0} is the peak axial magnetic field and r is the distance from the axis.

The induced electric field accelerates electrons within the plasma, which then collide with and ionize neutral gas atoms leading to a self-sustaining discharge. The (electron) plasma current in turn induces a current back in the induction coil, opposite to that which is driven through the coil. The resistance of the induction coil therefore increases in the presence of a plasma load.

A parasitic capacitance can exist between the induction coil and plasma due to the often high voltage across the coil, and due to the dielectric wall and plasma sheath effectively acting as a capacitor. Power can therefore be coupled to the plasma by both inductive coupling and capacitive coupling in an inductive discharge [46].

2.1.1 General Plasma Properties of Inductively Coupled Plasma

Charge separation can occur naturally in plasma due to the mobility of electrons being greater than the heavier ions, resulting in electric fields caused by localized variations in charge density. The electrons and ions tend to move in turn to screen these electric fields to maintain neutrality. The characteristic distance over which charge carriers shield the electric fields is given by the Debye length [46]. In non-equilibrium plasma, where the electron temperature is higher than that of ions, the Debye length λ_d is given by:

$$\lambda_d = \left(\frac{\epsilon_0 k T_e}{n_e e^2} \right)^{1/2} \quad (2.4)$$

where ϵ_0 is the permittivity of free space, k is the Boltzmann constant, T_e is the electron temperature in Kelvin, n_e is the plasma electron density and e is the charge of an electron. For inductively coupled plasmas with characteristic high density in the region $10^{16} \leq n_e \leq 10^{18} \text{m}^{-3}$, the Debye length is typically very small, of the order of several microns [46].

Oscillations of the electrons and ions will occur due to their movement to screen the disturbances in charge density. The characteristic frequency of the oscillations is termed the *plasma frequency* and provides a fundamental time-scale for plasma processes [46]. As electrons are lighter than ions and generally have greater thermal velocities, the plasma frequency can be approximated by the electron plasma frequency:

$$\omega_{pe} = \frac{(kT_e/m_e)^{1/2}}{\lambda_d} = \left(\frac{e^2 n_e}{\epsilon_0 m_e} \right)^{1/2} \quad (2.5)$$

where m_e is the electron mass.

In bounded plasmas, electrons and ions will diffuse to the walls of the containing vessel and recombine on the surface. Due to the higher mobility of electrons, electron flux to the walls will be greater than the ion flux and a potential gradient will form close to the wall, with the plasma at a positive potential with respect to the wall [46]. The retarding electric field to electrons will act to repel electrons at the plasma boundary in order to maintain quasineutrality within the bulk of the plasma. The region where quasineutrality does not hold near the plasma boundary is called the *sheath* [46].

The general non-linear equation governing the potential across the sheath derived from Poisson's equation and assuming $n_e = n_i$ at the plasma-sheath boundary [46], is given by:

$$\frac{d^2\phi}{dx^2} = \frac{en_s}{\epsilon_0} \left[\exp \frac{e\phi}{kT_e} - \left(1 - \frac{\phi}{\epsilon_s} \right)^{-1/2} \right] \quad (2.6)$$

where n_s is the plasma density at the sheath edge and ϵ_s is the initial energy of ions (at the plasma-sheath boundary) which enter the sheath, given by:

$$e\epsilon_s = \frac{1}{2} M_i u_s^2 \quad (2.7)$$

Equation 2.6 can be shown to only have stable solutions when the velocity of ions is sufficiently high, such that:

$$u_s \geq u_B = \left(\frac{kT_e}{M_i} \right)^{1/2} \quad (2.8)$$

This is the *Bohm sheath criterion* which states that in order for a stable and monotonically decreasing potential to form across the sheath, the velocity of ions that enter the sheath must be greater than the *Bohm velocity* given above [46,47]. In order for the ions to reach this velocity, the ions must fall through a potential in the plasma of at least $(kT_e/2e)$ volts.

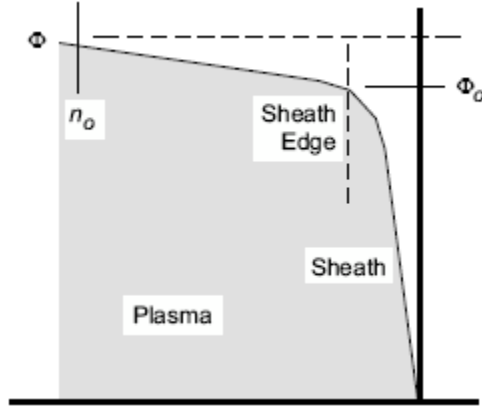


Figure 2.1. Diagram to illustrate the presheath and sheath regions in a plasma ^[47].

The plasma produces this required potential drop across a region which is known as the *presheath* in order to accelerate the ions (as depicted in Figure 2.1) [46,47].

The extent to which RF fields interact with plasma depends on the electron plasma frequency ω_{pe} , the applied RF frequency ω_{rf} , and electron collisions occurring in the plasma, as these determine the electrical conductivity of the plasma and the degree to which electromagnetic waves are attenuated in plasma [46].

The (complex) electrical conductivity $\bar{\sigma}$ of an inductive plasma is given by:

$$\bar{\sigma} = \frac{e^2 n_e / m_e}{\nu_{eff} + i\omega_{rf} + \omega_c^2 / (\nu_{eff} + i\omega_{rf})} \quad (2.9)$$

where ν_{eff} is an effective electron momentum-transfer collision frequency depending on the collisional processes in the plasma [46] and ω_c is the electron cyclotron (or gyro) frequency given by:

$$\omega_c = \frac{eB_z}{m_e} \quad (2.10)$$

If $\omega_c \ll \omega_{rf}, \nu_{eff}$ then the complex plasma conductivity reduces to:

$$\bar{\sigma} = \frac{e^2 n_e}{m_e (\nu_{eff} + i\omega_{rf})} \quad (2.11)$$

Also, if $\omega_{rf} \ll \nu_{eff}$, the plasma conductivity reduces further to what is termed the *dc plasma conductivity* [46]:

$$\sigma_{dc} = \frac{e^2 n_e}{m_e \nu_{eff}} \quad (2.12)$$

The effective distance that an electromagnetic field penetrates into a conducting material such as plasma, is termed the skin depth which is defined as "*the depth below the surface of a conductor which is carrying a current at a given frequency due to electromagnetic waves incident on its surface, at which the current density decays to 1/e of the current density at the surface*" [48]. The skin depth therefore defines the volume over which RF energy is transferred to the plasma electrons from the RF fields.

When electron collisions occur at a much slower rate compared to the RF period (where $\nu_{eff} \ll \omega_{rf}$) the skin depth can be found to be independent of the RF frequency [46] and is given by:

$$\delta_p = \left(\frac{m_e}{e^2 \mu_0 n_e} \right)^{1/2} \quad (2.13)$$

In the collisional regime, where $\nu_{eff} \gg \omega_{rf}$, the skin depth is:

$$\delta_c = \left(\frac{2}{\omega_{rf} \mu_0 \sigma_{dc}} \right)^{1/2} \quad (2.14)$$

and decreases as RF frequency increases. At high frequencies and high plasma density, the skin depth may become much less than the radius of a cylindrical, bounded plasma and power will mainly be deposited within a ring around the edge of the plasma.

The real part of the inverse plasma conductivity defines the plasma resistance. In the case of cylindrical discharges this can be written as:

$$R_p = Re \left[\frac{1}{\sigma} \right] \frac{l_{path}}{A_{path}} \quad (2.15)$$

where l_{path} and A_{path} are the circumference and cross sectional area of the plasma ring formed as a result of the skin effect [46]. Assuming a plasma radius r , length l_p and skin depth δ , the plasma resistance can be given by:

$$R_p = \frac{\pi r}{\sigma_{dc} l_p \delta} \quad (2.16)$$

2.1.2 Heating of Electrons and Non-Linear Effects in Inductively Coupled Plasma

There are several different heating mechanisms important for transferring energy to electrons within plasmas; ohmic heating, collisionless heating (or stochastic heating), resonant wave-particle interaction and secondary electron emission. In ICP discharges the dominant processes are ohmic and collisionless heating [46, 49].

At high pressures (generally >20 mTorr) where $\nu_{eff} \gg \omega_{rf}$, heating is predominantly through ohmic (or Joule) heating of electrons via collisions with neutral background particles. The electron mean-free path in this collisional regime is small compared to plasma dimensions, typically the skin depth of inductive plasma [46].

At low pressures, where $\nu_{eff} \ll \omega_{rf}$ the electron mean-free path is larger than the characteristic plasma dimension. Little heating via collisions with neutral particles can occur, but heating is attributed to resonant interaction of electrons with electromagnetic fields [46]. In this collisionless regime, electrons in the bulk plasma enter the skin layer and feel a force due to the RF field. When the electrons approach the sheath at the edge of the plasma they are repelled back towards the bulk. If the time the electrons spend within the skin layer is less than the RF period, then the electrons effectively see a DC field and can gain energy from the field.

For the case when:

$$\frac{\bar{u}_e}{2\delta} \gg \omega_{rf}, \nu_{en} \quad (2.17)$$

where \bar{u}_e is the mean electron thermal velocity, electrons will traverse the skin layer in a small fraction of the RF period [46, 50]. These high energy electrons can then transfer a considerable amount of energy to the bulk plasma through electron-neutral collisions. Power can therefore be deposited beyond the classical skin depth, and in this case the skin depth is defined by an *anomalous* skin depth [46, 50] given as:

$$\delta_a = \left(\frac{C_a \bar{u}_e}{2\omega_{rf} \delta_p} \right)^{1/3} \delta_p \quad (2.18)$$

where C_a is a constant, of the order unity, which depends on the electron thermal velocity, skin depth and RF frequency [46].

In this anomalous regime, non-local electrodynamic effects due to electron thermal motion and non-linear Lorentz forces can result in the RF current in the plasma not being locally coupled with the RF field and can also occur in a non-monotonic spatial distribution of the RF field [50]. The electric field does not decay exponentially into the plasma as would be expected, and regions of negative power absorption have been observed for such cases [50,52]. A second harmonic current circulating in an opposite direction around the main discharge current has also been observed [50, 51]. This will counteract, to some degree, the current induced in the induction coil by the main discharge current which acts to increase the resistance of the induction coil.

2.1.3 Transformer Model for Inductive Coupling

An inductive discharge can be considered as a transformer, with the plasma modelled as a one-turn secondary coil of an air-core transformer. This has been analyzed for a cylindrical discharge by Gudmundsson and Lieberman [53]. The primary of the transformer is the induction coil with N turns, coil radius b and coil length l_c . The equivalent circuit model of an inductive discharge is given in Figure 2.2.

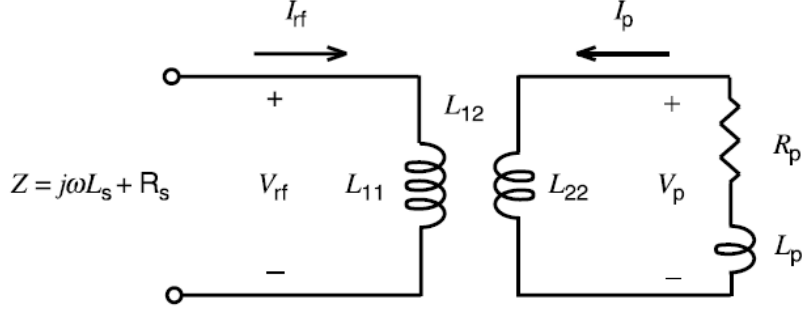


Figure 2.2. Equivalent circuit model of an inductive discharge modeled as a transformer ^[46].

The power absorbed by an inductive plasma is related to the plasma discharge current and plasma resistance through:

$$P_{abs} = \frac{1}{2} I_p^2 R_p \quad (2.19)$$

with R_p given by Equation 2.16 and $I_p = J_\theta l_p \delta$ (where J_θ is the current density).

The magnetic field produced by the discharge current in the skin layer of the plasma is $H = J_\theta \delta$ and the magnetic flux linked by the discharge current is:

$$\Phi = L_{22} I_p = \mu_0 \pi r^2 H \quad (2.20)$$

This gives the plasma self-inductance as:

$$L_{22} = \frac{\mu_0 \pi r^2}{l_p} \quad (2.21)$$

A phase lag between the induced RF electric field in the plasma and the RF conduction current occurs due to finite electron inertia. This results in an additional inductance term to the usual magnetic energy storage inductance (self-inductance) [46]. The electron inertia inductance is determined from the imaginary part of the plasma conductivity and is given by:

$$L_p = \frac{R_p}{\nu_{eff}} \quad (2.22)$$

The self-inductance of the primary coil and the mutual inductance between the induction coil and plasma can be evaluated from the inductance matrix for the transformer circuit [46]:

$$V_{RF} = i\omega_{rf}L_{11}I_{RF} + i\omega_{rf}L_{12}I_p \quad (2.23)$$

$$V_p = i\omega_{rf}L_{12}I_{RF} + i\omega_{rf}L_{22}I_p \quad (2.24)$$

The self-inductance of the primary coil is:

$$L_{11} = \frac{\mu_0\pi b^2 N^2}{l_c} \quad (2.25)$$

The mutual inductance of the coil and plasma is:

$$L_{12} = \frac{\mu_0\pi r^2 N}{l_p} \quad (2.26)$$

The source impedance seen at the coil terminals can also be evaluated using $V_p = -I_p(R_p + i\omega_{rf}L_p)$ to give:

$$Z_s = \frac{V_{RF}}{I_{RF}} = i\omega_{rf}L_{11} + \frac{\omega_{rf}^2 L_{12}^2}{R_p + i\omega_{rf}(L_{22} + L_p)} \quad (2.27)$$

with impedance defined by $Z_s = R_s + i\omega_{rf}L_s$ [46].

For high density plasma $R_p^2 + \omega_{rf}^2 L_p^2 \ll \omega_{rf}^2 L_{22}^2$ due to the skin depth being less than the plasma radius. Therefore, the source inductance and resistance can be approximated to be:

$$L_s \approx \frac{\mu_0\pi r^2 N^2}{l_p} \left(\frac{b^2}{r^2} - 1 \right) \quad (2.28)$$

$$R_s \approx N^2 \frac{\pi r}{\sigma_{dc} l_p \delta} \quad (2.29)$$

The RF source current can then be calculated from the absorbed power and the RF source voltage knowing the source impedance [46]:

$$P_{abs} = \frac{1}{2} |I_{RF}|^2 R_s \quad (2.30)$$

$$V_{RF} = I_{RF} |Z_s| \quad (2.31)$$

The RF source impedance is usually terminated with 50Ω. It is important to match the source impedance to the plasma impedance to maximise power coupling between the induction coil and plasma by inserting a matching network between the radio frequency generator and induction coil.

2.1.4 Discharge Modes in Inductively Coupled Plasma

When varying RF power to an ICP, an abrupt change from a low-intensity plasma to a much brighter plasma is often observed [54]. The low density plasma observed at low power is generally attributed to stray capacitive coupling between the inductive coil and plasma due to a voltage difference across the coil [46]. This discharge mode is usually termed the ‘capacitive’ or ‘E-mode’. On increasing RF power, a sudden jump in plasma density and luminosity occurs. The discharge is then driven by true inductive coupling and this mode is termed the ‘H-mode’. The electron density characteristically increases by one or more orders of magnitude during an E-H transition, indicating a large change in coupling efficiency [54].

Plasma resistance determines the power absorbed by a plasma for a given RF source current. At low density, the plasma conductivity is low and RF fields can fully penetrate into the plasma. In this case, plasma resistance can not be approximated by Equation 2.16. For low density plasma, absorbed power is evaluated to be [46]:

$$P_{abs} = I_{RF}^2 \frac{\pi e^2 n_e v_{eff} \mu_0^2 N^2 r^4}{8 m_e l_p} \quad (2.31)$$

At low density, the power absorbed by a plasma is seen to be proportional to electron density. On increasing RF power, the electron density increases linearly until a threshold density is

reached where the RF fields start to become attenuated by the plasma, resulting in the skin effect.

At high density, the plasma resistance is given by Equation 2.16. Since plasma conductivity is proportional to n_e whilst skin depth is proportional to $n_e^{-1/2}$ it can be seen that:

$$P_{abs} \propto n_e^{-1/2} I_{RF}^2 \quad (2.32)$$

The power absorbed by a plasma at a fixed RF source current therefore peaks at a given plasma density as density is increased. This is shown in Figure 2.3.

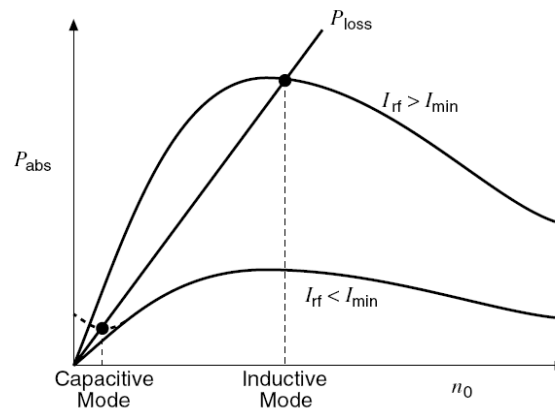


Figure 2.3. Absorbed power against plasma density for an inductive discharge for different values of source current [46].

For a stable discharge to occur, the power absorbed by a plasma must balance the power dissipated by it. The overall power balance of a discharge provides an estimate of the minimum coil current required to maintain a stable discharge [46, 53].

When the RF coil current is raised above the minimum current required for an inductive discharge, the ionization rate slightly exceeds the diffusion losses and the electron density starts to increase. This will continue until a density is reached where the skin effect has a significant effect on the attenuation of the RF fields in the plasma. The spatially averaged ionization rate will then start to decrease until a stationary state is reached producing a stable discharge. The skin depth must be of the order of the plasma radius or smaller for a stable inductive discharge [53].

At low powers and low densities, the main source of power deposition may be through stray capacitive coupling from the inductive coil. Power absorbed by plasma through capacitive coupling increases with sheath voltage, which can be approximated by:

$$V_{sh} = V_{RF} \frac{s_m}{b - r + s_m} \quad (2.33)$$

where s_m is the sheath thickness. The sheath thickness is inversely proportional to electron density through the Child-Langmuir law [46]. Therefore, as electron density decreases, capacitive coupling to the plasma increases. At very low densities, the power absorbed through capacitive coupling may be the only source of power deposition sufficient to balance power losses and maintain a discharge. Increasing the source current for the discharge to that required to maintain an inductive discharge will then result in an abrupt rise in the plasma density and luminosity.

2.1.5 Discharge Diagnostics of Inductively Coupled Plasmas

An array of diagnostic tools and techniques has been developed over past decades to provide information on plasma processes [55, 56]. The simplest of these is the electrostatic probe, first introduced by Mott Smith and Langmuir in 1926 [57]. Analysis of measurements taken with these probes is far more complicated for RF plasmas than for DC plasma discharges, as oscillations of the plasma potential can lead to severe distortions of the I-V characteristic. Problems associated with diagnostics of RF plasmas can be found in [55-59].

Despite the numerous plasma diagnostic techniques available, a definitive method to determine plasma density still does not exist. Numerous methods are applied, which are often compared to validate results. A summary of different diagnostic tools and techniques relevant to RF plasmas and their use are provided in Table 2-2.

In this work, triple Langmuir probes were used to probe the inductive discharge of the MiDGIT RF ion thruster. A review of Langmuir probe diagnostics and a summary of triple Langmuir probe theory are provided in Appendix A.

	Electrostatic Probe	Advanced Actinometry	SEERS *	Microwave Interferometry	Impedance Probe	Rogowski Coil
V_P	x				x	
n_e	x		x	x		
T_e	x	x				
v_{en}			x			
P_{abs}			x			
V_{RF}					x	
I_{RF}					x	x
Z_{load}					x	
R_{load}					x	
L_{load}					x	
C_{load}					x	
(Ref)	[55,56,58]	[56]	[60]	[46, 55,56]	[61]	[62,63]

* Self Excited Electron Resonance Spectroscopy

Table 2-2. Plasma diagnostic methods and their measurement capability.

2.2 RADIO FREQUENCY ION THRUSTERS

Radio frequency ion thrusters use an inductive discharge for the generation of plasma. The majority of research into radio frequency ion thrusters has been conducted by the University of Giessen since the 1960's, culminating in the development of the commercial range of RIT thrusters in collaboration with EADS Lampoldshausen [44]. RF ion thrusters have also been developed by LABEN Proel Technologie Division [64], Busek [24, 25] and Pennsylvania State University [65,66].

2.2.1 General Design

The design of a radio frequency ion thruster is based on the standard configuration for an ICP source. An ac current is supplied to a helical induction coil surrounding a cylindrical, ceramic discharge chamber to generate an RF field. A gas feed system at one end of the discharge chamber supplies propellant to be ionized; the inert gas xenon is typically used but previously RF ion thrusters have been operated on mercury and cesium due to their relatively high charge-to-mass ratios [67]. The RF magnetic field penetrates the discharge chamber inducing an azimuthal electric field, which accelerates electrons to provide the ionization. The generated ions are extracted from the plasma, accelerated and focused by a multi aperture grid system to produce thrust.

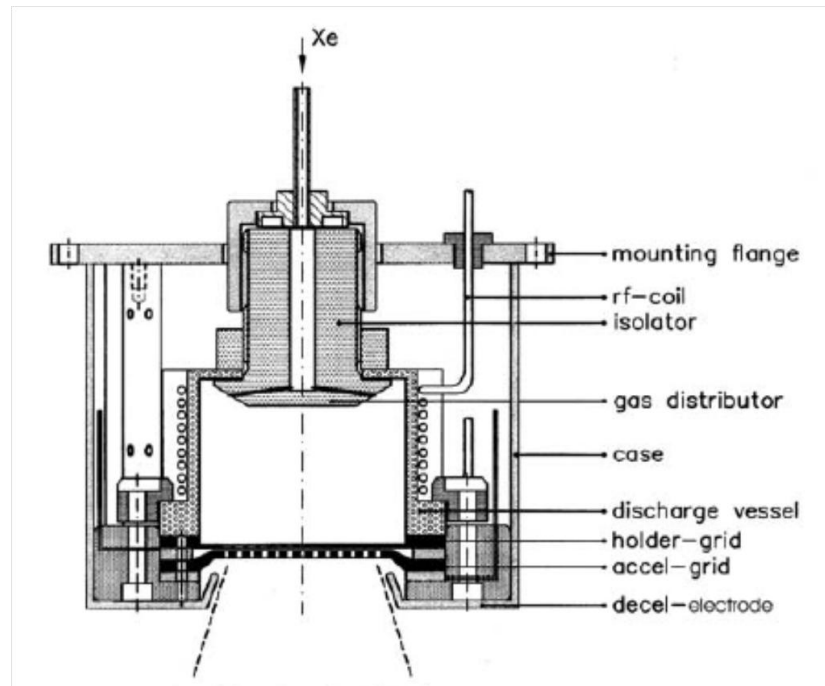


Figure 2.4. Schematic of the RF ion thruster, RIT-4 ^[70].

The general design of an RF ion thruster can be seen in Figure 2.4; thruster and system components comprise:

- Discharge Chamber

A cylindrical, ceramic vessel surrounded by an induction coil is used as the discharge chamber. The coil is usually fabricated from silvered copper wire or tubing. Favoured materials for the discharge chamber have been quartz and more recently alumina.

- Gas feed system

A gas feed system, consisting of feed line, isolator and gas distributor is located at the back of the discharge chamber. The gas distributor, normally a flat perforated plate, injects gas into the discharge chamber almost perpendicular to the thruster axis by use of angled nozzles. Injecting gas perpendicularly increases the time neutrals reside in the discharge volume and are available for ionization. Macor and stainless steel are materials commonly used for the distributor. The gas distributor plate floats at the plasma potential and therefore an isolator is required to separate the grounded feed line and the gas distributor. Quartz has been used for the isolator.

- Extraction grid system
Ions are extracted and accelerated by a multi-aperture grid system, usually comprising two but occasionally three grids. The accelerator grid is fabricated from graphite due to its low sputtering rate but other materials used for extraction grids have been molybdenum, titanium and invar.
- Anode
An anode is used to collect electrons equivalent to the number of ions ejected from the thruster. The gas distributor and screen grid of the extraction system have each been used as an anode in the past.
- Thruster Housing
A Faraday shield is placed around the discharge chamber and induction coil to shield surrounding components from the RF field. The shield also provides a mounting interface to the spacecraft.
- Neutralizer cathode
A neutralizer cathode is located outside of the discharge chamber to neutralize the ejected ion beam to prevent spacecraft charging effects.
- Flow Control Unit (FCU)
Xenon flow to the thruster and neutralizer is monitored and controlled by an automatic FCU.
- Power Supply and Control Unit (PSCU)
The PSCU controls the beam supply, accelerator grid supply, RF-generator and neutralizer supply. It can also provide a telemetry and telecommand interface between thruster and spacecraft.
- RF Generator
The RF generator comprises an oscillator circuit, RF power amplifier circuit and a matching circuit to supply the RF power to the induction coil. The matching circuit is employed to maximise the coupling efficiency between the induction coil and plasma. Poor coupling can lead to high heat load of components within the RFG, which may be life-limiting on long duration missions.

- Propellant storage and supply

A single propellant tank is often used and a system of pipes, valves and pressure transducers supply the propellant gas from the tank to a series of thrusters.

2.2.2 Thruster Ignition

The ignition of an inductive discharge requires that a sufficient number of impact ionizations occur due to collisions between either free electrons naturally present in the gas or those supplied by an external electron source and the neutral gas atoms. The induced E_0 field within the discharge chamber is often not sufficient to accelerate electrons to high enough energies within one half period of the RF cycle for ionization to occur. Elastic collisions between electrons and neutrals within the E_0 field region which reverse the direction of the electron as the direction of the E_0 field changes enables the electrons to accumulate energy from the field. Provided that the electrons undergo enough collisions before being lost to the walls, the electrons can therefore reach energies required for ionization. Greatest power coupling between the RF field and the plasma can be achieved when the electron-neutral collision frequency matches the RF driving frequency [46].

Prior to ignition of an inductive discharge, relatively high RF currents are typically applied to the induction coil. Due to the resistance of the coil, a large voltage difference can therefore exist between the ends of the coil. Capacitive coupling between the induction coil and plasma leads to radial and axial electric fields in the plasma which can be considerably greater than the induced azimuthal electric field [67]. Capacitive coupling can therefore constitute a significant fraction of the energy coupling to plasma electrons. However, it is difficult to ignite an inductive discharge by capacitive coupling alone below neutral pressures of ~ 10 mTorr and as stated, an external electron source is often needed. Ignition of RF ion thrusters has been reported however whereby a high potential difference is applied between the accelerator grid and screen grid or accelerator grid and anode whilst applying a large impulse to the gas flow [27, 65]. Use of the thruster's neutralizer as an electron source for discharge ignition however removes the need for the large impulses in gas flow thereby reducing propellant requirements.

The flux of electrons ($\Gamma = n_e u$) that undergo collisions with neutral atoms within a distance dx , can be written in the form:

$$d\Gamma = -\Gamma n_g \sigma dx \quad (2.34)$$

where Γ is the incident flux of electrons on the number of neutrals per unit volume n_g within dx , and σ defines the collision cross-section, given by:

$$\sigma = \pi a^2 \quad (2.35)$$

with a being the molecular diameter of the neutral gas molecules (the scale of the electron being negligible). The molecular diameter for xenon, assuming a variable hard sphere (VHS) model, is given as 5.74×10^{-10} m [69].

The fraction of the incident electron flux that undergoes collisions can then be determined by integration of Equation 2.34 to be:

$$\frac{\Gamma}{\Gamma_0} = (1 - e^{-n_g \sigma x}) \quad (2.35)$$

The minimum neutral pressure required for discharge ignition as a function of the electron flux undergoing collisions can therefore be expressed from Equation 2.35 assuming an ideal gas at a temperature T_g :

$$P_{min} = -\frac{kT_g}{\sigma x} \ln \left(1 - \frac{\Gamma}{\Gamma_0} \right) \quad (2.36)$$

Here, x can be taken to be the skin depth of the E_0 field within the discharge chamber.

The minimum pressure required for ignition of an inductive discharge for xenon and argon as a function of the flux of electrons that undergo collisions with neutrals within a skin depth of 1.4cm (equivalent to the radius of the discharge chamber for the MiDGIT breadboard thruster) is presented in Figure 2.5 and can be seen to be of the order several mTorr.

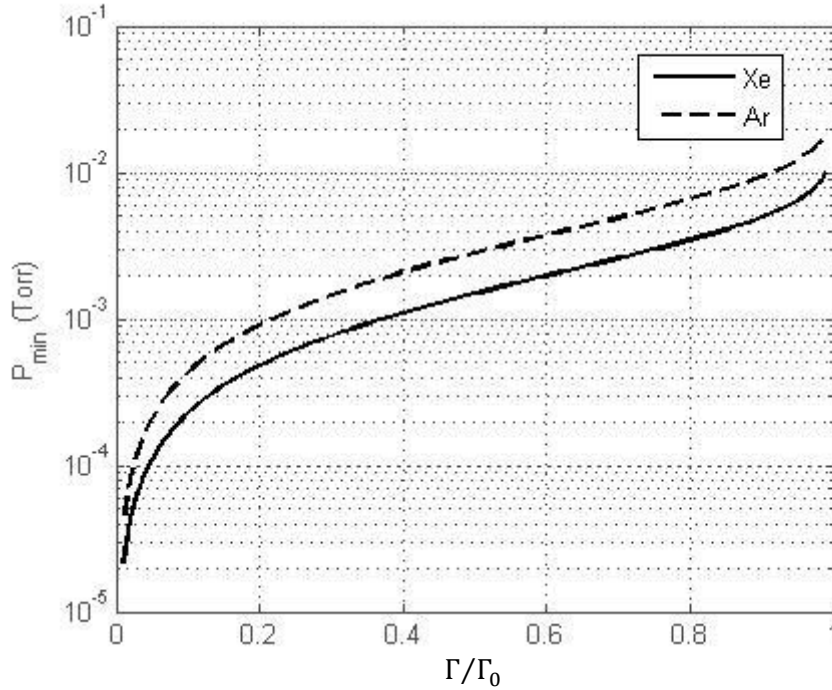


Figure 2.5. Minimum pressure required for ignition of an inductive discharge in Xe and Ar as a function of the electron flux undergoing collisions within a skin depth of 1.4 cm.

As previously stated, the discharge of an RF ion thruster is typically ignited by use of the external neutralizer [70]. Following ignition of the neutralizer, propellant is introduced to the discharge chamber and the RF generator is powered on. A positive high voltage is then supplied to an anode, being either the gas distributor plate or screen grid, to attract electrons into the discharge chamber. At a sufficient electron density an inductive discharge is ignited. Once the discharge has stabilised, the voltage to the anode can be switched off. A self-sustaining discharge is then achieved by subsequent collisions between electrons and low-energy neutrals. The ion density in the plasma, and therefore thrust level, is controlled by varying the RF power and flow rate to the discharge chamber [70].

2.2.3 Ion Extraction

The ions generated within the discharge are extracted and accelerated by a set of two, or sometimes three, multi-aperture grids biased to high potentials. A sheath forms at the upstream surface of the first grid, which is biased to a high positive potential between 1-2kV with respect to ground (or common potential of the spacecraft). This grid is often referred to as the *screen grid*. The plasma assumes a potential just above that of the screen grid due to the formation of the sheath. The second grid, located in close proximity to the screen grid, is

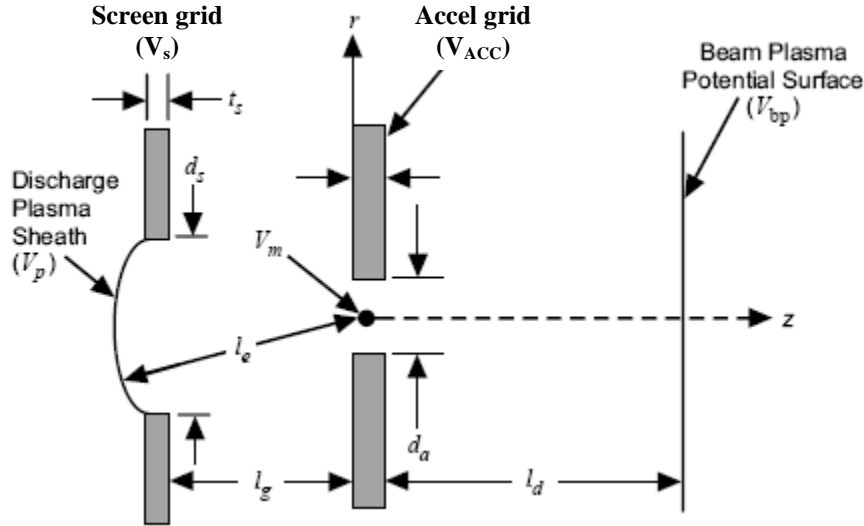


Figure 2.6. Schematic of two grid ion extraction, indicating modified sheath width, l_e , due to curvature of the plasma sheath^[47].

termed the *accelerator grid* and is biased to a large negative potential, typically between -100V and -500V with respect to ground (or common potential). Ions that diffuse to the sheath edge upstream of the screen grid are accelerated across the sheath and either impinge on the upstream face of the screen grid or pass through the apertures, where they are accelerated to high velocity due to the high potential difference between the screen and accelerator grids. The apertures in the accelerator grid are set to be smaller than those of the screen grid to reduce the neutral flux that is lost from the discharge chamber through the grids. The screen grid is responsible for focussing the extracted ions through the accelerator grid apertures. It is also important that the negative potential of the accelerator grid be sufficient to prevent electrons external to the thruster from backstreaming through the grids into the discharge chamber, which can cause localised heating within the discharge chamber and in some cases overload the screen supply [47].

The ion current that can be extracted through each aperture of the grid set is limited by the ion space charge in the gap between the screen and accelerator grid, governed by the Child-Langmuir law, which is given by:

$$J_0 = \frac{4}{9} \epsilon_0 \left(\frac{2e}{M_i} \right)^{1/2} \frac{V^{3/2}}{s^2} \quad (2.37)$$

where s is the spacing between two electrodes.

The maximum beam current that can be extracted for a given acceleration voltage is termed the *perveance* of the grids:

$$P = \frac{I_b}{V^{3/2}} \quad (2.38)$$

The sheath formed upstream of the screen grid apertures is not planar but curved, depending on the electric field between the grids and the plasma density at the sheath edge. A modified sheath width to represent the curved sheath can be used in the Child-Langmuir equation to provide an estimate of the maximum current that can be extracted from a specified grid set.

For a two grid system, with dimensions as defined in Figure 2.6, the maximum beam current is given by:

$$I_b^{max} = \frac{4\epsilon_0}{9} \sqrt{\frac{2e V_T^{3/2}}{M_i l_e^2}} A_g T_s \quad (2.39)$$

where A_g is the active grid area (including apertures), T_s is the transparency of the screen grid to ions, $V_T = V_s + |V_{ACC}|$ and the modified sheath thickness is:

$$l_e = \sqrt{(l_g + t_s)^2 + \frac{d_s^2}{4}} \quad (2.40)$$

The optical transparency of the screen grid is the open area of the grid defined by:

$$T_{s,opt} = \frac{N\pi d_s^2}{4} \quad (2.41)$$

with N being the number of apertures [47]. Due to the focussing effect of ions through the screen grid apertures from the curved surface of the sheath, the ion transparency of the screen grid tends to be slightly greater than the optical transparency [47].

Equation 2.39 can be shown to lead to an estimate for the maximum thrust achievable at perveance for the grids, given as:

$$T_{max} = \frac{4 \epsilon_0 \alpha_{TCF} A_g T_s}{9 e} \sqrt{\frac{2e V_T^{3/2}}{M_i l_e^2}} M_i \sqrt{\frac{2e V_b}{M_i}} \quad (2.42)$$

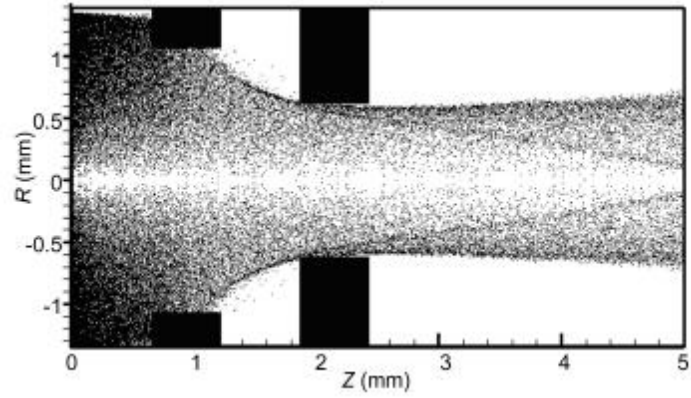
where V_b is the beam voltage and α_{TCF} is a thrust correction factor that accounts for losses due to beam divergence and multiply charged ions [47]. The maximum thrust can be increased by either increasing the screen grid transparency (simply by increasing the number of apertures) or by increasing the electric field between the grids. Increases to the beam voltage however require an increase to the accelerator grid voltage to prevent electron backstreaming.

An estimate of the negative accelerator grid potential at which electron backstreaming will occur for a given beam voltage can be determined from the following equation [73]:

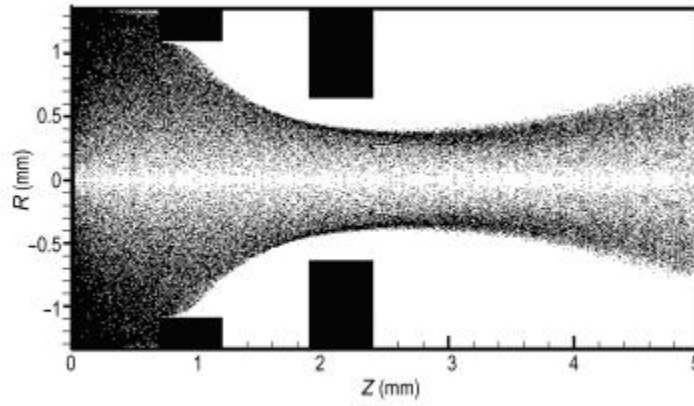
$$|V_{ebs}| = \frac{V_b}{2\pi \frac{l_e}{d_a} \exp\left(\frac{t_a}{d_a}\right) - 1} \quad (2.43)$$

Good focussing of beam ions by a grid set and optimum performance will only occur over a small range of plasma conditions however. At high plasma density, the sheath width will decrease and, upstream of the screen grid apertures, the sheath will become flatter. If the beam voltage is too low, ions will be poorly focussed and can start to impinge directly on the accelerator grid (as shown in Figure 2.7(a)). The onset of direct ion impingement on the accelerator grid in this case defines the *perveance limit* of the grids [47].

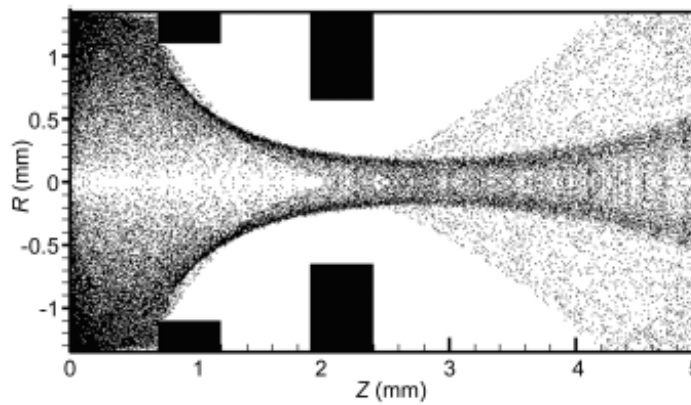
At low plasma density, the sheath width increases and the sheath will move further into the discharge chamber and become more convex with respect to the surface of the screen grid. If the beam voltage is too high for the ion beamlet current extracted, the beamlets will be over focussed, which can lead to the ions crossing over in between the grids and then impinging on the accelerator grid (see Figure 2.7(c)). Some ions extracted from the surface of the sheath at high curvature (at large radii from the aperture centreline) can even cross over and strike the opposite side of the screen grid. For these conditions, the grids are considered to be operating *under perveance* [47].



(a)



(b)



(c)

Figure 2.7. Ion extraction simulations performed by Zhong et al. indicating (a) over perveance, (b) perveance, (c) under perveance and cross-over^[71].

Direct ion impingement on the grids must obviously be avoided to minimise erosion and prolong the lifetime of the grids. However, even when the beamlets are properly focussed, ions can undergo charge-exchange (CEX) collisions with neutrals in between the grids. These collisions result in a fast neutral being generated and a slow thermal ion. The slow thermal ions generated between the grids tend to be attracted to the negatively biased accelerator grid and still have sufficient energy to sputter the surface of the grid when they strike it. Grid erosion by sputtering from CEX ions is the main life-limiting mechanism of the grids [47].

The neutral gas that escapes through the grids can be determined by the neutral flux on the grids and the optical transparency of the grids:

$$Q = \frac{1}{4} n_g \bar{u} f_c A_g T_{a_opt} \quad (2.44)$$

where f_c is the Clausing factor, which is applied to account for the reduced conductance of the grids due to their finite thickness. Accurate estimates of the Clausing factor can be obtained by Direct Simulation Monte Carlo (DSMC) techniques but requires computational effort [69]. Therefore, f_c is often assumed to be ~ 0.5 [47]. The neutral gas velocity is given by:

$$\bar{u} = \left(\frac{8kT_g}{\pi M_i} \right)^{1/2} \quad (2.45)$$

The optical transparency of the grids is often taken to be that of the accelerator grid, ignoring any effect from the screen grid. Closs [67] replaces the combined terms $f_c A_g T_{a_opt}$ with the following which is considered to represent a more accurate estimate of the accelerator grid open area:

$$C_f = \frac{5 + \frac{4t_a}{d_a}}{20 + \frac{38t_a}{d_a} + 12 \left(\frac{t_a}{d_a} \right)^2} \pi d_a^2 \quad (2.46)$$

2.2.4 Main Losses for RF Ion Thrusters

A stable plasma discharge requires that the power absorbed by a plasma must balance the power dissipated. A considerable amount of power that goes into the plasma to generate the ions can be wasted through excitation of neutrals, which is the cause of the characteristic glow of the discharge [67]. Power can also be wasted in the generation of doubly-charged ions, though in RF ion thrusters these typically account for less than 1% of the total ions [40].

A constant flux of ions and flux of electrons flow to the walls of the discharge chamber, which are then lost by recombination at the surface. The ions fall across a potential of $kT_e/2e$ volts to the edge of the plasma due to the presheath and are then accelerated across the plasma sheath to the walls. The energy removed from the plasma by these ions is then:

$$\varepsilon_i = \frac{kT_e}{2e} + \phi_p \quad (2.47)$$

where ϕ_p is the plasma potential.

The thermal energy carried away by the electrons is:

$$\varepsilon_e = \frac{2kT_e}{e} + \phi_p \quad (2.48)$$

The surface-area-to-volume ratio is therefore an important consideration regarding wall losses.

A considerable amount of the RF power delivered by the RF amplifier circuit is lost through ohmic heating in the induction coil, thruster housing and components of the matching circuit. Improving the efficiency of RF generators is a key task for future RF ion thrusters [93].

Numerical simulations of the Busek BRFIT-7 thruster performed by Tsay identified that ohmic losses contributed to 7% of the power losses in the thruster (as shown in Figure 2.8) [25]. Wall losses contributed 5%. The bulk of the power went into the ion beam, with the beam power defined as the ion beam current multiplied by the net acceleration voltage [25].

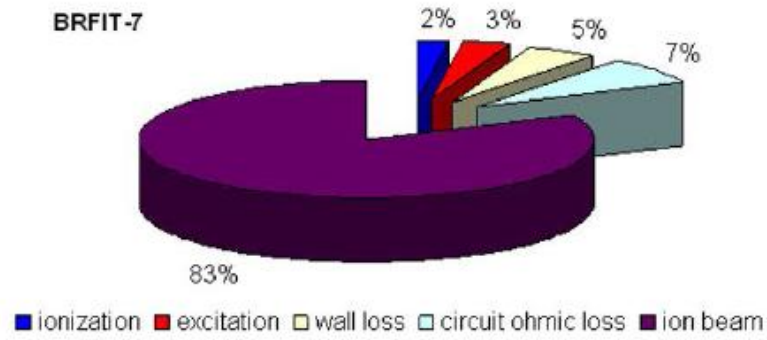


Figure 2.8. Power losses determined via numerical simulation of the BRFIT-7 thruster ^[25].

2.2.5 Thruster Performance

The thrust generated by any type of gridded ion thruster can be defined by:

$$T = \alpha_{TCF} I_b \sqrt{\frac{2V_b M_i}{e}} \quad (2.49)$$

where I_b is the ion beam current extracted, V_b is the applied beam voltage, M_i is the mass of a propellant ion and e is the electron charge. A thrust correction factor α_{TCF} is applied to account for thrust losses due to beam divergence, multiply charged ions and neutral efflux [47].

As stated in Chapter 1, the specific impulse is a measure of the efficiency of a thruster and is given by:

$$I_{sp} = \frac{T}{\dot{m}g_0} = \frac{v_{ex}}{g_0} \quad (2.50)$$

The mass utilization efficiency defines the proportion of the propellant mass supplied to a thruster that is ionized and then extracted to provide the thrust:

$$\eta_m = \frac{I_b M_i}{e \dot{m}} \quad (2.51)$$

where \dot{m} is the propellant mass flow rate.

The electrical efficiency of a thruster is the ratio of the beam power to the total power input to the thruster:

$$\eta_e = \frac{P_b}{P_T} \quad (2.52)$$

For an RF ion thruster, the electrical efficiency is defined as:

$$\eta_e = \frac{I_b V_b}{I_b V_b + P_{rf}} \quad (2.53)$$

where P_{rf} is taken to be the forward RF power delivered by the RF amplifier circuit to take into account ohmic, dielectric and radiation losses in the induction coil and matching circuit. An ideal thruster would have perfect coupling between the induction coil and plasma and no power would be consumed by circuit elements. The ultimate electrical efficiency (though unachievable) would then be given by:

$$\eta_{e_ult} = \frac{I_b V_b}{I_b V_b + P_{abs}} \quad (2.54)$$

where P_{abs} is the power absorbed by the plasma.

The cost of producing a given beam current is given by:

$$\eta_d = \frac{P_{rf}}{I_b} \quad (2.55)$$

and is often referred to as the discharge loss, with units of W/A or equivalently eV/ion. Values less than approximately 400eV/ion are considered acceptable for conventional ion thrusters.

The total thruster efficiency can be given by the product of the electrical efficiency and mass utilization, taking into account any thrust correction factors:

$$\eta_T = \alpha_{TCF}^2 \eta_m \eta_e \quad (2.56)$$

2.2.6 Advantages of RF Ion Thrusters

The use of an inductive plasma discharge removes the need for an internal cathode, as required by DC ion thrusters and Hall Effect Thrusters, and also the need for any permanent magnets to confine the plasma electrons. The absence of electrodes in direct contact with the plasma in RF ion thrusters ensures prolonged operational lifetime and high reliability compared to many other types of ion thruster. Lifetimes greater than 20,000 hrs have been achieved by the RIT-10 thruster operated at 15 mN [44].

The low mean electron temperature of inductive plasmas results in very few multiply charged ions being produced, typically <1% within RF ion thrusters [40]. This reduces discharge losses, improving thrust efficiency. The low electron temperature also means the plasma potential is kept relatively low and below the sputter threshold of materials used for the discharge chamber and screen grid [40, 93]. Erosion of the grids is more easily kept to a minimum compared to DC gridded ion thrusters.

Thrust level can be controlled by both RF power and propellant flow rate, with plasma density increasing linearly with RF power. The thrust accuracy and stability are only dependent on the power supplies and flow controllers used. RF ion thrusters also demonstrate a fast response rate; if RF power is varied, the plasma responds within a few RF periods and therefore reaches a new equilibrium within a few microseconds. The inherent stability of the inductive discharge and the fast response time provide very low thrust noise levels and therefore make RF ion thrusters particularly suitable for missions requiring precision attitude control [40].

2.2.7 RIT Development

RF ion thrusters utilizing an inductive discharge initially looked unfavourable compared to DC ion thrusters due to the RF-coupling and matching issues. A research and development program was therefore initiated by Giessen University in the 1960's to develop and optimize the RF ion thruster. A summary of all R&D activities conducted by Giessen is given by Loeb et al. [44].

Initial efforts focused on the development of a 10cm diameter engine, the RIT-10 thruster. Optimization of the thruster focused on the effect of discharge chamber length, applied RF frequency, coil and grid geometry, discharge pressure and applied power [44]. Discharge and

beam diagnostics were also performed. These tests provided improved understanding of RF ion thruster operation and led to the development of an enhanced 10mN RIT-10 prototype. This prototype was operated continuously for 8150 hrs at 10mN during which a 10% increase in RF power was observed whilst beam current remained constant [68]. The power increase was attributed to sputtered carbon from the accelerator grid forming a conductive layer on the internal wall of the discharge chamber, though no visual observation of this has been published [68].

Improved RF coupling methods were also investigated using a RIT-10 prototype [72]. To avoid RF losses due to eddy currents induced in conductive thruster components, the use of a ferrite shield around the discharge chamber and induction coil was investigated. Ferrite was selected for the Faraday shield as it would also act to intensify the magnetic field within the discharge chamber. Geometry of the ferrite shield was optimised by measuring the effect of the shield on the internal and stray magnetic fields. The combined inductance of a ferrite shield and inductor coil is higher than that of a coil alone [72]. The relation between RF current I_{RF} and inductance L is given by:

$$L = \frac{\phi_{RF}}{I_{RF}} \quad (2.57)$$

where ϕ_{RF} is the magnetic flux [72]. The required RF coil current for a given magnetic flux is therefore reduced by addition of a ferrite shield. Performance of a RIT-10 thruster was measured with and without a ferrite shield. Power consumption and discharge pressure were found to be reduced whilst efficiency was increased [72].

Starting in the late 1970's two scaled-up versions of the RIT-10 thruster were also developed, the 50mN RIT-15 thruster and the 250mN RIT-35 thruster [44]. All RIT thrusters developed to date have shown good performance with specific power values comparable to DC ion thrusters in the range 25-30 W/mN, at high specific impulse of 3000-4000s. Discharge efficiency of RF ion thrusters is predominantly governed by ion losses to walls. A RIT-15 thruster was therefore modified to have a conical discharge chamber to reduce the ratio of surface area to volume. Ion production costs for this 'RIT-XT' model was reduced by 23%. The conical chamber was also found to have better mechanical properties with respect to vibration loads [44] and this design has been implemented on most RF ion thrusters to date.

2.2.8 Miniature RF Ion Thrusters

The requirement for thrusters of low mN thrust level has driven interest in the miniaturization of ion thruster technologies [7]. Reduction in discharge chamber dimensions increases the ratio of surface-area to volume, resulting in increased ion production costs and reduced efficiency. Several scaling-down studies have been conducted to determine whether ion thrusters can be successfully scaled down to the required thrust levels at acceptable efficiencies [23, 26]. The absence of discharge electrodes in RF ion thrusters has made them more favourable for scaling down than DC ion thrusters. Miniature RF ion thrusters have been investigated by the University of Giessen [26, 27], Busek [24, 25] and Pennsylvania State University [65].

In 2004, the University of Giessen initiated a program to investigate the scaling down of their industrialized RIT-10 thruster down to μN level for precision attitude control applications. This study established a number of scaling laws for the RIT range of RF ion thrusters to enable the optimisation of thruster geometry and working parameters [26]. Key factors that were identified to affect the efficiency of RF power coupling to the plasma were the geometry of the RF-coil, the excitation frequency and the surface area-to-volume ratio of the plasma [26].

The discharge pressure P , applied RF frequency ν_{rf} and discharge chamber radius R , are coupled together by the following relation.

$$P \propto \nu_{rf} \propto 1/R \tag{2.58}$$

Reducing the dimensions of a discharge chamber requires an increase to the discharge pressure and frequency. This is a result of increased wall losses and the skin effect, as a stable inductive discharge requires the skin depth to be of the order or less than radius of the discharge chamber. Also, ohmic heating of the plasma electrons increases as the skin depth decreases. However, ohmic losses in the induction coil and other circuit components will increase with increasing RF frequency too; an optimal operating frequency will therefore exist for each RF ion thruster depending on the particular ohmic losses, dielectric losses and radiation losses of the components used [25,67].

The ionization efficiency is affected by chamber geometry through the surface-area-to-volume ratio. The length of a discharge chamber should be minimized to reduce

recombination losses at the walls. However, the chamber should be kept sufficiently long so that neutrals are retained in the discharge volume for a sufficient time for ionization [26]. An optimal length for a discharge chamber therefore exists. An empirical relation for optimum chamber length was established by the University of Giessen [26]. The length of a 4cm diameter RIT thruster operated with Xe was varied by using a moveable quartz plate within a discharge tube to limit the discharge volume. The results of these tests led to the relation for optimal length:

$$l_{opt} = (2R)^{0.66} + d \tag{2.59}$$

where d is the depth of the extraction grid system. This relation applies for RF ion thrusters operated with xenon only [26].

Based on performance data obtained for the RIT-10 thruster and basic plasma physics of inductive discharges, the performance of four micro-RIT thrusters with diameters 1-4cm were predicted. Figure 2.9 shows the three discharge control parameters calculated from the scaling laws for this set of micro-thruster. The scheduled performance data is given in Table 2-3.

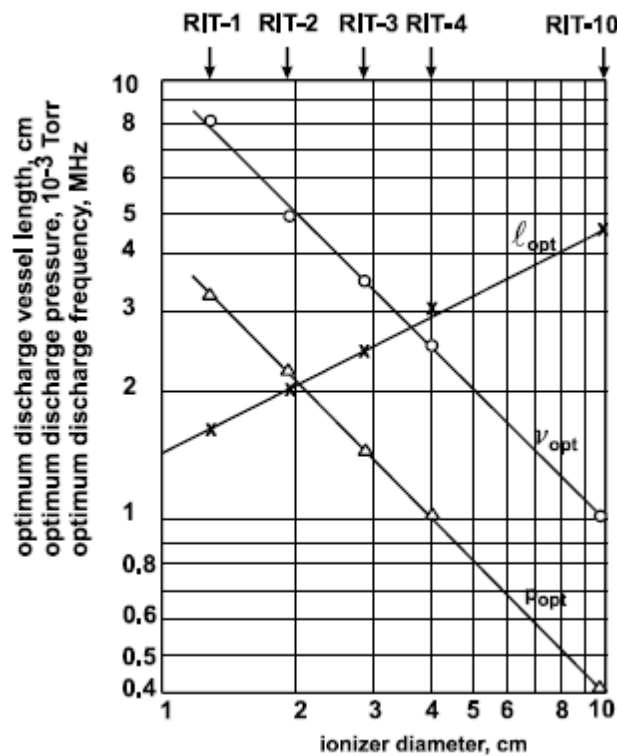


Figure 2.9. Scaling laws for the RIT microthrusters [26].

	RIT-4	RIT-3	RIT-2	RIT-1
Discharge chamber diameter (cm)	4	2.8	1.9	1.25
Discharge chamber length (cm)	2.9	2.4	1.9	1.5
Number of apertures	151	55	19	7
Open area fraction (%)	34.1	25.3	19.0	16.1
RF Frequency (MHz)	2.5	3.5	5	8
Number of coil turns	6	5	4	3
Nominal thrust (mN)	2.5	1	0.35	0.1
Ion beam current (mA)	44.4	17.8	6.2	1.8
Discharge power (W)	26.0	13.5	5.9	2.15
Ion production cost (eV/ion)	585	760	950	1200
Electrical efficiency (%)	66.7	60.9	55.6	50.0
Discharge pressure (mTorr)	1.0	1.4	2.1	3.2
Total gas flow rate (sccm)	0.853	0.367	0.148	0.0595
Neutrals flow rate (sccm)	0.230	0.117	0.0608	0.0342
Specific impulse (s)	3187	2969	2567	1860
Specific power (W/mN)	32.8	35.9	39.2	44.1
Propellant efficiency (%)	73.0	68.0	58.8	42.6

Table 2-3 – Scheduled performance data for the RIT microthrusters ^[26].

Thrust was calculated based on grid open area assuming constant grid geometry, grid voltage and plasma density for all RIT thrusters. Ion production costs were extrapolated from those measured for the RIT-10 and RIT-XT thrusters [26].

In 2007 performance tests were conducted on prototypes of the RIT-2 and RIT-4 thrusters within the BIGMAC vacuum facility at Giessen to verify the predicted data [41]. The thrusters were manufactured with interchangeable grids to achieve different thrust ranges. The RIT-4 prototype was fitted with grids of 7 and 151 holes while the RIT-2 was operated with only the 7 hole grid system. Thrust was controlled using a beam current controller to vary the applied RF power whilst maintaining a constant beam current.

The RIT-4/151 thruster was shown to provide stable thrust over the range 150 μ N–3.5mN with specific impulse >3700s using beam voltages between 1000-1400V [41]. The specific power was calculated to be 40W/mN and mass utilization efficiency up to 80%. Discharge pressure was not measured but calculated to be approximately 0.4mTorr. The thrust range measured for the RIT-4/7 thruster was 10 μ N–200 μ N but a decrease in power efficiency was observed.

The RIT-2/7 showed comparable thrust levels to the RIT-4/7 but with a reduced power demand and increased flow rate demand.

The RIT-4/7 was operated in a steady state mode, by use of the beam current controller, at a thrust level of $75\mu\text{N}$ and a beam voltage of 1700V . Beam probe tests showed a beam divergence of 15.2° , well within the limit generally required for spacecraft [41]. Thrust increments of $0.44\mu\text{N}$ were achieved by varying the RF power, with a rise time $<20\text{ms}$ [41].

In 2009, an optimized 2.5cm diameter RIT-2.5 thruster was developed [93]. The design incorporated a semispherical discharge chamber as for the larger, conventional RF ion thrusters. Experiments showed that RF power was reduced by 15%-25% through use of a conical discharge chamber compared to a cylindrical one, with a corresponding increase in electrical efficiency [93]. The gas distributor was also redesigned, with 12 micro-nozzles located around the circumference of the screen grid to inject gas axially into the discharge chamber, close to the walls where electron temperature is greatest in order to improve ionization efficiency. The third major modification compared to the other RIT microthrusters was the inclusion of a third closed grid to reduce neutral losses and to shield the accelerator grid from CEX ions created near the exit plane of the thruster [93]. The RIT-2.5 thruster was operated at various beam potentials, with grids of 37 apertures and demonstrated thrust levels between $50\mu\text{N}$ – $575\mu\text{N}$ and specific impulse between 363s – 2861s . Electrical efficiency and mass utilization efficiency were between 10%-50%; the lowest discharge loss was $\sim 2438\text{ eV/ion}$ [93].

These results demonstrate an impressive thrust range for the RIT microthrusters but highlight the difficulty in achieving sub- μN to mN thrust levels required for formation flying missions by a single gridded ion thruster. Limitations exist due to the focussing range of the ion extraction grids and the optimal transfer of power to sustain the discharge against losses.

2.2.9 Numerical Models of Miniature RF Ion Thrusters

The development and optimisation of miniature RF ion thrusters has progressed mainly by experimental methods, though some analytical models have been used to understand the discharge processes [24,25,66]. A simple performance model for a miniature RF ion thruster was developed by Tsay to support experimental work carried out by Busek on a 3cm diameter RF ion thruster [24]. A 1D axisymmetrical model, coupling a transformer circuit model with particle and energy balance equations and an ion extraction model, was used to analyse

characteristics and performance of the thruster. A similar approach was taken by Mistoco and Bilen to develop a 2D numerical model of the MRIT thruster investigated by Pennsylvania State University [66].

Results of Tsay's model were compared with experimental results obtained by Busek of the 3cm diameter thruster. Control parameters were fixed with a xenon flow rate of 1 sccm, RF frequency of 1.41 MHz and 27W RF power. Electron temperature and density were not measured during experiments which could provide a comparison for the model. However, results of beam current showed reasonable agreement between the experimental results and those predicted by the model. For power levels of 10-40W, the model predicted electron temperatures between 2.7 - 4.2 eV and values for plasma density of the order 10^{17} m^{-3} [24].

RF coupling was found to decrease when flow rate to the thruster was reduced, as expected. A slight decrease in thruster performance was observed for increasing wall temperature. Assuming neutrals to be in thermal equilibrium with the walls, this was attributed to more neutrals escaping from the thruster due to their higher energy, resulting in a decrease to the propellant utilization fraction. Mass utilization efficiency was found to range between 58% - 78% and electrical efficiency between 53% - 68%. A 2mN thrust was calculated, with specific impulse above 2000s whilst power consumption was below 80W. The model indicated that the miniature RF ion thruster could achieve performance levels comparable to the miniature DC ion thruster MIXI developed by Wirz [23]. The performance model was useful for investigating characteristics of the thruster but the use of a 1D global model, which determines volume averaged parameters of the plasma, does not provide a tool for optimizing discharge chamber design.

Tsay went on to develop a 2D numerical model for RF ion thrusters involving fluid assumptions [25]. Processes such as magnetic field diffusion, coupling between the coil and plasma and ambipolar diffusion were included. The Busek 3cm diameter BRFIT-3 thruster was simulated, although the fluid assumptions were only considered loosely valid for the plasma conditions and geometry of this miniature RF ion thruster. A xenon flow rate of 1sccm was applied with RF powers between 44W-54W. Anode current showed good agreement with experimental results. Electron temperature was simulated to be of the order 3.5eV. Electrical efficiency was found to be ~50%. A breakdown of the different loss mechanisms for the simulation identified that ohmic circuit losses increased substantially compared to the larger diameter BRFIT-7 ion thruster. This was attributed to the higher operating frequency required to decrease the skin depth to match the reduced dimensions of the BRFIT-3 thruster. The power losses for the BRFIT-3 thruster are given in Figure 2.10 which can be compared with

those of the BRFIT-7 thruster in Figure 2.8. Wall losses also contributed a significant proportion of the power losses in the miniature RF ion thruster.

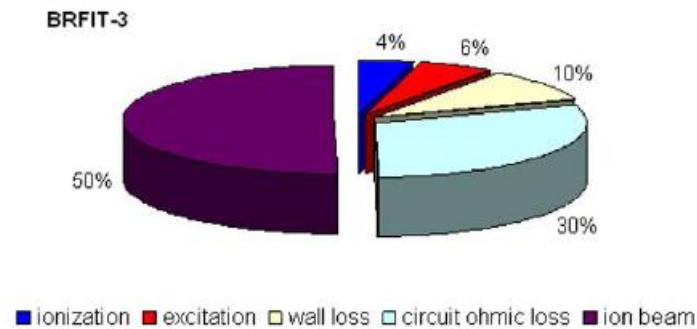


Figure 2.10. Power losses determined via numerical simulation of the BRFIT-3 thruster ^[25].

2.3 SUMMARY

An inductive discharge provides a highly efficient means of producing high density plasma for the ionization stage of a gridded ion thruster. This has been demonstrated by the commercial range of RIT thrusters.

The inductively coupled plasma of an RF ion thruster has the following general characteristics:

- High plasma density ($\sim 10^{17} \text{ m}^{-3}$) at low pressure ($< 10 \text{ mTorr}$).
- Non-equilibrium plasma; electron temperatures are of the order 2-4eV, ion and neutral temperature can be approximated as that of a gas at room temperature or they can be assumed to be in thermal equilibrium with the walls of the discharge chamber.
- Small Debye length of several microns.
- Low plasma potential.

Radio frequency power is transferred to plasma electrons via ohmic heating and collisionless heating processes. At low pressures $< 10 \text{ mTorr}$, collisionless heating dominates and occurs within the skin layer of the plasma. A skin depth of the order of the plasma radius or less is important for maintaining a stable inductive discharge. The absorbed power controls the plasma density; gas pressure controls the electron collision frequency and mean-free-paths of the species within the plasma. Control variables for RF ion thrusters are therefore the applied

RF power and the propellant mass flow rate. Optimization of the RF power coupling into the plasma is critical for enhancing thruster efficiency.

A key advantage of an RF ion thruster is that no electrodes are in direct contact with the plasma. This is one of the reasons why RF ion thrusters have been attractive for scaling down to provide low thrust levels in the μN - mN range. The efficiency of RF ion thrusters decreases on scaling down however due to the increasing surface area-to-volume ratio and the increase in operating frequency required to scale down the skin depth accordingly. Increases in efficiency can be achieved through the choice of optimal discharge chamber geometry, optimal transparency of the ion extraction system for ions and neutrals and the optimal magnetic field induction and configuration.

Chapter Three

3. The MiDGIT Thruster

The Miniaturised Differential Gridded Ion Thruster is a novel concept based on conventional RF ion thruster technology that is expected to achieve an unprecedented throttling range and thrust resolution by the differential control of opposing ion beams. This chapter provides a brief overview of the MiDGIT thruster and system, highlighting advantages and issues related to the operation of a differential ion thruster.

3.1 MiDGIT SYSTEM CONCEPT

The Miniaturised Differential Gridded Ion Thruster System is proposed as an all-electric propulsion system for providing both coarse and fine thrust control in the μN - mN thrust range. The MiDGIT thruster is designed with the goal of achieving thrust levels down to $1\mu\text{N}$, with sub- μN resolution, by the differential control of separate ion beams extracted through grid sets at opposite ends of a common discharge chamber. Conventional ion thrusters exhibit a minimum threshold in generated thrust due to the balance of power against discharge losses and also due to neutral flux escaping from the thruster. The very low μN thrust levels required for formation flying missions are very difficult to achieve. The concept of ‘*differential*’ ion beam control however would allow an ion thruster to operate at stable discharge conditions but achieve very low thrust levels by producing a net imbalance in the currents of extracted ion beams. More notably, if opposing ion beams can be perfectly matched and neutral flux from either end of the thruster can be assumed to be equal, this would theoretically permit throttling down to null thrust. Higher thrust levels in the mN range could also be achieved, with high specific impulse, by blocking neutral flow to one half of the discharge chamber, permitting single ion beam operation as for conventional ion thrusters.

The MiDGIT thruster utilizes a radio frequency (RF) inductive plasma discharge for ionization of propellant gas. Inductively coupled plasma discharges generate plasma with high

electron density at low pressures without the need of internal electrodes. This simplifies the design of the thruster compared to DC ion thrusters and should improve operational lifetime.

A schematic of the basic configuration of the MiDGIT thruster is given in Figure 3.1. The differential (twin-ended) concept restricts the position of a gas distribution system, comprising propellant feed, isolator and gas distributor, to be located centrally along the discharge chamber. Two independent RF induction coils are located either side of the gas distributor. An earth screen is positioned around the discharge chamber and induction coils to shield external components from electromagnetic fields. The extraction grid sets at either end of the thruster consist of an accelerator grid and a screen grid. The screen grid acts as an anode to collect electrons equivalent to the number of ions extracted from the discharge. Measurement of the screen grid current therefore allows monitoring of the ion beam current, and consequently thrust. A neutralizer is located close to the thruster for beam neutralization, preventing ions backstreaming to the spacecraft.

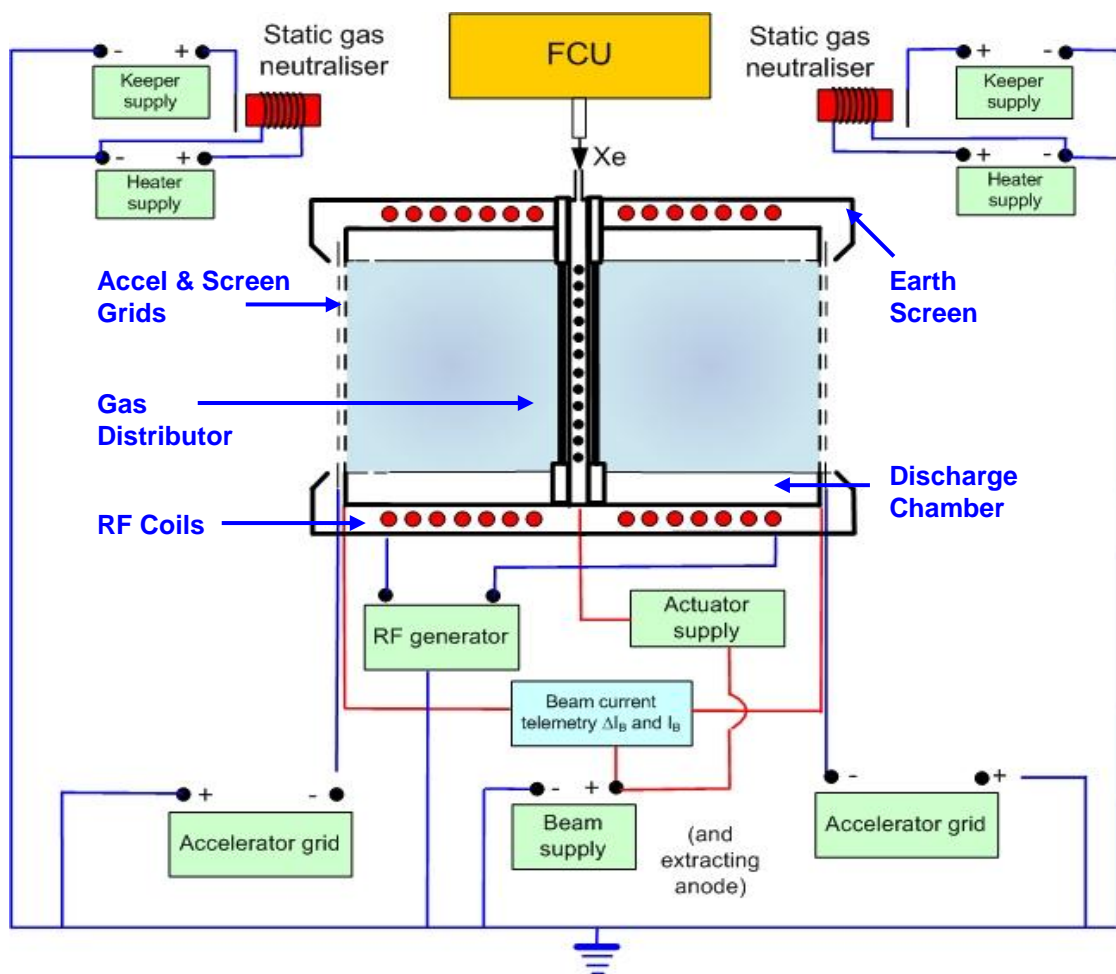


Figure 3.1 – Schematic of the MiDGIT Architecture.

3.1.1 Control Modes

3.1.1.1 Fine Thrust Control

Thrust level is controlled in conventional RF ion thrusters by controlling ionization rate through the propellant mass flow rate and RF power, with fixed potentials applied to the extraction grids. It is known however that variation of the electrostatic field between the extraction electrodes of ion optic systems affects the geometry of the plasma sheath formed upstream of the grids [47,71]. Sheath geometry in turn influences the focussing of ion beamlets through the grid apertures (as outlined in section 2.2.3) and, to a small degree, the ion current that can be extracted due to changes in sheath surface area due to changes in the curvature of the sheath. PIC simulations of ion extraction through a two grid system performed by Zhong et al [71] in particular demonstrate that as the potential applied to the accelerator grid becomes increasingly negative, the sheath moves away from the upstream surface of the screen grid, moving further into the discharge chamber, and becomes more convex with respect to the plane of the screen grid (indicated in Figure 3.2).. At large negative potentials, the curvature of the sheath can lead to over-focussing and cross-over of the ions, resulting in large divergence angles for the beamlets (shown Figure 3.3).

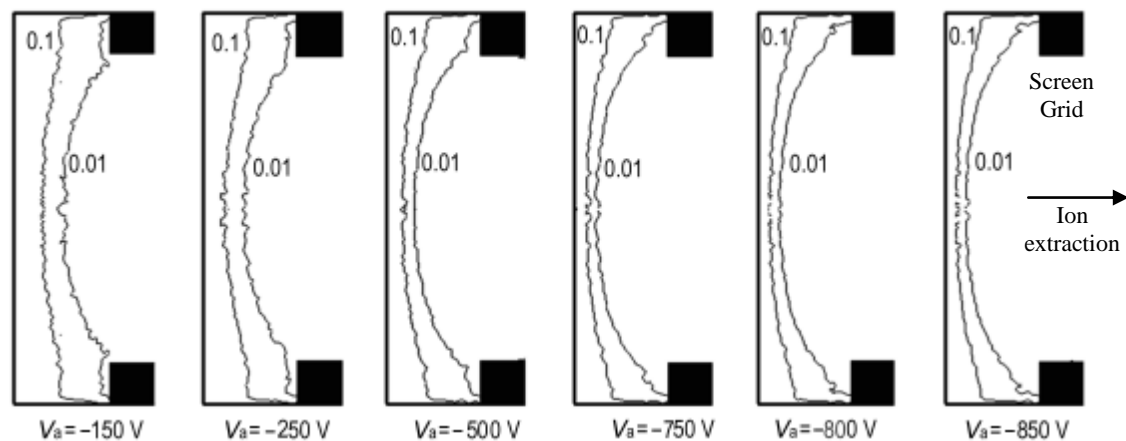


Figure 3.2. Sheath geometry indicated by the ratio of electron density to ion density upstream of the screen grid for different accelerator grid potentials (*Accel grid not shown*)^[71]. The plasma sheath boundary is taken to be where $n_e/n_i = 0.01$.

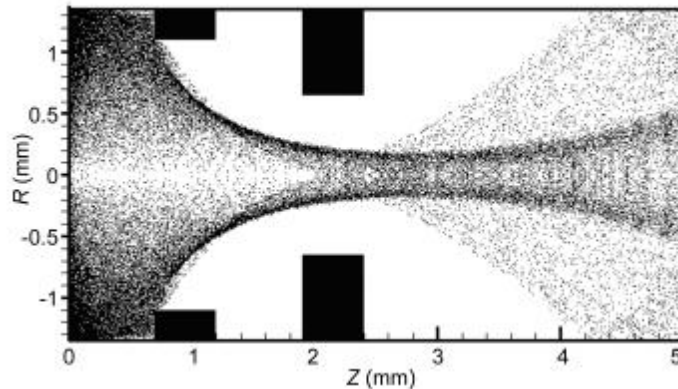


Figure 3.3. Ion distribution through a two grid extraction system simulated by Zhong et al. displaying over-focussing for $V_{ACC} = -800V$ ^[71].

It was originally proposed by QinetiQ that very fine control of the ion beam current for the MiDGIT thruster could be achieved by fine adjustment of the accelerator grid voltage. Very precise thrust down to very low level could then be achieved by creating a net imbalance in the thrust generated from opposing ion beams. During fine thrust control mode, the MiDGIT thruster would therefore be operated at a set propellant mass flow rate and RF power, while the potential of the accelerator grids on either end of the thruster would be adjusted.

Another method for differential ion beam control proposed during the course of this work to provide fine thrust control is by means of variation of the RF power on each end of the thruster. Power coupling between the induction coil and plasma of an inductive discharge is mainly governed by the RF current in the induction coil. It was proposed that varying the power delivered to the plasma on each end of the thruster, by controlling the RF current in each of the induction coils, could lead to a higher plasma density on one end and therefore, a higher beam current on that end.

Controlling the thruster during differential operation will rely on resolving the individual currents of the screen grids. As stated, gas will be injected into the discharge chamber by a gas distributor located mid-way along the length of the chamber. It is assumed that neutral distribution will be fairly uniform throughout the volume of the discharge chamber due to the low operating pressures expected and that neutral flux through each grid set will be the same for such a configuration. Therefore, any net thrust component from neutrals should be cancelled.

The disadvantage of differential beam control for achieving very low thrust levels is that specific impulse will be comparatively poor to that of other miniature ion thrusters that can achieve the same thrust levels, due to the extraction of two beams. Overall system advantages of using a thruster with both precision and coarse propulsion capabilities however may offset any extra propellant requirements due to differential thrust control.

3.1.1.2 Coarse Thrust Control

Orbit control manoeuvres will require higher thrust levels in the mN range and large thrust variations but will not require as high a precision as fine pointing manoeuvres. During coarse thrust control, the MiDGIT thruster will therefore be operated as a conventional gridded ion thruster, extracting only one ion beam. The accelerator and screen grid potentials will be fixed while the mass flow rate and RF power will be varied to control beam current. To achieve higher specific impulse levels than for differential operation, a mechanical shutter will be activated to close off one end of the discharge chamber. Two gating mechanisms will be required; one either side of the central gas distributor. It is suggested that each mechanism could consist of a single ceramic plate moved by piezoelectric actuators. Only the coil on the active end of the thruster will be powered, with the redundant coil left open-circuit.

3.1.2 Concept Advantages

The differential concept of the MiDGIT thruster will provide significant system advantages over other types of micropropulsion systems for spacecraft requiring both coarse and precision control. Use of a single thruster with both coarse and precision thrust capabilities will halve the number of thrusters required compared to systems using two types of thruster, permitting mass savings and simplification of the power control system. As only a single propellant will be required, compared to cold gas and FEEP systems that are often baselined for formation flying spacecraft, mass savings could be achieved by reduction of the number of propellant tanks, pipework and valves. The main disadvantage for a differential ion thruster, as previously stated, is that specific impulse will be low during differential operation compared to conventional single-ended thrusters and power consumption will be higher.

3.2 SYSTEM CONSIDERATIONS

3.2.1 Flow Rate Control

Ion production is dependent on propellant flow rate into the discharge chamber. The accuracy and resolution of the flow control unit (FCU) is a concern for conventional ion thrusters for achieving the demanding requirements for fine thrust control. The use of a common plasma discharge during differential operation of the MiDGIT thruster however should eliminate any effects due to flow oscillations. A simpler FCU could therefore be used for the MiDGIT thruster compared to other miniature ion thrusters for fine thrust control.

3.2.2 Beam Supply Control

Thrust resolution and repeatability can be affected by noise from the power supply and control unit (PSCU). The beam supply to the extraction grids at either end of the thruster will be connected in parallel for the MiDGIT thruster. Any oscillation in voltage should therefore be supplied to both grid sets at the same time and be effectively cancelled.

3.2.3 Beam Telemetry

The beam current on each end of the thruster must be monitored to a sufficient accuracy over an entire mission. A 12-bit telemetry system would be sufficient to provide a thrust resolution of $0.25\mu\text{N}$ for a thrust range up to 1mN . During fine thrust control, with a specified thrust range up to $150\mu\text{N}$, the thrust resolution would be of the order 37nN .

3.2.4 Thrust Vector Stability

The thrust vector is predominantly affected by the alignment between the accelerator and screen grid. The grids must therefore be aligned with minimum relative offset to each other and also to the opposing grid set to ensure minimal disturbance torques. A self-aligning grid system could be used to minimize mechanical misalignments.

3.2.5 Neutralization

A neutralizer must be used to prevent backstreaming of beam ions onto the spacecraft. Hollow cathodes are generally used as neutralizers for EP systems, where propellant gas is heated to generate plasma from which an electron beam can be extracted. A single hollow cathode neutralizer could generate a force of the order of several μN for typical operating conditions, which must be continually compensated to achieve the low thrust levels required for fine thrust control. Ideally, a non-gas flow neutralizer should be used, such as a field emission electron source, but these technologies are still in development stages and so do not have flight heritage.

3.3 GENERAL DESIGN CONSIDERATIONS

3.3.1 Discharge Chamber Material

Inductively coupled plasmas require dielectric discharge chambers. Due to high temperatures involved in the discharge process ceramics are used, with favoured materials being quartz and more recently alumina. Five materials were investigated for the discharge chamber of the RIT-4 ion thruster by the University of Giessen; alumina, quartz, boron nitride, Teflon and magnesia silicate (Stenan) [74]. Both Teflon and Stenan were found to be degraded during investigation due to ion bombardment and thermal degradation. Quartz and alumina showed the best electrical and mechanical properties. Other machinable ceramics often used for discharge components are Macor and Shapal-M (AlN). Material properties of these ceramics are compared alongside quartz and alumina in Table 3-1.

	Alumina (Al₂O₃)	Shapal-M (AlN)	Macor	Quartz (SiO₂)
Density (g/cm)	3.77	2.9	2.52	2.2
Hardness (kgf/mm²)*	1175	390	230	600
Compressive Strength (MPa)	2100	1200	345	1100
Dielectric Constant	16.7	7.1	6.0	3.75
Dielectric Strength (kV/mm)	9.1	40	40	40
Thermal Conductivity (Wm⁻¹K⁻¹)	18	90	1.46	1.30
Coefficient of Thermal Expansion (°C)	8.1e-6	4.8e-6	9.3e-6	0.55e-6

* 1 kgf/mm² = 9.80665×10⁶ Pa

Table 3-1 – Properties of ceramics considered for the MiDGIT discharge chamber.

Ceramic compounds with various AlN content have been investigated for Hall Effect thrusters as AlN has a high thermal conductivity [75]. Erosion of ceramic material due to sputtering is the driving factor in the lifetime of discharge chambers for these thrusters; sputtering yield being dependent on working temperature of a material and increases as temperature rises [75]. However, sputtering of the discharge chamber is not considered an issue for RF ion thrusters

due to the relatively low energies of ions. Materials with high thermal conductivity may however reduce thermal gradients along the discharge chamber due to localized heating from the plasma, which may be of particular importance for differential operation of the MiDGIT thruster. Also, neutral temperature may be reduced to minimize the flux of neutrals escaping through the extraction grids.

Macor has been used by Penn State University for the discharge chamber of an RF micro-ion thruster [65]. Macor has a much lower thermal conductivity than alumina and Shapal-M, meaning that it can provide a better thermal barrier to thruster components surrounding the discharge chamber, particularly the induction coil for which resistance must be minimized.

Quartz has the best electrical properties, with a high dielectric strength and the lowest dielectric constant, meaning that any capacitive coupling between the coil and plasma may be reduced. However, alumina displays the best mechanical properties. Shapal-M is a good compromise between the two but its high thermal conductivity may be a concern if heating of the induction coils is determined to be an issue.

3.3.2 Discharge Chamber Geometry

The scaling laws for the RIT microthrusters provide a basis for defining the geometry of the MiDGIT thruster. Discharge efficiency is mainly affected by the geometry of a discharge chamber through the surface-area-to-volume ratio, which increases substantially for small diameter thrusters. A simple numerical model of a RF ion thruster by Tsay identified that wall losses contributed 10% to the power losses of a 3cm diameter RF ion thruster [25]. An optimisation study of discharge chamber geometry was performed by Closs for the RIT-XT thruster, which identified that a conical design of discharge chamber provided a reduction in RFG power input by up to 25% and significant mass savings due to a reduction in size compared to the previous RIT-XT design [67]. The improvements were mainly achieved through the removal of the back wall required for a cylindrical discharge chamber. Conical chambers clearly provide benefits for conventional, single-ended RF ion thrusters but may not be particularly beneficial for a differential ion thruster utilizing a common discharge chamber.

3.3.3 Coil Geometry

The electromagnetic field decays exponentially from an induction coil dictating that the coil should be located in direct contact with the discharge chamber for greatest efficiency. However, heating of the discharge chamber by the plasma may significantly affect the resistance of the coil, and therefore lower the power coupling efficiency.

Due to the skin effect, the field within the wire of the induction coil will decay to a value of e^{-1} within a few microns from the outer surface of the wire; hence current will be carried along a thin layer on the surface of the coil. Hollow copper tubes may therefore be used for the coil to reduce mass. Silver coated tubes may also be used to reduce coil resistance but will incur higher costs.

3.3.4 Gas Distributor

Historically, gas distributors for ion thrusters have often been designed as multi-aperture showerhead-type plates at the rear of the discharge chamber to provide a uniform injection of neutral gas to the ionization region. To enhance ionization efficiency by increasing the residence time of neutrals within the discharge chamber, the apertures or nozzles of the distributor plate can be angled to inject gas perpendicular to the thrust axis.

The concept of the MiDGIT thruster restricts the position of the gas distributor to be located mid-way along the length of the discharge chamber. An annular gas distributor was therefore proposed by the author, comprising a ceramic plenum annulus with injection holes machined along the inner wall of the annulus in order to inject neutrals from the edge of the discharge chamber towards the centre. It was proposed that such a design of distributor would:

- Maximise the residence time of neutrals within the discharge chamber due to radial injection.
- Enhance ionization efficiency by injecting gas into the skin layer, close to the walls of the discharge chamber where electron temperature is expected to be greatest.
- Provide uniform neutral distribution within the discharge chamber provided flow rate through each injection hole is equal.
- Help dampen oscillations in the neutral flow through the use of an effective plenum.
- Permit the gas distributor to be integrated into the walls of the discharge chamber.

A survey of existing literature indicated that a similar geometry for an annular gas distributor was previously investigated for a RF ion thruster by Iwata and Takegahara [76]. The design implemented however consisted of a plenum chamber internal to the discharge chamber, injecting neutrals outwards from the centre of the discharge chamber towards the walls through 2mm diameter injection holes. The possibility of integrating a gas distributor into the walls of the discharge chamber would reduce discharge losses due to a lower surface-area-to-volume ratio inside the discharge chamber, and therefore improve efficiency.

The dimensions of an annular gas distributor may be restricted however if machined into the walls of the discharge chamber. Restrictions to the design of the gas distributor for the MiDGIT breadboard thruster can be found in [77]. Of concern to the design of the breadboard gas distributor was the minimum diameter that could be achieved through the process of drilling of the injection holes; the minimum hole diameter was stated to be 0.5mm due to available drill bits. The actual diameter of the injection holes for the breadboard gas distributor was larger, being 1mm. At the typical operating pressures and flow rates expected for the MiDGIT thruster, Direct Simulation Monte Carlo (DSMC) simulations of the neutral flow using DS2V [69] indicated such a relatively large diameter of injection hole would provide a non-uniform distribution of gas around the periphery of the discharge chamber, as outlined by the author in [77] and depicted in Figure 3.4. The impact of this on discharge parameters and efficiency was not assessed at the time. Hole diameters $\leq 0.1\text{mm}$ are expected to be required for uniform neutral injection [77].

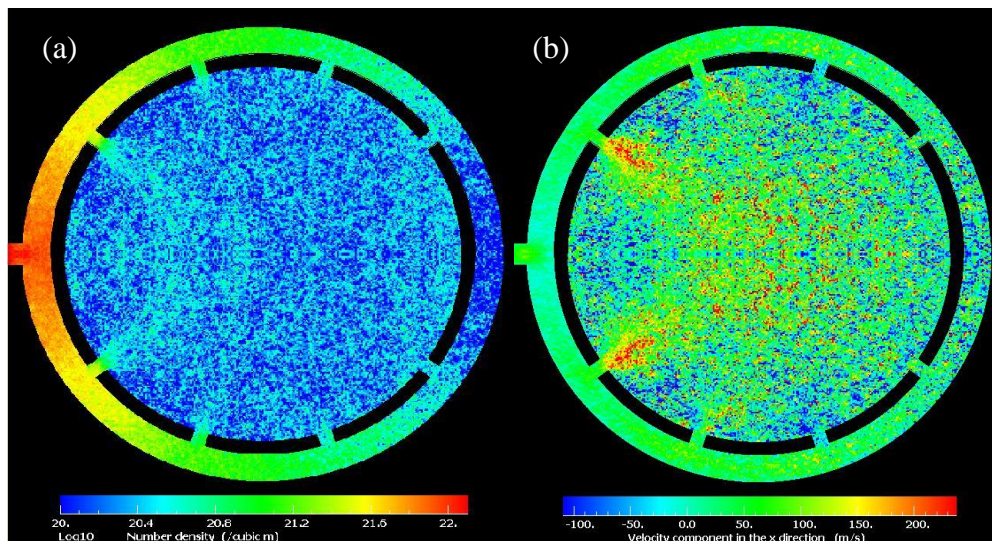


Figure 3.4. Plot of (a) neutral number density and (b) neutral velocity for an annulus with eight 1mm diameter injection holes at a flow rate of 0.35 mgs^{-1} .

3.4 PROTOTYPE AND BREADBOARD THRUSTER MODELS

3.4.1 Prototype Configuration

A prototype of the MiDGIT thruster was constructed, based on design proposals by the author and QinetiQ, to address early design issues by investigating different configurations for the thruster and to provide an indication of baseline performance. The prototype consisted of a 70 mm x 38 mm OD alumina tube with two induction coils located either side of the gas feed into the discharge chamber. The internal diameter of the discharge chamber was approximately 33 mm. The gas feed consisted of a single 3.2 mm diameter PTFE pipe supported by a macor tube. The discharge chamber was manufactured in two sections so that shutter plates could be positioned in the middle of the discharge chamber for operating the thruster in single-end and differential modes. The ends of the thruster were identified as shown in Figure 3.5. Different coil assemblies could also be wound around the exterior of the discharge chamber for investigating coil geometry. One configuration of the prototype thruster that was tested is displayed in Figure 3.5. The configuration that displayed the best performance utilized two 6 turn coils with a pitch of 3.2mm formed from 0.8mm diameter enamelled copper wire and graphite grids with 37 apertures. Results presented for the prototype thruster in this work were obtained with this configuration. Grid geometry is presented in Table 3-2 and the predicted perveance and electron backstreaming limit determined from equations 2.39, 2.42 and 2.43 for various grid potentials relevant to this work are presented in Table 3-3. It can be seen that the prototype grids were not designed to meet the requirements for coarse thrust mode; the main purpose of the prototype thruster was to provide an insight into the design and operation of an RF ion thruster.

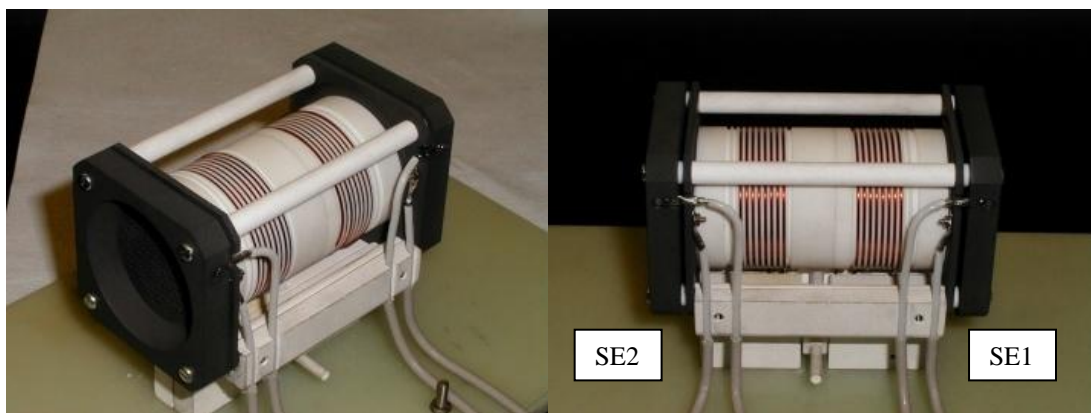


Figure 3.5. Images of the MiDGIT prototype with earth screen removed.

	Screen Grid	Accel Grid
Aperture diameter, d (mm)	2.15	1.50
Grid thickness, t (mm)	0.30	1.00
Grid gap, l_g (mm)	1.00	
Number of apertures	37	37
Material	graphite	graphite

Table 3-2 – Summary of the grid geometry for the MiDGIT prototype.

$ V_b $ (V)	$ V_{ACC} $ (V)	I_B (Perveance) (mA)	T_{max} (Perveance) (mN)	$ V_{EBS} $ (V)
950	95	7.61	0.387	74.4
1176	250	12.32	0.686	92.14
1300	250	13.74	0.817	101.9

Table 3-3 – Electron backstreaming limit and maximum beam current and thrust at perveance predicted for the MiDGIT prototype grids.

3.4.2 Breadboard Configuration

Outputs from the prototype test phase of the MiDGIT thruster were considered during the design of an improved breadboard model. The discharge chamber of the breadboard thruster consisted of a cylindrical tube machined from alumina with an inner diameter of 28mm, comparable to the RIT-3 RF ion thruster. Discharge losses in RF ion thrusters are mainly governed by ion losses to the walls. Although the use of conical discharge chambers have been shown to provide significant improvements to mass utilization efficiency and power, the discharge chamber for the MiDGIT breadboard model was kept cylindrical due to available resources and ease of manufacture. An annular gas distributor was incorporated into the walls of the discharge chamber to provide radial injection of neutrals and to keep a uniform internal diameter along its length. The discharge chamber was machined in three sections consisting of two main ionization regions, each 32.75 mm in length, and a central region incorporating the gas distributor. The internal annulus of the gas distributor was 2mm wide and eight 1mm

diameter injection holes were drilled around the inner wall to provide gas injection points. The distributor section was 3mm wide in total and a single PTFE gas feed supplied gas to the annulus. Ceramic shutter plates were machined from alumina that could be slid manually across the diameter of the discharge chamber either side of the distributor, as displayed in Figure 3.6. Two induction coils were wound directly onto the discharge chamber, each with 6 turns of 0.8mm diameter enamelled copper wire and a pitch of 3.2mm. The extraction grid sets comprised a molybdenum screen grid and a graphite accelerator grid, each fabricated with 55 apertures (shown in Figure 3.7). The grid design was based on that of the T5 ion thruster grids which are optimized for an accelerator grid voltage of -250V and beam voltage of 1176V. Grid geometry is presented in Table 3.4 for the breadboard model; the main difference from the geometry of the prototype grids being a reduced grid gap and increased grid open-area. As can be seen from Table 3.5, the extraction grids for the breadboard thruster should provide a suitable thrust range considering coarse thrust requirements. The ends of the thruster were identified as shown in Figure 3.7.

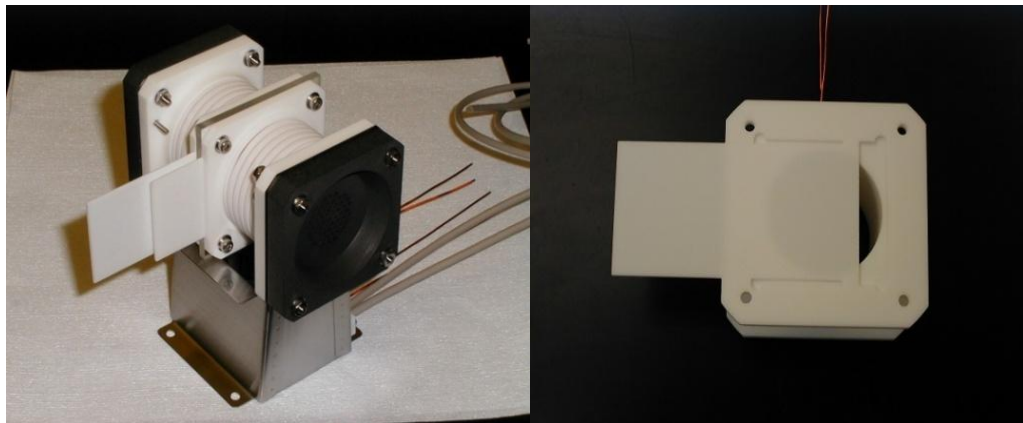


Figure 3.6. Images of the MiDGIT breadboard thruster displaying ceramic shutter plates.

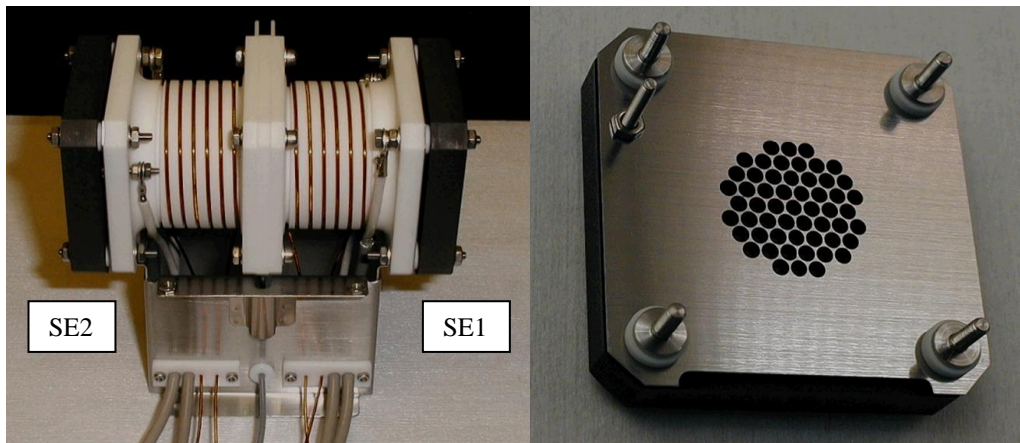


Figure 3.7. Images of the MiDGIT breadboard thruster and extraction grids.

	Screen Grid	Accel Grid
Aperture diameter, d (mm)	2.15	1.50
Grid thickness, t (mm)	0.30	1.00
Grid gap, l_g (mm)	0.75	
Number of apertures	55	55
Material	molybdenum	graphite

Table 3-4 – Summary of the grid geometry for the MiDGIT breadboard.

$ V_b $ (V)	$ V_{ACC} $ (V)	I_B (Perveance) (mA)	T_{max} (Perveance) (mN)	$ V_{EBS} $ (V)
950	95	14.25	0.725	84.4
1176	250	22.72	1.285	104.4
1300	250	25.74	1.531	115.5

Table 3-5 – Electron backstreaming limit and maximum beam current and thrust at perveance predicted for the MiDGIT breadboard grids.

Chapter Four

4. Experimental Arrangement & Procedures

Test campaigns were performed on prototype and breadboard models of the MiDGIT thruster in order to provide verification of the differential ion thruster concept, to investigate design issues and demonstrate preliminary performance. Two vacuum facilities were available during the course of this work. Performance tests were carried out on both the prototype and breadboard thrusters at the QinetiQ Large European Electric Propulsion (LEEP) facilities. Discharge tests and investigations specific to differential thrust control involving the prototype thruster were performed within the EP1 vacuum facility at the University of Southampton. An overview of each facility is provided and the experimental arrangement and procedures employed during the test campaigns are described.

4.1 OPERATING MODES AND ELECTRICAL CONFIGURATION

As outlined in Chapter 3 the MiDGIT thruster is designed with the ability to be operated in a single ion beam mode and also a *differential* mode, where two opposing ion beams are extracted from a common discharge. The general thruster configuration for each operating mode is described below.

4.1.1 Single-End Configuration

It is proposed that a gating mechanism comprising a ceramic plate driven by piezoelectric actuators could be used to close one half of the discharge chamber of the MiDGIT thruster to enable single end (SE) operation. A fully automated system was beyond the scope of this work however. Therefore, the prototype and breadboard thrusters were configured for SE operation by manual insertion of a ceramic plate to one side of the central gas distributor to restrict neutral flow. The induction coil on the blocked end of the thruster was left open-

circuit to reduce power loss due to mutual coupling between the coils. Thrust was controlled by varying the propellant flow rate and RF power while fixed potentials were applied to the extraction grids. A schematic of the electrical configuration of the MiDGIT thruster for SE operation is displayed in Figure 4.1.

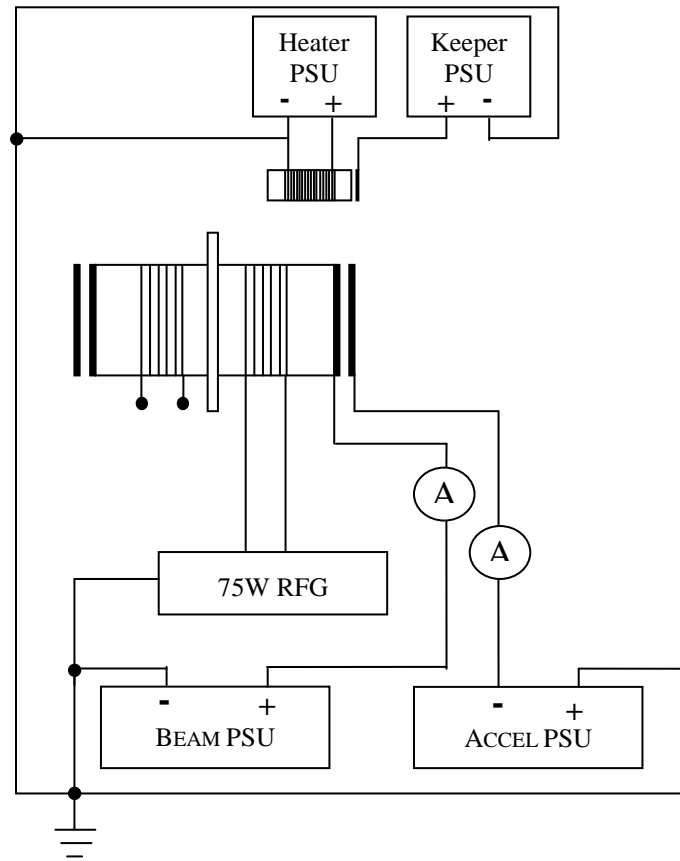


Figure 4.1. Electrical configuration of MiDGIT thruster and T5 hollow cathode neutralizer during single-end operation.

4.1.2 Differential Configuration

Two methods were proposed for achieving differential control; independent variation of the accelerator grid potentials to induce changes in sheath geometry upstream of each screen grid which would lead to a net offset in the extracted ion beam currents, and variation of RF power on each end of the thruster to generate a higher plasma density on one end and ultimately a differential thrust.

It is proposed that variation of the RF power on each end of the thruster could be achieved by the use of two separate induction coils located either side of the central gas distributor, controlled independently by two separate radio frequency generator (RFG) circuits. During the test campaigns on the MiDGIT thruster, two separate radio frequency generators were not available at the same time for testing. A single RFG was therefore used but connected to two separate matching units to vary the match, and consequently the power, to each coil. The matching units that were used utilize a T-type matching circuit consisting of two variable capacitors and an inductor; the equivalent circuit is represented in Figure 4.2. For a given inductor setting, the match and therefore RF power delivered to an antenna (induction coil in this case), can be varied by adjusting the values of the capacitor on the transmitter side (C_T) and the antenna side (C_A).

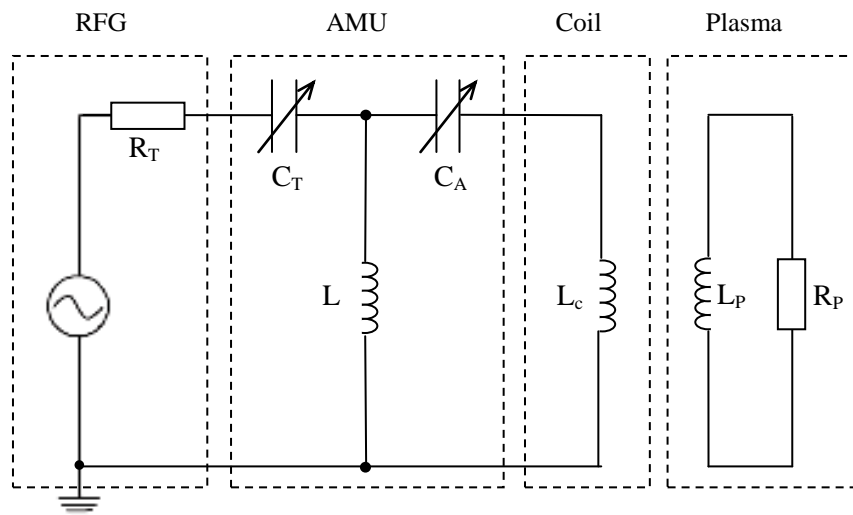


Figure 4.2. Equivalent circuit of RFG and antenna matching unit.

The general electrical configuration of the MiDGIT thruster for differential operation is displayed in Figure 4.3.

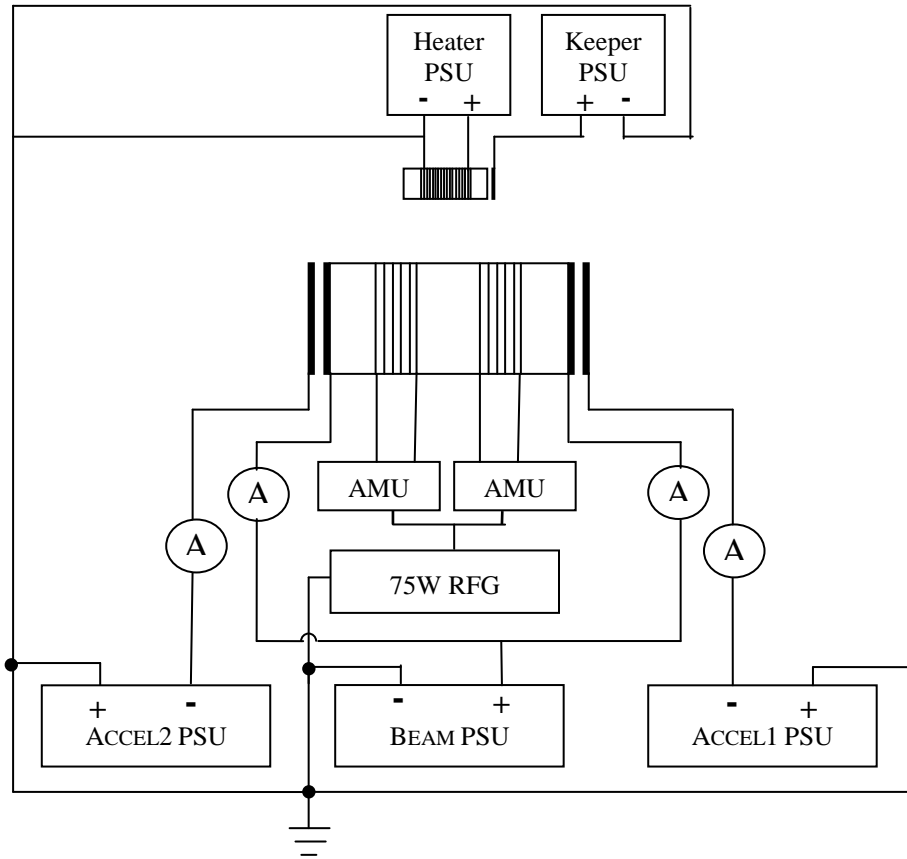


Figure 4.3. Electrical configuration of MiDGIT thruster and T5 hollow cathode neutralizer during differential operation.

4.2 LEEP-1 VACUUM FACILITY

4.2.1 Vacuum Chamber

Performance tests of the prototype and breadboard thrusters, and ultimately a detailed characterization of the MiDGIT breadboard thruster, were performed within the loadlock of the QinetiQ LEEP-1 vacuum facility. The loadlock (displayed in Figure 4.4) consists of a 0.75m diameter x 1.40m cylindrical glass vacuum chamber which permitted visual observation of the thruster assembly throughout all tests. A Pfeiffer Balzers TCP5000 controller and TPH2200 turbomolecular pump system, backed by a Pfeiffer DUO 120A roughing pump was used to pump the loadlock to a base pressure of approximately 5×10^{-6} mbar. A Pfeiffer Balzers dual pressure gauge package comprising Pirani and cold cathode ion gauges was used to monitor the background pressure within the chamber. Grafoil sheets, 30cm x 25cm in dimension, were mounted at each end of the loadlock at a distance of 50cm from the ends of the thruster to act as beam targets during beam extraction. A 4-way SMA vacuum feedthrough was used for transmission of the RF lines between the external RF generator and thruster mounted within the chamber. SMA connectors permitted a 50Ω match on either side of the vacuum feedthrough. Additional high voltage CF feedthroughs were used for transmission of electrical lines.



Figure 4.4. The loadlock of the LEEP-1 vacuum facility at QinetiQ.

4.2.2 Thruster Interface

An interface plate was assembled to which prototype or breadboard models of the MiDGIT thruster could be mounted (see figure 4.5). The plate was designed so that different models could be easily interchanged and loaded into the LEEP-1 loadlock. The thruster was mounted on a FR4 mounting block to isolate the thruster body. A T5 hollow cathode neutralizer was mounted to one side of the thruster for use during ion beam extraction. A 60W tungsten filament (not shown) was also mounted on the opposite side of the thruster for use as an electron source for discharge ignition. The interface plate provided terminal block connections for the high voltage grid potentials, low voltage connections for the neutralizer assembly, RF connections for the induction coils and a means to secure the gas feed line.

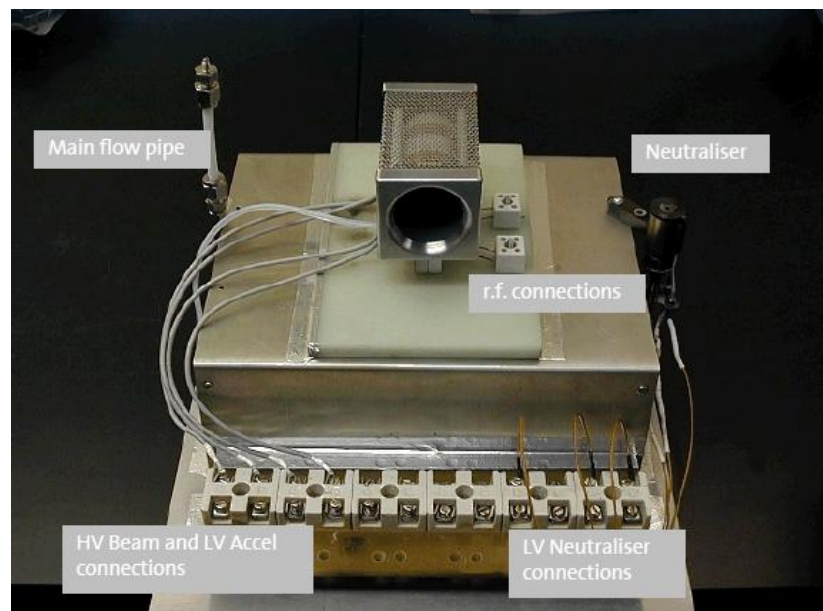


Figure 4.5. Mounting plate with attached neutralizer and flow pipe showing the MiDGIT prototype thruster.

4.2.3 Radio Frequency Generator

The MiDGIT development programme did not allow for the additional development of a dedicated, vacuum compatible radio frequency generator (RFG) for the thruster. An external RFG comprising COTS components was therefore constructed (displayed schematically in Figure 4.6). Though locating the RFG externally to the vacuum chamber would knowingly incur significant power losses due to the length of the transmission lines and the feedthrough connections required, this was considered to be acceptable for the development stage of the MiDGIT thruster; the main objective being to provide a proof-of-concept.

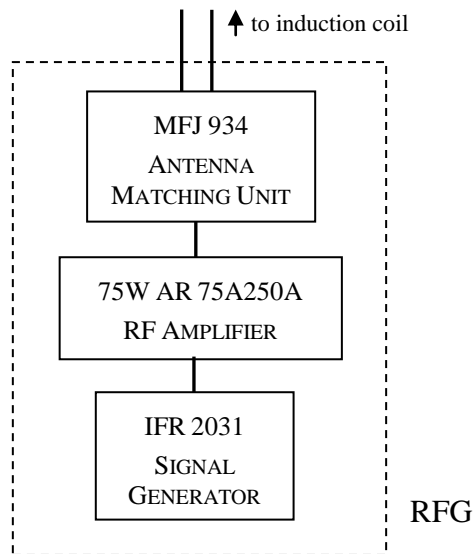


Figure 4.6. Schematic of RFG comprising signal generator, RF amplifier and matching unit.

RF power was supplied by a RFG comprising an IFR 2031 variable frequency signal generator (10kHz-2.7GHz, 0.1Hz resolution) connected to an Amplifier Research 75A250A 75W RF power amplifier. The output signal from the signal generator was selected as a Bessel sine wave and was checked on an oscilloscope. An antenna matching unit (AMU) was connected between the RF amplifier and thruster to manually match the impedance of the induction coils to the output impedance of the RF amplifier (50Ω). During single end operation of the thruster, a single MFJ-934 AMU was connected between the RF amplifier and the driven induction coil, while for differential operation the RF amplifier was connected to two separate AMUs using a BNC T-piece connector. The separate units of the RFG were connected using 50Ω coaxial cables, while twisted-pair cables, approximately 4m in length and constructed from high current PTFE coated wire, were used between the AMU and thruster.

RF frequency and power were both controlled digitally via the signal generator. The IFR 2031 signal generator provided an RF power output range of -144dBm to +13dBm with 0.1dB resolution and was connected via GPIB to a PC running LabVIEW to automatically log the signal frequency and output RF power (in dBm) at a rate of 1Hz during thruster operation.

The Amplifier Research 75A250A RF amplifier is specified to provide an output of approximately 75W ($\pm 4\%$) for an input signal of +1dBm at the highest gain setting over the frequency range 1MHz - 10MHz [78].

Conversion of power from decibels to Watts is given by:

$$P_1 = P_0 10^{(dB/10)} \quad (4.1)$$

where P_1 is a measured power level with respect to a reference power level P_0 in Watts. Therefore, an estimate of forward RF power delivered by the RF amplifier to drive the antenna matching unit and thruster in Watts was determined from the output power of the signal generator (in dBm) according to:

$$P_{fw} = 75x10^{\left(\frac{dBm-1}{10}\right)} (\pm 4\%) \quad (4.2)$$

Additionally, the RF power delivered to the thruster will be attenuated by the transmission lines between the AMU and thruster due to ohmic losses, dielectric losses and also radiation losses as the fields of each wire in the twisted-pair cable will not perfectly cancel. Power loss in RF transmission lines is not linear in nature but increases logarithmically with length, highlighting the need to minimize cable length and the number of connections. During characterisation of the MiDGIT breadboard thruster, the lines connecting the AMU and the induction coils were measured to have an attenuation factor of approximately (0.67 ± 0.01) for coil 1 and (0.66 ± 0.01) for coil 2 by measuring the voltage across the terminals of the AMU and each induction coil on an oscilloscope for various RF power levels at the operating frequency of the thruster. The attenuation factor was calculated from the ratio (V_{coil}^2/V_{AMU}^2) as displayed in Table 4-1.

An estimate of the maximum forward RF power to each induction coil of the MiDGIT thruster can therefore be determined taking into account the attenuation factor:

$$P_{fw} = 0.67x75x10^{\left(\frac{dBm-1}{10}\right)} (\pm 4.3\%) \quad (4.3)$$

This value will still incorporate losses in the matching unit, RF amplifier and induction coil.

Coil 1				Coil 2			
P_{fw} (dB)	V_{AMU}^2	V_{coil}^2	$\left(\frac{V_{coil}^2}{V_{AMU}^2}\right)$	P_{fw} (dB)	V_{AMU}^2	V_{coil}^2	$\left(\frac{V_{coil}^2}{V_{AMU}^2}\right)$
-24.0	43.6	29.2	0.6697	-24.0	39.7	25.0	0.6297
-23.8	44.9	30.3	0.6748	-23.8	41.0	27.0	0.6585
-23.6	47.6	31.4	0.6597	-23.6	42.3	28.1	0.6643
-23.4	50.4	33.6	0.6667	-23.4	44.9	29.2	0.6503
-23.2	53.3	34.8	0.6529	-23.2	46.2	30.3	0.6558
-23.0	53.3	37.2	0.6607	-23.0	49.0	32.5	0.6633
-19.0	144.0	96.0	0.6667	-19.0	123.2	81.0	0.6575
-18.8	148.0	100.0	0.6757	-18.8	130.0	84.6	0.6508
-18.6	156.3	104.0	0.6654	-18.6	134.6	88.4	0.6568
-18.4	163.8	110.3	0.6734	-18.4	139.2	92.2	0.6624
-18.2	171.6	114.5	0.6672	-18.2	146.4	96.0	0.6557
-18.0	176.9	118.8	0.6716	-18.0	153.8	100.0	0.6502
		Mean	0.6670	-17.8	161.3	106.1	0.6578
		1-σ	0.0067	-17.6	169.0	112.4	0.6651
						Mean	0.6556
						1-σ	0.0089

Table 4-1 – Attenuation of RF power between AMU and induction coil at 5.25MHz.

An indication of forward and reflected RF power in Watts was also provided by means of an analogue (SWR) power meter incorporated into each AMU. RF power delivered to the induction coil would typically be determined by the difference between the forward and reflected power:

$$P_c = P_{fw} - P_r \tag{4.4}$$

Comparison of the forward RF power measured by the SWR meter and that determined from Equation 4.3 indicated however that the power displayed by the SWR meter was significantly overestimated compared to the signal generator (as can be seen in Figure 4.7). A correction factor between the forward RF power of the SWR meter and the signal generator was determined in order to provide another means of estimating the RF power delivered to the

induction coil, particularly useful for estimating the power to each induction coil during differential operation. The correction to the forward RF power of the SWR meter was calculated as:

$$P'_{fw} = 0.67 \times 5.1869 \exp(0.0292 P_{SWR}) \quad (\pm 4.9\%) \quad (4.5)$$

The reflected RF power can then be subtracted to estimate the power delivered to the induction coil. Insertion of a lossy transmission line between a SWR power meter and an antenna however leads to the reflected power being underestimated at the point where the meter is located due to attenuation down the transmission line. The estimated power delivered to the induction coil P_c will therefore be an upper estimate.

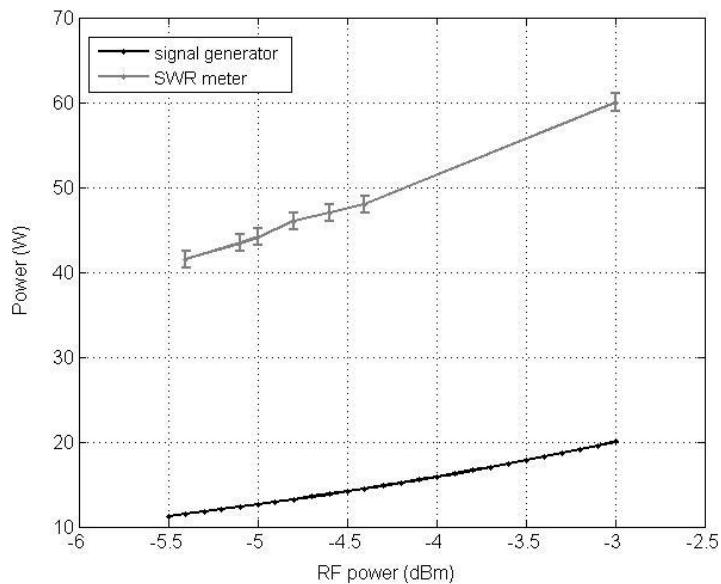


Figure 4.7. Comparison of measured RF forward power determined from signal generator and that displayed by SWR power meter.

4.2.4 Power Supplies and Meters

The units for the RFG were mounted within a rack including 3 Glassman 60V, 5A low voltage power supplies. These were used to power the neutralizer keeper and heater and also a 60W tungsten filament used for discharge ignition. A separate high voltage rack was assembled by QinetiQ to supply the HV beam and accelerator grid potentials and monitor the grid currents. The HV rack consisted of the following units:

Supply / Meter	Quantity	Unit
Beam PSU	1	1kV Glassman high voltage DC supply (floating)
Accel PSU	2	1kV Bertran 205B-01R high voltage DC supply
Beam current sense	2	Agilent 34401A DMM (floating)
Accel current sense	2	Agilent 34401A DMM
Beam voltage sense	1	Agilent 34401A DMM

Table 4-2 – Beam and accelerator grid supplies and meters.

The units that were not required to be floating were commoned to the ground point of the vacuum chamber. Grid voltages and currents could either be read directly from the front panel of the supplies and digital multi-meters (DMMs) or logged automatically via LabVIEW at a rate of 1Hz.

The beam voltage was limited to 1kV during initial characterisation of the MiDGIT thruster as a higher voltage supply was not available at time of testing. The beam and accelerator grid potentials were therefore set as 950V/95V respectively during nominal operation of the thruster. The perveance limit of the breadboard grids was calculated to provide a maximum thrust of $\sim 725\mu\text{N}$ at these potentials. It was known that characterisation of the breadboard thruster would therefore not be able to demonstrate thrust up to 1mN required for coarse thrust control, but these grid potentials were still considered acceptable to demonstrate a reasonable thrust range for characterising SE (coarse thrust) performance.

4.2.5 Propellant Feed System

A schematic of the propellant flow control system used is displayed in Figure 4.8. Both the MiDGIT thruster and T5 neutralizer were operated on xenon. The flow control system utilizes a supply of argon to produce an absolute xenon gas pressure. A proportional pressure

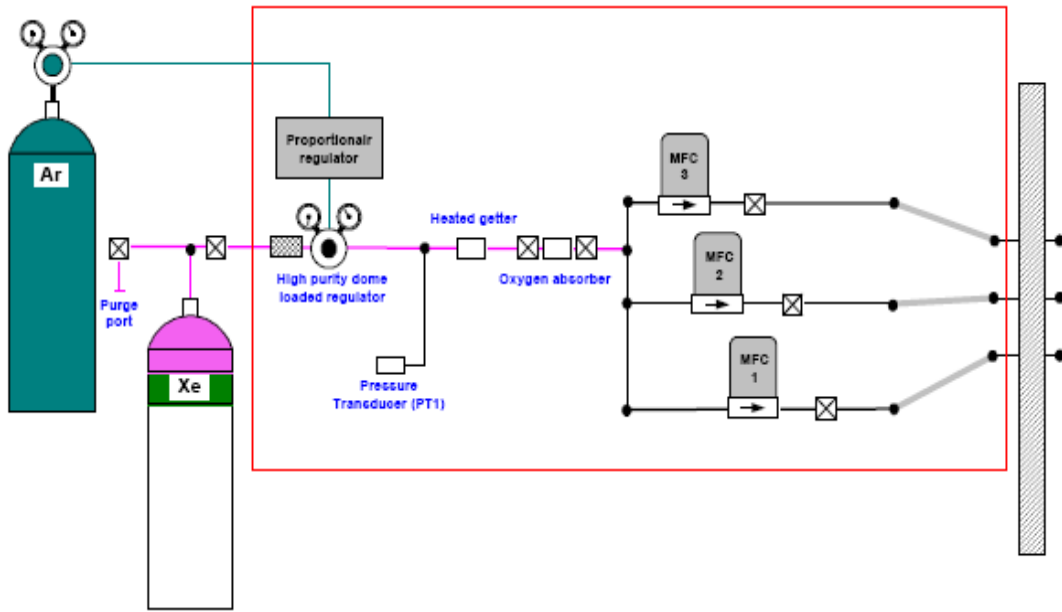


Figure 4.8. Schematic of flow control system for MiDGIT testing.

regulator controls the output pressure from the propellant tank. Residual impurities in the xenon gas flow were removed from the feed line by a heated getter and oxygen trap. Xenon flow to the thruster and neutralizer were controlled independently by an Aera ROD-4 control unit connected to two Aera FC-D980C mass flow controllers. The mass flow controllers were calibrated by the manufacturer on air. Accuracy of the Aera FC-D980C mass flow controller is stated to be within $\pm 1\%$ of the commanded flow between 25-100% of the full-scale range, and within $\pm 0.25\%$ of the commanded flow for 2-25% of the full-scale range [79]. The equivalent flow rate for xenon in sccm was automatically calculated and displayed by the ROD-4 control unit using the gas correction factor supplied by the manufacturer.

Propellant flow rates are often presented as a mass flow rate in mgs^{-1} . For an ideal gas at standard temperature and pressure, conversion of volumetric flow rate (sccm) to mass flow rate (mgs^{-1}) can be shown to be:

$$\begin{aligned}
 1 \text{ sccm} &= 4.47796 \times 10^{17} \left[\frac{\text{atoms}}{\text{s}} \right] \times 1.660539 \times 10^{-27} \times M_a \times 10^6 \\
 &= 7.43583 \times 10^{-4} M_a \left[\frac{\text{mg}}{\text{s}} \right]
 \end{aligned}
 \tag{4.6}$$

where M_a is molecular mass (amu).

For xenon, with a molecular mass of 131.293 and gas compressibility factor of 0.9931468, the conversion is therefore given by:

$$1 \text{ sccm (Xe)} = \frac{9.76272 \times 10^{-2} \left[\frac{mg}{s} \right]}{0.9931468} = 0.098301 \left[\frac{mg}{s} \right] \quad (4.7)$$

During characterisation of the MiDGIT breadboard thruster, the Aera FC-D980C mass flow controller supplying the thruster had to be changed between characterisation of the two single ends of the thruster. The SE1 configuration of the breadboard thruster was therefore operated with an Aera FC-D980C MFC with a full-scale range of 5sccm, while the SE2 configuration was operated with an Aera FC-D980C MFC with a 10sccm full-scale range. Subsequent characterisation of the differential configuration was also performed with the 10sccm MFC. The mass flow controller supplying the T5 neutralizer was not altered and was another Aera FC-D980C MFC with a 10sccm full-scale range.

Calibration checks of the MFCs were performed by flowing xenon through the MiDGIT breadboard thruster and measuring the chamber pressure for various cold flow rates. The 5sccm mass flow controller used during characterisation of the SE1 configuration is referred to as MFC1 while the 10sccm mass flow controller used during SE2 characterisation is referred to as MFC2. The calibration checks indicated good repeatability for each MFC but a significant variation in chamber pressure was observed for a commanded flow between all three controllers (shown in Figure 4.9). An independent flow calibration system was not available and it was not possible at the time to perform a calibration against another mass flow controller. Correction factors between MFC1 and MFC2 were therefore determined by fitting the measured chamber pressures for each MFC and determining the relationship between MFC1 and MFC2 (see Figure 4.10 and Figure 4.11). Assuming the flow rate delivered by MFC2 to be correct, the correction to the commanded flow of MFC1 was determined to be:

$$\dot{m}'_1 = 93.09 \exp(0.5648 \dot{m}_1) - 93.14 \exp(0.5282 \dot{m}_1) \quad (4.8)$$

Alternatively, assuming MFC1 to be correct, the correction to MFC2 was determined as:

$$\dot{m}'_2 = 0.4419 \exp(0.3589 \dot{m}_2) - 0.4122 \exp(-0.9982 \dot{m}_2) \quad (4.9)$$

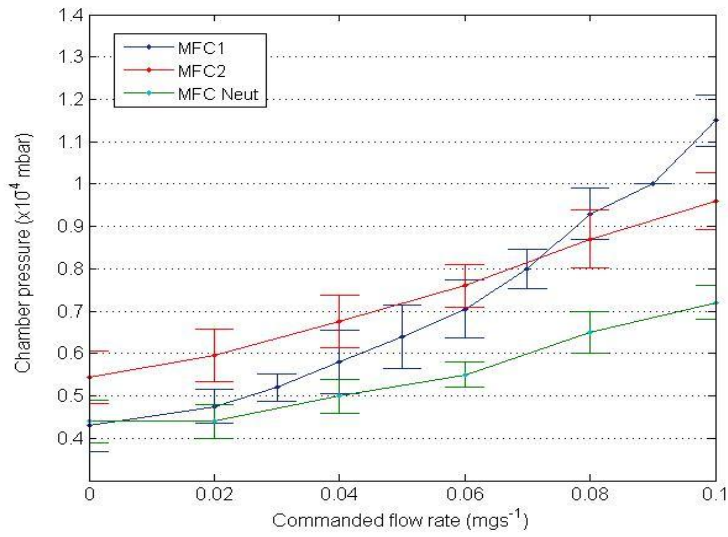


Figure 4.9. Chamber pressure for a commanded flow rate.

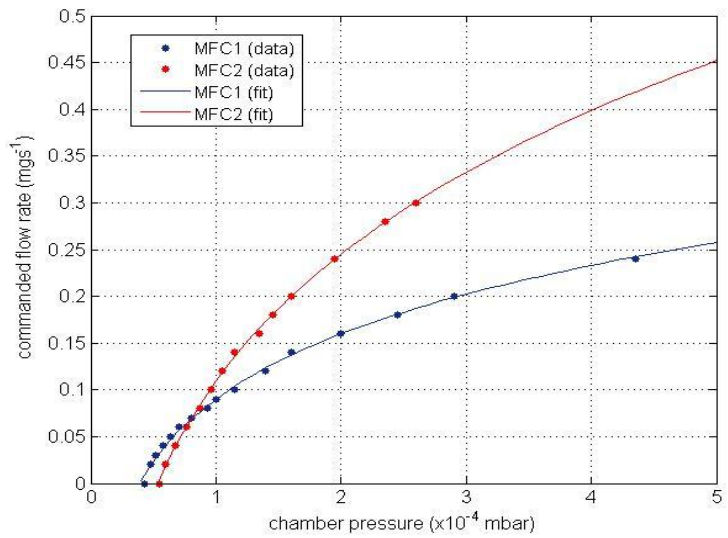


Figure 4.10. Comparison of chamber pressure for MFC1 and MFC2 flow controllers.

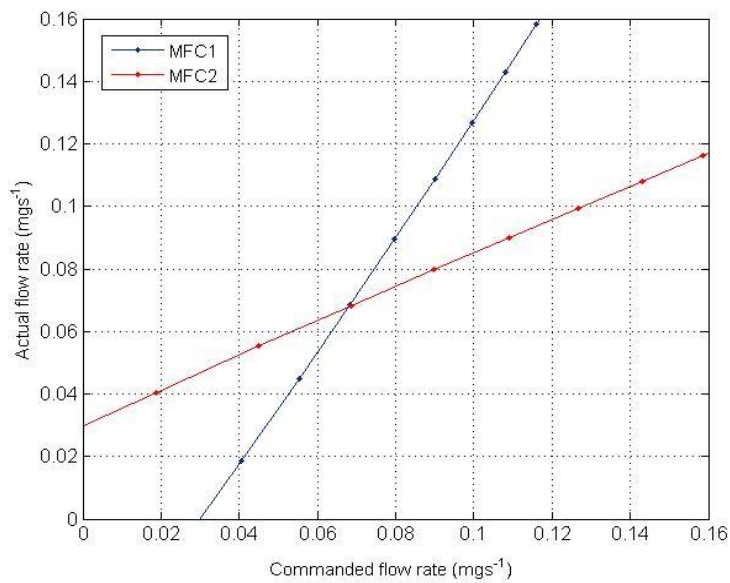


Figure 4.11. Corrected flow rate for MFC1 and MFC2.

4.2.6 Diagnostic Equipment

A rotatable beam probe system (previously assembled by QinetiQ) was mounted within the LEEP-1 loadlock chamber to obtain radial profiles of extracted ion beams from which beam current and beam divergence could be estimated. The beam probe consisted of a single screened faraday cup with 73 apertures of 0.1mm diameter, mounted on a rotatable arm driven by a motor. The faraday cup was positioned 21 cm from the exit plane of the accelerator grid and rotated about a vertical axis coincident with the grid centerline (as depicted in Figure 4.12(a)). The faraday cup was aligned mechanically and the probe arm rotated by manual control of the stepper motor. The faraday cup was biased to a potential of 50V, while the retarding grid was biased to -90V by a Glassman XM 120-0.5 power supply. Probe current was read directly from a Keithley 6157A electrometer.

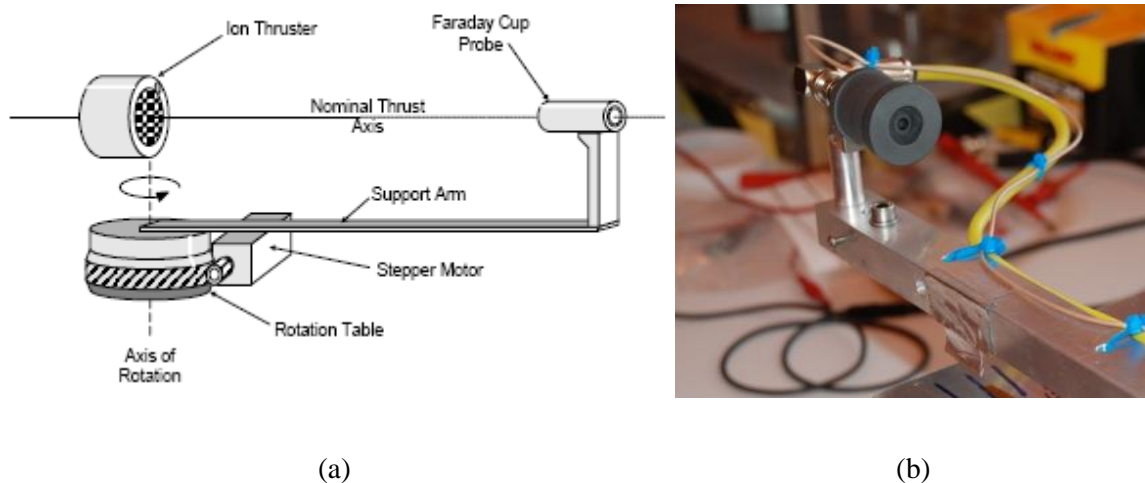


Figure 4.12. Beam probe system displaying (a) schematic of probe orientation ^[80] and (b) image of screened faraday cup.

4.2.7 Thruster Operation and Procedures

4.2.7.1 Thruster Installation

Following insertion of the MiDGIT thruster within the LEEP-1 loadlock, the chamber was pumped down to a base pressure of approximately 5×10^{-6} mbar and the thruster outgassed for a minimum of 12 hours. After an initial 2 hour period, the heater to the T5 hollow cathode neutralizer was switched on and heater current set to 1.0A. The neutralizer was then outgassed for the remaining 10 hours.

4.2.7.2 Discharge Ignition

A 60W tungsten filament mounted to one side of the thruster was used as an electron source for discharge ignition. With vacuum pressure less than 5.0×10^{-5} mbar, xenon flow rate to the thruster was set on the Aera ROD-4 control unit directly or commanded via LabVIEW. The RF frequency and power were then set either on the front panel of the signal generator or through LabVIEW. The impedance of the induction coil was then matched to the output impedance of the RF amplifier by manually tuning the antenna matching unit for minimum reflected power, as indicated by the SWR meter on the AMU. The power to the tungsten filament was then ramped up to provide a source of electrons. Once a discharge had been ignited, the power to the filament was switched off and the AMU again tuned for minimum reflected power due to the change in impedance resulting from the plasma load. The discharge was then left to stabilize.

4.2.7.3 Ion Beam Extraction

A T5 hollow cathode neutralizer was used for beam neutralization during characterization of the MiDGIT breadboard thruster. Once a stable inductive discharge had been achieved, the keeper supply to the anode plate of the neutralizer was connected. Xenon flow rate to the T5 neutralizer was then set to 0.15mgs^{-1} and the neutralizer heater current set to 1.0A. After 15 minutes, the neutralizer keeper supply was switched on and the keeper current set to 0.3A. A potential of +950V was then applied to the screen grid of the MiDGIT thruster and a potential of -95V to the accelerator grid by manual control of the Glassman and Bertran HV supplies. The screen and accelerator grid currents were monitored to identify that an ion beam was being extracted. Grid voltages and currents were logged automatically via LabVIEW at a rate of 1Hz, along with thruster flow rate, RF frequency and forward RF power.

4.3 EP1 VACUUM FACILITY

4.3.1 Vacuum Facility

Additional discharge tests and investigations regarding differential control were performed on the MiDGIT prototype model within the EP1 vacuum rig at the University of Southampton. The vacuum chamber consists of a 0.50m diameter by 0.50m cylindrical stainless steel vacuum chamber pumped by a water-cooled Pfeiffer Balzers TPH520 (500l/s) turbomolecular pump, controlled by a Pfeiffer Balzers TCP380 control unit and backed by a Pfeiffer Balzers DUO 016B rotary vane pump. The chamber could be pumped to a base pressure of $\sim 10^{-6}$ mbar. A Pfeiffer Balzers TPG300 dual pressure gauge package was used to monitor the chamber pressure. The Pirani gauge monitors pressure down to 5×10^{-4} mbar, while the cold cathode ion gauge monitors pressure in the range 5×10^{-3} mbar – 1×10^{-9} mbar. Switching between the two gauges occurs automatically via the TPG300 display unit. The pressure gauge heads are mounted on KF25 and KF40 ports on top of the chamber.

An ISO500 flange mounted on rails acts as the chamber door allowing ease of access to the chamber. A thruster back plate is mounted to the inside of the door, spaced 155mm off from the surface, permitting various configurations of thruster and diagnostics to be mounted within the chamber. The chamber door has four CF35 ports for instrument feedthroughs and three gas feed lines. Two ISO160 ports located either side of the chamber allow optical access or additional electrical feedthroughs depending on requirements. A cylindrical water-cooled copper shroud fitted internally along the length of the vacuum chamber is used to dissipate heat load during thruster operation.

4.3.2 Thruster Interface

Discharge diagnostics and beam extraction tests were performed on the MiDGIT prototype model configured for differential operation within the EP1 vacuum chamber. The thruster was mounted on a FR4 mounting block to isolate the thruster body. High voltage terminal block connections were mounted to one side of the mounting block for the high voltage grid lines. A 100W tungsten filament was also mounted close to one end of the thruster to enable discharge ignition.

For the discharge diagnostic tests, the FR4 mounting block was attached to the thruster back plate on the chamber door to provide solid support for the thruster and diagnostic probes. The

thruster was mounted horizontally to allow the diagnostic probes to be easily aligned by use of probe mounting brackets.

During the beam extraction tests, the thruster was mounted centrally within the vacuum chamber to enable two ion beams to be extracted. A 25cm stainless steel pole was mounted to the back plate of the chamber door to which the thruster, mounted on the FR4 block, was attached by brackets to enable the thruster to be orientated along the axis of the chamber. A rotary feedthrough mounted on the chamber door permitted a 100W tungsten filament to be moved close to the extraction grids on one end of the thruster for discharge ignition. Prior to beam extraction, the filament was rotated away from the grids to prevent sputtering. Two separate tungsten filaments, mounted either end of the thruster were used to assist with beam neutralization. Hot-filament neutralizer cathodes are required to be located within an ion beam to provide adequate conductivity to the beam [81]. The tungsten filaments were therefore positioned so that they would be within the edge of each beam. Initially, Grafoil sheets grounded to the chamber and mounted approximately 13cm from either end of the thruster were used as beam targets. Neutralization arcs [81] were observed within the chamber for this configuration however and could only be prevented by removal of the Grafoil sheets, resulting in the ion beams impinging on the end wall of the chamber and the back plate attached to the chamber door. Secondary electron emission from the conducting surfaces of the chamber, supplemented by electron emission from the filament cathodes, was then sufficient to provide beam neutralization. Sputtered material from the chamber would obviously be of concern but this arrangement was considered acceptable as the beam extraction tests would be the final tests performed on the prototype thruster. All electrical lines to the thruster and filaments were either fed along the mounting pole or fed in to the thruster mid-way along the length of the thruster so that no lines would be directly within either beam.

4.3.3 Radio Frequency Generator

The units comprising the RFG assembled for the testing activities at the QinetiQ LEEP facilities were not available for use during the additional tests performed at the University of Southampton. A separate RFG was constructed consisting of a Digimess SG100 (1-30 MHz) variable frequency signal generator connected to an EMI AO75 75W RF power amplifier. A MFJ-941E antenna matching unit was connected between the RF amplifier and coil 1 and a MFJ-934 antenna matching unit was connected between the RF amplifier and coil 2 by use of a BNC T-piece connector. The front panel of the EMI AO75 RF amplifier displayed the

forward and reflected power in Watts delivered by the RF amplifier to the AMUs and thruster. RF frequency and forward power were controlled manually via the control dials on the signal generator, thus not providing as great a resolution as the IFR 2031 signal generator used during the QinetiQ LEEP testing activities.

Initially, a 4-way SMA vacuum feedthrough was used to pass the RF transmission lines into the chamber. This was separate to the one used at QinetiQ. During early tests, one of the SMA connectors failed, suspected to be the result of a high RF current surge through the connector. The feedthrough was replaced by a high voltage, high current CF electrical power feedthrough. Though the CF power feedthrough would present a power loss due to mismatch of the impedance at the connection, the RF power delivered to the induction coils was still found to be sufficient to operate the thruster. Twisted-pair cables constructed from PTFE coated wire were used between the AMUs and the induction coils, with a total length of approximately 1m. The attenuation factor for each transmission line was found to be (0.72 ± 0.06) in the same manner as that described in section 4.2.3. The slightly lower loss could be attributed to the shorter length of wire required for the EP1 vacuum chamber, despite the fact that a 50Ω matched feedthrough was not used.

4.3.4 Propellant Feed System

Propellant flow to the thruster was controlled by a Sierra Instruments Micro-Trak 101 mass flow controller, calibrated for use with argon. The mass flow controller was stated to have a full-scale range of 5.6 sccm for argon at STP, with an accuracy of $\pm 1\%$ of the full-scale range [82]. Flow rate was controlled and read directly via the Pilot module attached to the MFC. The MiDGIT thruster was operated on xenon; a gas correction factor was therefore applied to the measured flow rate according to:

$$Q_{Xe} = \frac{GCF_{Xe}}{GCF_{Ar}} Q_{Ar} \quad (4.10)$$

where Q is volumetric flow rate in sccm and GCF_{Xe} , GCF_{Ar} are gas correction factors for xenon and argon, given by the manufacturer as 1.443 and 1.398 respectively [82]. The equivalent flow rate for xenon determined from the displayed flow rate for argon is then simply:

$$Q_{Xe} = 1.032 Q_{Ar} \quad (4.11)$$

The inlet pressure of the Sierra Instruments Micro-Trak 101 MFC is limited to 2 bar. The pressure upstream of the MFC was therefore set to 1.5 bar by a high accuracy two-stage pressure regulator that controls the outlet pressure of the xenon gas from the gas storage cylinder. An oxygen trap was inserted inline upstream of the MFC to remove any impurities in the feed line.

Significant noise was initially observed on the flow rate displayed by the MFC at high RF powers, with a resulting fluctuation in chamber pressure. This was mitigated by shielding the power cable and power adaptor for the MFC and inserting an isolator inline between the MFC and vacuum chamber. Calibration curves obtained by flowing cold xenon through the MiDGIT prototype thruster showed little hysteresis, as indicated in Figure 4.13.

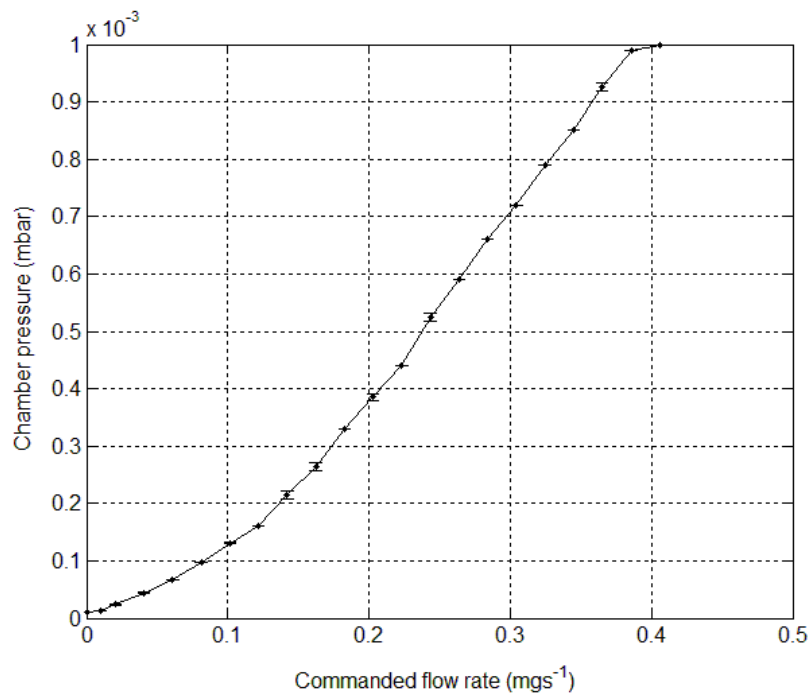


Figure 4.13. Typical flow calibration curve for Micro-Trak 101 MFC with xenon.
(commanded flow corrected from argon)

4.3.5 Power Supplies and Meters

The HV rack assembled by QinetiQ was also used for the tests performed at the University of Southampton to supply the beam and accelerator grid potentials and monitor the grid currents (see Table 4.2). The 100W tungsten filament used for discharge ignition was powered by a Zenith Electrical Co. Ltd. 0-270V Variac (variable transformer) connected to mains power, allowing the filament to be powered on and off at a switch. The tungsten filaments used for beam neutralization were powered by a Glassman LV80-37 DC power supply (80V, 37A) commoned to chamber ground. The other grounded power supplies and DMMs were grounded to the same point.

4.3.6 Diagnostics

4.3.6.1 Rogowski Coils

The power absorbed by an inductive discharge is dependent on the electron plasma density and the RF current in the induction coil [46]. The coil current however is affected by the impedance matching circuit, particularly by the values of the tuning capacitors, and variations in the maintenance and onset currents of the H-mode can result depending on the configuration of the matching circuit [83].

Two Rogowski coils were used to monitor the RF current in each induction coil during tests performed on the MiDGIT prototype at the University of Southampton. The Rogowski coil is a relatively simple device based on Ampere's and Faraday's laws, used as a non-intrusive method of measuring alternating current [62]. A Rogowski coil generally consists of a toroidal solenoid that encircles a conductor through which ac current is passed. The ac current induces a voltage in the Rogowski coil according to:

$$V_{coil} = -\frac{d\Phi}{dt} = -\mu_0 n A \frac{dI}{dt} \quad (4.12)$$

where Φ is the magnetic flux linked by the coil, n is the number of turns per unit length of the coil and A is the cross-sectional area of each coil turn. Integration of the voltage signal from a Rogowski coil allows the waveform of the current to be resolved in shape, phase and magnitude [62].

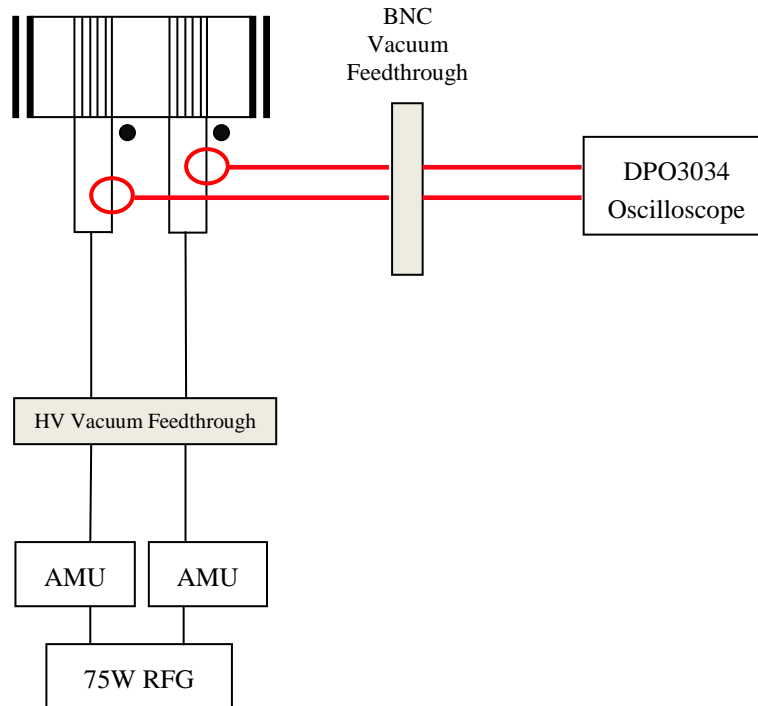


Figure 4.14. Schematic of Rogowski coil mounting.

The Rogowski coils installed in the set-up within the EP1 vacuum chamber were two vacuum compatible PEM /5.5/2/100M/2 Rogowski coils (custom-made for a separate development program of a micro-PPT ongoing between MarsSpace and the University of Southampton [37]). The coils had a circumference of 100mm and were assembled with a 1m 75Ω coaxial cable terminated with a BNC connector. The Rogowski coils were calibrated by PEM for a frequency of 10kHz and the resulting coil sensitivities were quoted as 5.69 nVs/A for coil 1 (SN: 0382) and 5.89 nVs/A for coil 2 (SN: 0383). The Rogowski coils were therefore not expected to provide an accurate measurement of the magnitude of the RF coil currents for the MiDGIT thruster, as the operating frequency of the MiDGIT thruster would drive the Rogowski coils beyond their linear range, but it was proposed that the Rogowski coils would be useful in monitoring large variations in RF current between the two induction coils. Construction of Rogowski coils and associated integrating circuits for accurate measurement of low magnitude, high frequency current is very complicated; Argüeso, Robles and Sanz [62] outline some of the issues in resolving accurate current waveforms from the voltage output of Rogowski coils at high frequencies.

The PEM Rogowski coils were mounted at the inputs of the induction coils of the MiDGIT thruster as depicted in Figure 4.14. The voltage at the input leg of each induction coil was checked on a Tektronix DPO3034 (300 MHz, 2.5GS/s) digital oscilloscope to ensure that the

RF currents supplied to each coil were in-phase. The Rogowski coils were mounted so that the input wire of each induction coil was inserted through the centre and normal to the plane of each Rogowski coil as accurately as possible. The Rogowski coils were then connected to a BNC vacuum feedthrough to pass the induced signal to an oscilloscope located outside the vacuum chamber. A Tektronix DPO3034 digital oscilloscope was used to integrate the voltage signals from the Rogowski coils, giving an output in Vs. The voltage waveforms could also be saved automatically by the oscilloscope.

4.3.6.2 Triple Langmuir Probes

Discharge diagnostics were performed on the MiDGIT prototype thruster using triple Langmuir probes. A brief background into Langmuir probes and a summary of triple Langmuir probe theory is provided in Appendix A.

Within inductive plasma discharges, Langmuir probes should be inserted normal to the induced electric field to prevent an RF voltage being induced along the probe [84]. Ideally, the triple Langmuir probes used for the discharge diagnostics of the MiDGIT thruster would have been inserted radially into the discharge chamber at several locations along the length of the thruster. The geometry of the induction coils of the MiDGIT thruster makes this difficult. Therefore, the Langmuir probes were inserted through the extraction grids on either end of the thruster, which also prevented modifications having to be made to the discharge chamber.

The apertures of the accelerator grids for the MiDGIT thruster are 1.50 mm in diameter, restricting the diameter of probe that can be inserted through the grids. Additionally, Langmuir probes must be constructed from very thin or very thick wire in order for collisionless Langmuir probe theories to be applied [58]. Individual Langmuir probes were therefore constructed from 0.1mm diameter tungsten wire inserted through a 50mm length of alumina tube with an outer diameter of 1.2mm and bore diameter of 0.2mm. The tungsten wire was secured within the tube using ceramic paste. The exposed wire at the tip of the probe was cut to a length of ~5mm using a scalpel blade and checked using digital callipers. The connecting end of the tungsten wire was spliced with the multi-strand core of RG178U coaxial cable and soldered. Ceramic beads were then positioned over the connection providing a reasonably tight fit to the alumina tube and RG178U cable, which were then covered with kapton tape. Triple Langmuir probes constructed from a 4-bore 1.2mm diameter alumina tube were also assembled in a similar manner by inserting three individual tungsten wires, 0.1mm in diameter, through three of the bores. Variation of the potentials applied to

two of the wires were observed to influence the floating potential of the third wire during initial tests for this configuration of triple Langmuir probe, indicating that the probe sheaths were interacting. Three individual Langmuir probes, inserted through separate grid apertures, were therefore used in a floating triple Langmuir probe configuration as outlined in Appendix A and shown schematically in Figure 4.15. The centre wire of the coaxial cable for each probe was connected to an isolated pin of a CF instrument feedthrough mounted on the chamber door. The outer shield of each coaxial cable was grounded to the chamber.

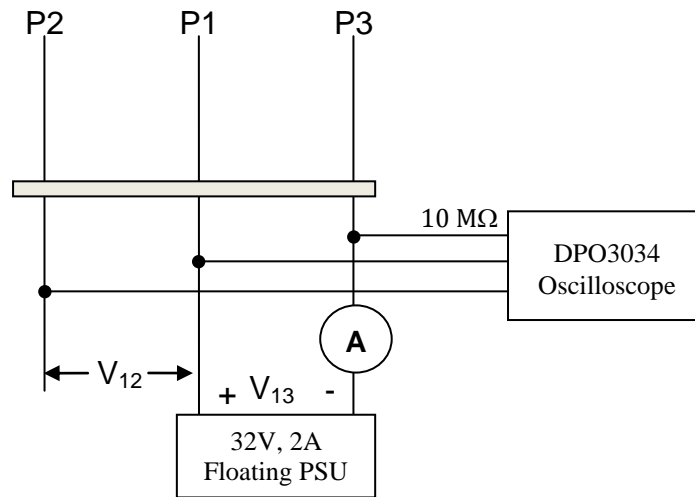


Figure 4.15. Configuration of triple Langmuir probes for measuring electron temperature and density. (A bias potential of at least $2kT_e/e$ volts is applied between two of the probes while a third is left floating. The potential of each probe was measured on a digital oscilloscope using $10M\Omega$ Tektronix P6139A voltage probes).

The theory behind triple Langmuir probes is derived under the assumption that the probes are operated in a collisionless, thin sheath regime [85]. This condition specifies that the mean free paths for both ion-ion and ion-electron collisions must be greater than the Debye length ($\lambda_{ii}/\lambda_d > 1$, $\lambda_{ie}/\lambda_d > 1$) and the probe radius ($Kn_{ii}, Kn_{ie} > 1$) for the assumption of a collisionless plasma to hold, and that the probe radius must be greater than the Debye length (*ie.* $\xi = r_p/\lambda_d > 1$) for the assumption of a thin sheath to hold. Additionally, theory used in the analysis of the triple Langmuir probe data obtained in this work was developed from the Orbital Motion Limited (OML) theory of Chen (see Appendix A), which has been shown to be valid for conditions where $\xi < 3$ [86].

The mean free paths for ion-ion and ion-electron collisions are given by:

$$\lambda_{ii} = \frac{\bar{u}_i}{\nu_{ii}} \quad (4.13)$$

$$\lambda_{ie} = \frac{\bar{u}_e}{\nu_{ie}} \quad (4.14)$$

where ν_{ii} and ν_{ie} are the respective collision frequencies and $\bar{u}_{i,e}$ is the mean thermal velocity of ions or electrons given by:

$$\bar{u}_i = \left(\frac{8kT_i}{\pi M_i} \right)^{1/2} \quad (4.15)$$

$$\bar{u}_e = \left(\frac{8kT_e}{\pi m_e} \right)^{1/2} \quad (4.16)$$

The ion-electron collision frequency can be determined from:

$$\nu_{ie} = 2.9 \times 10^{-12} \frac{n_e \ln \Lambda}{T_{eV}^{3/2}} \quad (4.17)$$

where electron temperature is given in electron volts (T_{eV}) and Λ is the plasma parameter. A function for $\ln \Lambda$ is given as:

$$\ln \Lambda = 23 - \frac{1}{2} \ln \left(\frac{10^{-6} n_e}{T_{eV}^3} \right) \quad (4.18)$$

The ion-ion collision frequency can be determined in relation to the electron-electron coulomb collision frequency by:

$$\nu_{ii} = \left(\frac{m_e}{M_i} \right)^{1/2} \left(\frac{T_e}{T_i} \right)^{3/2} \nu_{ee} \quad (4.19)$$

with:

$$v_{ee} = 5 \times 10^{-12} \frac{n_e \ln \Lambda}{T_e^{3/2}} \quad (4.20)$$

The given relations allow the range of electron temperature and plasma density over which the requirements of a collisionless, thin sheath are valid with respect to the Langmuir probes used in this work to be determined. Assuming ions to be in thermal equilibrium with neutrals with a temperature of 400K, the Debye length and mean free paths for ion-ion and ion-electron collisions in a xenon discharge are given in Table 4-3 for various n_e and T_e . The results of Table 4-3 indicate that the Langmuir probes are sized appropriately for a suitable range of electron temperature and plasma density expected for a 3cm diameter RF ion thruster ($T_e \sim 2-4\text{eV}$, $n_e \sim 10^{17} \text{ m}^{-3}$) [24].

T_e (eV)	n_e (m^{-3})	λ_{ii} (mm)	λ_{ie} (m)	$\frac{\lambda_{ii}}{\lambda_d}$	$\frac{\lambda_{ie}}{\lambda_d}$	Kn_{ii}	Kn_{ie}	ξ
2	5.0×10^{16}	0.2714	1.575	5.771	33498	5.427	31499	1.064
	2.5×10^{17}	0.0583	0.338	2.771	16085	1.165	6764	2.378
3	7.0×10^{16}	0.1868	2.440	3.839	50129	3.736	48792	1.027
	2.5×10^{17}	0.0552	0.721	2.143	27911	1.104	14416	1.942
4	9.0×10^{16}	0.1417	3.290	2.860	66396	2.835	65811	1.009
	2.5×10^{17}	0.0532	1.235	1.790	24704	1.064	24704	1.682
5	1.2×10^{17}	0.1047	3.798	2.181	79147	2.094	75959	1.042
	2.5×10^{17}	0.0518	1.878	1.557	56472	1.035	37549	1.504

Table 4-3 – Conditions for which a collisionless, thin sheath can be assumed for a 0.1mm diameter wire Langmuir probe inserted into a xenon discharge.

Requirements are $(\lambda_{ii}/\lambda_d > 1)$, $(\lambda_{ie}/\lambda_d > 1)$, $Kn_{ii}, Kn_{ie} > 1$ and $1 < (\xi = r_p/\lambda_d) < 3$.

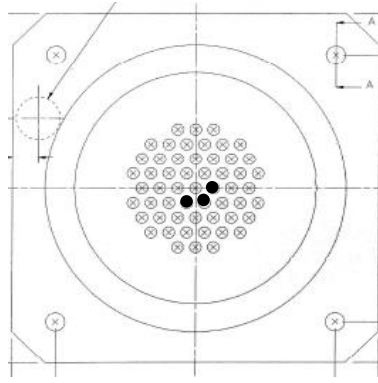


Figure 4.16. Orientation of triple Langmuir probe tips inserted through the extraction grids of the MiDGIT prototype thruster. (*note: schematic displays grids of the breadboard thruster but probe orientation was the same through the prototype grids*).

As previously stated, three individual Langmuir probes configured as a triple Langmuir probe, were inserted through the extraction grids on either end of the MiDGIT prototype thruster for obtaining axial measurements of electron temperature and density. The probes were inserted through the apertures depicted in Figure 4.16, resulting in a separation distance of $\sim 2.452\text{mm}$ between each probe. The separation distance was sufficiently large with respect to expected Debye length to ensure that no interaction between the probe sheaths would occur, however spatial resolution was severely impacted. The aspect ratio of the probe tips was approximately $l_p/r_p = 100$ meaning end effects could be ignored [56].

No suitable linear translation or rotary feedthrough was available for the EP1 vacuum chamber to act as a translation stage for the triple Langmuir probes. The probes therefore had to be manually repositioned, requiring considerable pump-down and outgassing time, limiting the amount of data that could be obtained. Probe mounting brackets were constructed from stainless steel, which were bolted to the back plate of the vacuum chamber door to ensure the probes were inserted horizontally through the grid apertures. The probe mounting brackets provided some linear movement to allow the probes to be positioned at various distances into the discharge chamber. The position of the probe tips within the discharge chamber was determined by aligning marked distances along the alumina tubes with the outer surface of each accelerator grid.

A potential was applied between two of the probe tips for each triple Langmuir probe by a floating Labonetzgerat 32V, 2A regulated power supply. The potentials of the two biased probes and the floating probe were measured on a Tektronix DPO3034 (300MHz, 2.5GS/s) digital oscilloscope using $10\text{M}\Omega$ P6139A voltage probes. The dc component of the current collected by the negatively biased probe was measured by an Agilent 34401A DMM.

4.3.7 Thruster Operation and Procedures

4.3.7.1 Thruster Installation

Once the thruster had been mounted either to the back plate of the chamber door for discharge diagnostics or centrally within the chamber for beam extraction, and all electrical connections checked, the chamber was roughed to a pressure of approximately 2.5×10^{-3} mbar. The water supply to the turbo pump and copper shroud was then switched on and the TPH520 turbomolecular pump powered via the TCP380 control unit to pump the chamber to a base pressure of $\sim 5 \times 10^{-6}$ mbar. During outgassing, a full electrical inspection was repeated

4.3.7.2 Discharge Ignition

A 100W tungsten filament was used as an electron source for discharge ignition. During discharge diagnostic tests, the filament was mounted directly on the FR4 mounting block close to one end of the thruster. For beam extraction tests, the filament was positioned close to the extraction grids facing the chamber door by use of a rotary vacuum feedthrough. Xenon flow rate to the thruster was set by the Sierra Instruments Micro-Trak mass flow controller by entering the set-point into the Pilot module attached to the MFC. The RF frequency was set on the Digimess SG100 signal generator and the RF amplifier switched on. The RF power was then ramped up using the control dial on the signal generator. The antenna matching units were tuned for minimum reflected power, as indicated by the SWR meters on the AMUs, and the power to the filament switched on via the switch on the variac. Power to the filament could be increased or decreased as required by the control dial on top of the variac. Once a discharge had been ignited, the power to the filament was switched off and the AMUs again tuned for minimum SWR. The discharge was then left to stabilize. Prior to beam extraction, the filament attached to the rotary feedthrough was rotated away from the extraction grids so that it would not be located within the beam

4.3.7.3 Ion Beam Extraction

Two tungsten filaments, one located either end of the thruster, were used to assist with beam neutralization during beam extraction tests. Once a stable discharge had been achieved, power to the filaments was increased by the Glassman LV80-37 DC power supply. A potential of +950V was then applied to the screen grids of the thruster and a potential of -95V to the accelerator grids by manual control of the Glassman and Bertran HV power supplies. The screen and accelerator grid currents were monitored to identify that an ion beam was being extracted. Grid voltages and currents were logged automatically via LabVIEW. The voltage signal from each Rogowski coil was sampled by the Tektronix DPO3034 digital oscilloscope and saved to a text file for analysis in Matlab. Forward and reflected RF power was read

directly from the front panel of the RF amplifier.

4.3.7.4 Triple Langmuir Probe Measurements

Estimates of electron temperature and plasma density were obtained by triple Langmuir probes inserted through the extraction grids on both ends of the MiDGIT prototype thruster. Once a stable discharge had been obtained, the RF power was recorded manually from the front panel of the RF amplifier. The voltage signal from each Rogowski coil was then sampled and saved to text file via the oscilloscope. A potential bias was applied between two of the probe tips of each triple Langmuir probe and the floating potential of the third probe tip checked to ensure that the probe sheaths were not interacting. The potentials of all three probe tips for each triple Langmuir probe were then measured using the P6139A voltage probes and the signals saved to text file by the digital oscilloscope. A potential bias was then applied between two different probe tips of each triple Langmuir probe and the measurements repeated. Finally, the potential bias was applied to the last combination of two probe tips of each triple Langmuir probe and again, measurements repeated. The surface area of each probe tip is assumed to be the same and also the impedance of each probe assumed to be approximately the same, therefore the 3 sets of triple Langmuir probe measurements should display little variation.

Chapter Five

5. Coarse Thrust Control

Orbit maintenance, stationkeeping and reconfiguration manoeuvres of microspacecraft require thrust levels in the mN range but control accuracy is less stringent than for pointing or alignment manoeuvres, leading to impulse bit requirements of the order 100 μ Ns [87]. The MiDGIT thruster is designed to have the capability of being operated in a single ion beam mode to provide continuous, coarse thrust control at mN level required for orbital manoeuvres, while providing relatively high specific impulse necessary to minimize propellant requirements. Orbit and attitude control requirements identified by Jameson for formation flying spacecraft define the requirements for the MiDGIT thruster [42]. Requirements specific to coarse thrust control are reiterated in Table 5-1.

Coarse Thrust range	150μN to >1mN
Coarse Thrust repeatability	0.5mN
Specific impulse	>1500s @ 1mN
Specific power	<50W/mN
Thrust actuation frequency	100Hz
Thrust response time	60ms

Table 5-1 – Propulsion requirements specific to coarse thrust control.

Performance tests were conducted on a breadboard model of the MiDGIT thruster configured for single-end (SE) operation to determine the feasibility of SE thruster operation by use of a simple gating mechanism across the discharge chamber. Characterisation of the breadboard thruster was conducted at the QinetiQ Large European Electric Propulsion (LEEP) facilities; tests reported in this chapter were carried out in collaboration between the author and QinetiQ. The experimental arrangement and procedures employed during characterisation of the MiDGIT breadboard thruster are given in Chapter 4. Data was obtained to determine thrust range, specific impulse, specific power and beam divergence for SE mode to evaluate preliminary performance of the breadboard thruster against coarse thrust requirements.

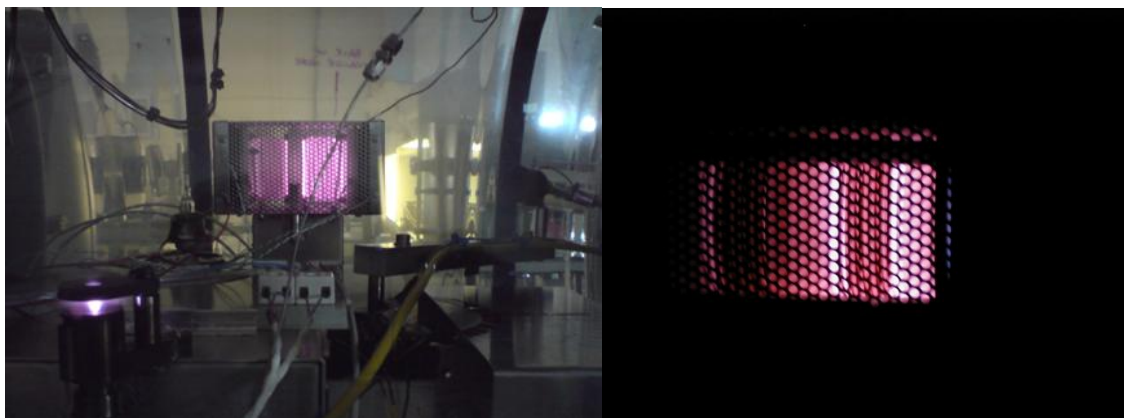
5.1 THRUSTER CONFIGURATION

A detailed description of the MiDGIT breadboard design can be found in section 3.4. Table 5-2 provides a summary of the configuration of the MiDGIT breadboard thruster for single-end (coarse thrust) operation.

Discharge chamber diameter	2.8 cm
Number of grid apertures	55
Grid open-area	32.4 %
Number of coil turns	6
Operating frequency	5.25 MHz
Beam voltage	950V
Accelerator grid voltage	-95V

Table 5-2 – Summary of breadboard configuration for single-end operation.

Performance tests were conducted on both ends of the MiDGIT breadboard thruster configured for single-end operation. The thruster was operated on xenon at various discharge conditions at a frequency of 5.25 MHz, with an accelerator grid voltage of -95V and beam voltage of 950V. The background pressure during operation was of the order 10^{-4} mbar. Images of the MiDGIT breadboard thruster operating in SE mode are shown in Figure 5.1.



(a)

(b)

Figure 5.1. Images of the MiDGIT breadboard thruster operating in single-end mode, with T5 hollow cathode neutralizer shown in (a).

5.2 DISCHARGE IGNITION

Discharges were ignited for the SE1 and SE2 configurations at similar RF power levels and flow rates. The SE1 configuration repeatedly required a minimum flow rate of $(0.150 \pm 0.005) \text{ mgs}^{-1}$ and forward RF power of $(14.2 \pm 0.8) \text{ W}$ for ignition, whilst the SE2 configuration required a slightly higher commanded flow rate of $(0.160 \pm 0.010) \text{ mgs}^{-1}$ at the same forward RF power. These flow rates can be converted to equivalent neutral pressures within the discharge chamber of approximately 6.61 mTorr and 7.05 mTorr respectively according to Equations 2.44 and 2.46, assuming a gas temperature of 300K in the discharge chamber prior to ignition. Neutral pressures between 1mTorr to 10mTorr are typically required for ignition of RF ion thrusters, as discussed in section 2.2.2 and defined by Equation 2.36.

The higher flow rate required for discharge ignition for the SE2 configuration can be attributed to the uncertainty on the flow rates delivered by the different MFCs employed, though the following factors could also contribute to variations in ignition parameters:

- Minor differences in grid transparency between configurations due to manufacturing tolerances affecting neutral pressure within the discharge chamber, though this would be negligible.
- Minor differences in discharge chamber geometry between configurations affecting neutral pressure and electron losses within the discharge chamber.
- Neutral leaks past the shutter plate reducing pressure within the active end of the discharge chamber.
- The distance of the electron source from each end of the thruster; a lower conductance of electrons to the discharge chamber would lead to a higher neutral pressure being required to increase e-n collision frequency.

Ignition parameters can be expected to be the same however for identical thruster configurations and matched conditions.

Once discharges had been ignited for the SE1 and SE2 configurations, it was then possible to reduce the flow rate to $<0.06 \text{ mgs}^{-1}$ and RF forward power to $<14\text{W}$ whilst maintaining the discharge, partly as a result of the additional electron-electron coulomb collisions contributing to heating of the plasma electrons alongside electron-neutral collisions. Though electron-neutral collisions dominate over coulomb collisions in low pressure inductive plasmas,

coulomb collisions can still provide a significant portion of the energy transfer in low temperature plasmas. It is in fact coulomb collisions which drive the EEDF to a Maxwellian like distribution in low pressure ICPs [46].

Discharges were generally ignited with the filament acting as an electron source but ignition was also demonstrated by use of the T5 hollow cathode neutralizer at the same thruster flow rate and RF power level by application of a high positive potential to the screen grid whilst the accelerator grid was switched off. During testing it became increasingly harder to re-ignite a discharge, with either the filament or neutralizer, following long periods of thruster operation due to the thruster body heating up. Steady state thermal data obtained by QinetiQ [88] indicated that the temperature of the ceramic discharge chamber on the active end of the thruster in SE configuration could reach up to 200°C after approximately 30 minutes of operation at nominal thrust levels. Significant heating of the induction coil could therefore result, increasing the resistance of the coil, leading to a reduced E_0 field in the discharge chamber. Visual inspection of the breadboard thruster following SE characterisation did not detect any significant amounts of conductive material deposited on the interior or exterior of the discharge chamber due to sputtering of the grids or beam targets which could have screened capacitive fields that might have contributed to discharge ignition. It was observed that increasing the flow rate above 0.4 mgs⁻¹ enabled a discharge to be ignited when the discharge chamber temperature was high; attempts to adjust the match on the AMU to maximize the RF power delivered to the coil had no beneficial effect on discharge ignition for this set-up.

Difficulty in igniting a discharge associated with heating of the induction coil affecting its electrical resistance could pose an operational issue for a miniature RF ion thruster. If ignition becomes impossible with the neutralizer when the flow rate is set to the maximum limit of the propulsion system's Flow Control Unit, a separate filament located much closer to the extraction grids may be needed to facilitate a higher flux of electrons into the discharge chamber so that the neutral pressure required for discharge ignition, and therefore flow rate, can be brought within reasonable limits. The use of an additional filament close to the grids would impact thruster lifetime however due to wear and lifetime issues of the filament as a result of ion bombardment. (It must be noted at this point, that no optimization of the induction coil was conducted for the MiDGIT breadboard thruster in the early stage of development. Thermal modeling of the MiDGIT thruster and optimization of the coil geometry would enable coil resistance to be reduced).

Ignition by use of filament cathodes has not been reported to be an issue for the μ NRIT-2 and μ NRIT-4 thrusters at xenon flow rates $<0.05\text{mgs}^{-1}$ [27]. Performance tests of these thrusters were conducted within facilities where the background pressure was maintained below 1.3×10^{-6} mbar [27]. The background pressure in the LEEP-1 loadlock during operation of the MiDGIT breadboard thruster however was of the order 10^{-4} mbar. The number of collisions between electrons and background neutrals in the vacuum chamber may have been of sufficient magnitude at these pressures to affect the conductance of electrons from the filament or neutralizer to the thruster. Operation of the MiDGIT breadboard thruster in a higher vacuum environment, permitting a higher flux of electrons to reach the discharge chamber, would identify whether the MiDGIT thruster could be ignited at much lower flow rates than those required during the breadboard characterisation.

5.3 OPERATIONAL ENVELOPE

The plasma density in inductive discharges can be controlled by varying applied RF power and gas flow rate as these affect the ionization rate through the energy transferred to plasma electrons and the electron-neutral collision frequency. Two control variables are therefore available for controlling beam current and consequently the thrust level of RF ion thrusters. Throttling of the MiDGIT thruster during coarse thrust mode is intended to be achieved by variation of the RF power and propellant flow rate with fixed potentials applied to the extraction grids, as for conventional RF ion thrusters.

Initially, RF power and xenon flow rate to the MiDGIT breadboard thruster were coarsely adjusted during beam extraction to identify an approximate operational envelope for the SE1 and SE2 configurations; the main objective being to identify the threshold below which an inductive discharge could not be maintained during beam extraction.

The beam and accelerator grid currents measured for the SE1 and SE2 configurations are displayed in Figures 5.2 and 5.3, with the associated RF power for each operating point recorded in Table 5-3.

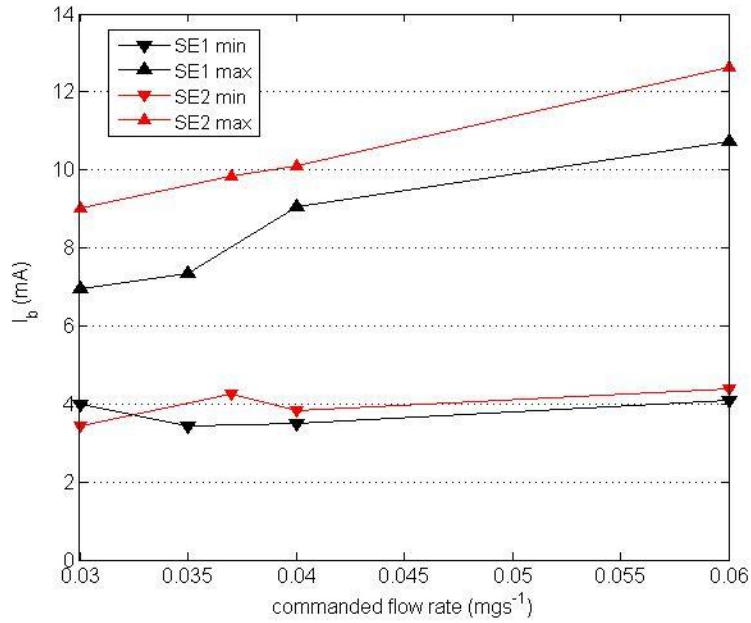


Figure 5.2. Maximum and minimum beam current measured during initial adjustment of flow rate and RF power ($V_b = 950V$, $V_{ACC} = -95V$).

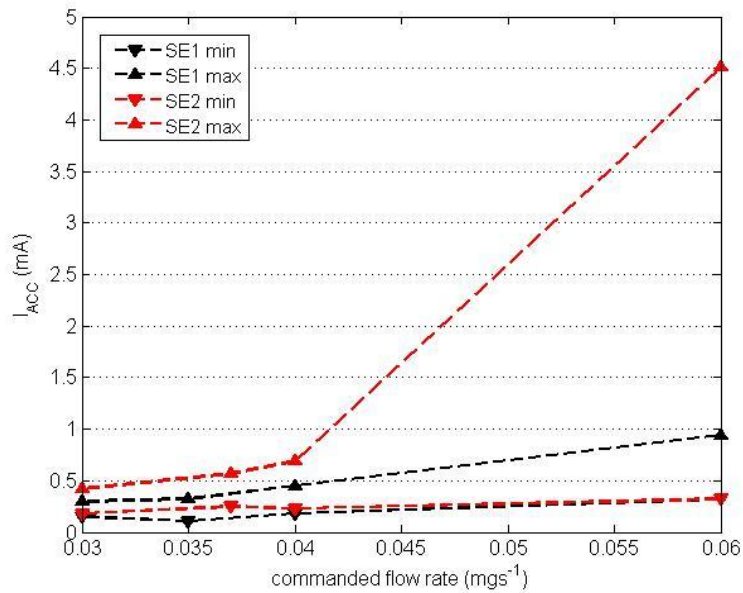


Figure 5.3. Accelerator grid currents measured during initial adjustment of flow rate and RF power ($V_b = 950V$, $V_{ACC} = -95V$).

	\dot{m} commanded (mgs ⁻¹)	\dot{m} corrected (mgs ⁻¹)	P_{fw} (W)	I_b (mA)	I_{acc} (mA)	I_{acc}/I_b (%)	T (μ N)
SE1	0.030	0.002	18.24	3.98	0.15	3.76	202.38
	0.035	0.011	15.18	3.42	0.11	3.22	173.90
	0.040	0.020	13.84	3.51	0.18	5.13	178.48
	0.060	0.056	11.78	4.08	0.32	7.84	207.46
	0.030	0.002	20.00	6.95	0.3	4.32	353.39
	0.035	0.011	20.00	7.34	0.32	4.36	373.22
	0.040	0.020	20.00	9.05	0.45	4.97	460.17
	0.060	0.056	17.03	10.72	0.94	8.77	545.09
SE2	0.030	0.047	13.22	3.43	0.18	5.25	174.41
	0.037	0.051	12.62	4.25	0.25	5.88	216.10
	0.040	0.052	12.33	3.83	0.23	6.01	194.75
	0.060	0.063	11.51	4.39	0.32	7.29	223.22
	0.030	0.047	20.00	9.01	0.42	4.66	458.14
	0.037	0.051	20.00	9.84	0.57	5.79	500.34
	0.040	0.052	20.00	10.11	0.69	6.82	514.07
	0.060	0.063	20.00	12.65	4.51	35.65	643.23

Table 5-3 – Grid currents measured during initial variation of flow rate and RF power. (Given are the commanded flow rates and corrected flow rates assuming either MFC1 or MFC2 is incorrect).

The minimum beam current that could be maintained for both the SE1 and SE2 configurations at this stage was of the order 3.4mA, equivalent to a thrust level of approximately 175 μ N (as calculated from Equation 2.49 assuming $\alpha_{TCF} = 1$).

At the same RF forward power of 20W, a much higher beam current was extracted for SE2 for a commanded flow rate indicating that neutral pressure within the discharge chamber was higher for SE2 compared to SE1. Calibration checks of the two different MFCs used for SE1 and SE2 identified a significant discrepancy between the two MFCs (as outlined in section 4.2.5). Corrections to the commanded flow rates were identified for the two different MFCs, depending on whether MFC1 or MFC2 was considered to be correct; these are applied to the commanded flow rates for SE1 and SE2 in Table 5-3. If the flow rate delivered by MFC2 is considered to be correct for the flow rate commanded, the corrected flow rates for MFC1 can be seen to be too low to give the performance observed. Therefore, MFC1 was considered to provide reasonable flow rates and corrections were applied to MFC2 only.

The accelerator grid current was observed to be considerably high for both SE1 and SE2, of the order 5% of the beam current due to the relatively high background pressure during operation. Typically, ion thrusters are operated in pressures $\sim 10^{-5}$ mbar to minimize facility

effects [89]. The background pressure and accelerator grid current were considered to be acceptable for the development stage of the MiDGIT breadboard thruster however, as the primary objective was to provide a proof-of-concept for the thruster, though operation within a higher vacuum environment would be essential for performance and lifetime testing of any future engineering model. A significant increase in accelerator grid current was observed for the SE2 configuration at a commanded flow rate of 0.06 mgs^{-1} , suggesting direct ion impingement on the accelerator grid was occurring at this operating point.

5.4 PERFORMANCE MAPPING

The minimum and maximum flow rates and RF power levels identified during the preliminary tests defined an operational envelope for the SE1 and SE2 configurations; 50 operational points were then selected by QinetiQ within these envelopes for performance mapping.

Plots of the measured beam current and accelerator drain current ($I_{\text{ACC}}/I_{\text{B}}$) against RF power for different flow rates are displayed in Figures 5.4 and 5.5 for the SE1 and SE2 configurations. Forward RF power delivered to the induction coil in Watts was calculated from the output RF power measured by the signal generator according to Equation 4.3, with the minimum and maximum forward power estimated as $(12.05 \pm 0.72)\text{W}$ and $(20.01 \pm 1.20)\text{W}$ respectively. Background pressure was in the range $1.4 \times 10^{-4} \text{ mbar}$ - $2.2 \times 10^{-4} \text{ mbar}$ during operation of SE1, whilst for SE2 the background pressure varied less with flow rate and was lower, between $1.0 \times 10^{-4} \text{ mbar}$ - $1.2 \times 10^{-4} \text{ mbar}$, due to the discrepancy between the two MFCs (see section 4.2.5). Current to the accelerator grid resulting from CEX ions was therefore observed to be $\sim 5\%$ of the beam current for the SE2 configuration at low RF power and flow rate, while for SE1 the accelerator grid current varied between 3%-6%.

At RF power levels greater than $\sim 17.5\text{W}$ and flow rates greater than 0.050mgs^{-1} for SE1 and 0.055mgs^{-1} for SE2, the accelerator grid current increased substantially for both the SE1 and SE2 configurations, indicating the onset of direct ion impingement on the accelerator grid. As discussed in section 2.2.3 ion impingement on the extraction grids of a thruster limits thruster lifetime through erosion of the grids and must be avoided [47]. Also, the onset of direct ion impingement establishes an upper limit for achievable thrust, as the actual thrust output at this point is lower than that predicted by the measured beam current.

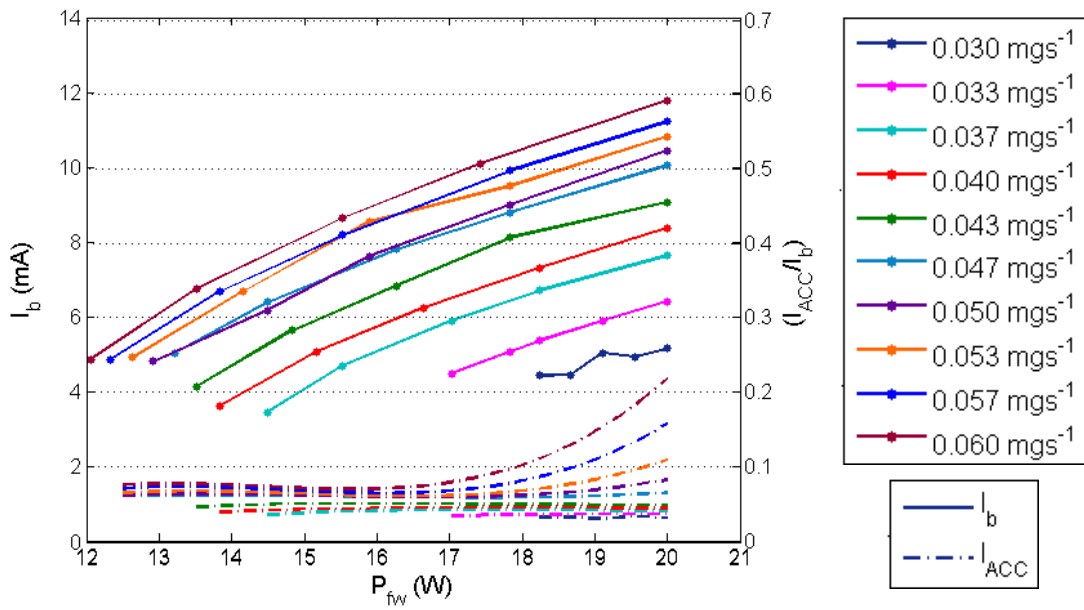


Figure 5.4. Beam current and accelerator drain current for the SE1 configuration for various flow rates and RF power ($V_b = 950\text{V}$, $V_{\text{ACC}} = -95\text{V}$).

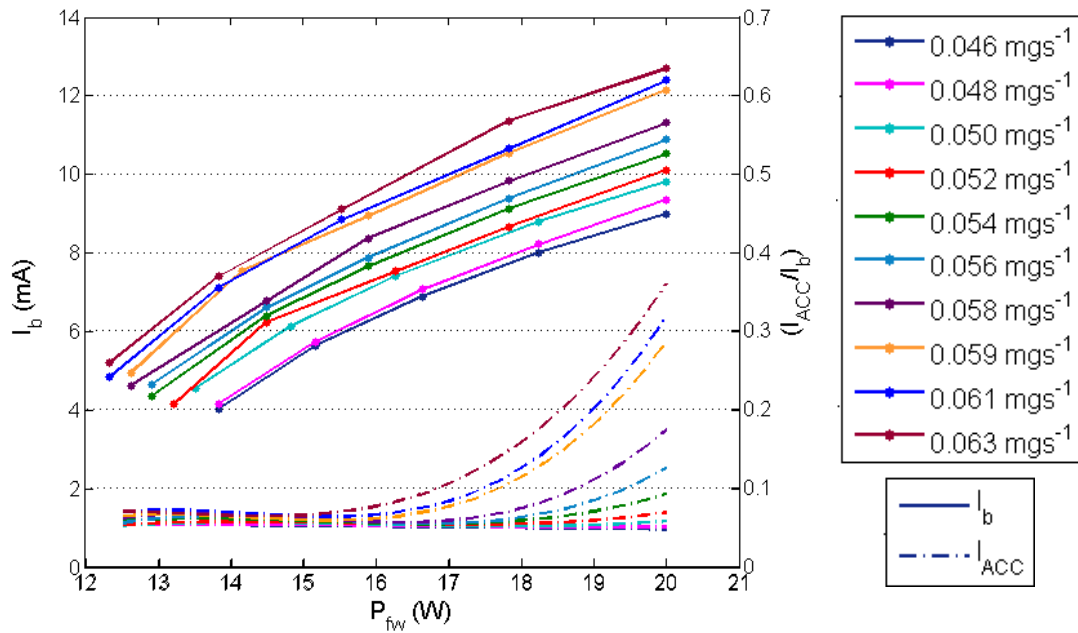


Figure 5.5. Beam current and accelerator drain current for the SE2 configuration for various flow rates and RF power ($V_b = 950\text{V}$, $V_{\text{ACC}} = -95\text{V}$).

The maximum beam current extracted at a beam and accelerator grid voltage of 950V/-95V prior to the onset of direct ion impingement was measured to be approximately 9.5mA for the SE1 configuration and 9.8mA for SE2. The maximum current extracted at perveance for the MiDGIT breadboard grids is determined to be approximately 14.3mA according to Equations 2.39 and 2.40 and values given in Table 3-4. A potential cause of the discrepancy could be an increased grid gap (l_g) to the stated cold gap value of 0.75mm, due to thermal expansion of the grids during beam extraction. According to Equations 2.39 and 2.40, and assuming all parameters other than the grid gap to be the stated values for the MiDGIT breadboard, a hot grid gap of the order 1.2mm would reduce the maximum beam current to the levels measured. Grid deformation due to thermal loads would be expected to be minimal for small diameter grids (< 5cm) however, and such a large increase in grid gap (~ 0.5mm) would need to be verified by measurement.

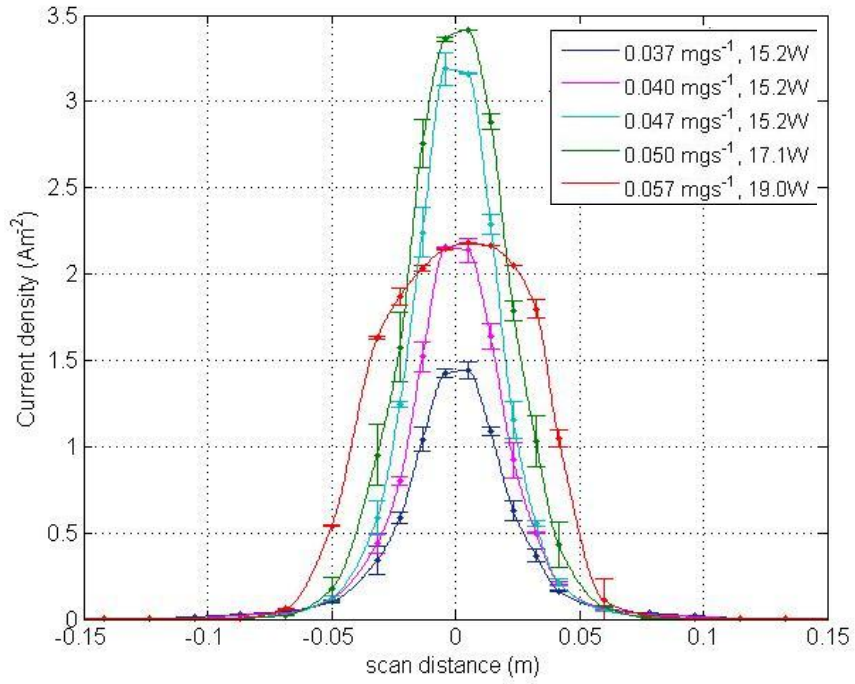
5.5 BEAM PROBE MEASUREMENTS

Radial profiles of the ion beams extracted from SE1 and SE2 were obtained at various operating points from which beam divergence could be estimated and an approximate thrust correction factor determined. The beam probe used consisted of a single screened faraday cup with 73 apertures, 0.1mm in diameter providing a maximum collection area of $5.73 \times 10^{-7} \text{ m}^2$. Current density was calculated from the measured beam probe current and the probe collection area. The beam probe was rotated in 5° steps between $\pm 45^\circ$ to $\pm 10^\circ$ and in 2.5° steps between -10° and $+10^\circ$ to obtain a suitable resolution of the beam whilst minimizing scan time. The beam probe was scanned twice across the beam for each operating point and the data averaged. Angular position was converted to distance according to:

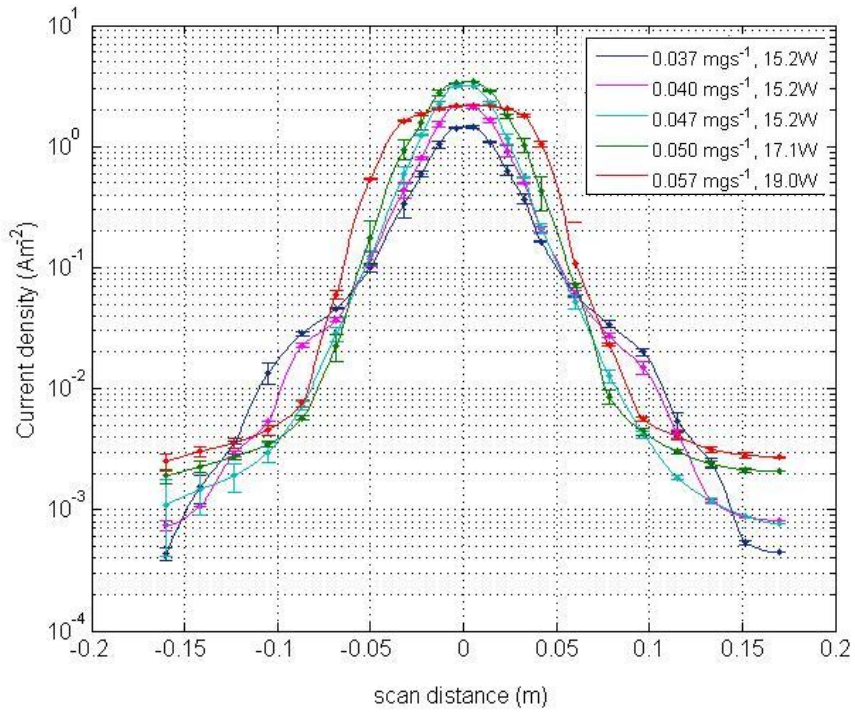
$$r = R_b \theta \frac{\pi}{180} \quad [m] \quad (5.1)$$

where θ is given in degrees and R_b is the radius of rotation, equivalent to the length of the beam probe arm of 0.21m.

The averaged data for each scan was then fit by spline interpolation. Plots of the beam profiles for the SE1 and SE2 configurations for the different operating points are presented in Figures 5.6 and 5.7, with the measured beam and accelerator grid currents for each operating point provided in Table 5-4.

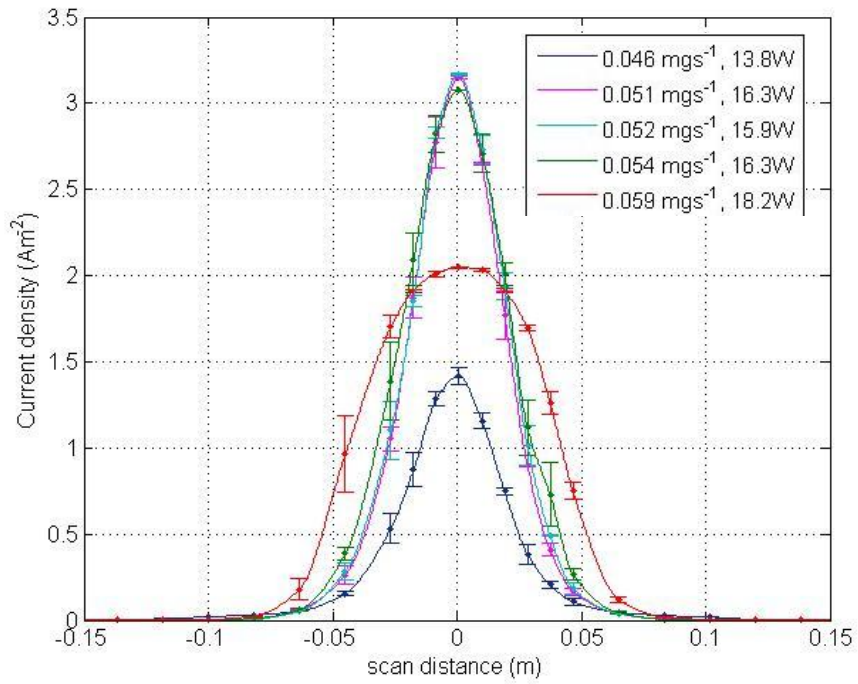


(a)

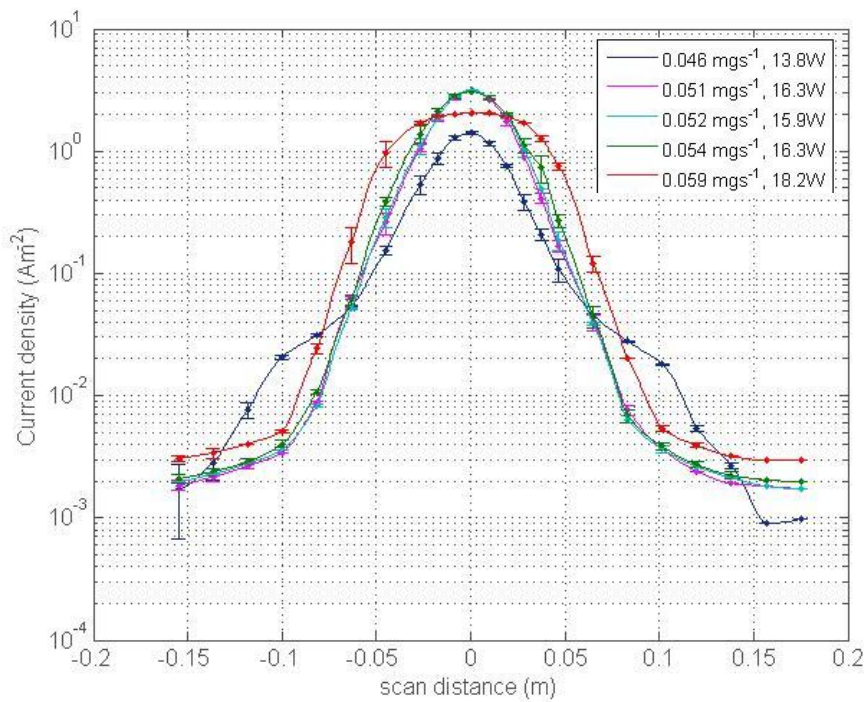


(b)

Figure 5.6. Beam profiles for the SE1 configuration for various flow rates and RF power (plotted on a log scale in (b)).



(a)



(b)

Figure 5.7. Beam profiles for the SE2 configuration for various flow rates and RF power (plotted on a log scale in (b)).

		\dot{m} (mgs ⁻¹)	P_{fw} (W)	I_b (mA)	I_{ACC}/I_b (%)	I_b^{est} (mA)	I_b^{est}/I_b (%)	θ_{div} (95%)	θ_{div} (2 σ)	α_{div}
SE1	TL1	0.037	15.2	3.46	4.91	3.09	89.3	43.87°	15.07°	0.992
	TL2	0.040	15.2	4.55	5.49	4.38	96.2	43.86°	12.67°	0.993
	TL3	0.047	15.2	6.30	6.03	6.06	96.2	43.87°	11.04°	0.992
	TL4	0.050	17.1	8.29	6.27	7.59	91.5	43.87°	11.54°	0.995
	TL5	0.057	19.0	10.69	9.73	7.63	71.4	43.87°	13.99°	0.991
SE2	TL1	0.047	13.8	3.71	4.58	3.00	80.9	43.87°	15.92°	0.990
	TL2	0.051	16.3	7.29	5.21	6.28	86.1	43.87°	12.59°	0.994
	TL3	0.052	15.9	7.18	5.43	6.52	90.1	43.86°	12.56°	0.994
	TL4	0.053	16.3	7.78	5.53	7.02	90.2	43.87°	13.15°	0.993
	TL5	0.059	18.2	10.18	8.15	7.41	72.8	43.87°	15.99°	0.989

Table 5-4 – Estimated beam current, beam divergence and thrust correction factor determined from the beam profiles of SE1 and SE2. (Also listed is the beam current determined from the grid currents).

The beam profiles plotted on a logarithmic scale can be seen to display two superimposed Gaussian-like distributions, resulting in a two-tier appearance. The low magnitude distribution of ion current at the periphery of the beam has previously been attributed to: highly divergent low-energy ions created near the exit plane of the thruster due to CEX collisions between beam ions and facility neutrals, to CEX ions created between the extraction grids at low propellant utilisation values and to scattering of central beam ions, with current density increasing at the periphery of the beam as the ratio of background neutral density to ion density increases [80, 90, 91]. Beam characterization by far-field probe measurements and at high background facility pressures, typically above $\sim 10^{-5}$ mbar, can therefore incur relatively large measurement uncertainties. Operation of the MiDGIT thruster within high pressures $>10^{-4}$ mbar was unavoidable as no facility with a higher pumping speed was available at time of testing. Characterization of the extracted ion beam to high accuracy was not required for the development stage of the MiDGIT breadboard however and reasonable estimates of beam current and the thrust correction factor due to beam divergence could still be obtained.

As can be seen from Figures 5.6 (b) and 5.7 (b) and from Table 5-4, the degree of scattering due to CEX collisions is significant at beam currents below ~ 6 mA (operating points TL1 & TL2 for the SE1 configuration, and TL1 for SE2) whilst at higher currents, where the ratio of background neutrals to beam ions is lower, the affect of CEX collisions on the beam is reduced. The accuracy to which beam current and beam divergence can be determined from the beam probe measurements should therefore be greater for the higher thrust levels compared to the lower thrust levels, where the periphery of the beam is more dispersed.

Assuming the ion beam to be azimuthally symmetric, beam current was estimated for each operating point for the SE1 and SE2 configurations by integration of the current density over the radial extent of the profile, as defined by Equation 5.2.

$$I_b = \frac{1}{2} \int_{-R}^R 2\pi r j_b(r) dr \quad (5.2)$$

with r being the arc length from the centreline of the beam probe system and R , the arc length at the maximum angular positions of $\pm 45^\circ$.

Beam current estimated from the beam profiles and that determined by the screen grid current agreed to within $\sim 10\%$ for the SE1 configuration and to within $\sim 15\%$ for SE2 up to approximately 8mA, as can be seen from Table 5-4. The lower beam current determined from the beam probe measurements compared to the screen grid current can mainly be attributed to CEX interactions and to the transmission factor of the screened faraday cup probe.

The divergence of an ion beam is typically defined by the half-cone angle that includes 95% of the total beam ions. Ion scattering and low-energy CEX ions resulting from a high background facility pressure (which increase current density on the periphery of the beam and which make the beam more diffuse at the edge) can therefore cause the beam divergence to be overestimated compared to operation in a higher vacuum environment, particularly if the beam probe is unable to fully screen the low-energy CEX facility ions.

Beam divergence calculated from the angle at which the current reached 95% of the estimated beam current for each operating point was found to be of the order 43.9° for both the SE1 and SE2 configurations (see Table 5.4) due to the contribution of ion current at wide angles. A separate estimate of beam divergence for the SE1 and SE2 configurations was also obtained by fitting a Gaussian function to the central region of the beam profile that should represent the undisturbed core beam current (as depicted in Figure 5.8). Though values for beam divergence derived in this manner are sometimes quoted in literature [91], the beam divergence quoted does not correctly represent the actual divergence of the beam as the influence of CEX ions created by collisions between beam ions and propellant neutrals between the extraction grids on the beam profile is ignored. The beam divergence estimated by Gaussian fit to the central region of the profile will therefore be lower than the true divergence of the beam, particularly for thrusters operating at low thrust density [80].

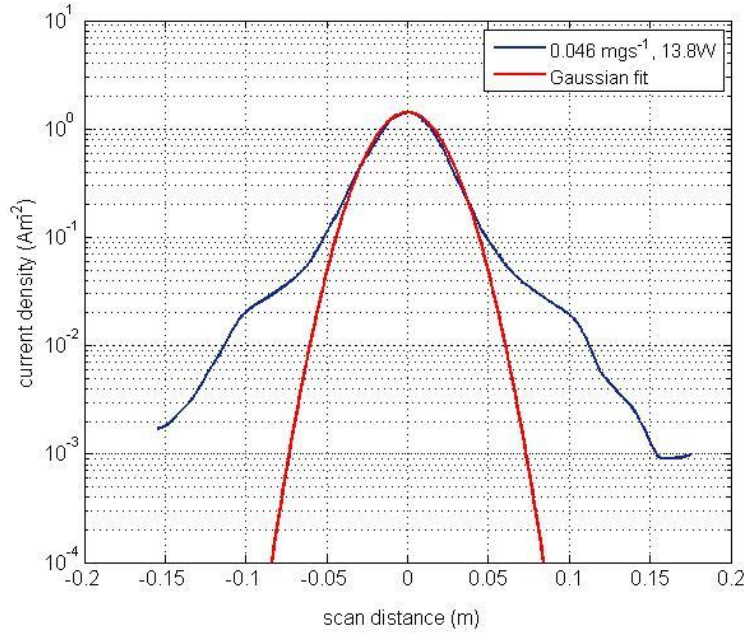


Figure 5.8. Example of a Gaussian fit to a beam profile affected by CEX collisions.

A Gaussian function of the following form was fit to the beam profiles obtained for the SE1 and SE2 configurations:

$$f(x) = Ae^{-\frac{(x-\mu)^2}{2\sigma^2}} \quad (5.3)$$

where A defines the amplitude of the distribution, μ is the mean of the distribution and σ is the variance which defines the spread of the distribution about the mean. Beam divergence was therefore taken as the 2σ deviation of the best-fit Gaussian to the central current density.

The beam divergence determined by the Gaussian fit for each operating point is plotted against beam current in Figure 5.9 for both the SE1 and SE2 configurations. Plots of the estimated beam current from the beam probe measurements to the measured (electrical) beam current, and also the accelerator grid current to beam current are given (Figure 5.10). The beam divergence displays a minimum within the range 6mA - 8mA for both SE1 and SE2. The higher divergence at low current, as mentioned, results from CEX interactions causing the periphery of the beam to be more diffuse due to the high ratio of background neutral density to ion density. Operation in a higher vacuum environment is expected to reduce the beam divergence estimated by Gaussian fit for the low thrust levels (<4mA) and for it to be more in line with those measured for the higher beam currents. Above beam currents of ~10mA, the estimated beam divergence is high for both the SE1 and SE2 configurations

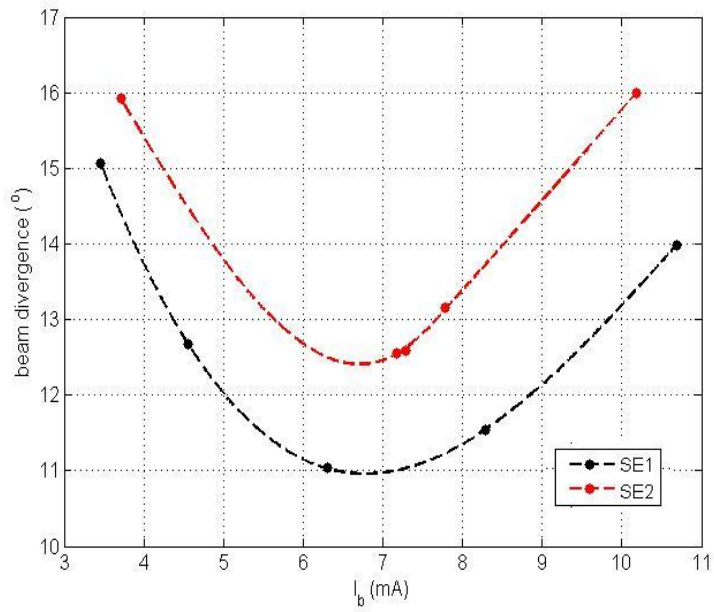


Figure 5.9. Estimated beam divergence against measured beam current for SE1 and SE2.

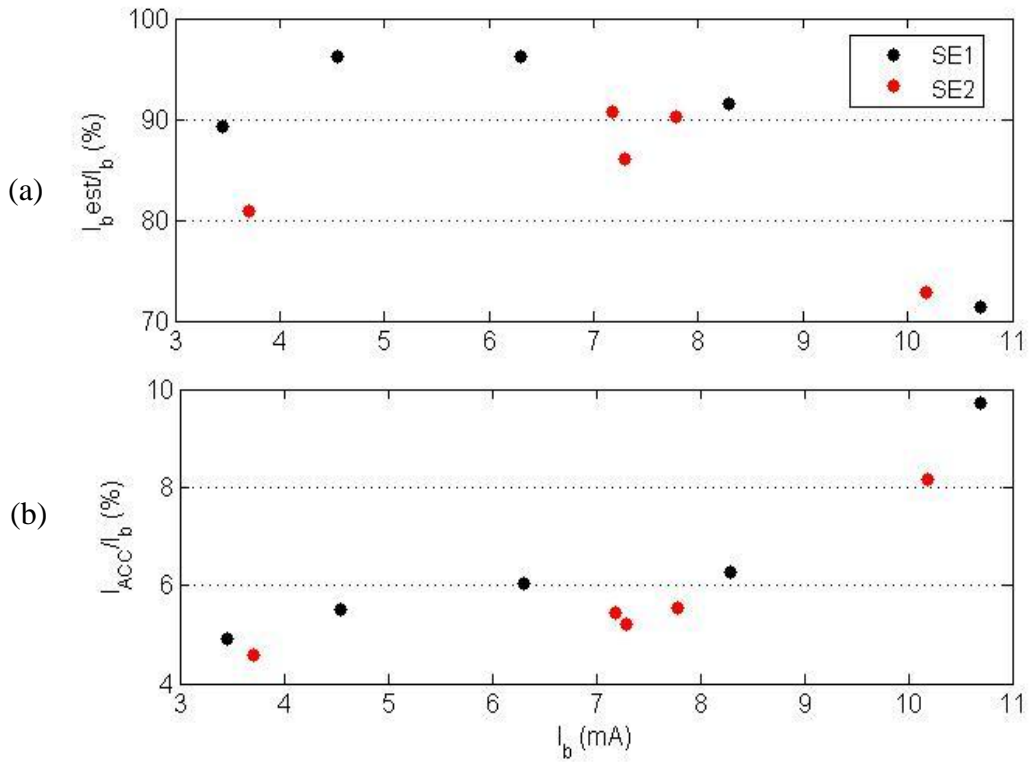


Figure 5.10. (a) Ratio of estimated beam current to measured beam current and (b) ratio of accelerator grid current to beam current for SE1 and SE2.

and the beam profiles can be seen to become flatter. The accelerator grid current increases substantially and the beam current estimated from the beam probe measurements is markedly reduced compared to the screen grid current. This is indicative of ion impingement on the accelerator grid due to operation at over-perveance; at high plasma density, the plasma sheath formed upstream of the screen grid will move closer to the grid and become flatter causing ions to directly impinge on the accelerator grid and the extracted beam to become more diffuse. The beam profiles support the observation made during performance mapping of 9mA being the approximate perveance limit for the MiDGIT breadboard thruster operating at a beam voltage of 950V and accelerator grid voltage of -95V in SE mode.

The estimates of beam divergence obtained at the intermediate thrust levels (between 6mA - 8mA) are least influenced by facility effects. The beam divergence in this range can be seen to be within approximately 12° for SE1 and 13° for SE2. Beam divergence is typically of the order 10° - 12° for conventional ion thrusters and beam divergence has been measured to be ~15.2° for the μ NRIT-4/7 thruster operating at 75 μ N with a beam potential of 1400V [41].

A thrust correction factor to account for divergence losses was also calculated from the beam profiles according to Equation 5.4 [23]; the results of which are presented in Table 5-4.

$$TCF = \frac{\frac{1}{2} \int_{-R}^R 2\pi r j_b(r) \cos\theta(r) dr}{\frac{1}{2} \int_{-R}^R 2\pi r j_b(r) dr} \quad (5.4)$$

Across the thrust range measured, the thrust correction factor calculated by Equation 5.4 varied by only a small amount (the relative standard deviation being 0.16% for SE1 and 0.23% for SE2), with thrust losses due to beam divergence <1% for both configurations between 6-8mA.

5.6 PERFORMANCE ANALYSIS

Performance of the two ends of the MiDGIT breadboard thruster was reasonably comparable considering the discrepancy in flow rate between the two configurations due to the different MFCs employed.

The measured beam profiles for the SE1 and SE2 configurations and the results obtained during performance mapping suggest that each configuration was operating above the perveance limit for flow rates $>0.05\text{mgs}^{-1}$ and RF power $>17.5\text{W}$ during operation at beam and accelerator grid voltages of $950\text{V}/-95\text{V}$. As previously mentioned, the onset of direct ion impingement on the accelerator grid establishes an upper limit to achievable thrust

Thrust was estimated from the measured beam currents and the divergence thrust correction factors determined for the SE1 and SE2 configurations according to Equation 2.49; no correction for multiply-charged ions was applied as the amount of double-ions was assumed to be $<1\%$ as is typically reported for RF ion thrusters [40]. Thrust and specific impulse determined for the SE1 and SE2 configurations are compared in Figure 5.11 for the operating points below the observed onset of ion impingement. The difference in performance observed is due to the discrepancy between the mass flow controllers used during the characterisation of each end; mass flow rate corrections were only applied to the MFC for the SE2 configuration, with the MFC for SE1 assumed to provide correct flow rates. This highlights the importance of accurate and reliable flow control systems for EP thrusters, as the performance and specific impulse of a thruster can be severely impacted.

The maximum thrust that should be achieved due to the perveance limit of the grids was calculated to be $\sim 725\mu\text{N}$ for the MiDGIT breadboard thruster operating at a beam voltage of 950V and accelerator grid voltage of -95V . Maximum thrust levels obtained prior to direct ion impingement were observed to be lower, of the order $\sim 500\mu\text{N}$. This equates to approximately 70% of the theoretical maximum thrust. Operation at lower perveance fractions would allow the lifetime of the accelerator grid to be extended, as the energy of CEX ions would be reduced, but this would impact performance [73]. Maximum thrust can generally be increased by increasing the screen grid ion transparency (by simply increasing the number of grid apertures) or by increasing the electric field in the acceleration region between the extraction grids by increasing the beam voltage [47].

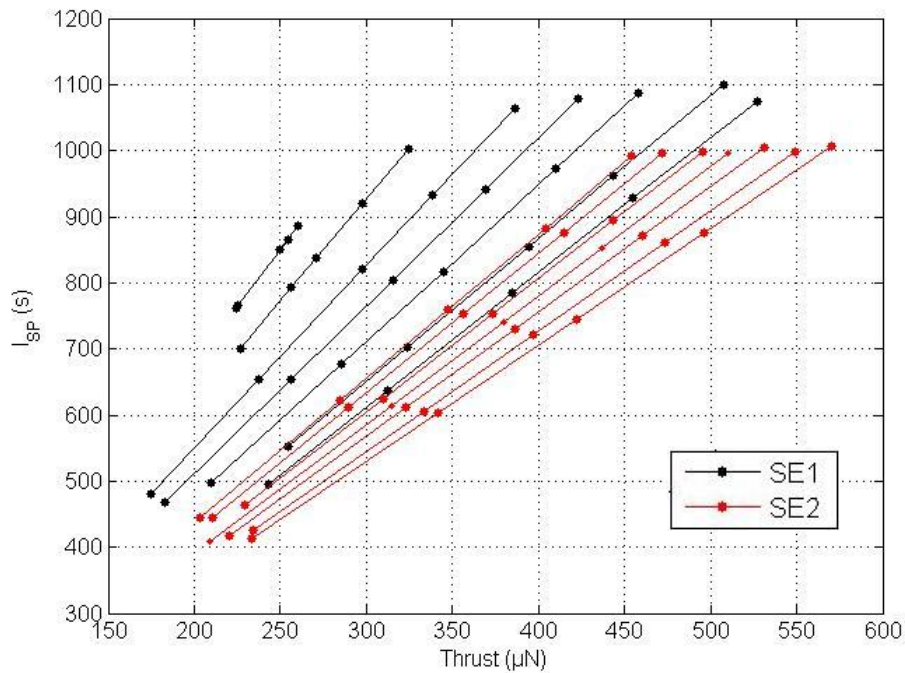


Figure 5.11. Specific impulse against thrust determined for the SE1 and SE2 configurations of the MiDGIT breadboard thruster for the operating points with $\dot{m} \leq 0.050 \text{ mgs}^{-1}$ for SE1 and $\dot{m} \leq 0.058 \text{ mgs}^{-1}$ for SE2 with $V_b = 950\text{V}$, $V_{ACC} = -95\text{V}$.

Propulsion requirements for the MiDGIT thruster limit specific power during coarse thrust operation to 50W/mN . Thrust and specific impulse determined for the SE1 and SE2 configurations against specific power are displayed in Figures 5.12 and 5.13. It can be seen that the performance of the MiDGIT thruster must be improved significantly to meet the requirements for coarse thrust mode (summarized in Table 5.1).

Thruster efficiency (determined from the product of mass utilization efficiency and electrical efficiency which are shown in Figure 5.14) was found to be poor for the breadboard design of the MiDGIT thruster and at these operating conditions, being less than 10%. Propellant efficiencies and electrical efficiencies up to 50% have been demonstrated for the RIT-2.5/37 miniature RF ion thruster at similar thrust levels [93]. The poor performance of the MiDGIT breadboard is partly due to the low beam voltage applied in these tests, limited by the available power supply, however, poor coupling between the RFG and plasma is evident from the high ion production costs, displayed in Figure 5.16, and the low electrical efficiencies.

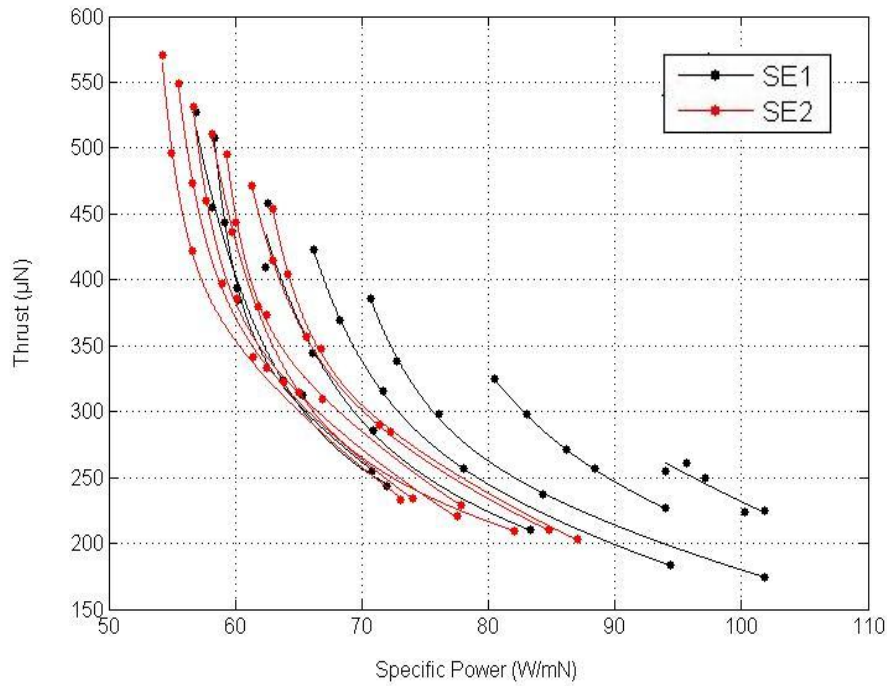


Figure 5.12. Thrust against specific power determined for the SE1 and SE2 configurations of the MiDGIT breadboard thruster (at operating points with $\dot{m} \leq 0.050 \text{ mgs}^{-1}$ for SE1 and $\dot{m} \leq 0.058 \text{ mgs}^{-1}$ for SE2 with $V_b = 950\text{V}$, $V_{\text{ACC}} = -95\text{V}$). (Coarse thrust requirements specify a limit of 50W/mN for specific power).

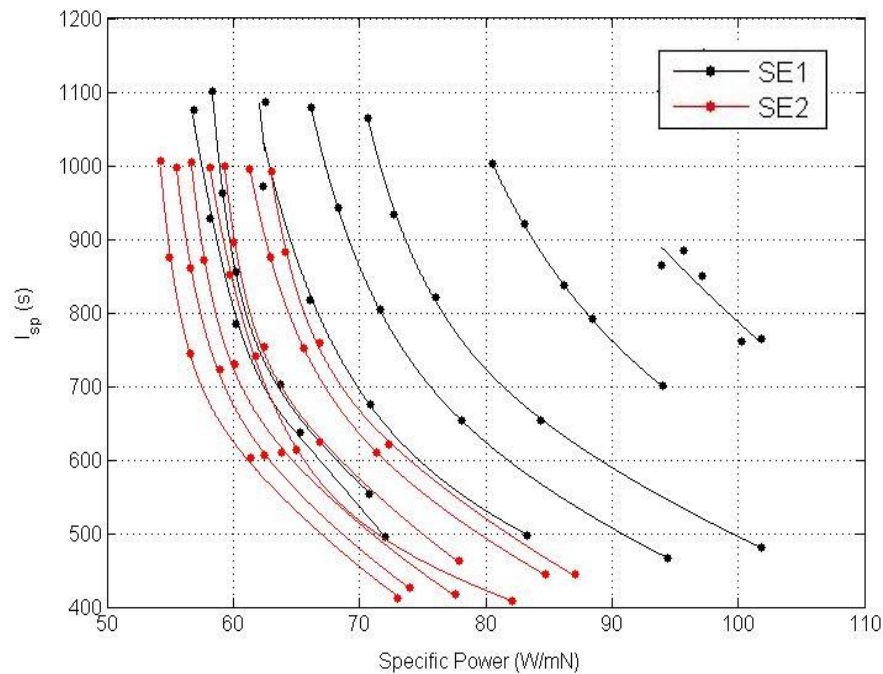


Figure 5.13. Specific impulse against specific power determined for the SE1 and SE2 configurations of the MiDGIT breadboard thruster (at operating points with $\dot{m} \leq 0.050 \text{ mgs}^{-1}$ for SE1 and $\dot{m} \leq 0.058 \text{ mgs}^{-1}$ for SE2 with $V_b = 950\text{V}$, $V_{\text{ACC}} = -95\text{V}$). (Coarse thrust requirements specify a limit of 50W/mN for specific power).

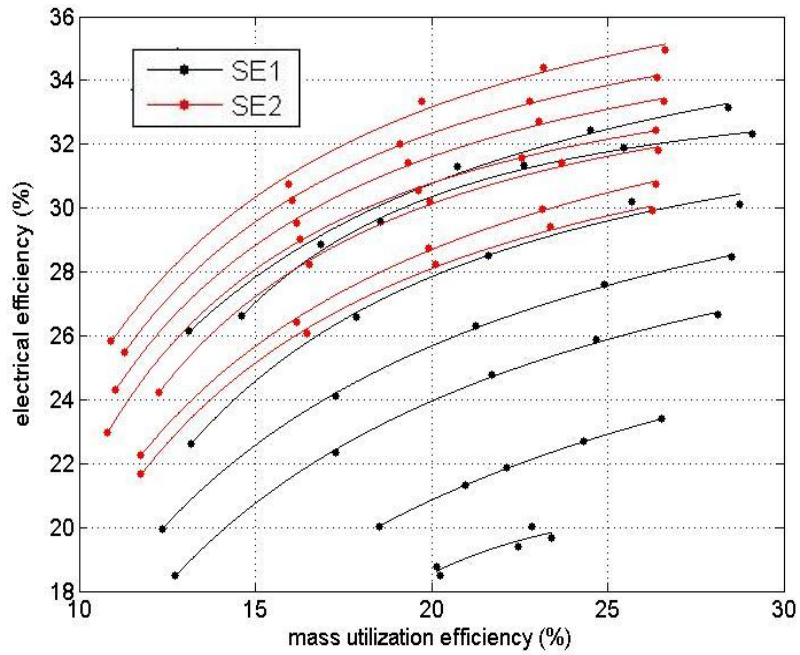


Figure 5.14. Electrical efficiency against mass utilization efficiency determined for the SE1 and SE2 configurations of the MiDGIT breadboard thruster (at operating points with $\dot{m} \leq 0.050 \text{ mgs}^{-1}$ for SE1 and $\dot{m} \leq 0.058 \text{ mgs}^{-1}$ for SE2 with $V_b = 950\text{V}$, $V_{ACC} = -95\text{V}$).

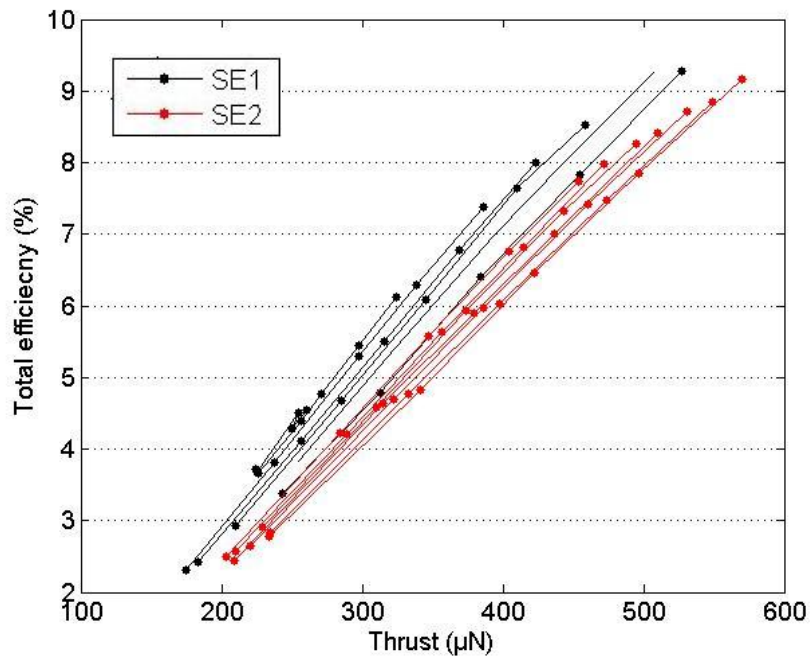


Figure 5.15. Total thruster efficiency determined for the SE1 and SE2 configurations of the MiDGIT breadboard thruster (at operating points with $\dot{m} \leq 0.050 \text{ mgs}^{-1}$ for SE1 and $\dot{m} \leq 0.058 \text{ mgs}^{-1}$ for SE2 with $V_b = 950\text{V}$, $V_{ACC} = -95\text{V}$).

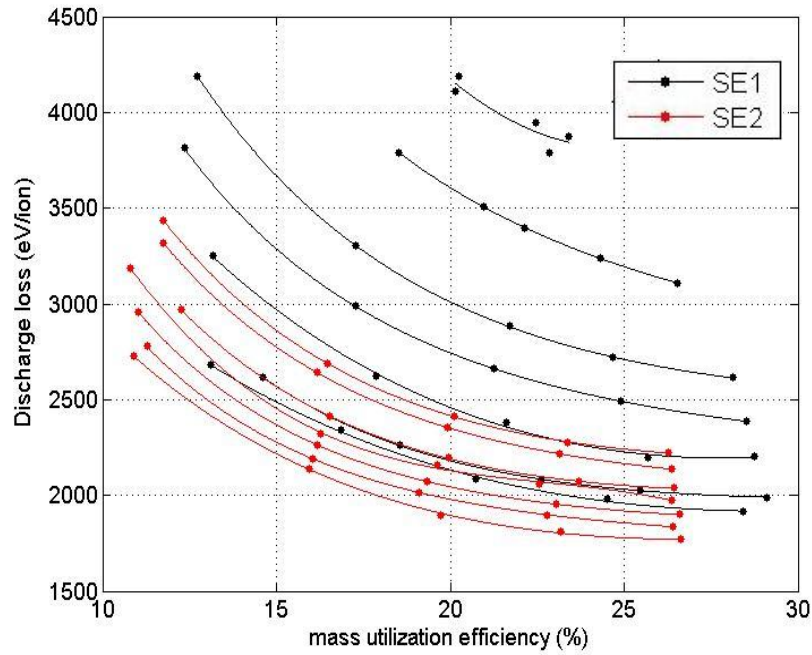


Figure 5.16. Discharge loss against mass utilization efficiency for the SE1 and SE2 configurations of the MiDGIT breadboard thruster (at operating points with $\dot{m} \leq 0.050 \text{ mgs}^{-1}$ for SE1 and $\dot{m} \leq 0.058 \text{ mgs}^{-1}$ for SE2 with $V_b = 950\text{V}$, $V_{ACC} = -95\text{V}$). (Discharge loss for the RIT-4/151 and the RIT-2.5/37 is of the order 800 eV/ion and 2400 eV/ion respectively).

The forward RF power used to determine these values is that delivered by the RF amplifier and therefore incorporates ohmic losses, dielectric losses and radiation losses in the matching unit, connectors and induction coil. Poor power coupling to the plasma is considered the main contributor to the poor performance of the MiDGIT breadboard thruster compared to other miniature ion thrusters [27,41,93]. Simulations of the BRIT3 RF ion thruster by Tsay demonstrated that 30% of the power losses were due to just ohmic losses of the matching circuit, and so, are important to minimize [25]. Wall losses contributed 10% to the power losses.

Electrical efficiency could be improved significantly for the MiDGIT thruster by use of a dedicated, vacuum compatible RFG located as close to the thruster as possible. Improvements could also be made to the induction coils to minimize coil resistance; use of silver coated, hollow copper tubing may present lower resistance than the small diameter enameled copper wire used for the breadboard thruster.

As previously stated, discharge losses are dominated by wall losses in miniature ion thrusters. Consideration could be given to optimize the geometry of the discharge chamber to reduce the

surface-area-to-volume ratio, as for the RIT-2.5 thruster, but consideration would also have to be given to the location and geometry of the inductions coils to provide optimal power coupling by the two coils during differential operation. Increasing ionization close to the screen grid may also enhance discharge efficiency to a small degree, as was demonstrated by the RIT-2.5 thruster through the use of gas injection near the perimeter of the screen grid [93].

Any improvements in either electrical efficiency or mass utilization efficiency however occur at the cost of the other. A given beam current can either be achieved at a low flow rate and high RF power or high flow rate and low RF power [93]. This must be considered when optimizing a RF ion thruster for a particular application; significant effort could be made to optimize electrical efficiency for a mission limited in power but propellant costs will be incurred, or mass utilization efficiency could be optimized for missions with limited propellant provided that sufficient power is available.

5.7 ADDITIONAL PERFORMANCE TESTS BY QINETIQ

Additional performance tests were conducted by QinetiQ on the MiDGIT breadboard thruster configured for SE operation. A brief summary of some of the key results of these tests are included to provide a more rounded assessment of the performance of the MiDGIT breadboard thruster.

5.7.1 Extended Thrust Capability

It was proposed that the upper limit on the thrust achieved by the MiDGIT breadboard model in SE mode, dictated by the onset of direct ion impingement, could be improved by operating the thruster within a higher vacuum environment and at a higher beam voltage. The MiDGIT breadboard thruster was therefore operated within the LEEP-3 vacuum facility by QinetiQ when this chamber became available [100]. The background pressure was improved to 2.1×10^{-5} mbar during operation and the beam voltage increased up to 1300V using a higher voltage power supply. The negative accelerator grid voltage was increased to -250V in order to prevent electron backstreaming, although theoretically, a potential of approximately -120V should be sufficient to prevent electron backstreaming (as presented in Table 3-5). Maximum thrust was increased to $\sim 780\mu\text{N}$ for the conditions specified in Table 5-5.

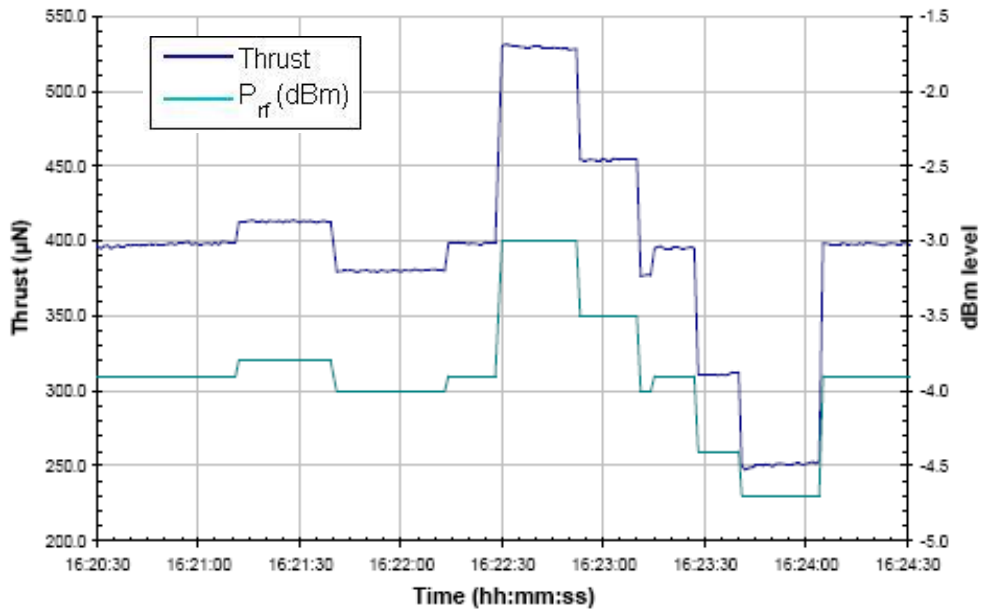
Max Thrust	~780 μ N
Flow rate	0.10 mgs ⁻¹
Forward RF power	30W
Beam potential	1300V
Accelerator potential	-250V
Operating frequency	5.25 MHz
Number of apertures	55
Background pressure	2.1 x 10 ⁻⁵ mbar

Table 5-5 – Maximum thrust achieved by operating the MiDGIT breadboard thruster at higher beam potential and lower background pressure^[100].

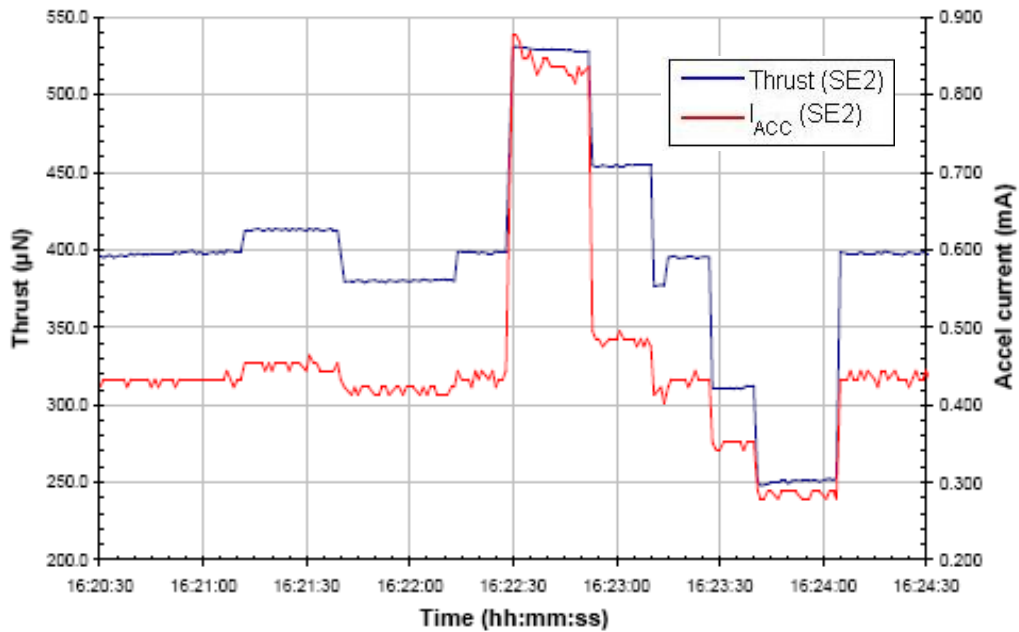
5.7.2 Thrust Stepping

Step wise thrust variation was demonstrated for the MiDGIT breadboard thruster by incrementing the RF power level set by the signal generator. The thruster was operated by QinetiQ at various flow rates with beam and accelerator grid voltages of 950V/-95V [88]. Large positive steps in thrust could be achieved of the order 100 μ N - 200 μ N for a +1dB change in forward RF power (an example is given in Figure 5.17).

Thrust resolution and repeatability of the MiDGIT thruster will be dependent on the resolution and accuracy of the RFG and flow control unit (FCU). The resolution of the IFR 2031 signal generator used during the MiDGIT breadboard characterisation was limited to 0.1dB. Thrust resolution was observed to be of the order 15 μ N - 25 μ N for the SE1 and SE2 configurations due to a 0.1dB change in RF power, as summarised in Table 5-6. At this level of performance, a thrust resolution of < 0.5 μ N would demand an RF supply with resolution of the order 0.01dB. Lower thrust resolution could obviously be achieved by reducing the number of apertures of the extraction grids but this would impact the maximum thrust level.



(a)



(b)

Figure 5.17. Thrust stepping of the SE2 configuration of the MiDGIT breadboard thruster operated at 0.051 mgs^{-1} with $V_b = 950\text{V}$, $V_{ACC} = -250\text{V}$. Thrust level and forward RF power (in dBm) are displayed in (a) while thrust and accelerator grid current are displayed in (b) ^[88].

	\dot{m} (mgs ⁻¹)	P_{fw} (W)	ΔT due to 0.1dB step (μ N)
SE1	0.037	14.5	20.3
	0.040	14.5	18.2
	0.043	14.8	15.6
	0.047	15.2	15.1
	0.050	17.0	15.7
SE2	0.047	14.8	25.4
	0.051	15.9	19.7
	0.052	15.9	15.4
	0.053	16.3	17.8
	0.058	17.8	14.2

Table 5-6 – Minimum thrust step at various flow rates for the SE1 and SE2 configurations of the MiDGIT breadboard thruster due to a 0.1dB change in forward RF power ^[88].

5.8 SUMMARY

Characterisation of the two single-end configurations of the MiDGIT breadboard thruster was performed in order to determine preliminary performance with regards to coarse thrust requirements. SE operation of the thruster has initially demonstrated thrust levels between 200 μ N-500 μ N and specific impulse of 400s-1100s with beam and accelerator grid voltages of 950V/-95V respectively. Beam profiles were obtained in order to provide verification of the measured electrical thrust and to determine a thrust correction factor to account for losses due to beam divergence. The extracted ion beams were observed to be affected by CEX interactions at low beam currents due to the high background pressure during operation. Operation of the thruster within a higher vacuum environment will be essential for performance and lifetime testing of any future engineering or qualification models of the MiDGIT thruster to reduce sputtering of the accelerator grid due to CEX ions. Further testing of the MiDGIT breadboard thruster by QinetiQ has demonstrated that the maximum thrust, limited by direct ion impingement on the accelerator grid, can be increased to approximately 780 μ N by increasing the beam voltage to 1300V. The thruster was determined to be operating at approximately 70% perveance at maximum thrust for $V_b = 950$ V and approximately 51% perveance at maximum thrust for $V_b = 1300$ V. Maximum thrust could be increased further still by operating at even higher beam voltages or increasing the number of grid apertures, however these changes will impact the minimum thrust level. Thrust resolution was observed to be of the order 25 μ N worst-case, limited by the 0.1dB resolution of the signal generator

controlling the RF power level. Electrical efficiency was observed to be low and discharge loss observed to be high, indicating poor power coupling to the plasma. Significant improvements to electrical efficiency could be achieved by operating the thruster with an optimized RF supply located directly next to the thruster. The design of the induction coil should also be improved to minimize coil resistance. Heating of the coil was observed to be an issue due to the effect on coil resistance. An increase of up to approximately 50% in coupling efficiency would be required to reduce power levels and bring specific power more in line with the requirement of 50W/mN. This may also permit reductions in flow rate and the possibility of lowering the minimum thrust level.

A summary of single-end performance of the MiDGIT breadboard thruster is provided in Table 5-7, along with performance data of similar sized miniature RF ion thrusters as a comparison. It can be seen that the current configuration of the MiDGIT thruster is unable to meet the requirements specified for coarse thrust control. However, the RIT-4 and RIT-2.5 thrusters, at a more advanced stage of development, have demonstrated suitable performance for coarse thrust mode [27, 41, 93], and therefore, implementation of the specified changes to a MiDGIT engineering model should allow the requirements for coarse thrust mode to be achieved.

	SE1	SE2	RIT-4/7	RIT-4/151	RIT-2.5/37
Thrust range	175 μ N - 500 μ N †	200 μ N - 550 μ N †	10 μ N – 200 μ N	150 μ N – 3.5mN	50 μ N - 575 μ N
Specific impulse	500s – 1100s	400s – 1000s	3850s @ 250 μ N	>3700s @ 3.5mN	363s – 2861s
Flow rate *	0.030 mgs ⁻¹ - 0.050 mgs ⁻¹	0.046 mgs ⁻¹ - 0.056 mgs ⁻¹	0.004 mgs ⁻¹ – 0.008 mgs ⁻¹	-	0.014 mgs ⁻¹ – 0.021 mgs ⁻¹
Discharge power (P_{fw})	13W – 17.5W	13W – 17.5W	-	-	12.4W – 18.25W
Mass utilization efficiency	13% - 29%	11% - 27%	25% - 50%	80% @ 3.5mN	14.7% - 51.5%
Electrical efficiency	18% - 33%	22% - 35%	<50%	60% @ 3.5mN	4.2% - 46.5%
Specific Power	100 W/mN – 58 W/mN	85 W/mN – 55 W/mN	-	40W/mN @ 3.5mN	262 W/mN – 59.8 W/mN
Minimum Discharge Loss	1916 eV/ion	1770 eV/ion	-	769 eV/ion	2287 eV/ion
Beam divergence	<13° ^	<13° ^	<15.2°	-	-
Operating frequency	5.25 MHz		1 MHz	~2 MHz	2.9 MHz
Grid apertures	55		7	151	37
Beam potential	950V		1100V - 1600V	1400V	372V – 1980V
Accelerator potential	-95V		-100V to -200V	-100V	-100V

† Maximum thrust increased to ~780 μ N with $V_b = 1300V$

* Flow rate corrections applied to SE2

^ Estimated from Gaussian fit to central beam distribution, not accounting for effects on the beam due to CEX collisions

Table 5-7 – Summary of the performance of the SE1 and SE2 configurations of the MiDGIT breadboard thruster.
(neglecting neutralizer power and flow rate)
 (Performance data of the similar sized RIT-4 and RIT-2.5 thrusters are provided as a comparison ^[27, 41, 93]).

Chapter Six

6. Differential Thrust Control

High precision interferometry missions pose the greatest challenge to micropropulsion technologies in terms of spacecraft control. Propulsion systems capable of providing thrust levels down to $\sim 1\mu\text{N}$ with sub- μN resolution and very low noise will be essential for maintaining precision pointing during these missions. Requirements for fine thrust control are reiterated in Table 6-1.

Fine Thrust range	1 – 150μN
Fine Thrust resolution	<0.5μN
Fine Thrust repeatability	0.5μN
Specific impulse	>90s @ 12μN
Specific power	<50W/mN
Thrust actuation frequency	100Hz
Thrust response time	60ms

Table 6-1. Propulsion requirements specific to fine thrust control.

It is proposed that the MiDGIT thruster could provide very precise μN thrust levels through the differential control of opposing ion beams, whereby a net offset in thrust is produced by creating an imbalance between the extracted ion beams. The extraction and control of two independent ion beams from a common plasma discharge has never previously been reported for a gridded ion thruster. Test campaigns were performed on prototype and breadboard models of the MiDGIT thruster to provide a proof-of-concept and to investigate differential control methods for achieving the thrust requirements specified for fine thrust control. This chapter presents the results of the tests performed, summarising results and observations of significance to the design and operation of a differential RF ion thruster.

6.1 DISCHARGE IGNITION AND DUAL BEAM EXTRACTION

Stable discharges were achieved with the MiDGIT breadboard thruster configured for differential operation at the same frequency of 5.25 MHz as for single-end operation, indicating that the MiDGIT thruster can be operated in both thrust modes using a fixed-frequency RF source. Discharges could be ignited using similar settings on the antenna matching units to those used for SE operation for commanded flow rates between 0.35 mgs^{-1} - 0.38 mgs^{-1} (0.21 mgs^{-1} - 0.22 mgs^{-1} corrected flow rates) and forward RF power levels of $(20.0 \pm 1.2)\text{W}$ to $(31.7 \pm 1.9)\text{W}$, delivered by the RF amplifier to both AMUs and induction coils. The xenon flow rate to the MiDGIT breadboard thruster was controlled by MFC2 during differential characterisation, as was used with the SE2 configuration during single-end characterisation. Assuming grid transparency to neutrals is identical for both grids sets, the equivalent neutral pressure within the discharge chamber for the above flow rates can be calculated to be approximately 7.64 mTorr – 8.29 mTorr (4.58 mTorr – 4.80 mTorr corrected) using Equations 2.44 and 2.46 and assuming a gas temperature of 300K, comparable to the neutral pressure estimated for discharge ignition for the SE2 configuration. Forward RF power was up to twice that required for single-end discharge ignition, mainly due to the two AMUs and induction coils presenting double the power losses.

During differential beam tests of the MiDGIT prototype thruster (operated at 13.56 MHz) within the EP1 vacuum facility, discharge ignition was found to be difficult unless the tungsten filament was located directly in front of the grid apertures on one end of the thruster. Ignition required forward RF powers between 40-50W and xenon flow rates of $\sim 0.304 \text{ mgs}^{-1}$, similar to the MiDGIT breadboard thruster (operated at 5.25 MHz). Chamber pressure was relatively high in the EP1 facility at discharge ignition, of the order 9×10^{-4} mbar. Also, the open area of the extractions grids of the MiDGIT prototype thruster is lower than that of the breadboard thruster (see Chapter 3). These two factors will influence the conductance of electrons into the discharge chamber, which could explain the need for the filament to have been in close proximity to the grids for ignition of the prototype thruster within the EP1 chamber. This observation suggests that neutralizer or filament location may be of importance to miniature RF ion thrusters with low grid open areas, though ignition may be facilitated by the higher neutral pressure achieved for a given flow rate within the discharge chamber of very small devices (as observed for the RIT-2.5 thruster [93]). It was observed during differential tests on the MiDGIT prototype thruster within the EP1 facility that if a discharge was extinguished, the discharge could be easily re-ignited straight into the inductive mode without the need of the filament if a slight variation to the tuning capacitors of one of the AMUs was applied in rapid succession of the discharge going out. This was not observed

during the differential tests of the MiDGIT breadboard thruster at the QinetiQ LEEP facilities and is expected to be due to the higher operating pressure of the MiDGIT prototype during the tests performed within the EP1 chamber. Characterisation of self-ignition at high pressure will be of interest for any future testing activities as it will have implications on the response time of the thruster following a discharge outage.

The extraction of two stable ion beams was demonstrated for both the MiDGIT prototype and breadboard thrusters operated with a T5 hollow cathode neutralizer within the LEEP-1 loadlock facility. Dual ion beams were initially extracted for the conditions listed in Table 6-2 for the MiDGIT prototype and those listed in Table 6-3 for the MiDGIT breadboard thruster. The electrical thrust calculated from the beam current (with no thrust correction factor applied) is provided for the MiDGIT breadboard thruster as an indication of the possible thrust levels for these conditions. An image of the MiDGIT breadboard thruster operating in differential mode is given in Figure 6.1(a), while an image displaying dual beam extraction from the MiDGIT prototype is displayed in Figure 6.1(b).

	MiDGIT Prototype
Forward RF power	45W – 50W
Flow rate	0.06 mgs ⁻¹ - 0.11 mgs ⁻¹
Operating frequency	3.28 MHz
Background pressure	5.0 x 10 ⁻⁴ mbar

Table 6-2. Discharge conditions for the MiDGIT prototype for dual ion beam extraction.

\dot{m} (mgs ⁻¹)	P_{RF} (dB)	P_{RF} (W)	I_{b1} (mA)	I_{acc1} (mA)	I_{b2} (mA)	I_{acc2} (mA)	T_1 (μN)	T_2 (μN)
0.040	-1.6	27.6 ± 0.1	2.62	0.07	2.68	0.07	133.2	136.2
0.045	-1.0	31.7 ± 0.1	3.84	0.11	4.13	0.12	195.4	209.7
0.050	-0.2	38.1 ± 0.2	5.20	0.17	5.65	0.17	264.3	287.1

Table 6-3. Initial performance of the MiDGIT breadboard thruster during dual ion beam extraction, operating with $V_b = 950V$, $V_{ACC} = -95V$.

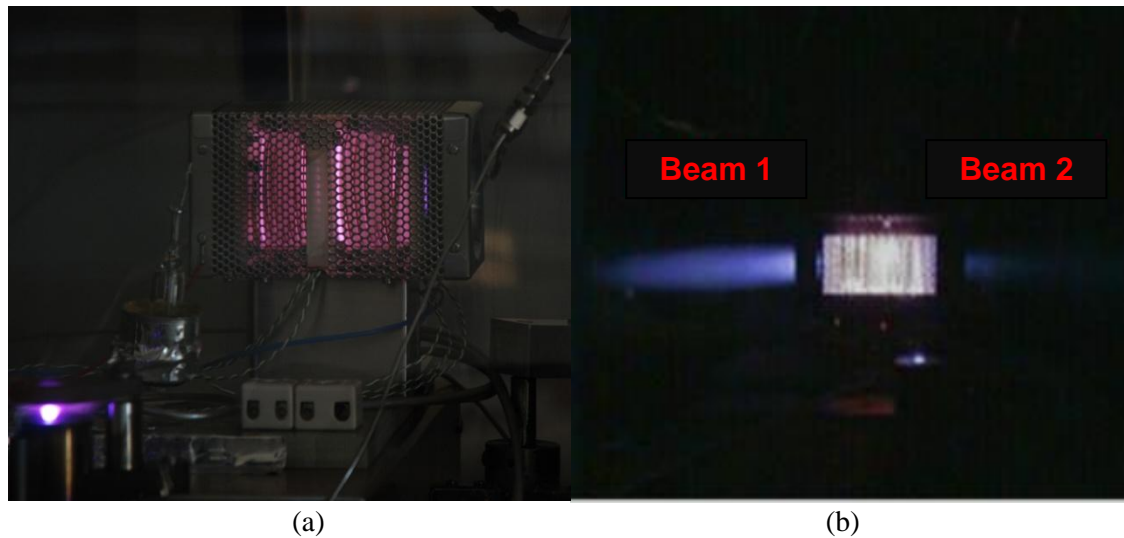


Figure 6.1. Images of (a) the MiDGIT breadboard thruster operating in differential mode, (b) dual ion beam extraction from the MiDGIT prototype thruster during variation of the accelerator grid potentials on either end. *(The electron backstreaming limit has been reached for SE1 in this image; therefore beam 1 shows a plume distinctive of electron backstreaming).*

6.2 DIFFERENTIAL THRUST CONTROL

The MiDGIT prototype thruster successfully demonstrated that two stable ion beams could be extracted from a common inductive plasma discharge. The MiDGIT breadboard thruster was then developed to demonstrate differential control of the ion beams and to characterise performance within both the single-end and differential modes for providing coarse and fine thrust control.

As detailed in previous chapters, two methods were proposed for differential thrust control; independent variation of the accelerator grid potentials to induce changes in sheath geometry upstream of each screen grid which would lead to a net offset in the extracted ion beam currents, and variation of RF power on each end of the thruster to generate a higher plasma density on one end and ultimately a net thrust out of that end.

6.2.1 VARIATION OF ACCELERATOR GRID POTENTIAL

Differential control by variation of the accelerator grid potential was investigated using the MiDGIT breadboard thruster within the LEEP-1 loadlock facility. The thruster was operated with a beam voltage of 950V and the accelerator grid potential on either end of the thruster was varied by manual control of the voltage applied by the Bertran HV DC power supplies. The grid currents on either end of the thruster were recorded automatically via LabVIEW as

an indication of thrust. Beam profiles were obtained as verification of the measured electrical thrust and to identify changes in the focussing of the ion beams due to variation of the accelerator grid potential. Only one ion beam could be measured however at any given time due to the availability of only one faraday cup probe and insufficient space within the LEEP-1 loadlock to rotate the probe through 360° . The accelerator grid potential was varied between -25V and -325V ; operation to -25V was performed in order to identify the onset of electron backstreaming. The accelerator grid potential of one grid set was varied while the accelerator grid potential on the other end of the thruster was kept constant at -75V . Due to time restrictions, tests were performed at two operating points; a relatively low plasma density level with flow rate and forward RF power of $0.052 \text{ mgs}^{-1} / 27.6\text{W}$, and a higher plasma density level at $0.058 \text{ mgs}^{-1} / 38.1\text{W}$ ².

Thrust calculated for the MiDGIT breadboard thruster operating at the grid perveance limit for these extraction potentials using Equation 2.42 is estimated to provide a net thrust range of over $250\mu\text{N}$ (see Figure 6.2). Operation at 55% of perveance would be expected to provide a net thrust range of $\sim 150\mu\text{N}$, as specified for fine thrust control. However, over-focussing and under-focussing of the extracted beamlets through the grid apertures, leading to direct ion impingement on the accelerator grid, will affect the thrust that can be achieved.

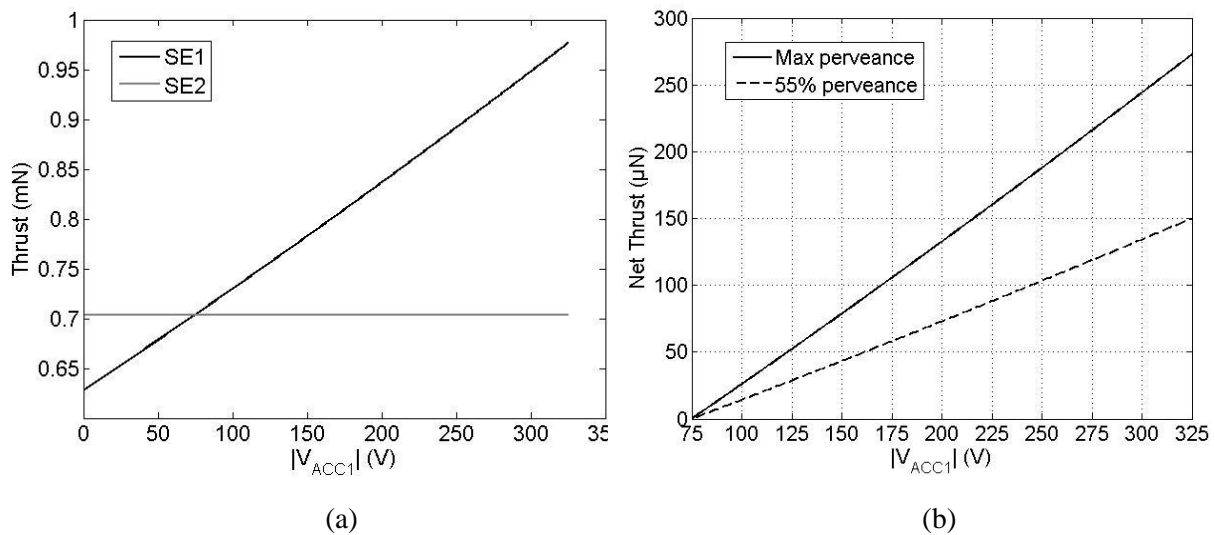


Figure 6.2. (a) Thrust calculated at perveance for the MiDGIT breadboard grids with a beam voltage of 950V and accelerator grid voltage of -75V for SE2 and varying accelerator grid voltage for SE1, (b) Net thrust due to varying accelerator grid voltage on SE1.

² These values are given with corrected flow rates for the MFC2 mass flow controller.

6.2.1.1 Operation at low density (0.052mgs^{-1} , 27.6W)

The grid currents measured with varying accelerator grid potential on SE1 and fixed potential on SE2 are displayed in Figure 6.3. The grid currents measured for the opposite case, with varying accelerator grid potential on SE2 but with SE1 fixed, are displayed in Figure 6.4. The results presented are the average of two values of the mean grid current measured at each potential, obtained from an increasing voltage ramp and decreasing voltage ramp. The tests were performed sequentially, with the thruster re-ignited between the variation of V_{ACC1} and V_{ACC2} . The difference in the magnitudes of the beam currents measured between the two cases is expected to be due to slight variations in the manual tuning of the capacitors of the two matching units to set the RF power and also due to thermal effects. Large errors on the averaged currents can be seen for voltages between -25V and -75V indicating hysteresis, thought to be the result of the thruster warming up over the duration of the voltage ramps. Electron backstreaming will also occur in this range of accelerator grid potential, which may add to the noise on the grid currents.

Beam profiles were taken on SE2 at various levels whilst V_{ACC1} or V_{ACC2} was varied. These are presented in Figures 6.5 and 6.6, and again are averages from measurements taken from an increasing and decreasing voltage ramp.

An increase in screen grid current and accelerator grid current with increasing magnitude of accelerator grid voltage above $|V_{ACC}|\sim 100\text{V}$ can be seen on the end of the thruster that is being varied, while I_{ACC} does not vary significantly for the opposing grid set over this range. The beam profiles taken of SE2 show that the extracted ion beam was affected by variation of V_{ACC2} but was unaffected by variation of V_{ACC1} on the other end of the thruster, indicating that independent control of the ion beams is possible by variation of the accelerator grid potentials. The slight reduction in beam current for the profiles at -150V and -250V compared to -55V and -75V when V_{ACC1} is varied is thought to be due to the thruster warming up over the duration of the test, increasing the resistance of the induction coils, and therefore, decreasing power coupling to the plasma as the test progressed.

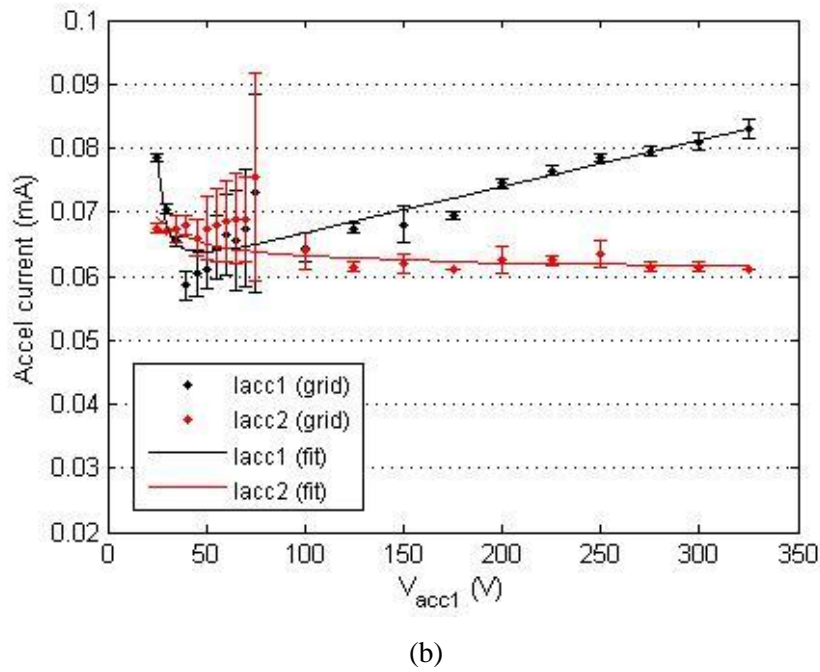
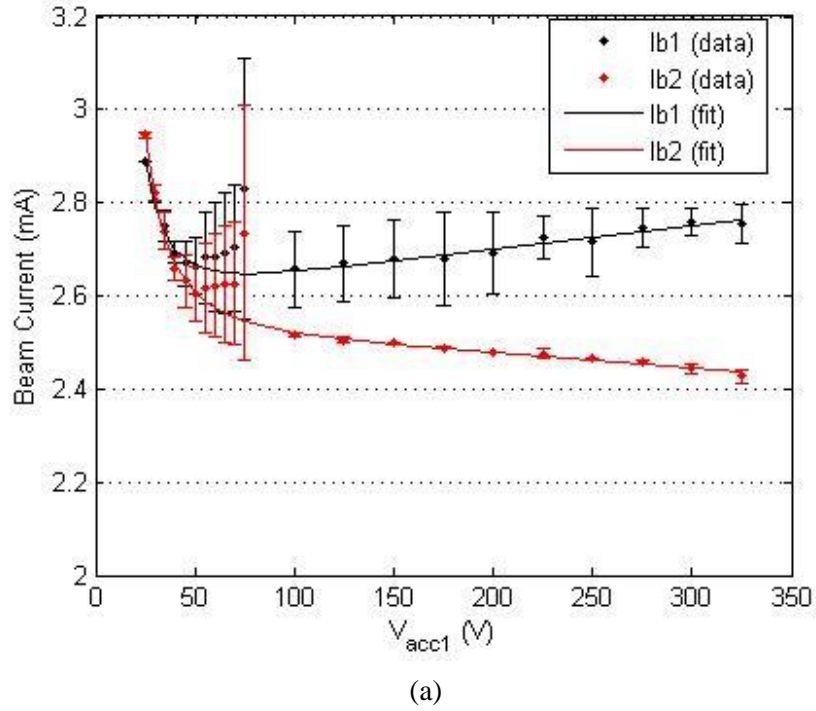
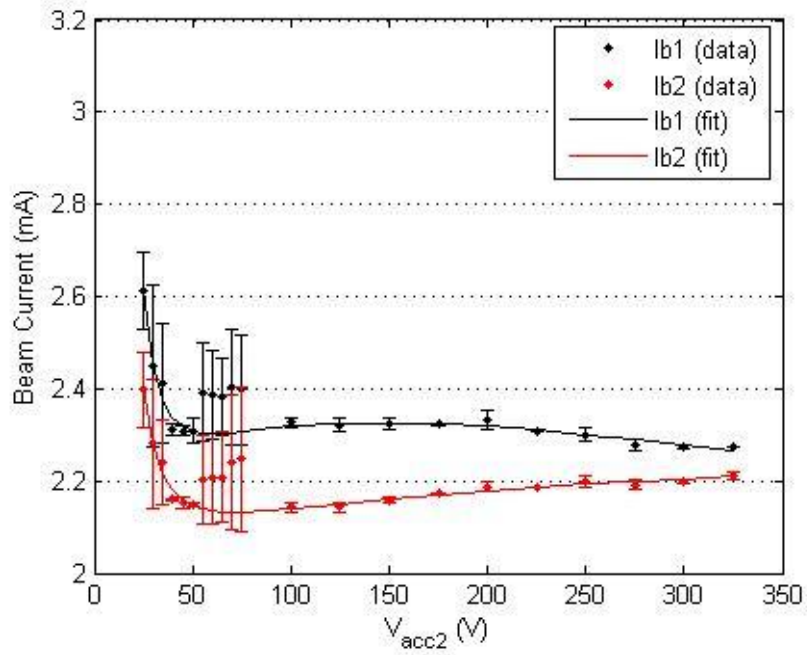
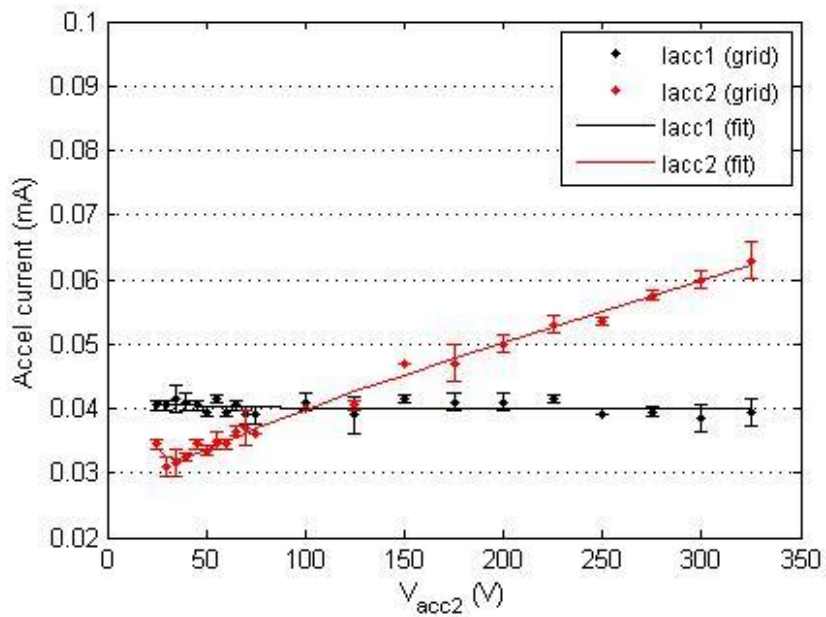


Figure 6.3. (a) Measured beam current for SE1 and SE2 during variation of V_{ACC1} (with $V_{ACC2} = -75V$, $V_b = 950V$, $\dot{m} = 0.052\text{mgs}^{-1}$, $P_{fw} = 27.6W$). (b) Measured accelerator grid currents for SE1 and SE2 during variation of V_{ACC1} .



(a)



(b)

Figure 6.4. (a) Measured beam current for SE1 and SE2 during variation of V_{ACC2} (with $V_{ACC1} = -75V$, $V_b = 950V$, $\dot{m} = 0.052mgs^{-1}$, $P_{fw} = 27.6W$).
 (b) Measured accelerator grid currents for SE1 and SE2 during variation of V_{ACC2}

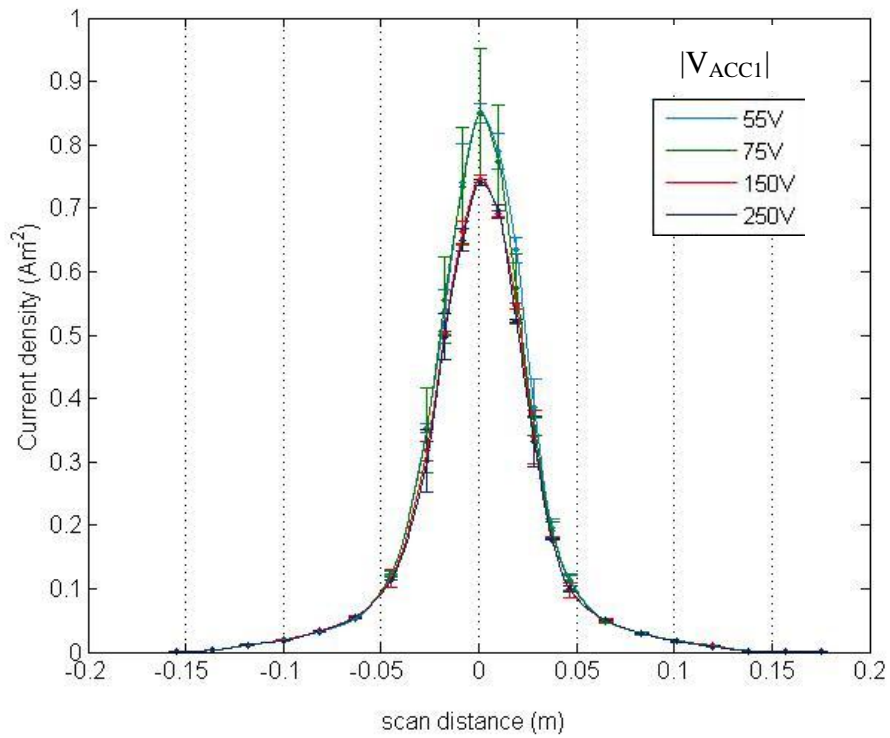


Figure 6.5. Beam profiles of the ion beam extracted from SE2 during variation of the negative accelerator grid potential V_{ACC1} (with $V_{ACC2} = -75V$, $V_b = 950V$, $\dot{m} = 0.052\text{mgs}^{-1}$, $P_{fw} = 27.6W$).

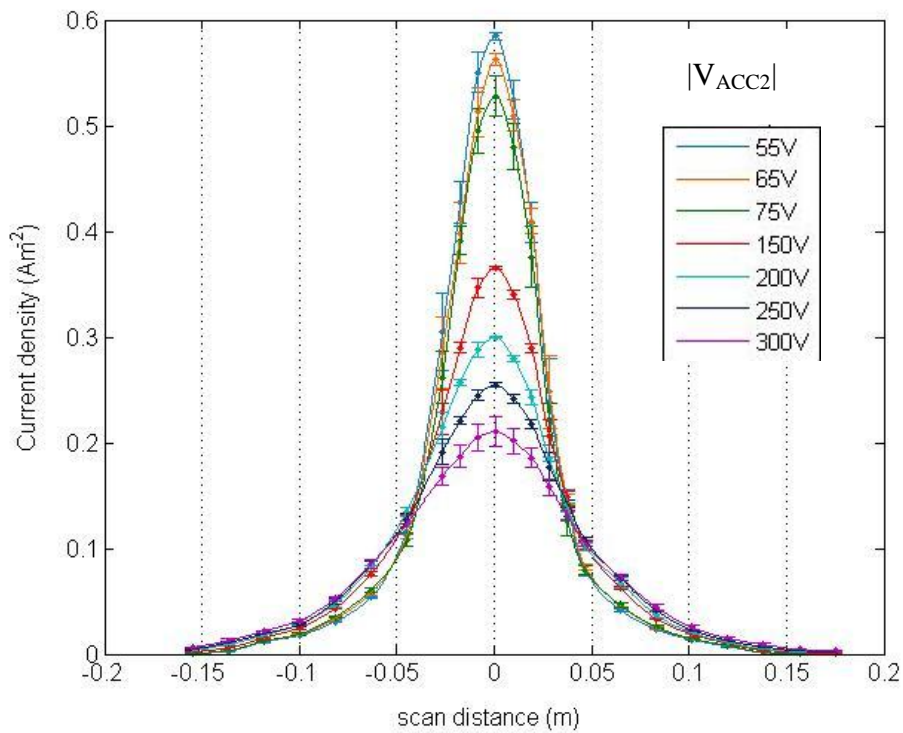


Figure 6.6. Beam profiles of the ion beam extracted from SE2 during variation of the negative accelerator grid potential V_{ACC2} (with $V_{ACC1} = -75V$, $V_b = 950V$, $\dot{m} = 0.052\text{mgs}^{-1}$, $P_{fw} = 27.6W$).

At more positive accelerator grid potentials above $-75V$, a sharp increase in screen grid current can be seen for both grid sets. This indicates the occurrence of electron backstreaming where the negative accelerator grid potential is insufficient to repel electrons external to the discharge chamber; the electrons can therefore backstream through the grid apertures and be accelerated axially through the plasma, striking the opposing screen grid resulting in an increased grid current. The screen grid current is used to monitor beam current in the MiDGIT thruster; electron backstreaming will therefore not permit the two beam currents to be resolved. It must also be avoided to prevent localized heating and possible overloading of the beam supply. This configuration of the MiDGIT thruster however provides a unique method for measuring the electron backstreaming limit of the extraction grids. Plots of the ratio of accelerator grid current to beam current for the MiDGIT breadboard thruster are provided in Figures 6.7 and 6.8 to provide a clearer indication of the onset of electron backstreaming.

The accelerator drain ratio (I_{ACC}/I_b) falls sharply for the extraction grid set that is not being throttled due to the increasing contribution of backstreaming electrons to the screen grid current as the accelerator grid potential of the opposite grid set becomes more positive than its electron backstreaming limit. This is most clearly seen in Figure 6.7 when V_{ACC1} is varied. As the extraction voltage for SE2 is not altered, and the plasma density in the vicinity of the screen grid of SE2 should not vary significantly, the geometry of the plasma sheath upstream of the screen grid on SE2 should not vary either. The ion beam current actually extracted from SE2 should therefore remain unaffected, as is observed in the beam profiles of SE2 (shown in Figure 6.5) and the relatively constant accelerator grid current (I_{ACC2}). As V_{ACC1} becomes more positive, the sheath upstream of each screen grid aperture on SE1 is expected to become flatter, resulting in ions directly impinging on the accelerator grid [71]. The accelerator drain ratio for SE1 therefore rises sharply, as observed in Figure 6.7. For this operating point at relatively low plasma density, the accelerator drain ratios for SE1 and SE2 start to vary significantly below $|V_{ACC}| \sim 60V$. Due to the large variations in the measured grid currents in this region however, the electron backstreaming limit is estimated to be $|V_{ebs}| \approx (60 \pm 10)V$. The accelerator grid voltage at the onset of electron backstreaming predicted for the MiDGIT breadboard grids from Equation 2.43 is $|V_{ebs}| = 84.4V$.

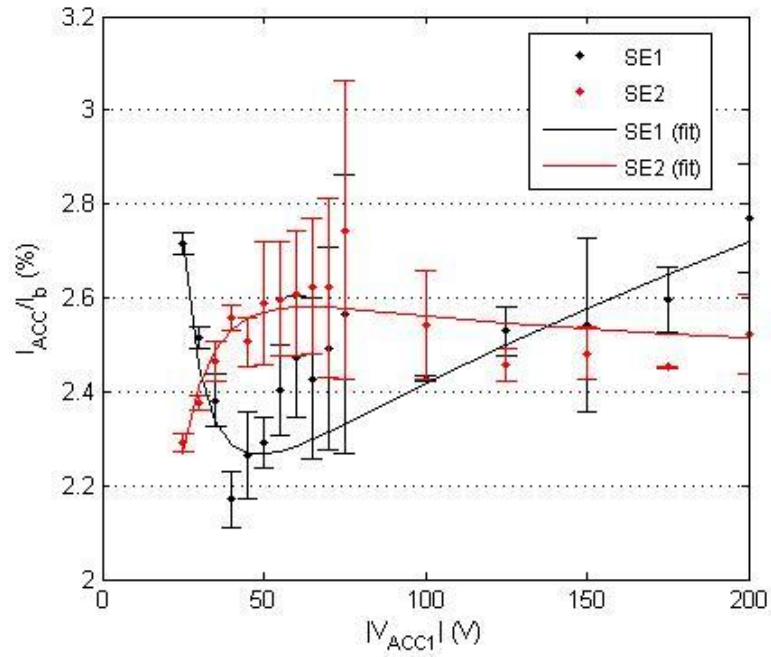


Figure 6.7. Accelerator drain ratio (I_{ACC}/I_b) for SE1 and SE2 during V_{ACC1} variation at 0.052mgs^{-1} , 27.6W.

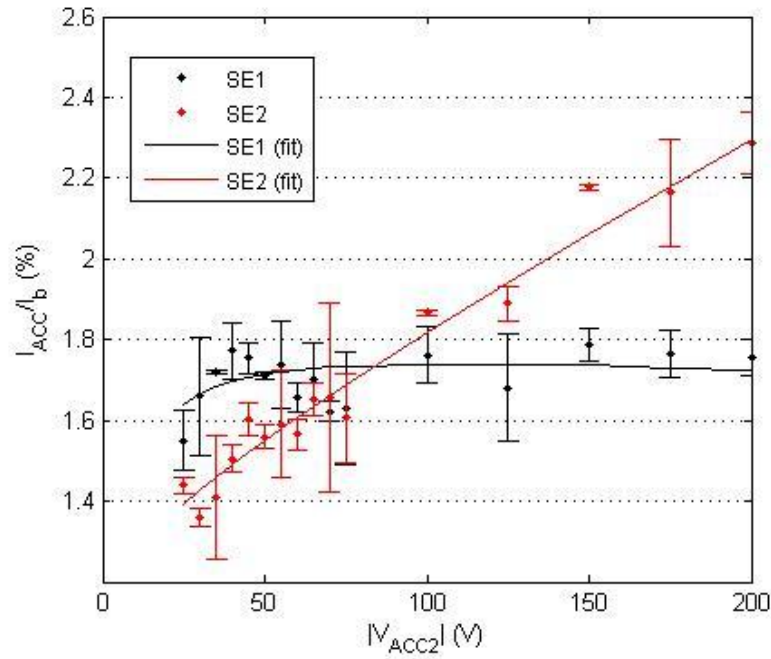


Figure 6.8. Accelerator drain ratio (I_{ACC}/I_b) for SE1 and SE2 during V_{ACC2} variation at 0.052mgs^{-1} , 27.6W.

As previously stated, at large negative accelerator grid potentials greater than $|V_{ACC}| \sim 100 \text{ V}$, a positive increase in screen grid and accelerator grid current is observed for the grid set that is being varied. Above the electron backstreaming limit, the sheath upstream of the screen grid will move away from the surface of the grid further into the discharge chamber and will become more convex as the accelerator grid potential becomes more negative [71]. The ion beam current extracted from the plasma is expected to increase due to the greater sheath surface area, however, the more convex sheath may also lead to over-focussing of the ion beamlets through the grid apertures resulting in direct ion impingement on the accelerator grid due to cross-over [47, 71]. The ion beam extracted from the thruster is also expected to become more diffuse [71]. The difference between the screen grid and accelerator grid currents should provide the approximate current of the extracted ion beam that provides thrust by accounting for ions lost from the beam which impinge on the accelerator grid.

Beam current calculated from the beam profiles of SE2 (as described in section 5.5) are compared with values of the beam current calculated from the difference in screen and accelerator grid currents in Figure 6.9. The two estimates of beam current for SE2 during V_{ACC1} variation agree well, with the SE1 and SE2 beam currents suggesting an increasing net thrust out of SE1. The beam currents for SE2 do not agree for the V_{ACC2} case; a large decrease in beam current on SE2 is indicated by the beam profile estimates, whereas the beam current calculated from the grid currents indicates a slight increase in beam current for SE2 with increasingly negative accelerator grid potential. The beam profiles obtained at $V_{ACC2} = -150\text{V}$ and -300V (shown in Figure 6.10) indicate that the extracted ion beam is becoming more diffuse with increasing $|V_{ACC}|$. Facility effects, such as CEX collisions between beam ions and background neutrals, will also influence the profile of the extracted ion beam. It could be proposed that as V_{ACC2} becomes increasingly negative, a greater number of beam ions are being scattered to large divergence angles and thus are not being detected by the beam probe. Rotation of the beam probe between $\pm 45^\circ$ was deemed sufficient to detect the majority of highly divergent beam ions, but repetition of the beam probe measurements to larger angles would be required to verify this.

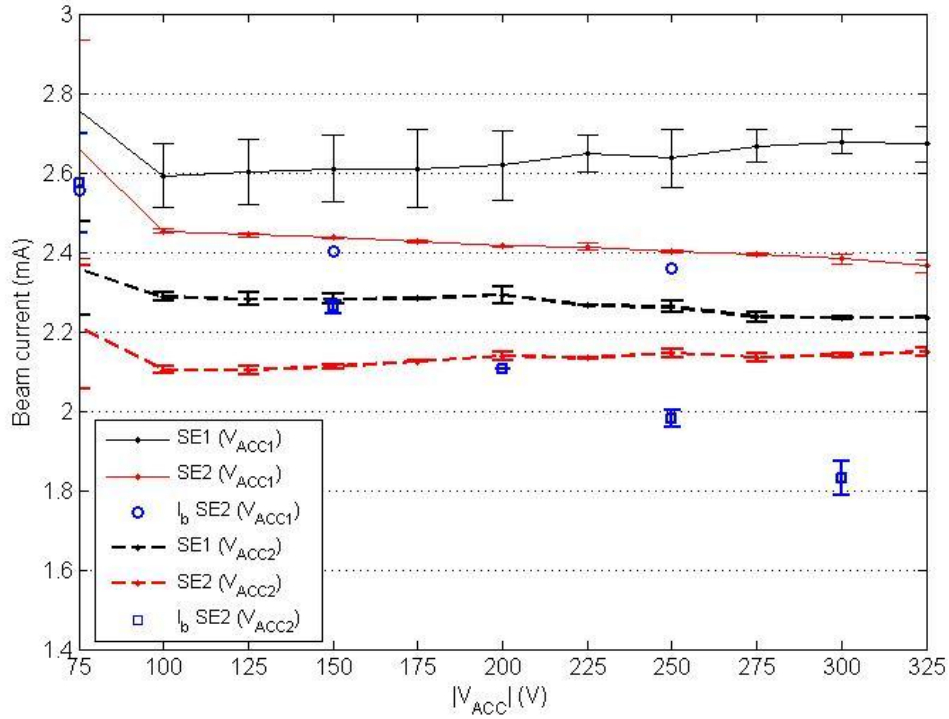


Figure 6.9. Beam current determined from measured grid currents for SE1 (black) and SE2 (red) whilst either V_{ACC1} (solid line) or V_{ACC2} (dashed line) is varied. Also presented is the beam current determined from beam profiles for SE2 during variation of V_{ACC1} (blue circles) or V_{ACC2} (blue squares). Good agreement can be seen during variation of V_{ACC1} but not for V_{ACC2} .

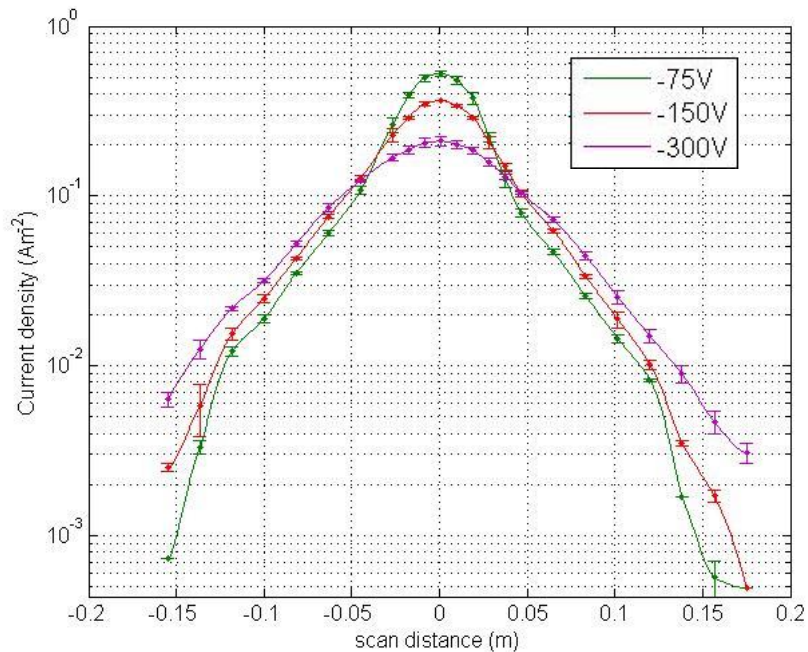


Figure 6.10. Log plots of the beam profiles of SE2 when $V_{ACC2} = -75V, -150V$ and $-300V$ (with $V_{ACC1} = -75V, V_b = 950V, \dot{m} = 0.052\text{mg s}^{-1}, P_{fw} = 27.6W$). The ion beam can be seen to become more diffuse as V_{ACC2} becomes increasingly negative.

Assuming the beam currents calculated from the grid currents are correct, variation of the accelerator grid potential on SE1 was determined to provide an increasing net thrust out of SE1 between $4\mu\text{N}$ - $15\mu\text{N}$ with increasing $|V_{ACC1}|$ (as shown in Figure 6.11). Variation of the accelerator grid potential on SE2 was determined to provide a decreasing net thrust out of SE1 from $10\mu\text{N}$ to $4\mu\text{N}$ with increasing $|V_{ACC2}|$; the net thrust out of SE1 being due to the higher beam current on SE1 compared to SE2.

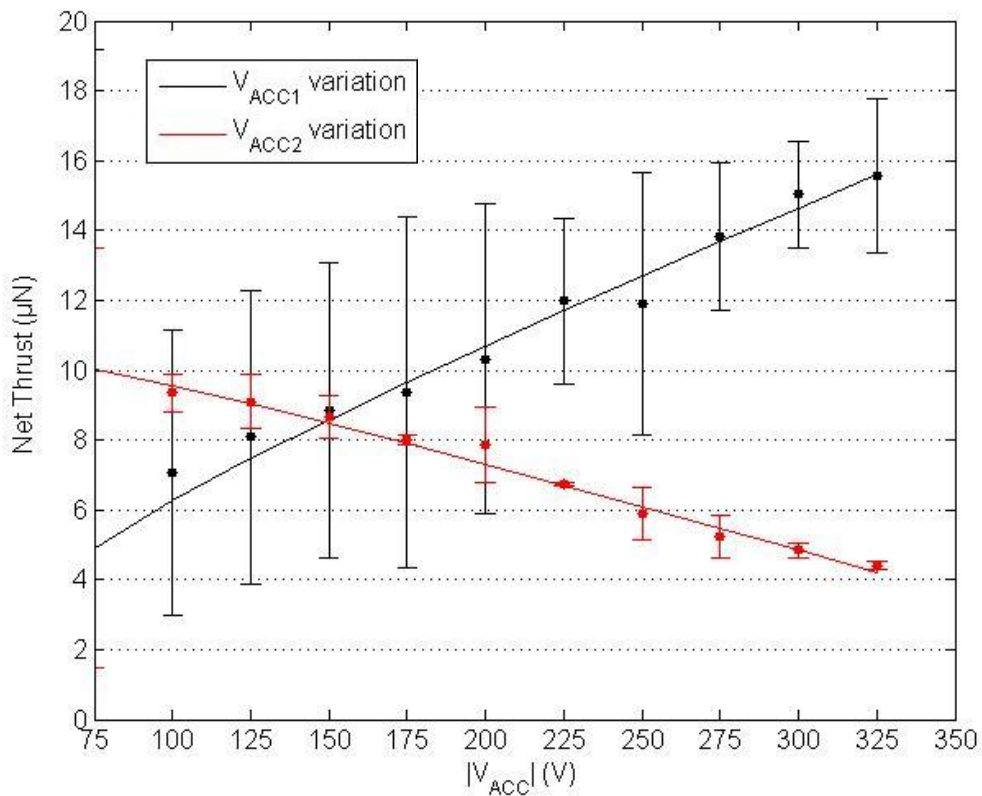


Figure 6.11. Net thrust out of SE1 determined from the measured grid currents for SE1 and SE2 during variation of the accelerator grid potential on either SE1 or SE2 at 0.052mgs^{-1} , 27.6W . (The beam current of SE1 was higher than SE2 in both cases, hence net thrust out of SE1).

6.2.1.2 Operation at high density (0.058mgs^{-1} , 38.1W)

The grid currents measured for varying accelerator grid potential at higher plasma density conditions (0.058mgs^{-1} , 38.1W) are presented in Figures 6.12 and 6.13. The corresponding beam profiles are presented in Figures 6.14 and 6.15.

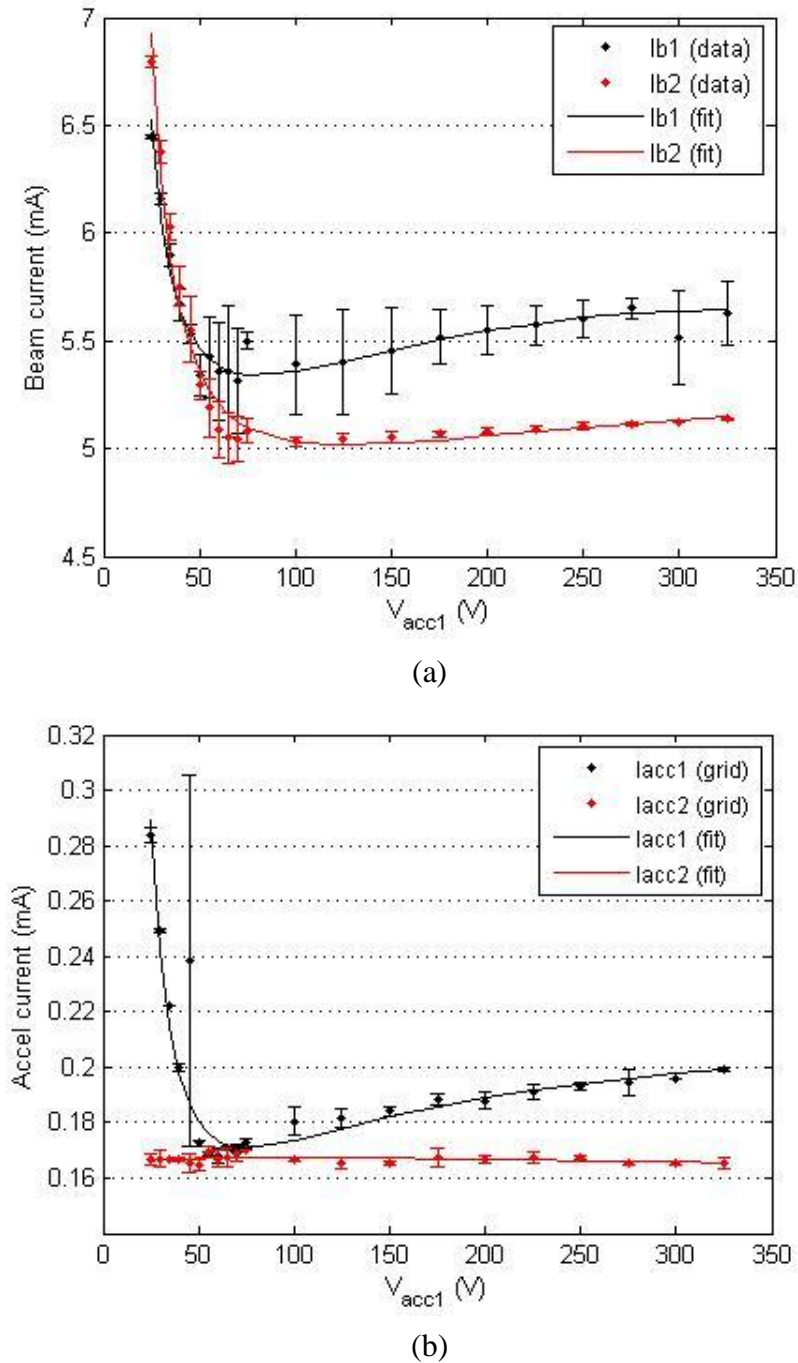
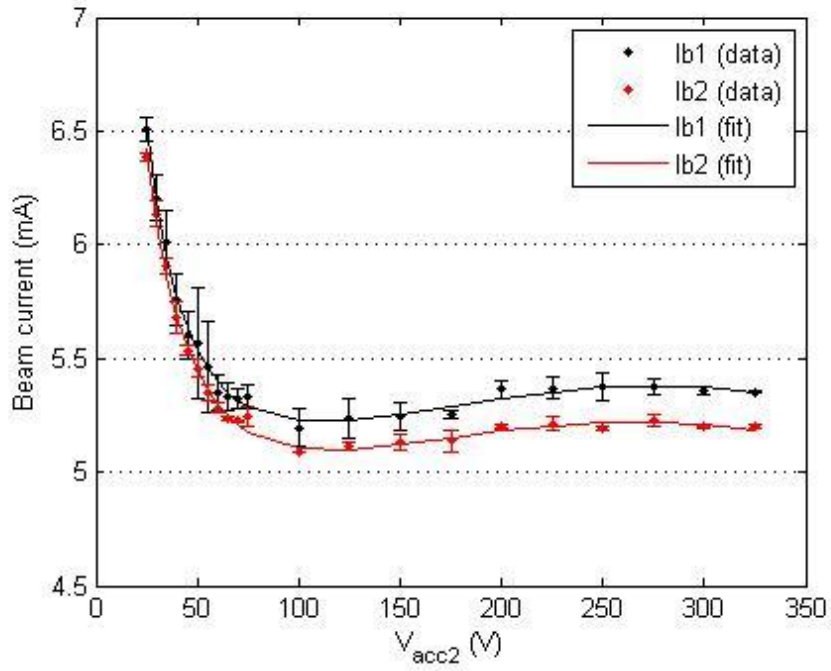
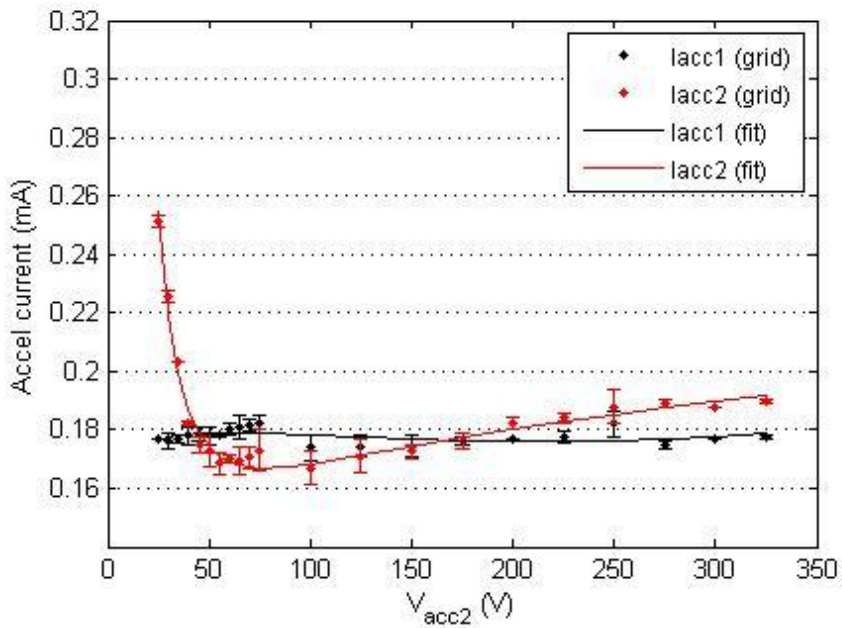


Figure 6.12. (a) Measured beam current for SE1 and SE2 during variation of V_{ACC1} (with $V_{\text{ACC2}} = -75\text{V}$, $V_b = 950\text{V}$, $\dot{m} = 0.058\text{mgs}^{-1}$, $P_{\text{fw}} = 38.1\text{W}$). (b) Measured accelerator grid currents for SE1 and SE2 during variation of V_{ACC1} .



(a)



(b)

Figure 6.13. (a) Measured beam current for SE1 and SE2 during variation of V_{ACC2} (with $V_{ACC1} = -75V$, $V_b = 950V$, $\dot{m} = 0.058\text{mgs}^{-1}$, $P_{fw} = 38.1W$).
 (b) Measured accelerator grid currents for SE1 and SE2 during variation of V_{ACC2} .

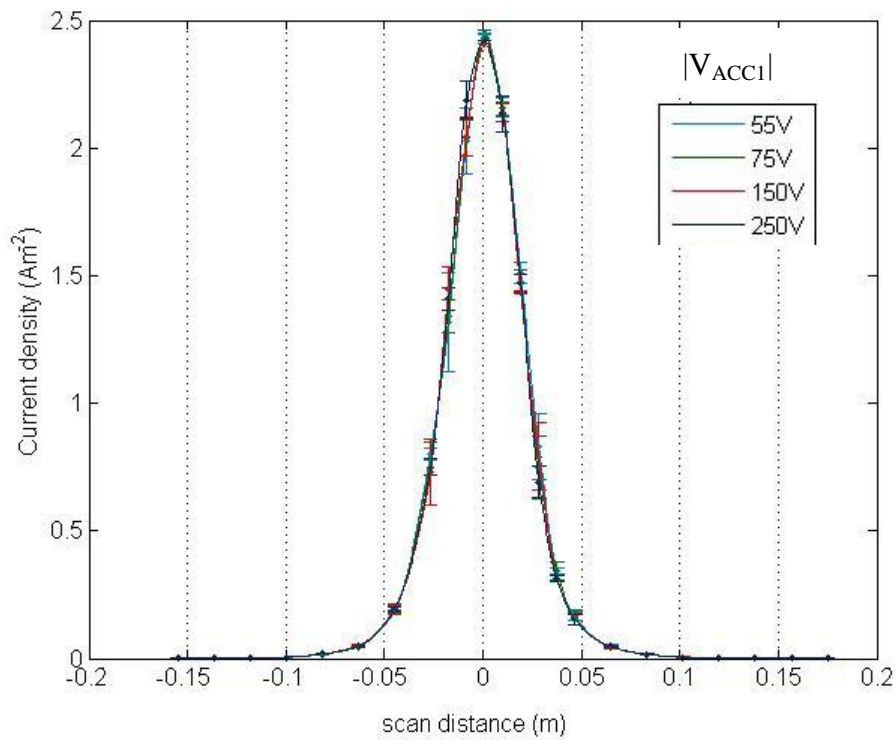


Figure 6.14. Beam profiles of the ion beam extracted from SE2 during variation of the negative accelerator grid potential V_{ACC1} (with $V_{ACC2} = -75V$, $V_b = 950V$, $\dot{m} = 0.058\text{mgs}^{-1}$, $P_{fw} = 38.1W$).

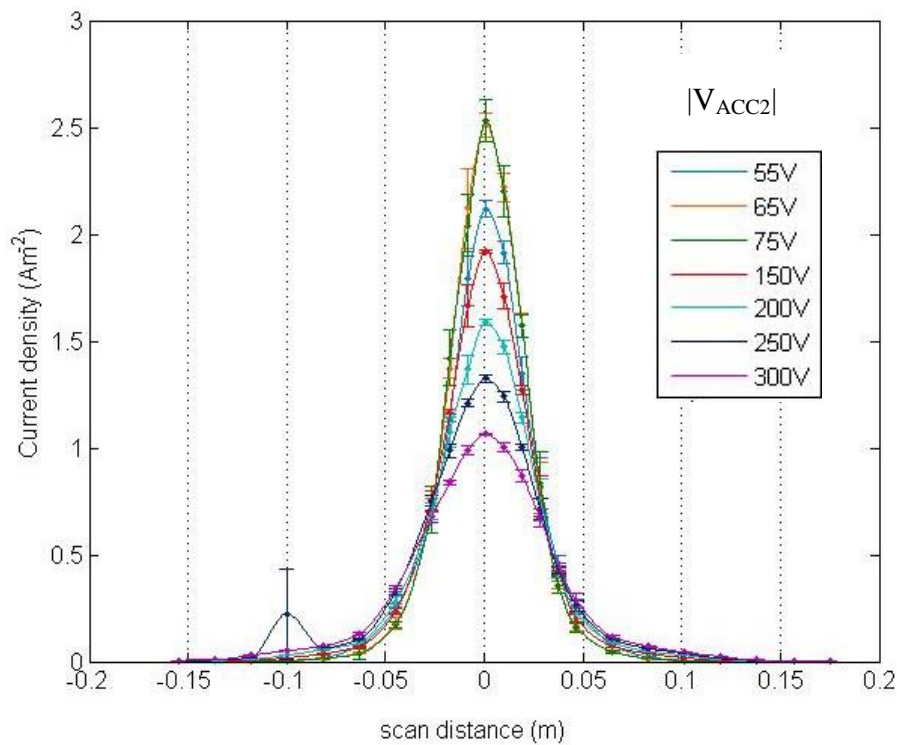


Figure 6.15. Beam profiles of the ion beam extracted from SE2 during variation of the negative accelerator grid potential V_{ACC2} (with $V_{ACC1} = -75V$, $V_b = 950V$, $\dot{m} = 0.058\text{mgs}^{-1}$, $P_{fw} = 38.1W$).

Again, the extracted ion beam from SE2 was observed to be unaffected by variation of the accelerator grid potential on SE1. The beam profiles taken of SE2 while V_{ACC1} was varied (displayed in Figure 6.14) show good agreement.

Plots of the accelerator drain ratio provide a clearer indication of electron backstreaming than for the results obtained at the lower density operating point. The accelerator drain ratios indicate a significant variation below $|V_{ACC}| \sim 70V$ in this case.

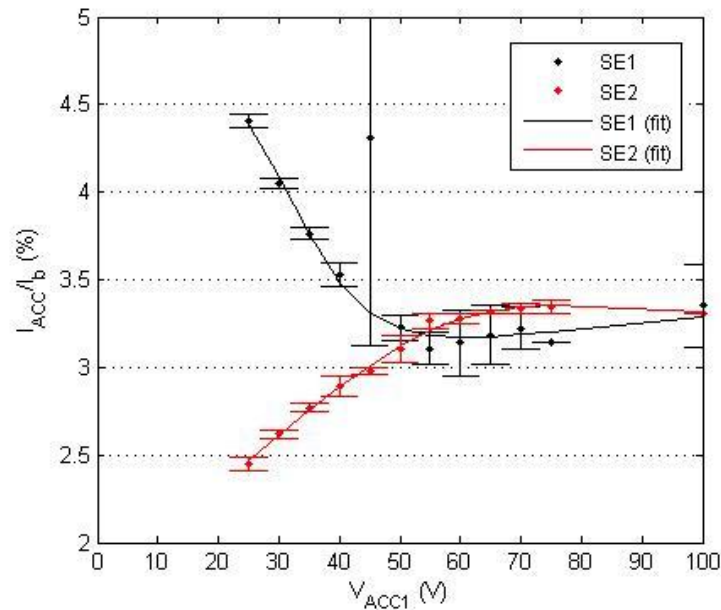


Figure 6.16. Accelerator drain ratio (I_{ACC}/I_b) for SE1 and SE2 during V_{ACC1} variation at 0.058mgs^{-1} , 38.1W.

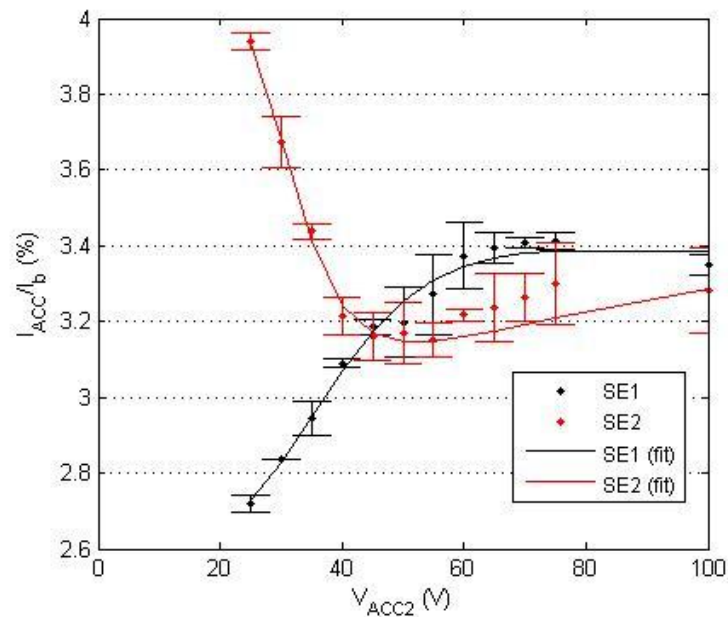


Figure 6.17. Accelerator drain ratio (I_{ACC}/I_b) for SE1 and SE2 during V_{ACC2} variation at 0.058mgs^{-1} , 38.1W.

The beam currents calculated from the beam profiles obtained of SE2 do not agree well with the beam currents calculated from the screen and accelerator grid currents of SE2, as displayed in Figure 6.18. The beam profiles estimate a much higher beam current for SE2 than measured from the grid currents. Facility effects due to the extraction of two ion beams within the relatively small loadlock vacuum chamber may have affected the beam probe measurements, with greater influence obviously at higher beam currents. As for the lower plasma density operating point, a large decrease in extracted ion beam current on SE2 is indicated by the beam profiles with increasingly negative V_{ACC2} . Beam profiles plotted on a logarithmic scale (displayed in Figure 6.19) indicate that the ion beam becomes more diffuse, but in this case a distinct two-tier profile is observed, which may be the effect of increased CEX collisions due to higher neutral pressure and also due to over-focussing of the ion beamlets (and therefore cross-over of the beam ions) affecting the beam profile.

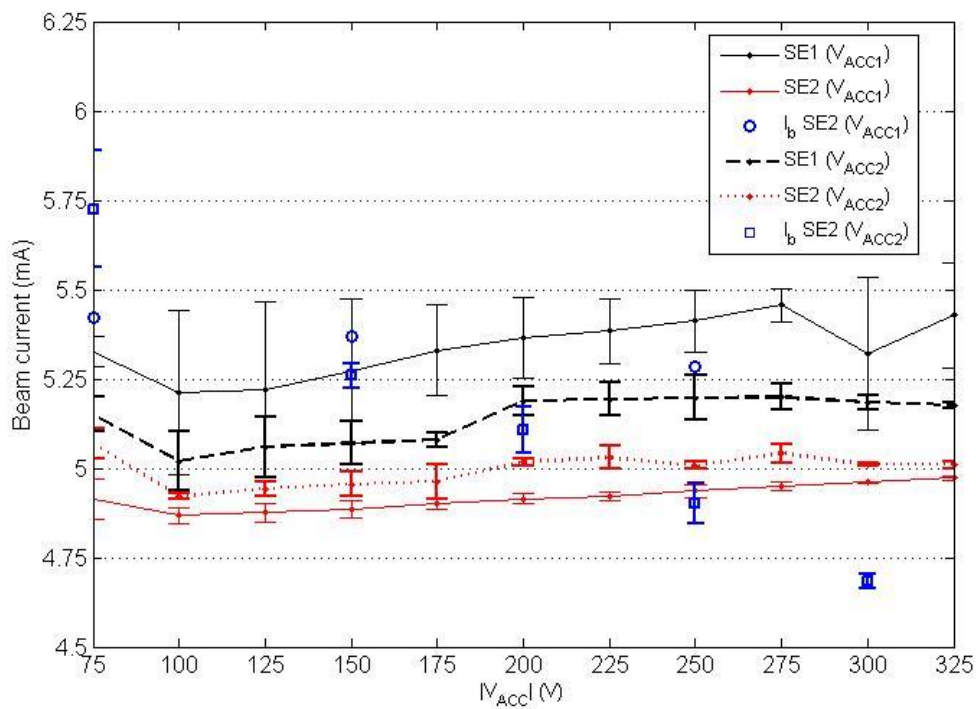


Figure 6.18. Beam current determined from measured grid currents for SE1 (black) and SE2 (red) whilst either V_{ACC1} (solid line) or V_{ACC2} (dashed line) is varied. Also presented is the beam current determined from beam profiles for SE2 during variation of V_{ACC1} (blue circles) or V_{ACC2} (blue squares). For this case at higher plasma density, the beam current determined from the beam profiles is not in agreement with that determined from the grid currents.

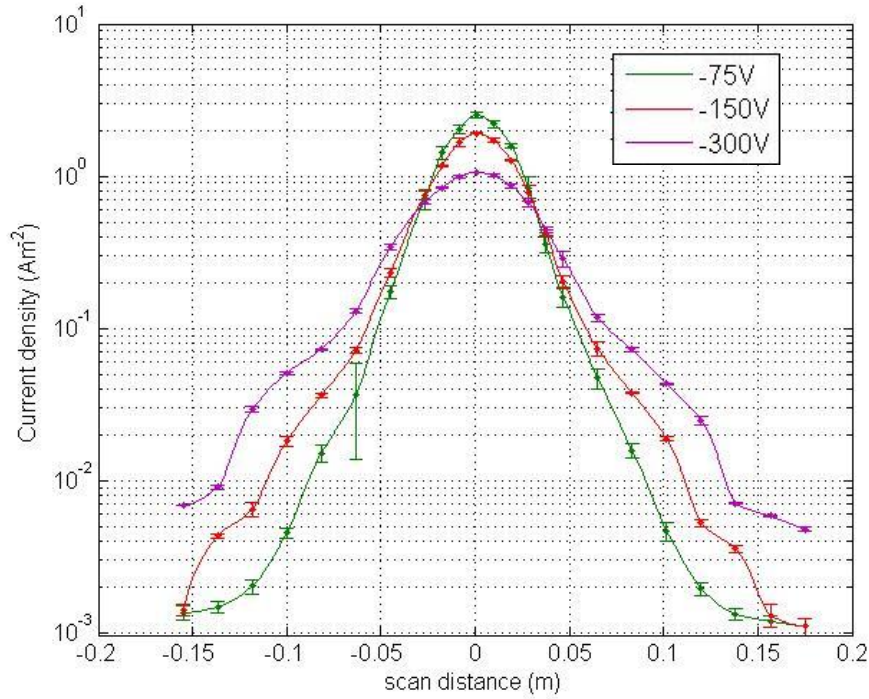


Figure 6.19. Log plots of the beam profiles of SE2 when $V_{ACC2} = -75V$, $-150V$ and $-300V$ (with $V_{ACC1} = -75V$, $V_b = 950V$, $\dot{m} = 0.058\text{mgs}^{-1}$, $P_{fw} = 38.1W$). The beam profiles display a two-tier distribution due to the greater amount of CEX collisions affecting the beam than for the lower plasma density case at 0.052mgs^{-1} , $27.6W$.

For operation at 0.058 mgs^{-1} , $38.1W$ (relatively high plasma density), the net thrust calculated from the beam currents indicates that an increasing net thrust out of SE1 between $18\mu\text{N}$ - $25\mu\text{N}$ was achieved by variation of V_{ACC1} , while a lower net thrust of $4\mu\text{N}$ - $9\mu\text{N}$ also out of SE1 was achieved by variation of V_{ACC2} . This is displayed in Figure 6.20.

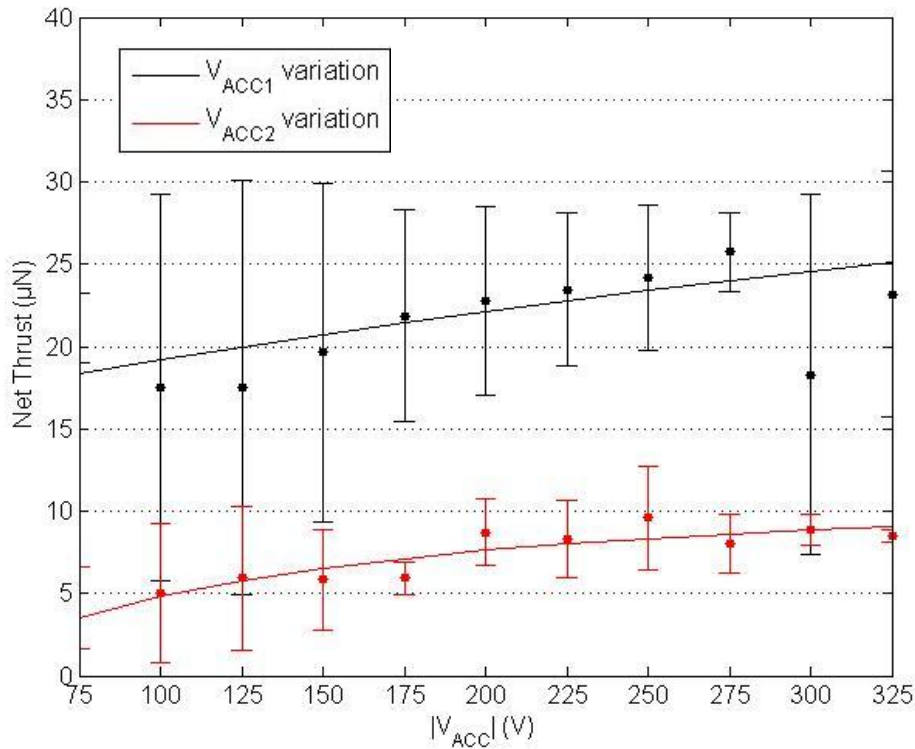


Figure 6.20. Net thrust out of SE1 determined from the measured grid currents for SE1 and SE2 during variation of the accelerator grid potential on either SE1 or SE2 at 0.058mgs^{-1} , 38.1W . (The beam current of SE1 was higher than SE2 in both cases, hence net thrust out of SE1).

6.2.1.3 Summary

The tests performed on the MiDGIT breadboard thruster investigating differential ion beam control by variation of the accelerator grid potential indicate that independent control of each ion beam is possible by this method. The onset of electron backstreaming was observed to occur in the vicinity of $V_{ACC} = -70\text{V}$, in relatively good agreement with the predicted electron backstreaming limit of -84.4V . In general, a positive increase in screen grid current and accelerator grid current with increasingly negative accelerator grid potential was observed for the grid set being varied. Beam profiles displayed some de-focussing of the extracted ion beam with increasing $|V_{ACC}|$. These results support the theory that the plasma sheath upstream of the screen grid apertures becomes more convex with increasingly negative V_{ACC} , as observed in the simulations of Zhong et al [71]. Net thrust calculated from the difference in beam currents (determined from the grid currents) on each end of the thruster was not found to be significant, equating to a net thrust between approximately $4\mu\text{N}$ - $25\mu\text{N}$ out of SE1 for variation of both V_{ACC1} and V_{ACC2} . This was due to a higher screen grid current measured for

SE1 compared to SE2 for all operating points, suggesting that power coupling between the induction coil and plasma on SE1 was greater than for SE2. It is expected that if the plasma conditions in the vicinity of the screen grids for SE1 and SE2 can be matched, a net thrust out of either end would be possible. Though the results suggest a fine thrust resolution could be achieved by variation of the accelerator grid potential, the results indicate that differential control by this method alone will not be able to achieve the 1 μ N-150 μ N thrust range required for fine thrust mode. Further consideration to the design of the extraction grids to determine effects of cross-over impingement on the accelerator grid would be needed to identify the maximum achievable thrust range. More importantly, the indicated (net) thrust up to 25 μ N was obtained by increasing the accelerator grid voltage to -325V; the accelerator grid voltage should ideally be kept to a minimum, typically of the order -100V, to minimize erosion of the accelerator grid by CEX ions [93].

6.2.2 VARIATION OF RF POWER

Power coupling between the coil and plasma of an inductive discharge is mainly governed by the RF current in the induction coil and the conductivity of the plasma due to the skin effect. The power absorbed by an inductive plasma can be expressed by:

$$P_{abs} = \frac{1}{2} |I_{RF}|^2 N^2 R_p \quad (6.1)$$

where N is the number of turns of the induction coil and R_p is the equivalent plasma resistance [46]. Following analysis of the tests performed on differential control by variation of the accelerator grid potential, it was proposed by the author that varying the power delivered to the plasma on each end of the MiDGIT thruster by controlling the RF current in each induction coil could lead to a higher plasma density on one end compared to the other and ultimately a net thrust out of that end.

6.2.2.1 Discharge Model

A 2D cylindrical, axisymmetric discharge model for the MiDGIT thruster was developed using the plasma simulation module of the commercial software package COMSOL Multiphysics to provide an insight into power coupling between two induction coils and a common plasma. Details of the model developed and assumptions involved are given in

Appendix B. COMSOL Multiphysics is a finite element analysis software package; the plasma module couples a two-term Boltzmann equation solver and reduced Maxwell field equations for the development of self-consistent numerical models of low temperature plasmas [94]. The validity of fluid assumptions in plasma models is governed by the mean free paths of the plasma species; the mean free paths must be considerably smaller than the characteristic length of the discharge (typically taken to be the radius of the discharge chamber) for fluid models to be able to provide accurate results comparable to experimental observations [51, 95]. Fluid models are typically valid for Knudsen numbers ($Kn = \lambda/L \leq 0.1$). The low operating pressure of the MiDGIT thruster ($< 5\text{mTorr}$) means that the electron collision mean free path can be several orders of magnitude greater than the dimensions of the discharge chamber. Therefore, fluid assumptions of the discharge model developed with COMSOL Multiphysics may not strictly be valid for the discharge conditions of the MiDGIT thruster. However, the model was developed not with the intention to provide accurate, quantitative information on plasma parameters for the MiDGIT thruster, but to provide an insight into the effect of varying the relative RF current in two induction coils on a plasma discharge common to both coils. It is noted that Particle-in-Cell Monte-Carlo-Collision (PIC MCC) models and hybrid models (combining both fluid assumptions and PIC-MCC) are more suited to modelling low pressure inductive discharges and are able to accurately capture non-local electron kinetic effects, but these models are computationally demanding and a PIC-MCC or hybrid discharge model of the MiDGIT thruster is beyond the scope of this work.

A xenon plasma discharge was simulated using COMSOL Multiphysics based on the geometry of the MiDGIT breadboard thruster with $v_{rf} = 5.25\text{ MHz}$. Simulations did not converge for neutral pressures below 20mTorr and RF coil currents of 20A (in each coil). This pressure is typically a factor of 5 times greater than the pressure expected for the MiDGIT thruster. The mean electron energy is a function of the reduced electric field strength ($E/P \equiv E/N$) and therefore, so too is the reduced electron mobility and the reduced electron diffusion coefficient [96, 97]. The same general distribution of plasma might therefore be expected for a plasma at lower pressure with the same reduced field (E/N) and electron temperature. The fluid equations and solver of the COMSOL Multiphysics plasma module has been found to reliably model plasma discharges with reduced electric field strengths up to 300 Townsend³ [98]. Above this value, the reliability of the results may be questionable and require validation against experimental measurements.

³ 1Td = 10^{-21} Vm^2

Plots of magnetic flux density and the induced electric field are displayed in Figures 6.21 and 6.22 for a discharge modeled with a relatively large spacing between the coils. The separation of the two induction coils creates a region of lower electromagnetic energy density between the coils, with the instantaneous magnetic field presenting a magnetic bottle configuration as can be seen in Figure 6.21. Resistive heating within the plasma, which defines regions of power deposition in the plasma, is displayed in Figure 6.23. Power can be seen to be deposited in a layer directly underneath each coil, governed by the skin depth.

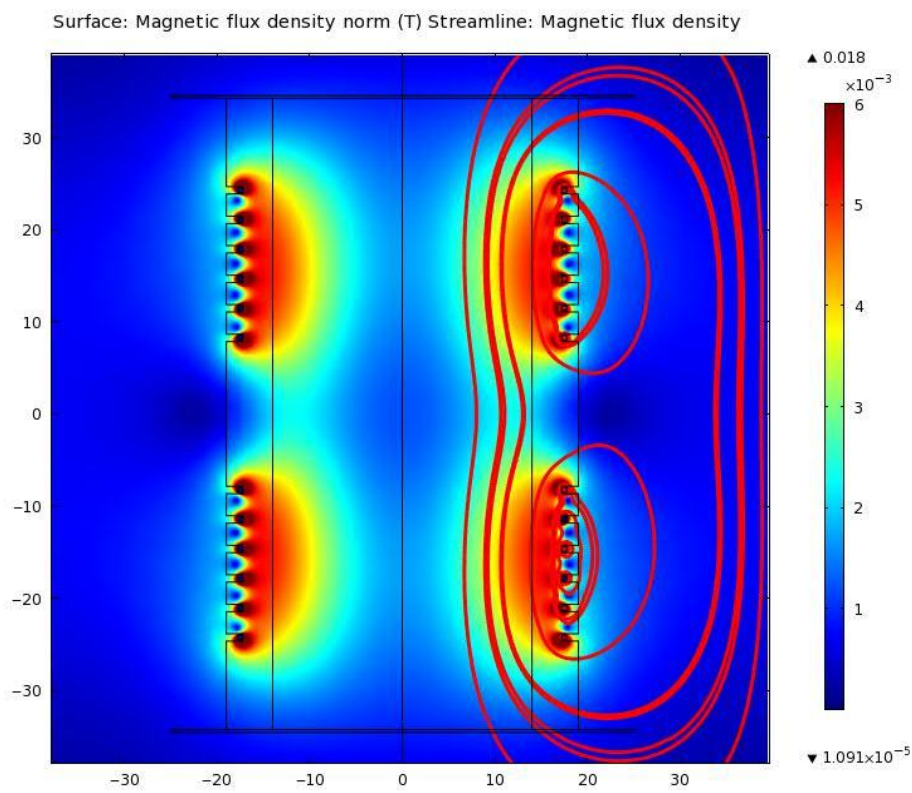


Figure 6.21. Magnetic flux density for two six-turn induction coils separated by 16mm.
($I_{RF} = 20A$, $\nu_{rf} = 5.25MHz$)

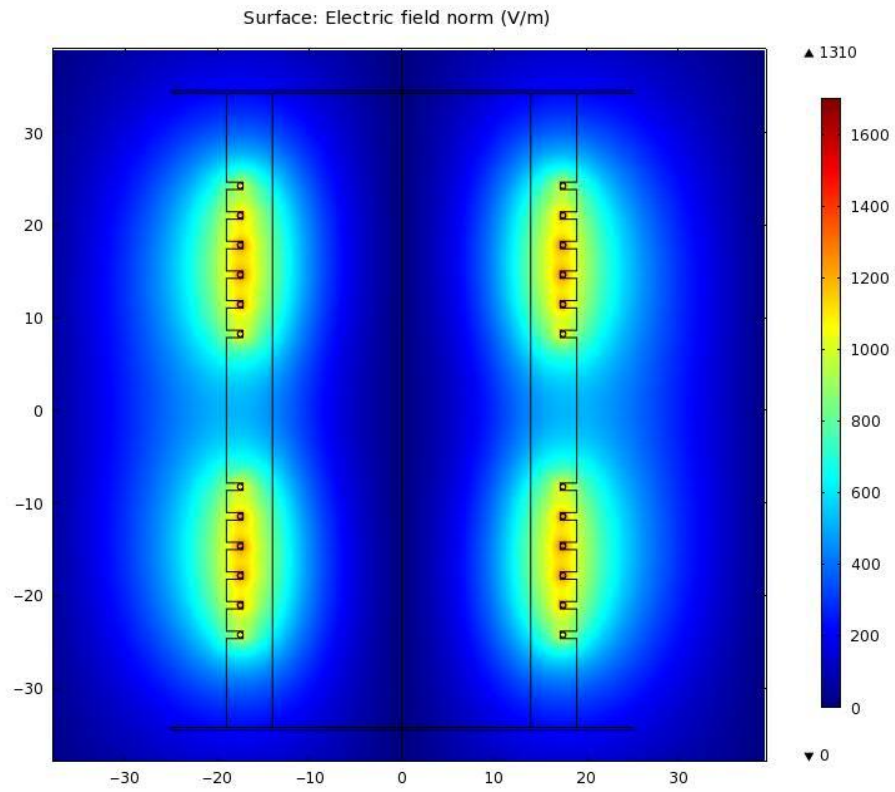


Figure 6.22. Electric field distribution for two six-turn induction coils separated by 16mm.
($I_{RF} = 20A$, $\nu_{rf} = 5.25MHz$)

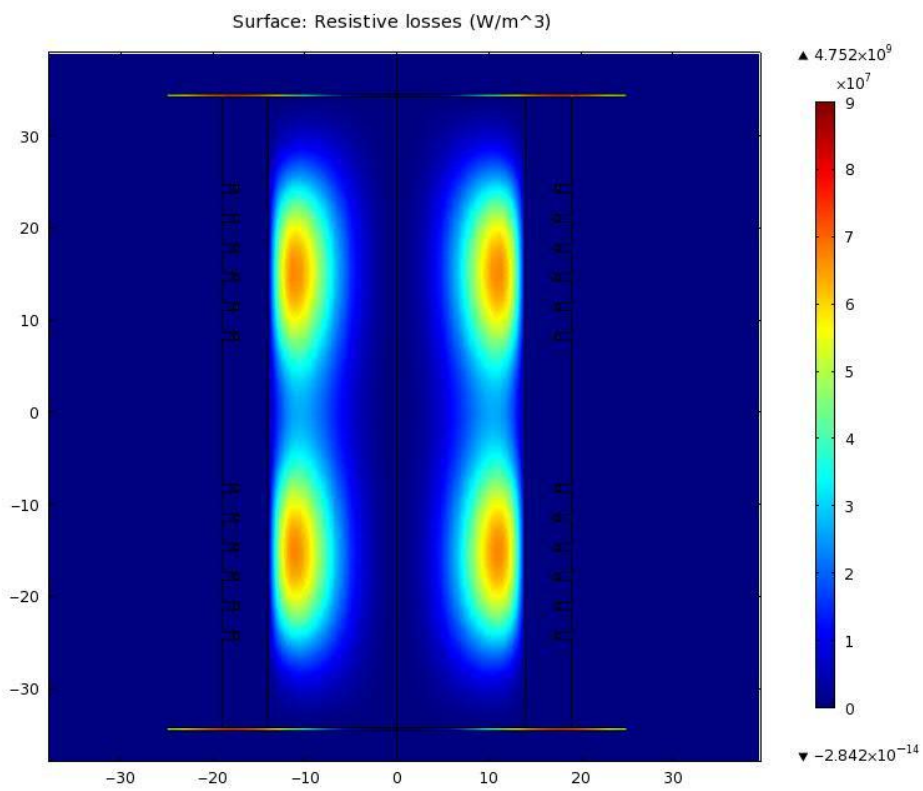


Figure 6.23. Resistive losses indicating power deposition within a Xenon discharge from two induction coils (neutral pressure, $P_n = 20mTorr$, current per coil, $I_{RF} = 20A$, $\nu_{rf} = 5.25MHz$).

Two dimensional plots of electron temperature, plasma density and plasma potential are given in Figures 6.24 – 6.26. The electron temperature is shown to be highest underneath the coils, correlated with the regions of highest power deposition, as would be expected. The plasma density and plasma potential are shown to be reasonably homogenous, peaking along the centre of the discharge chamber and falling off towards the walls and grids. The ions in the plasma are unconstrained by the RF magnetic field, and therefore, are accelerated from the plasma potential at the centre of the discharge across the pre-sheath to the edge of the plasma, where they are then lost across the sheath to the walls. The plot of ion flux displayed in Figure 6.27 shows that ions are predominantly lost radially to the walls of the discharge chamber. Lower plasma density is observed at the corners of the discharge chamber due to both the axial and radial acceleration of ions to the walls and grid surface, as was shown in the model by Tsay [25]. The electron temperature and plasma density are of the order $T_e \sim 5\text{eV}$ and $n_e \sim 10^{18} \text{ m}^{-3}$, higher than that expected for a 3cm diameter RF ion thruster ($T_e \sim 2\text{-}4\text{eV}$, $n_e \sim 10^{17} \text{ m}^{-3}$) [24] due to the high neutral density and coil current of the simulated case.

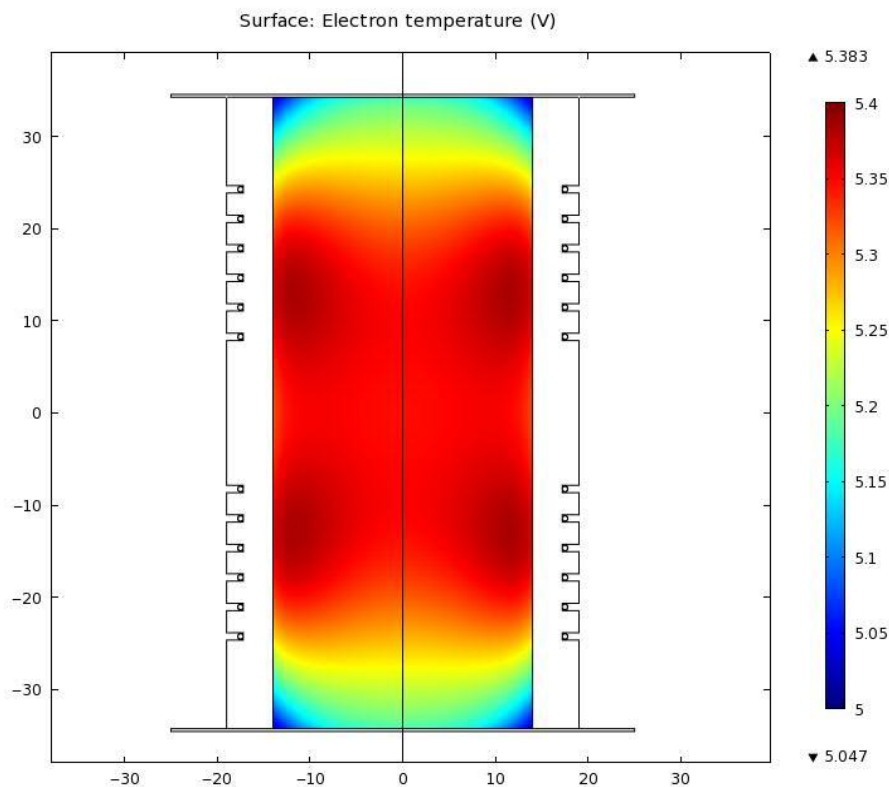


Figure 6.24. Electron temperature within a cylindrical xenon discharge. (neutral pressure, $P_n = 20\text{mTorr}$, current per coil, $I_{\text{RF}} = 20\text{A}$, $\nu_{\text{rf}} = 5.25\text{MHz}$)

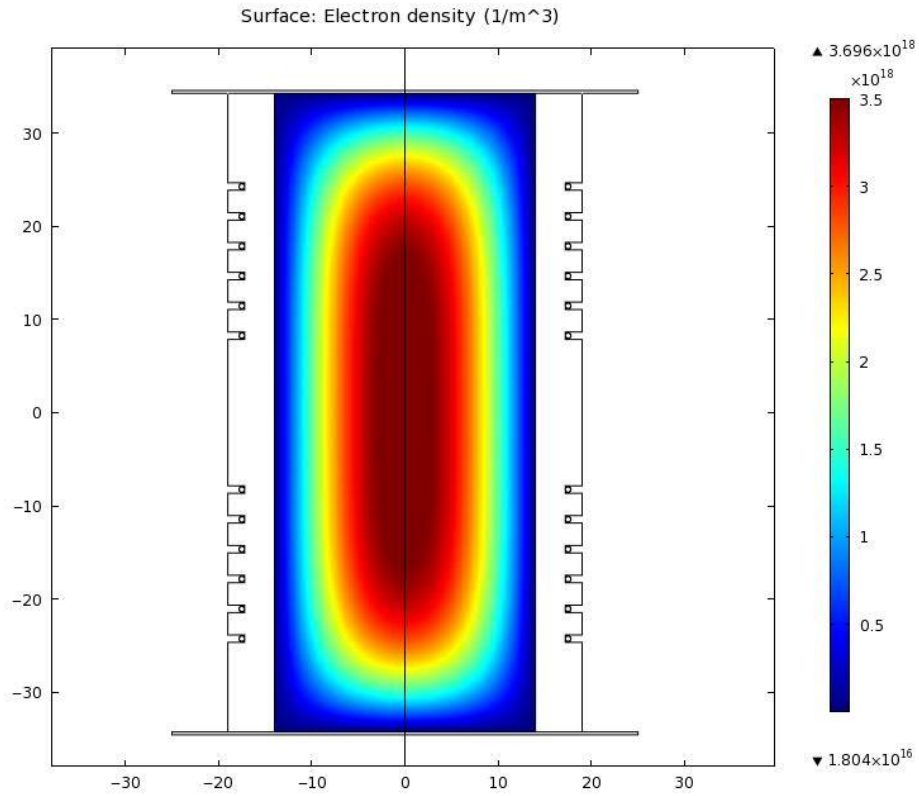


Figure 6.25. Electron density within a cylindrical xenon discharge.
(neutral pressure, $P_n = 20\text{mTorr}$, current per coil, $I_{\text{RF}} = 20\text{A}$, $\nu_{\text{rf}} = 5.25\text{MHz}$)

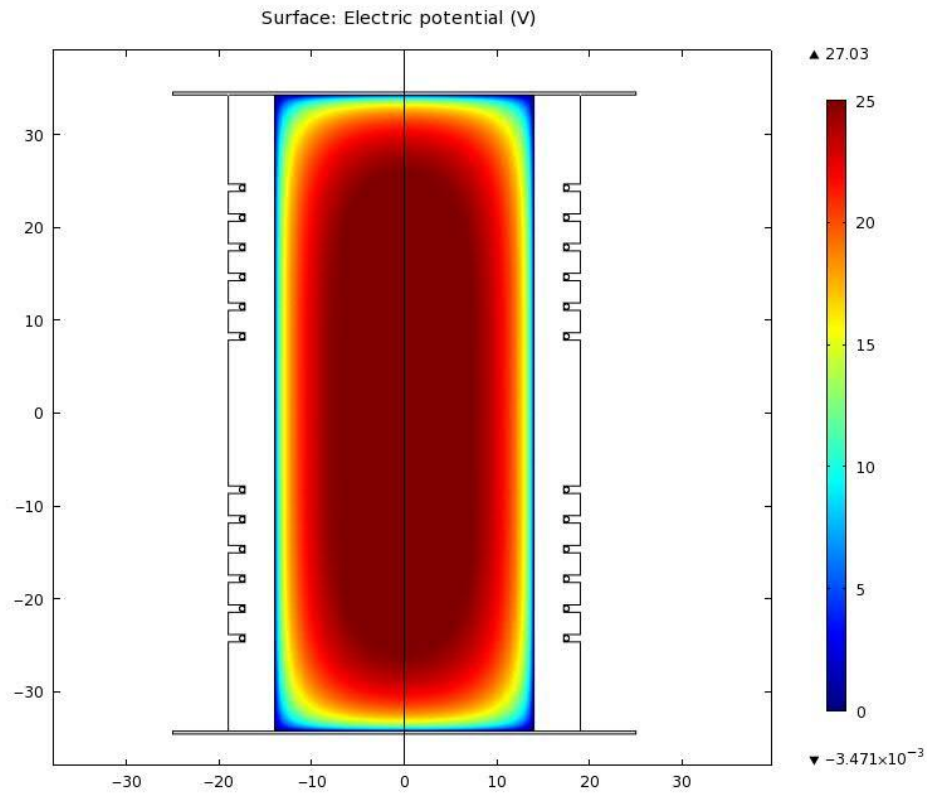


Figure 6.26. Plasma potential within a cylindrical xenon discharge.
(neutral pressure, $P_n = 20\text{mTorr}$, current per coil, $I_{\text{RF}} = 20\text{A}$, $\nu_{\text{rf}} = 5.25\text{MHz}$)

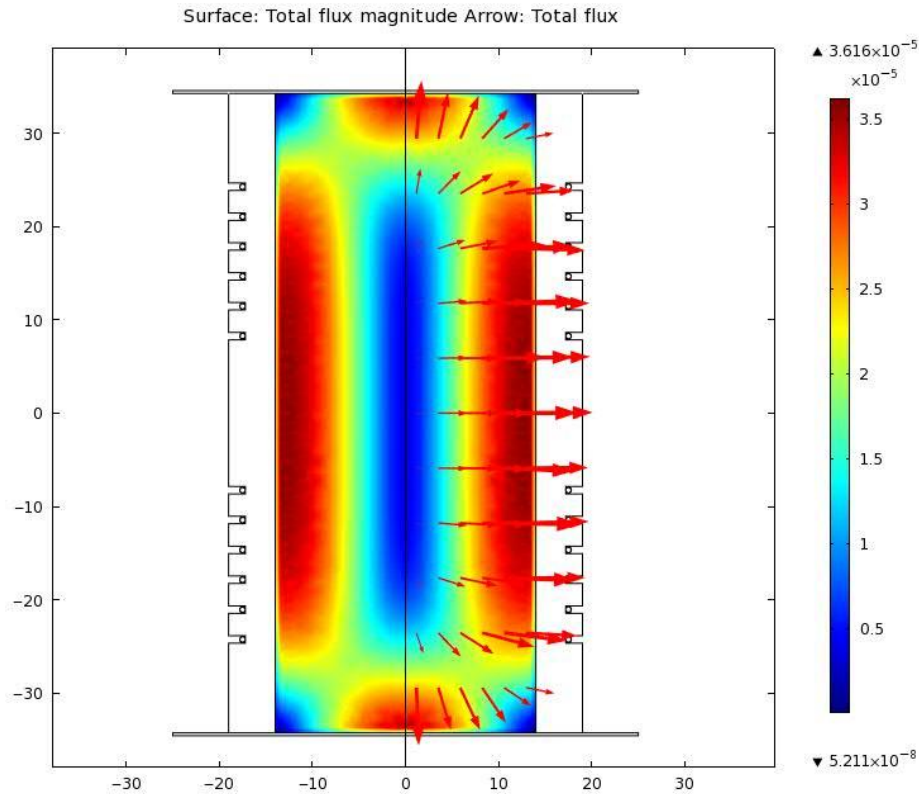


Figure 6.27. Ion flux indicating that ions are predominantly lost radially to the walls. (neutral pressure, $P_n = 20\text{mTorr}$, current per coil, $I_{RF} = 20\text{A}$, $\nu_{rf} = 5.25\text{MHz}$)

Simulations were found to converge at lower coil currents of 7.5A for $\nu_{rf} = 13.56\text{MHz}$, $P_n = 20\text{mTorr}$. A xenon discharge was modeled with these parameters and a smaller coil separation distance of 10mm , as was used for the MiDGIT breadboard thruster. The power deposited in the plasma (displayed in Figure 6.28) is increased in the region between the coils due to the reduced spacing. The electron temperature is therefore more uniform along the length of the discharge chamber underneath both induction coils. Plots of electron temperature, plasma density and plasma potential are given in Figures 6.29, 6.30 and 6.31. These were found to be $\sim 4\text{eV}$, $\sim 9 \times 10^{17}\text{m}^{-3}$ and $\sim 22\text{V}$ respectively. Though the electron temperature is more in line with that expected for the MiDGIT thruster ($2\text{-}4\text{eV}$) which operates at a much lower neutral pressure, the plasma density is approximately 5 times higher for the simulated discharge.

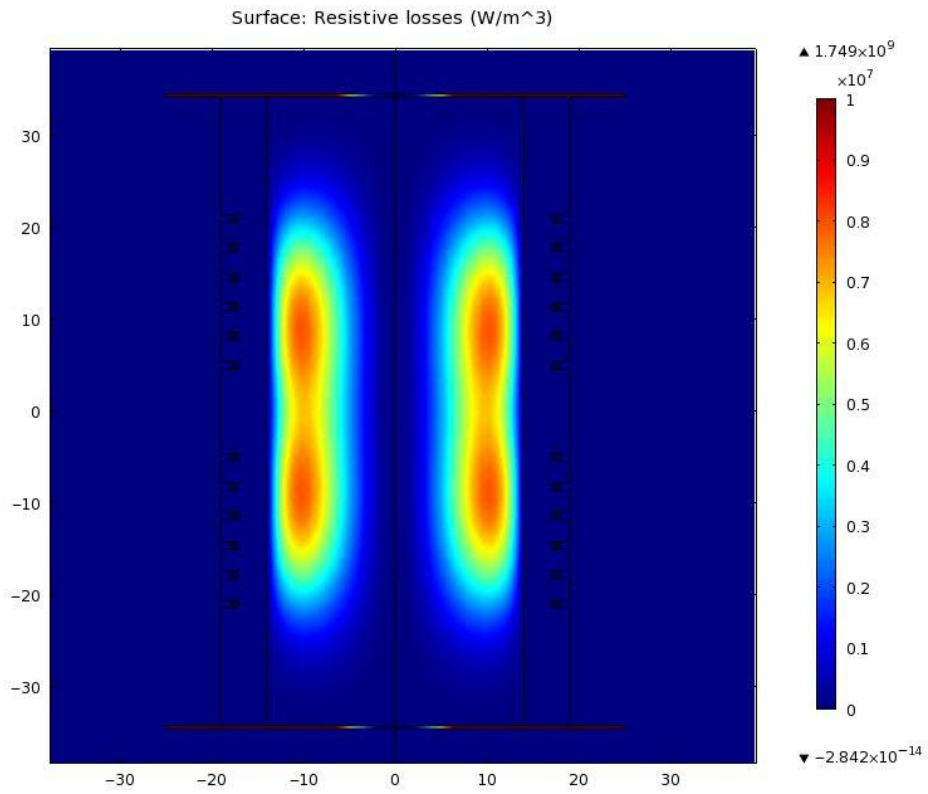


Figure 6.28. Resistive losses indicating power deposition, with a coil spacing of 10mm. (neutral pressure, $P_n = 20\text{mTorr}$, current per coil, $I_{RF} = 7.5\text{A}$, $\nu_{rf} = 13.56\text{MHz}$)

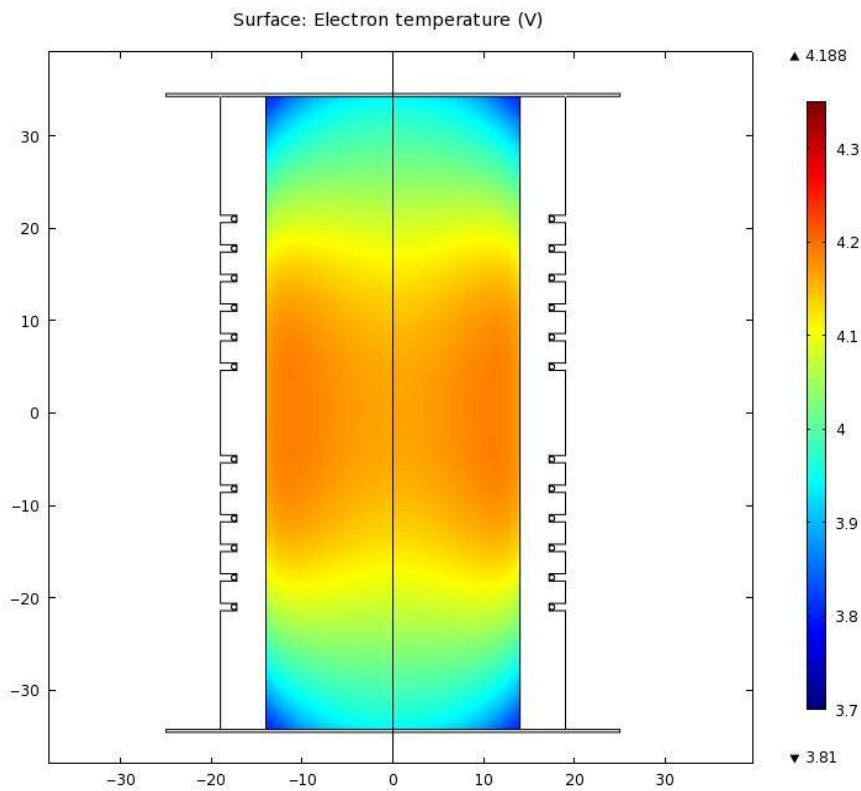


Figure 6.29. Electron temperature within a cylindrical xenon discharge. (neutral pressure, $P_n = 20\text{mTorr}$, current per coil, $I_{RF} = 7.5\text{A}$, $\nu_{rf} = 13.56\text{MHz}$)

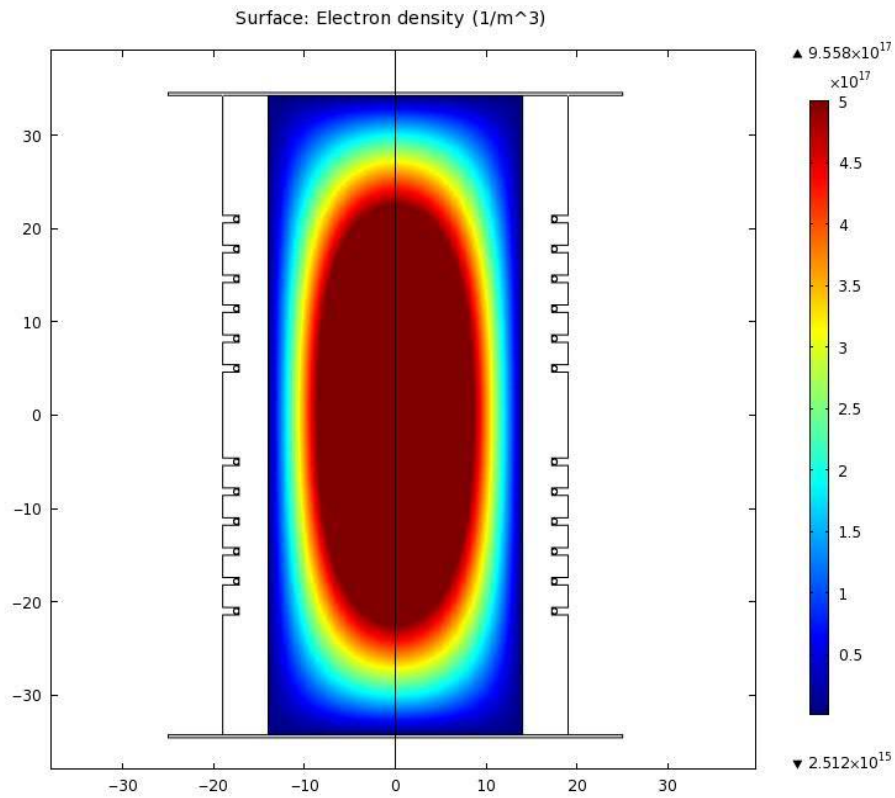


Figure 6.30. Electron density within a cylindrical xenon discharge.
 (neutral pressure, $P_n = 20\text{mTorr}$, current per coil, $I_{RF} = 7.5\text{A}$, $\nu_{rf} = 13.56\text{MHz}$)

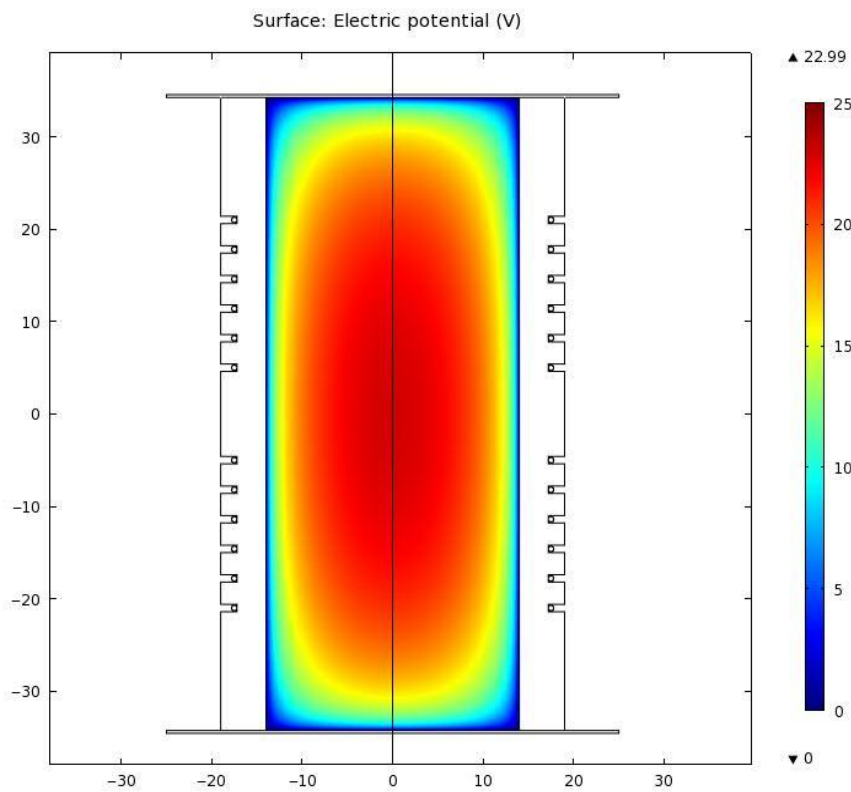


Figure 6.31. Plasma potential within a cylindrical xenon discharge.
 (neutral pressure, $P_n = 20\text{mTorr}$, current per coil, $I_{RF} = 7.5\text{A}$, $\nu_{rf} = 13.56\text{MHz}$)

The current in one of the induction coils for this model was increased to observe the effect on power coupling and plasma density. Plots of the resistive losses for three different cases are given in Figure 6.32. More power is deposited to the plasma underneath the coil with higher current, but resistive losses also increase slightly under the second coil. An increase in current is expected in the second coil when the current in the other coil is increased due to mutual coupling between the coils. Plots of electron temperature, plasma density and plasma potential along the axis of the discharge are given in Figures 6.33 - 6.35. The plasma density is only found to be increased significantly on one end of the discharge relative to the other by a relatively large variation in coil current. The plasma density is also mainly increased in the bulk of the discharge and a rapid fall off is still observed approaching the surface of the grids at either end of the discharge chamber.

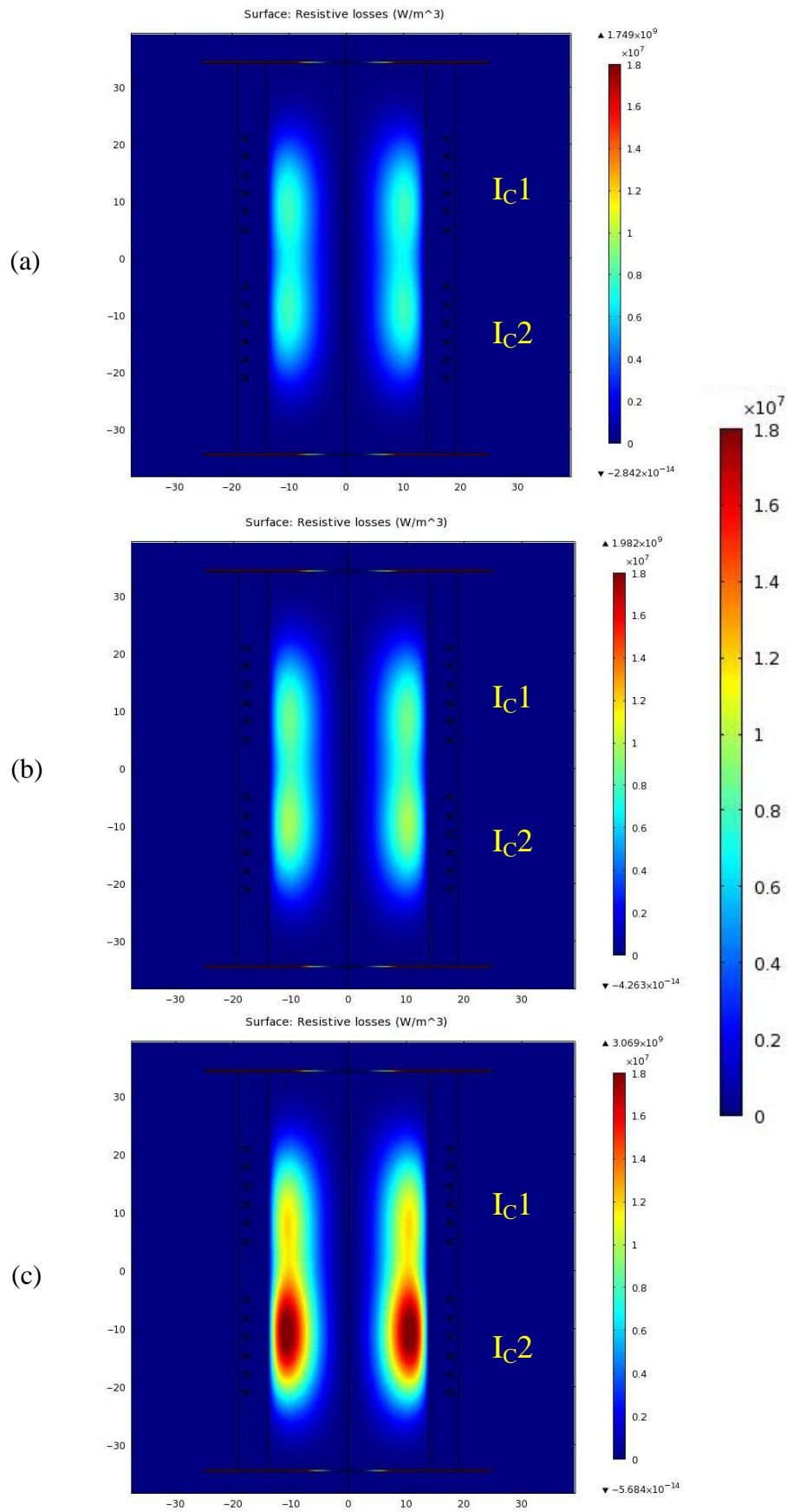


Figure 6.32. Resistive losses indicating power deposition with varying coil currents.
 (neutral pressure, $P_n = 20\text{mTorr}$, $\nu_{rf} = 13.56\text{MHz}$)
 (a) $I_{C1} = 7.5\text{A}$, $I_{C2} = 7.5\text{A}$ (b) $I_{C1} = 7.5\text{A}$, $I_{C2} = 8.0\text{A}$ (c) $I_{C1} = 7.5\text{A}$, $I_{C2} = 10.0\text{A}$

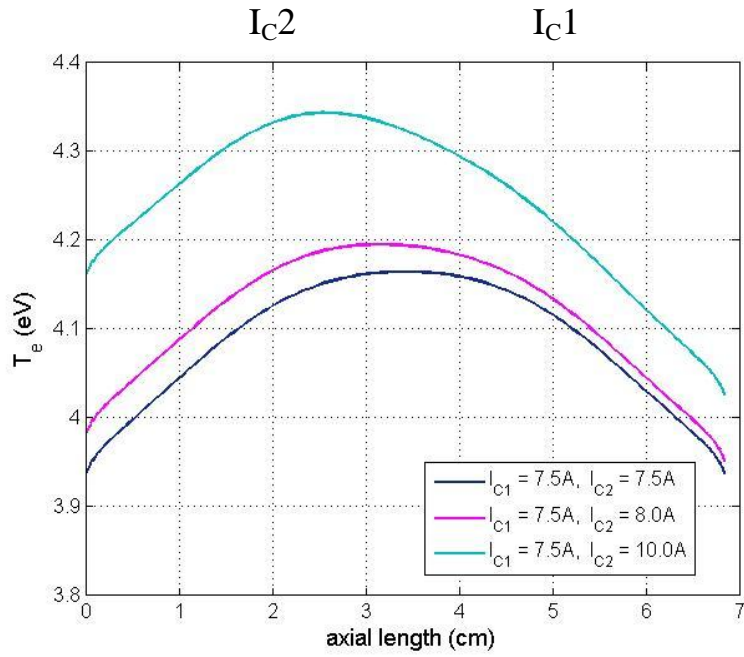


Figure 6.33. Electron temperature along discharge axis.
(neutral pressure, $P_n = 20\text{mTorr}$, $\nu_{rf} = 13.56\text{MHz}$)

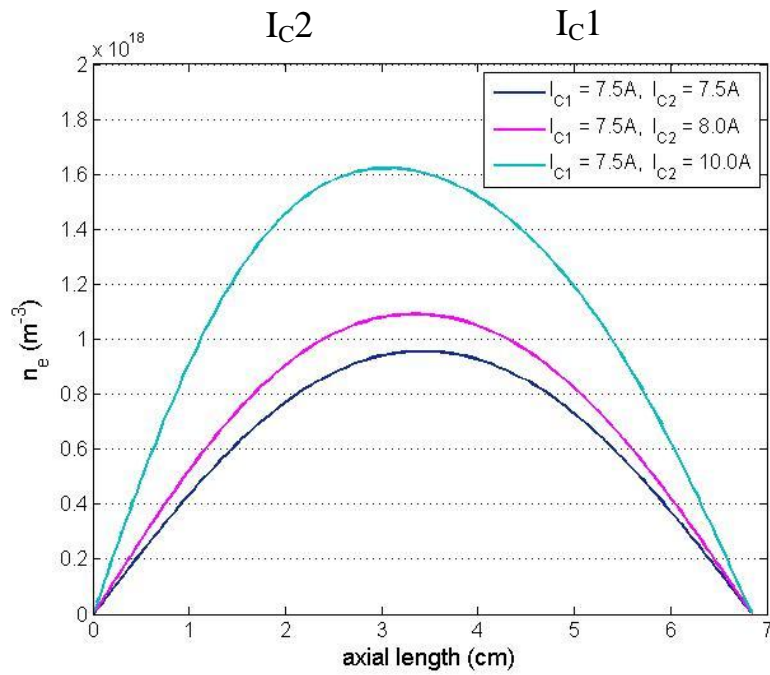


Figure 6.34. Plasma density along discharge axis.
(neutral pressure, $P_n = 20\text{mTorr}$, $\nu_{rf} = 13.56\text{MHz}$)

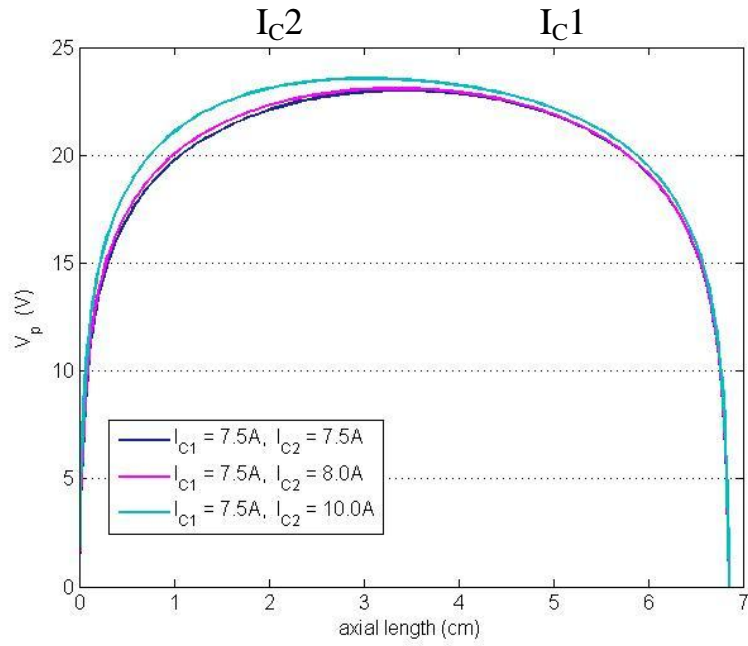


Figure 6.35. Plasma potential along discharge axis.
(neutral pressure, $P_n = 20\text{mTorr}$, $\nu_{rf} = 13.56\text{MHz}$)

The ion current that can be extracted through each grid set depends on the ion density at the plasma sheath upstream of each screen grid and also on the electron temperature through the Bohm current ($I_i \propto n_e \sqrt{T_e}$). Plots showing ion flux for the three cases are displayed in Figure 6.36; these indicate that the flux of ions towards the grid adjacent the coil with the highest RF current is greater than that towards the opposing grid. Though the plasma sheath is not resolved in the COMSOL model, the product ($n_e \sqrt{T_e}$) along each grid boundary is plotted for the three cases in Figure 6.37. The Bohm current across the sheath upstream of the grid closest to the coil with the highest RF current is expected to be greater than that for the opposing grid, with large variations in RF coil current required to generate large differences in the extracted beam currents.

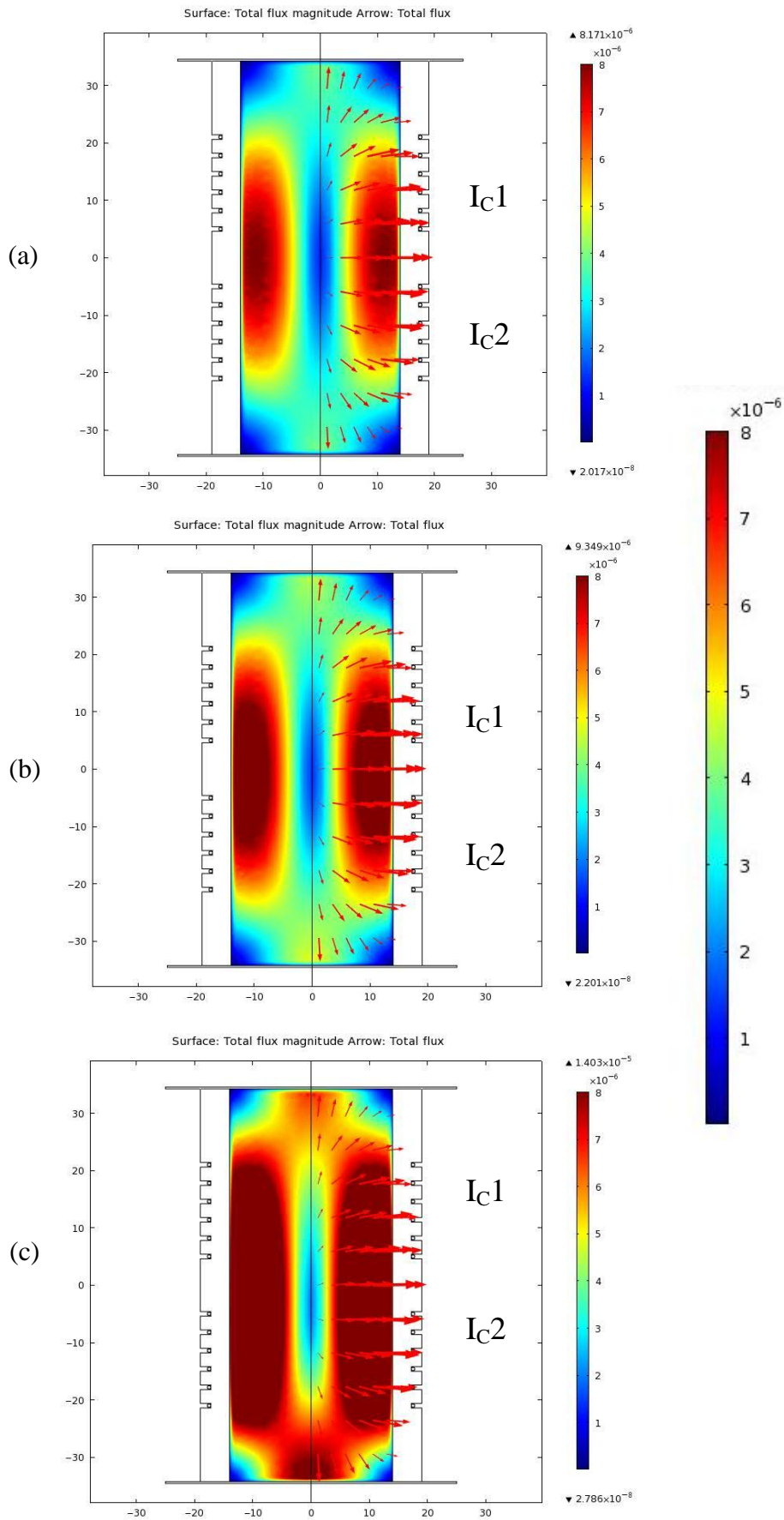


Figure 6.36. Ion flux with varying coil current on one end.
(neutral pressure, $P_n = 20\text{mTorr}$, $\nu_{rf} = 13.56\text{MHz}$)

(a) $I_{C1} = 7.5A, I_{C2} = 7.5A$ (b) $I_{C1} = 7.5A, I_{C2} = 8.0A$ (c) $I_{C1} = 7.5A, I_{C2} = 10.0A$

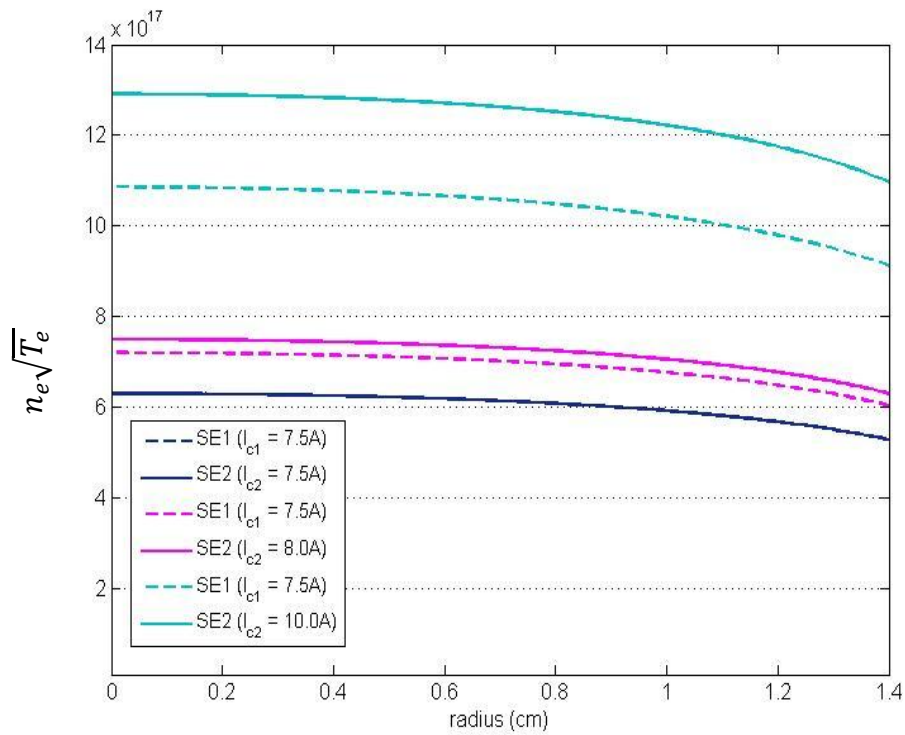


Figure 6.37. Comparison of plasma density and electron temperature along the boundary at each end of the discharge with varying coil current (Bohm current, $I_i \propto n_e \sqrt{T_e}$). (neutral pressure, $P_n = 20\text{mTorr}$, $\nu_{rf} = 13.56\text{MHz}$).

Though the discharge model developed with COMSOL Multiphysics may not provide accurate information on plasma parameters for the MiDGIT thruster, it is useful in demonstrating the principle by which extracted ion beams may be controlled independently by variation of the RF power to each induction coil of the thruster.

6.2.2.2 Discharge Diagnostics

An attempt to determine more reliable estimates of plasma parameters for the MiDGIT thruster was made by use of triple Langmuir probes. The tests also served as a means to physically investigate the effect of varying the relative RF current in the induction coils on the discharge during differential discharge operation.

Discharge diagnostics were performed on the MiDGIT prototype thruster operated on xenon within the EP1 vacuum facility. Initial tests on the prototype model at the QinetiQ LEEP facilities identified that the prototype model could be operated successfully at 3.28 MHz and operating frequencies above 11.0 MHz. During tests within the EP1 facility, discharges at 3.28 MHz could not be ignited due to the different set-up involved affecting power coupling to the thruster. An operating frequency of 13.56 MHz was therefore selected to provide stable and reliable operation. Triple Langmuir probes were constructed (as described in section 4.3.6.2) to perform diagnostics; these were inserted through the extraction grids on either end of the thruster to obtain measurements on both ends for the same discharge conditions. Rogowski coils were installed (as outlined in section 4.3.6.1) to monitor the RF current in each induction coil. The induced signals from the Rogowski coils were monitored and recorded by a Tektronix DPO3034 (300 MHz, 2.5GS/s) digital oscilloscope. The same oscilloscope was used to measure the probe voltages. The thruster was operated on xenon at a flow rate of 0.203 mgs^{-1} .

Axial discharge measurements were initially obtained with approximately equal currents applied to the induction coils (controlled via the tuning capacitors of each antenna matching unit). The coil currents were applied in phase, which was checked on the oscilloscope. Repeat measurements were then performed for the current ratios $(I_1/I_2) = 0.5$ and $(I_2/I_1) = 0.5$. Unfortunately, due to the limited number of ports on the vacuum chamber and no suitable linear translation or rotary feedthrough, the triple Langmuir probes had to be manually re-positioned between measurements. This did however allow the opportunity to investigate discharge repeatability. The coil currents were observed to be repeatable to within 0.1A over 20 measurements by manually re-setting the same capacitor settings on the AMUs between measurements. The repeatability of the coil currents and RF power delivered by the RF amplifier during measurements for the three test cases can be seen in Table 6-4. The rms coil currents were determined to be in the range 2-4A, as might be expected for a miniature RF ion thruster [67]. It must be noted however, that the Rogowski coils were originally calibrated at 10kHz and therefore current estimates may not be accurate, as the response of the Rogowski

Test case	($P_{fw} - P_r$) (W)	I_1 RMS (A)	I_2 RMS (A)
$I_1 = I_2$	40.1 ± 1.45	3.63 ± 0.06	3.59 ± 0.08
$I_1/ I_2 = 0.5$	23.3 ± 0.67	2.02 ± 0.11	3.77 ± 0.07
$I_2/ I_1 = 0.5$	25.8 ± 0.92	3.69 ± 0.05	1.94 ± 0.04

Table 6-4. Repeatability of measured forward RF power and rms coil currents (20 measurements) during the three test cases.

coils at MHz frequencies is expected to be non-linear. The Rogowski coils should still be useful for monitoring the relative currents in the induction coils however.

Estimates of electron temperature and density were obtained from the triple Langmuir probe measurements using the expressions derived by Kamitsuma et al [99] given in Appendix A. The equations require an estimate of T_i/T_e , which was taken to be 0.01 for this analysis (assuming an electron temperature of the order 3eV and an ion temperature of 0.03eV as might be expected for the MiDGIT discharge). The function $f(\phi_{d2})$ in the expression for plasma density was taken from Kamitsuma to be ~ 0.1 , based on the probe voltages measured (see Appendix A).

Axial profiles of the estimated electron temperature and plasma density measured for the different discharge states of the MiDGIT prototype thruster are given in Figure 6.38. Error bars indicate the uncertainty associated with averaging of three repeated measurements at each location, as described in section 4.3.7.4. The measurements display similar profiles to those observed for the discharge model developed in COMSOL Multiphysics, however the measured values are more in line with those expected for a 3cm diameter RF ion thruster ($T_e \sim 2\text{-}4\text{eV}$, $n_e \sim 10^{17} \text{ m}^{-3}$) [24]. The electron temperature and plasma density measured for the balanced current case are higher than for the other states due to the higher total power coupled to the plasma. The profiles provide a clear indication that the plasma density on each end of the thruster can be controlled by variation of the currents in the two induction coils, as expected from the discharge modelling.

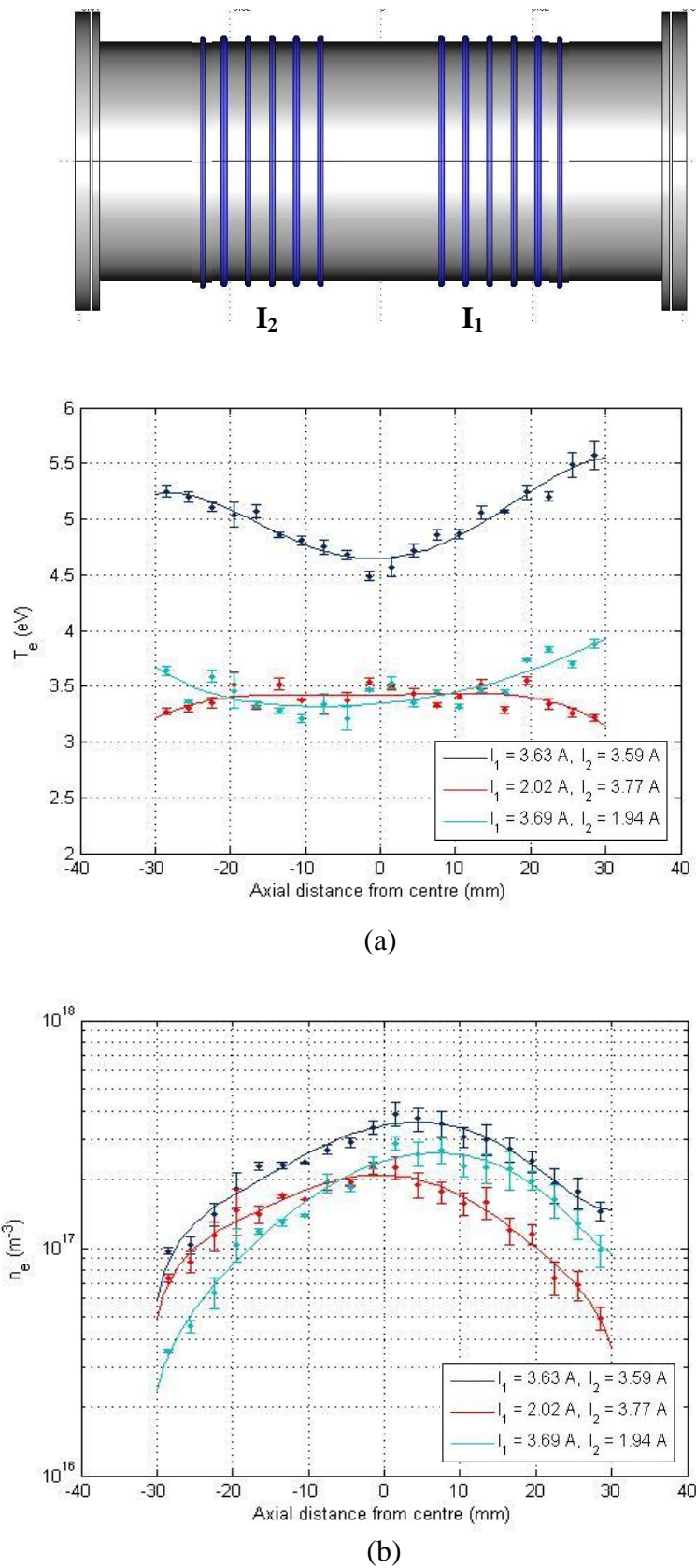


Figure 6.38. Axial estimates of (a) electron temperature and (b) electron density obtained by triple Langmuir probe for the MiDGIT prototype thruster ($\dot{m} = 0.203\text{mg s}^{-1}$, $\nu_{\text{rf}} = 13.56\text{MHz}$).

6.2.2.3 Demonstration of Differential Control

Beam extraction tests were performed on the MiDGIT prototype model within the EP1 vacuum chamber to provide an initial assessment of differential ion beam control by variation of RF power. Beam diagnostics were not performed within the EP1 chamber; only variations in grid currents could be monitored. Tungsten filaments were used for beam neutralization, which presented some issues as described in section 4.3.2.

Ion beams could be extracted for xenon flow rates between 0.06 mgs^{-1} and 0.30 mgs^{-1} at forward RF power levels greater than 23W delivered by the RF amplifier. Beam extraction was observed to become unstable at low flow rates after short durations, thought to be affected by the use of filaments and the chamber walls for beam neutralization. Operation at flow rates $\sim 0.20 \text{ mgs}^{-1}$ was required for stable extraction over long periods.

The MiDGIT prototype was therefore operated at a commanded flow rate of 2.0 sccm from the mass flow controller (equivalent to 0.203 mgs^{-1} xenon) at RF power levels of $\sim 30\text{W}$ and beam and accelerator grid potentials of 950V/-95V respectively. The thruster was operated at a frequency of 13.56 MHz. The inductor setting of each AMU was set to provide the best match for these conditions. The power delivered to each induction coil can be varied by adjusting the variable capacitor on the transmitter (RFG) side of the matching circuit (see section 4.1.2), which effectively varies the amount of power reflected back from the AMU towards the RF amplifier and that which is delivered forward of the AMU to the induction coil. The screen and accelerator grid currents were then monitored as the variable capacitor C_T of the AMU connected to coil 1 of the thruster was varied while the settings of AMU2 were kept constant. Rogowski coils provided an estimate of the RF current in each induction coil during tests. The variations in coil current and grid current with variation of the match to induction coil 1 are given in Table 6-5.

As the capacitor C_T was adjusted for AMU1, the phase difference between the current in induction coil 2 and that of coil 1 (measured on the oscilloscope via the Rogowski coil signals) was observed to increase, with a general decrease in the rms current of induction coil 1 and increase in rms current of coil 2 as can be seen in Figure 6.39. As C_T is varied to reduce the RF power delivered to induction coil 1, more power will be reflected back from AMU1, across the T-piece connector towards AMU2, resulting in a slight increase in current in coil 2.

AMU ₁ (C _T , L, C _A)	AMU ₂ (C _T , L, C _A)	(P _{tw} - P _r) (W)	I _{1 RMS} (A)	I _{2 RMS} (A)	θ ₂₋₁ (°)	I _{B1} (mA)	I _{B2} (mA)	I _{ACC1} (mA)	I _{ACC2} (mA)
(9.0, I, 9.0)	(4.0, I, 9.0)	32	0.229	4.857	102.4	2.06 ± 0.04	4.24 ± 0.16	0.18 ± 0.01	0.95 ± 0.22
(7.0, I, 9.0)	(4.0, I, 9.0)	28	1.237	4.582	76.5	1.64 ± 0.04	3.53 ± 0.12	0.11 ± 0.01	0.73 ± 0.18
(6.0, I, 9.0)	(4.0, I, 9.0)	25	1.558	4.399	66.2	1.71 ± 0.04	3.04 ± 0.07	0.12 ± 0.01	0.62 ± 0.09
(5.0, I, 9.0)	(4.0, I, 9.0)	26	2.474	4.216	41.3	2.04 ± 0.03	2.64 ± 0.02	0.13 ± 0.01	0.51 ± 0.02
(4.0, I, 9.0)	(4.0, I, 9.0)	28	2.429	4.078	31.2	2.41 ± 0.05	2.38 ± 0.06	0.19 ± 0.01	0.57 ± 0.02
(3.0, I, 9.0)	(4.0, I, 9.0)	29	2.612	4.216	24.8	2.77 ± 0.12	2.67 ± 0.13	0.20 ± 0.01	0.67 ± 0.06
(2.0, I, 9.0)	(4.0, I, 9.0)	31	2.704	4.262	21.7	2.97 ± 0.12	2.64 ± 0.08	0.22 ± 0.01	0.64 ± 0.05
(1.0, I, 9.0)	(4.0, I, 9.0)	32	2.795	4.262	13.6	3.33 ± 0.10	2.59 ± 0.08	0.25 ± 0.01	0.67 ± 0.04
(0.0, I, 9.0)	(4.0, I, 9.0)	33	2.933	4.262	8.8	3.54 ± 0.08	2.65 ± 0.05	0.27 ± 0.01	0.66 ± 0.05

Table 6-5. Beam and accelerator grid currents measured during differential operation of the MiDGIT prototype thruster at $\dot{m} = 0.203\text{mg s}^{-1}$, $\nu_{rf} = 13.56\text{MHz}$. Also listed are the capacitor and inductor settings of the AMUs and the rms current measured in each induction coil to indicate the effect of varying the transmitter tuning capacitor (C_T) of AMU1.

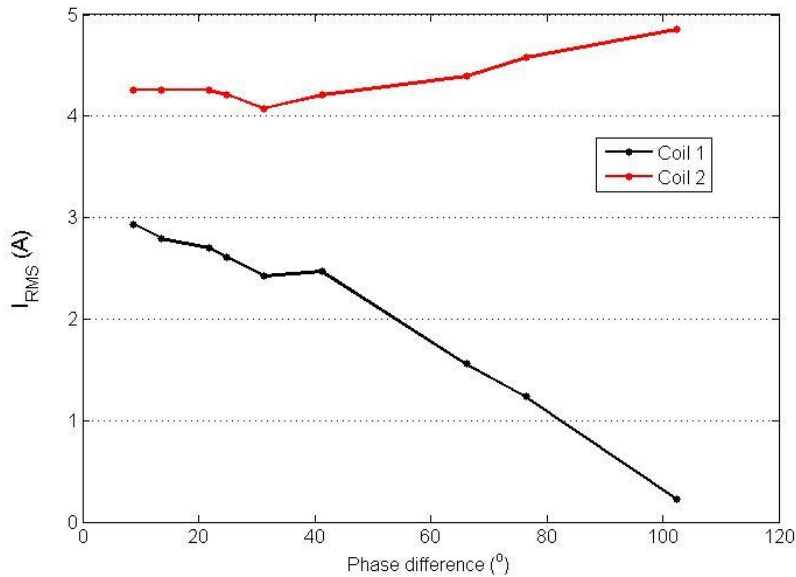


Figure 6.39. RMS coil current in induction coils 1 and 2 against phase difference between I_{C1} and I_{C2} during variation of the transmitter tuning capacitor on AMU1.

The beam and accelerator grid currents measured on each end of the thruster are displayed in Figure 6.40. Beam current can be seen to decrease on SE1 with decreasing coil current, indicating that plasma density is decreasing on SE1 as a result of the reduced power coupling. Accordingly, the beam and accelerator grid currents can be seen to increase for SE2 due to the increasing current in induction coil 2. Beam current can be seen to be equal at a phase difference of approximately 30° between the induction coil currents.

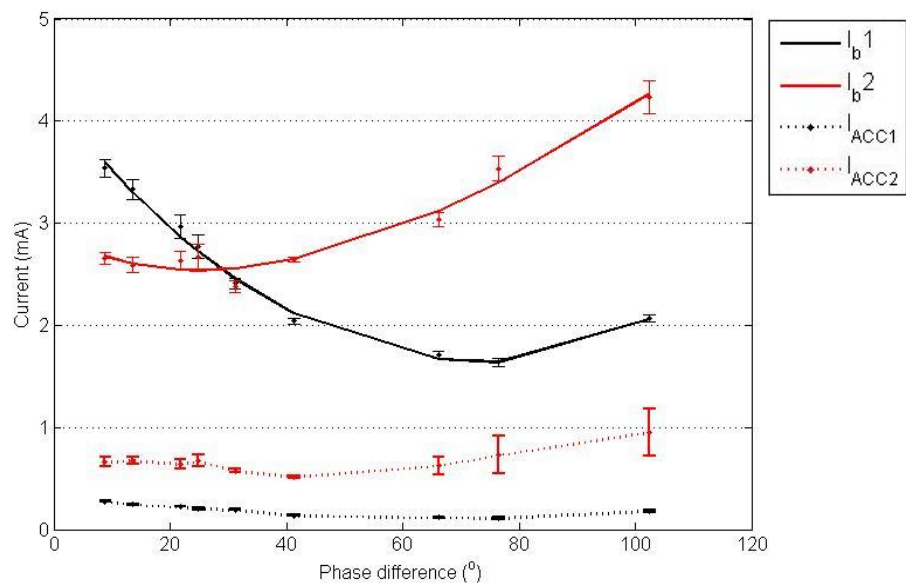


Figure 6.40. Beam and accelerator grid against phase difference between I_{C1} and I_{C2} during variation of the transmitter tuning capacitor on AMU1.

The resistance and reactance of an element define impedance according to:

$$Z = \sqrt{X_L^2 + R^2} \quad (6.2)$$

with the phase of an inductive impedance given by:

$$\theta = \tan^{-1}\left(\frac{X_L}{R}\right) \quad (6.3)$$

The phase difference of 30° observed between the currents of the induction coils to provide equal beam current suggests that the impedance of one of the coils (and associated connectors) of the MiDGIT prototype was greater than the other. Also, as the inductive reactance of each induction coil should not vary due to the fixed RF frequency, the increasing phase difference between the coil currents is a result of varying resistance of the coils, affected by the two-way coupling between coil and plasma.

The thrust calculated from the grid currents over the duration of the test are displayed in Figure 6.41, which effectively shows thrust stepping by variation of the capacitor C_T on the antenna matching unit. The net thrust determined from the difference of the beam currents is displayed in Figure 6.42. The grid currents could only be sampled at a maximum rate of 0.25Hz over the RS232 serial connections between the DMMs and PC running LabVIEW however, therefore the signals appear relatively noisy.

The results suggest that a net thrust out of either end of the thruster could be achieved, with a maximum net thrust of $\sim 115\mu\text{N}$ out of SE2 (not taking into account corrections for beam divergence or grid impingement). Specific impulse at a thrust level of $115\mu\text{N}$ would be $\sim 58\text{s}$, due to the relatively high flow rate required for stable, dual beam extraction from the MiDGIT prototype during this test. The smallest thrust step that could be achieved by manual control of the capacitor dial on the AMU was $\sim 4\mu\text{N}$. This suggests that plasma parameters and beam current are very sensitive to changes in the tuning capacitors, and a much finer thrust resolution would be expected for finer control of the variable capacitors.

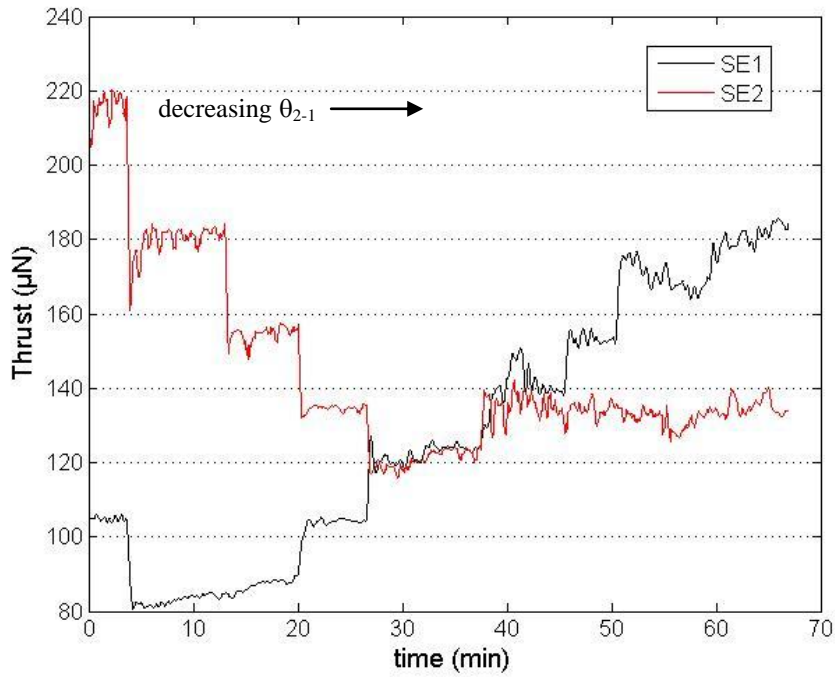


Figure 6.41. Thrust stepping by variation of the transmitter tuning capacitor on AMU1.
 ($V_{ACCl} = -95V$, $V_b = 950V$, $\dot{m} = 0.203\text{mgs}^{-1}$, $\nu_{rf} = 13.56\text{MHz}$)

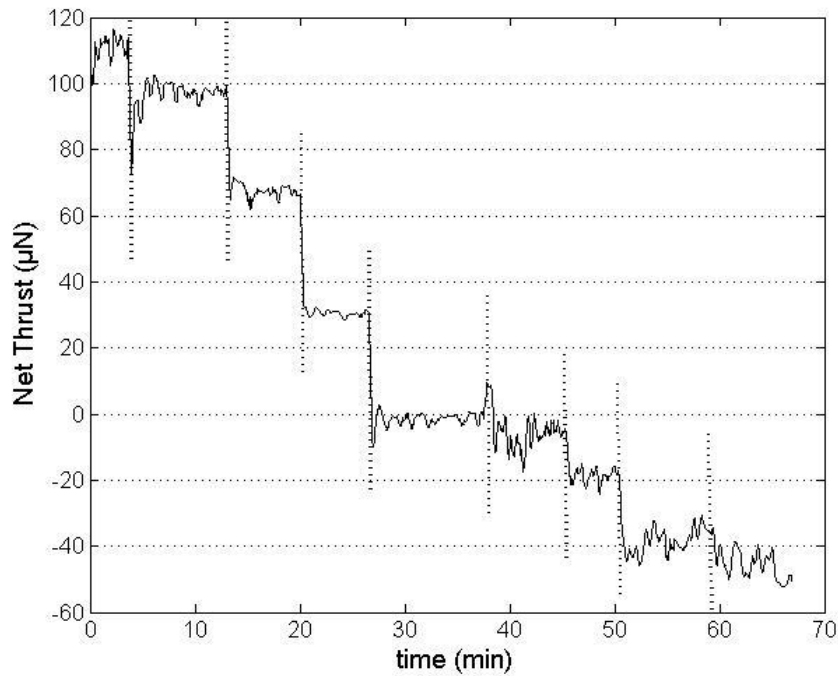


Figure 6.42. Net thrust during variation of the transmitter tuning capacitor on AMU1.
 (A positive thrust indicating net thrust out of SE2).
 ($V_{ACCl} = -95V$, $V_b = 950V$, $\dot{m} = 0.203\text{mgs}^{-1}$, $\nu_{rf} = 13.56\text{MHz}$)

6.2.2.4 Differential Thrust Performance

Differential beam tests were also performed on the MiDGIT breadboard thruster at the QinetiQ LEEP facilities to investigate differential thrust control by variation of RF power; the improved design of the breadboard thruster over the prototype model and the use of a hollow cathode neutralizer were expected to provide better performance. Beam profiles were obtained on one end of the thruster as verification of the electrical thrust. The current in each induction coil was not measured during tests. However, estimates of the RF power delivered to each induction coil were obtained from measurements of the forward and reflected power displayed by the SWR meter incorporated into each AMU using Equation 4.5.

The breadboard thruster was operated at a frequency of 5.25MHz and flow rate of 0.058 mgs^{-1} , with beam and accelerator grid potentials of 995V/-95V (slightly higher than nominal in an attempt to maximize thrust). The screen and accelerator grid currents were logged automatically at rate of 1Hz via LabVIEW while the match to each coil was varied in turn via the capacitor settings of the associated AMU. Beam profiles were taken of the ion beam extracted from SE1 only during variation of AMU1 or AMU2.

The variation in beam and accelerator grid currents and the estimated power to each coil during the duration of the test are displayed in Figure 6.43. The test was performed over a short duration and therefore the thruster was not allowed to thermally stabilize following a thrust step change to obtain steady state conditions. The beam current can be seen to gradually decrease with time following a thrust step change, particularly following large increases in RF power. Grid deformation due to thermal loads resulting in an increased grid gap would cause the beam current to decrease as observed.

As can be seen from Figure 6.43 however, a significant increase in RF power to one of the induction coils produces a significant increase in the beam and accelerator grid currents of the adjacent grid set. The grid currents of the opposing grid set remain relatively unaffected. This is also evident in the beam profiles obtained of SE1 during variation of AMU1 and AMU2 to vary RF power to either coil 1 or 2; the plots are displayed in Figures 6.44 and 6.45 respectively.

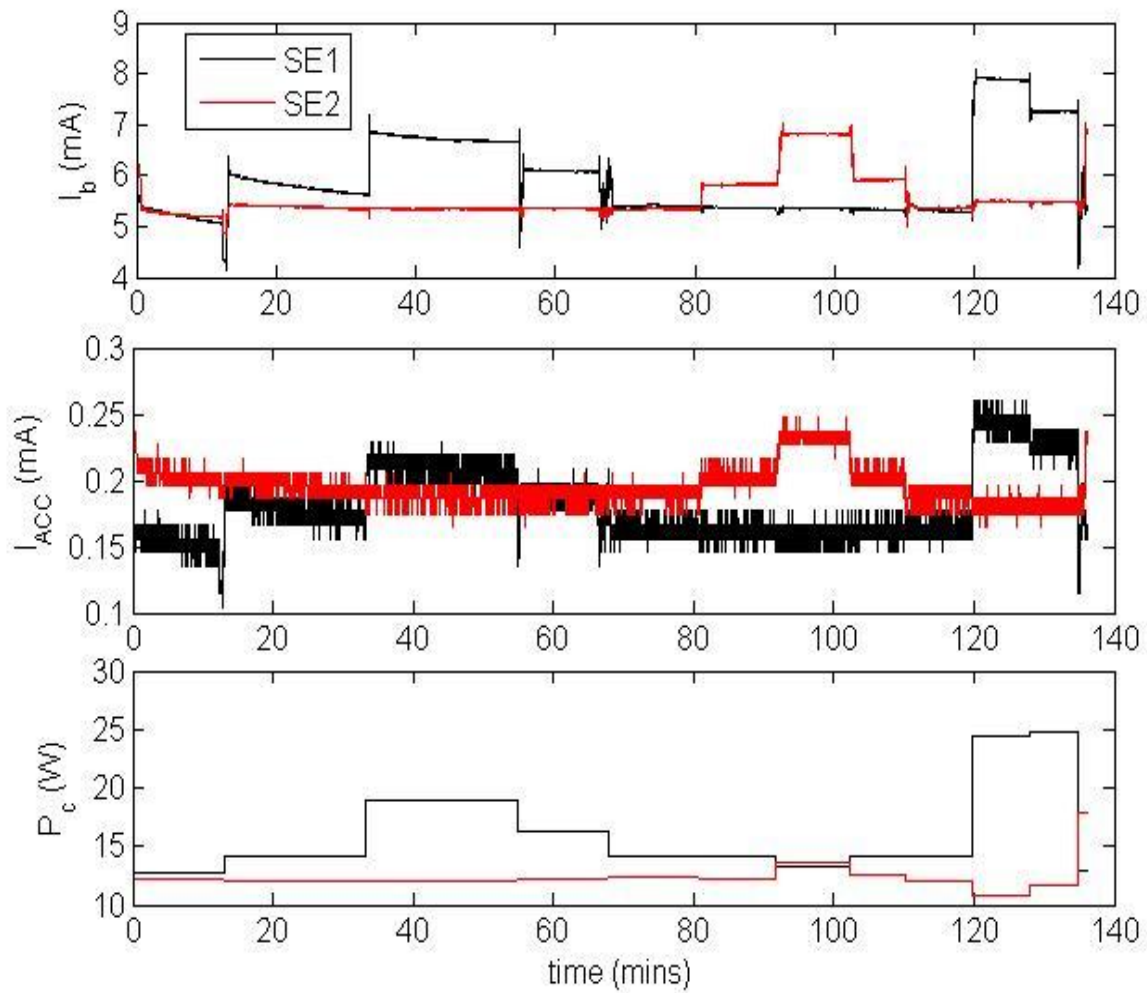


Figure 6.43. Beam and accelerator grid currents during differential operation of the MiDGIT breadboard thruster. RF power to each induction coil was varied by adjustment of the antenna matching units. ($V_{ACC1} = -95V$, $V_b = 995V$, $\dot{m} = 0.058\text{mgs}^{-1}$, $\nu_{rf} = 5.25\text{MHz}$)

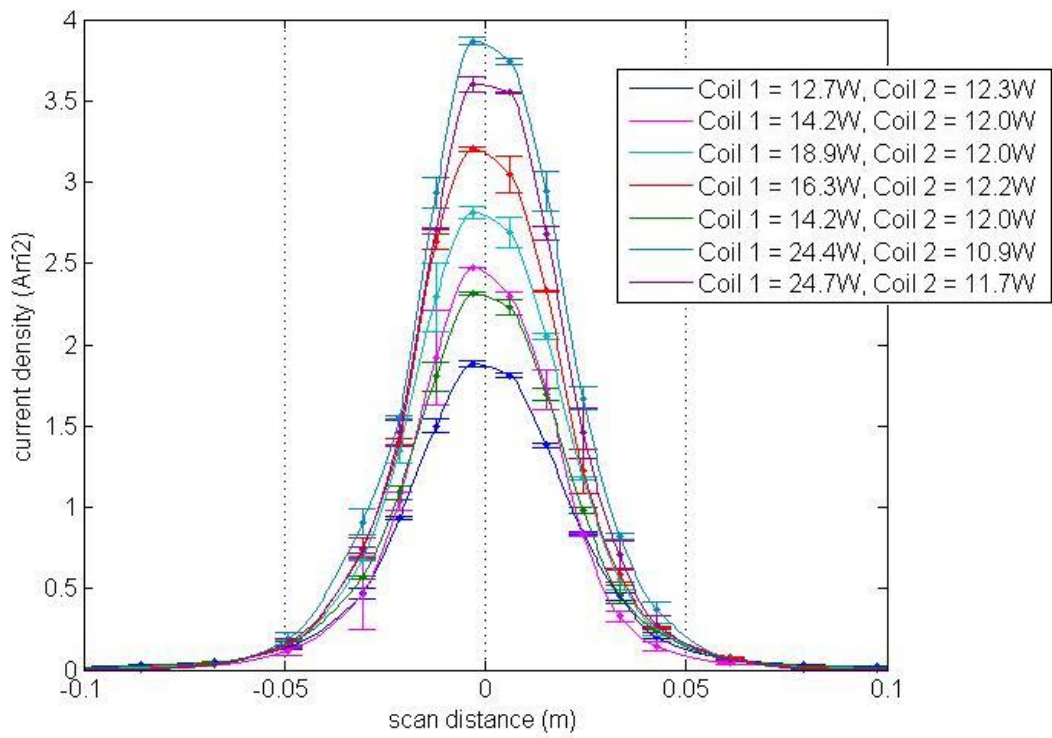


Figure 6.44. Beam profiles of the ion beam extracted from SE1 during variation of AMU1.
 $(V_{\text{ACC2}} = -95\text{V}, V_b = 995\text{V}, \dot{m} = 0.058\text{mgs}^{-1}, \nu_{\text{rf}} = 5.25\text{MHz})$.

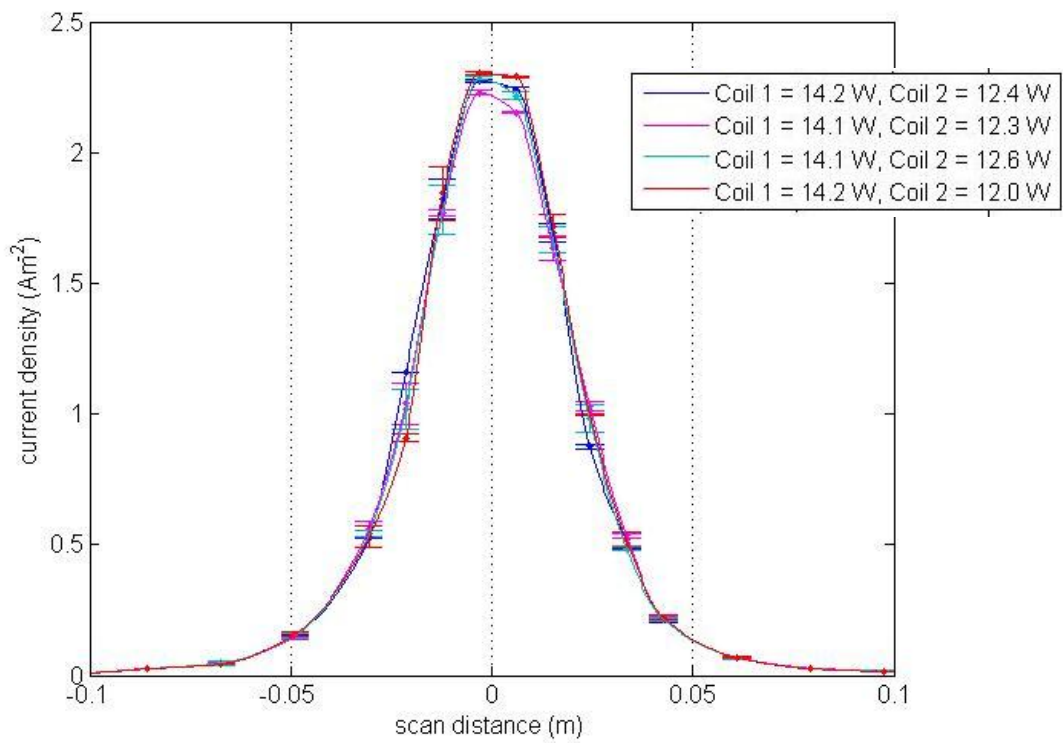


Figure 6.45. Beam profiles of the ion beam extracted from SE1 during variation of AMU2.
 $(V_{\text{ACC2}} = -95\text{V}, V_b = 995\text{V}, \dot{m} = 0.058\text{mgs}^{-1}, \nu_{\text{rf}} = 5.25\text{MHz})$.

Values of beam current were estimated from the beam profiles; these are compared in Figure 6.46 with estimates of the beam current determined from the difference between the measured screen grid and accelerator grid currents. The beam currents estimated from the beam profiles are within 80%-90% of the electrical estimates at low beam currents but show remarkable agreement at higher beam currents. Log plots of the beam profiles of SE1 display a two-tier profile at low beam currents but are more focused at high beam current, as shown in Figure 6.47. The underestimated beam current at low values could be attributed to a greater influence of CEX collisions on the beam ions, with more highly divergent ions created at low beam currents that are not detected by the beam probe.

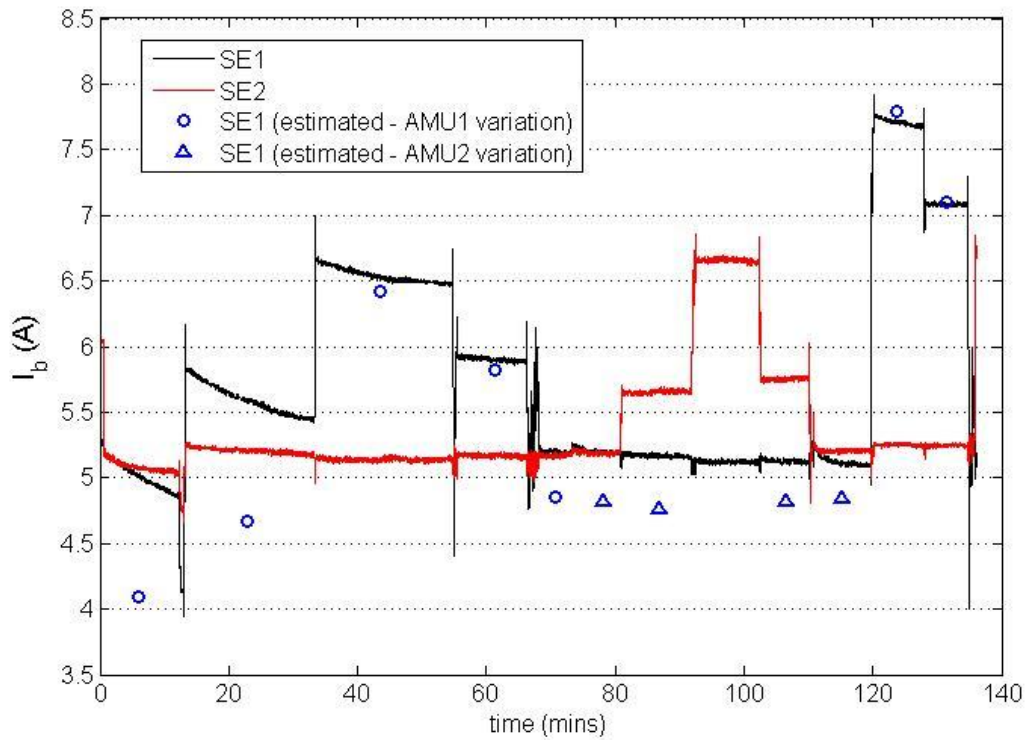


Figure 6.46. Beam current determined from measured grid currents for SE1 (black) and SE2 (red) whilst RF power to the two induction coils is varied via the antenna matching units. Also presented is the beam current determined from beam profiles of SE1 during variation of AMU1 (blue circles) and AMU2 (blue triangles).

($V_{ACC2} = -95V$, $V_b = 995V$, $\dot{m} = 0.058\text{mgs}^{-1}$, $\nu_{rf} = 5.25\text{MHz}$)

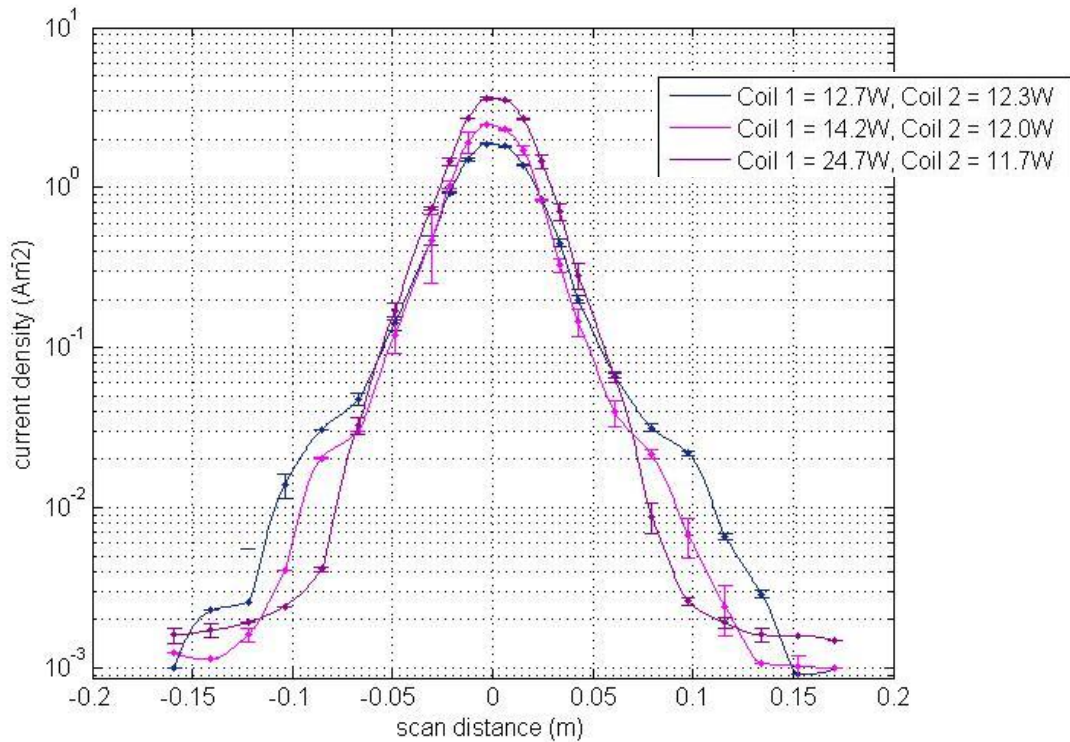


Figure 6.47. Log plot of beam profiles obtained of SE1 during variation of AMU1. The beam profiles at low power display a two-tier distribution indicating a greater percentage of CEX interactions influencing the beam.

($V_{ACC2} = -95V$, $V_b = 995V$, $\dot{m} = 0.058\text{mgs}^{-1}$, $\nu_{rf} = 5.25\text{MHz}$).

Thrust estimated from the beam currents for SE1 and SE2 is presented in Figure 6.48. A maximum net thrust of $\sim 125\mu\text{N}$ was achieved from the MiDGIT breadboard thruster operated at a flow rate of 0.058mgs^{-1} and beam and accelerator grid voltages of $995V/-95V$, with an equivalent specific impulse of $\sim 220\text{s}$ (see Figures 6.49 and 6.50). The thrust profiles also indicate that very low thrust levels down to $1\mu\text{N}$, and possibly sub- μN level, could be achieved if the thruster is allowed to thermally stabilize.

The requirement on specific impulse for fine thrust control will be challenging to meet. Specific impulse for the MiDGIT breadboard thruster during differential operation was of the order 70s at $40\mu\text{N}$ whereas requirements demand $>90\text{s}$ at $12\mu\text{N}$. It is important to minimize discharge losses for any thruster but more so for the MiDGIT thruster regarding differential operation.

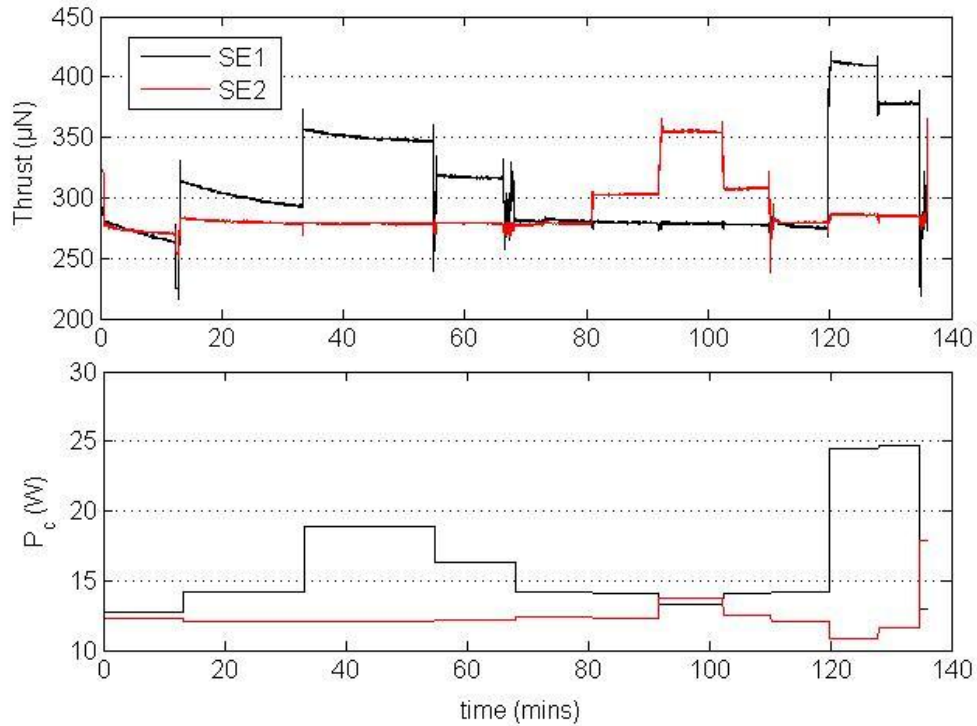


Figure 6.48. Thrust determined for SE1 and SE2 during differential operation of the MiDGIT breadboard thruster. RF power to each induction coil was varied by adjustment of the antenna matching units. ($V_{ACCI} = -95V$, $V_b = 995V$, $\dot{m} = 0.058mgs^{-1}$, $v_{rf} = 5.25MHz$)

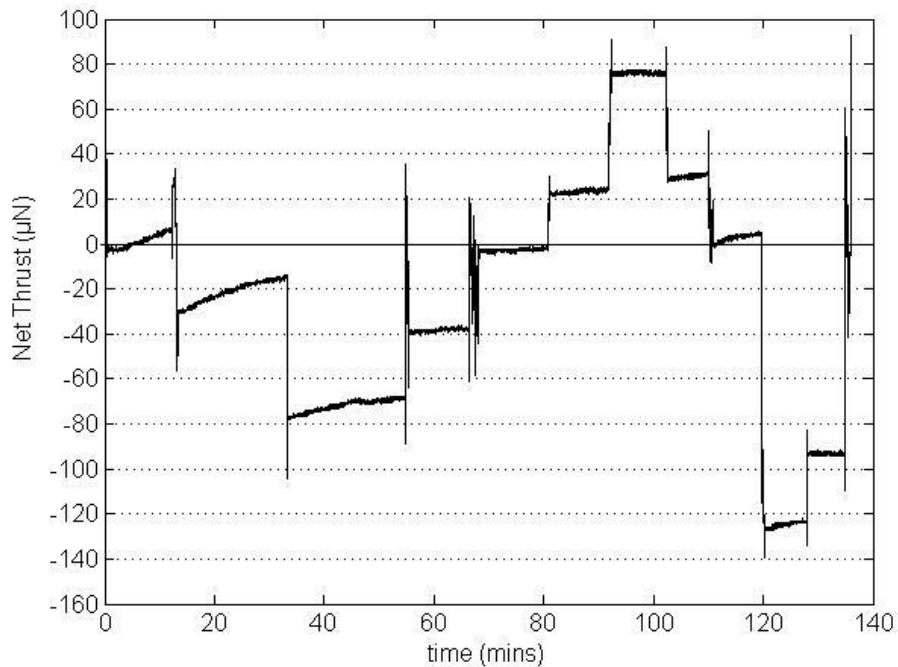


Figure 6.49. Net thrust during differential operation of the MiDGIT breadboard thruster. (A positive thrust indicating net thrust out of SE2)
($V_{ACCI} = -95V$, $V_b = 995V$, $\dot{m} = 0.058mgs^{-1}$, $v_{rf} = 5.25MHz$)

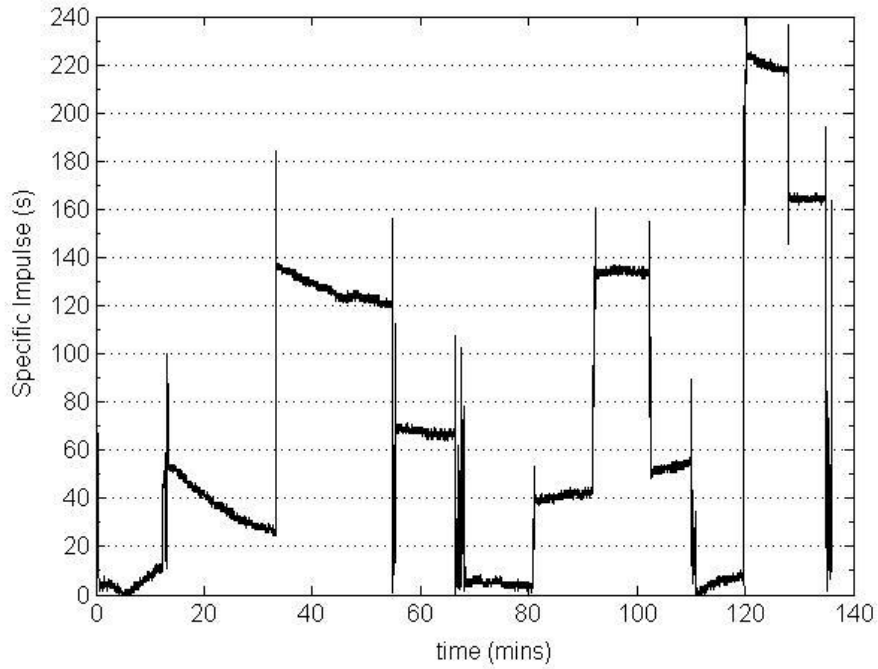


Figure 6.50. Specific impulse (determined from net thrust) during differential operation of the MiDGIT breadboard thruster. ($V_{ACC1} = -95V$, $V_b = 995V$, $\dot{m} = 0.058\text{mgs}^{-1}$, $\nu_{rf} = 5.25\text{MHz}$).

As can be seen from the initial tests on the MiDGIT prototype and breadboard models, differential control of the ion beams by variation of the RF power on each end of the thruster should be able to permit the full thrust range specified for fine thrust control to be achieved. The main disadvantage of the concept of a differential thruster however, is that due to the extraction of two ion beams to achieve very low thrust levels, the specific impulse will be low and the specific power very high compared to single-ended ion thrusters that can achieve the same thrust levels. Specific power for the MiDGIT breadboard thruster, incorporating the total beam power of the two extracted beams and the total power required for the two induction coils, can be calculated to be of the order of several 100 W/mN at best for these preliminary results.

6.2.2.5 Design Implications

As stated, with regards to differential operation of the MiDGIT thruster it will be particularly important to optimize mass utilization efficiency and electrical efficiency, and operate the thruster so as to keep total thruster efficiency at a maximum. It is therefore proposed that optimization of the geometry of the discharge chamber and the induction coils and optimization of the RF generator will be essential undertakings for any future engineering model to make it a viable option as a precision microthruster. However, even without re-designing the shape of the

discharge chamber, discharge losses could be reduced by minimizing the length of the discharge chamber for the MiDGIT thruster.

The grid to coil spacing could be reduced compared to the MiDGIT breadboard model. This would reduce wall losses but would also aid in increasing the ion density and electron temperature near the grids (as observed in Figures 6.51 to 6.55). Two discharge chambers were modeled in COMSOL Multiphysics; one with a grid to coil spacing of 10mm and one with a spacing of 15mm. The current in each induction coil was set to 7.5A for both cases and xenon neutral density kept constant at 20mTorr. The separation of the two induction coils was also kept constant at 10mm. The ion density and electron temperature along the grid boundary for the two cases are compared in Figure 6.54 and Figure 6.55 and can be seen to be higher for the reduced grid to coil spacing..

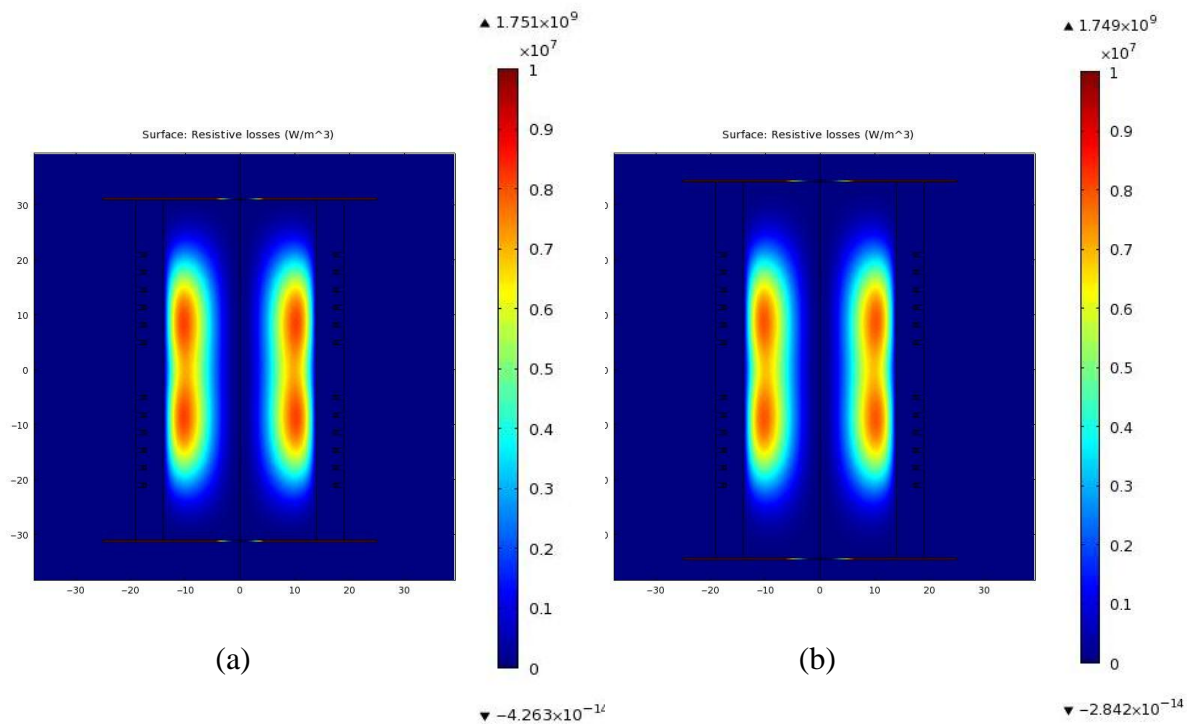


Figure 6.51. Resistive losses for a xenon discharge with a grid to coil spacing of (a) 10mm and (b) 15mm. (*neutral pressure* $P_n = 20\text{mTorr}$, *current per coil*, $I_{RF} = 7.5\text{A}$, $\nu_{rf} = 13.56\text{MHz}$).

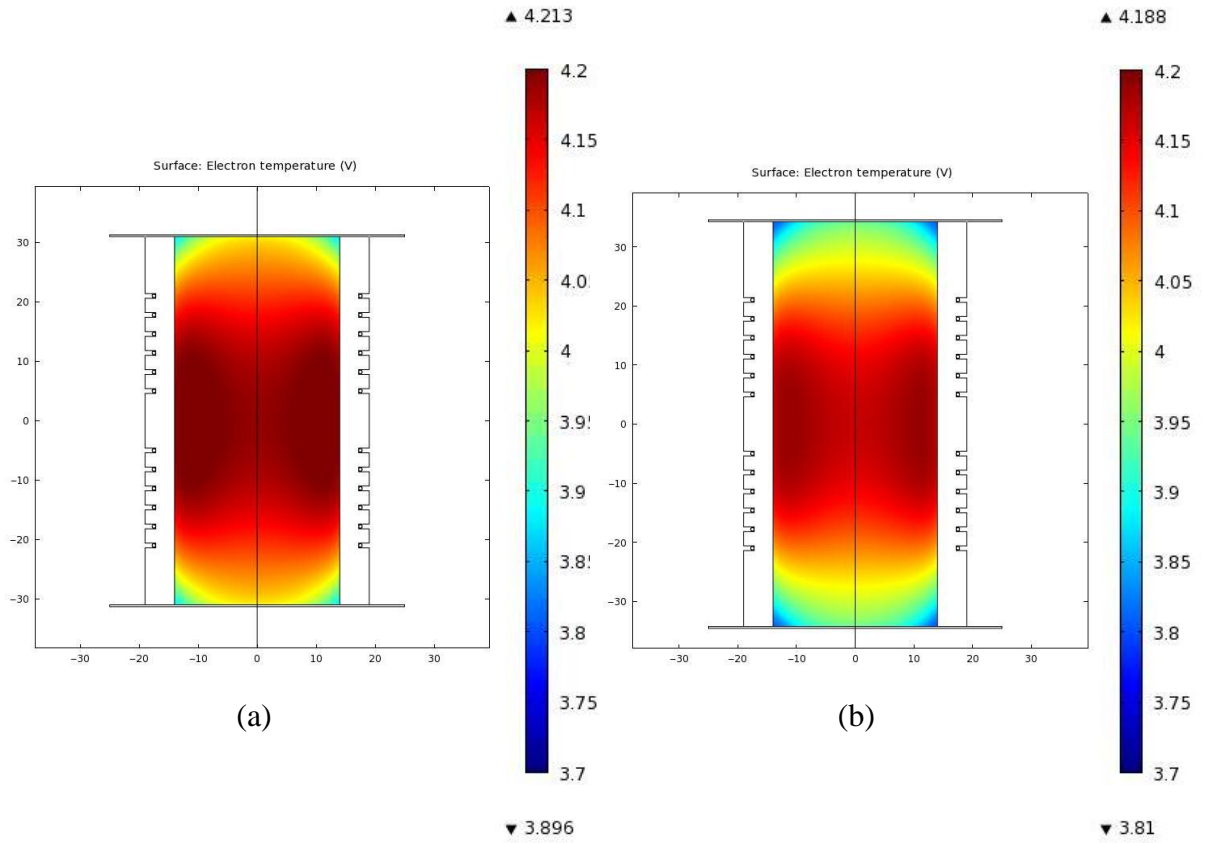


Figure 6.52. Electron temperature for a xenon discharge with a grid to coil spacing of (a) 10mm and (b) 15mm. (neutral pressure $P_n = 20\text{mTorr}$, current per coil, $I_{RF} = 7.5\text{A}$, $\nu_{rf} = 13.56\text{MHz}$)

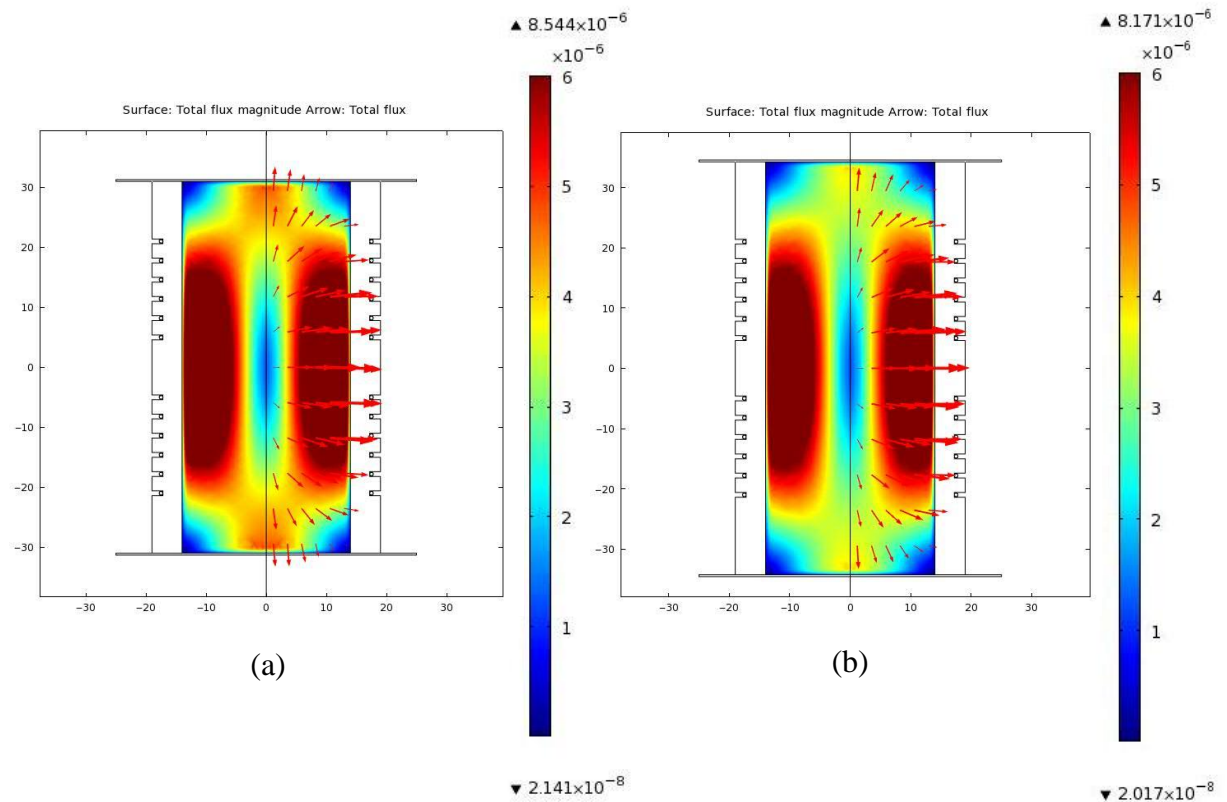


Figure 6.53. Ion flux for a xenon discharge with a grid to coil spacing of (a) 10mm and (b) 15mm. (neutral pressure $P_n = 20\text{mTorr}$, current per coil, $I_{RF} = 7.5\text{A}$, $\nu_{rf} = 13.56\text{MHz}$)

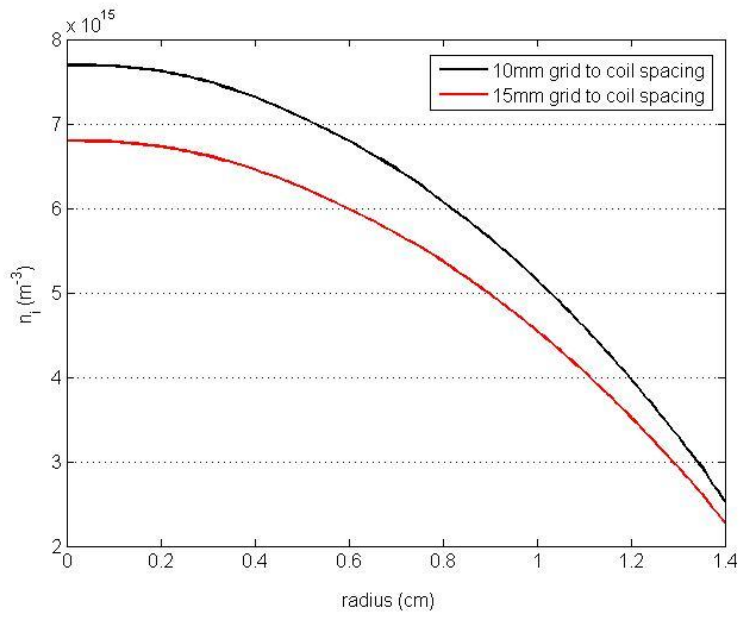


Figure 6.54. Comparison of ion density along grid boundary for a discharge with a 10mm grid-to-coil spacing and a 15mm grid-to-coil spacing.,
 (neutral pressure $P_n = 20\text{mTorr}$, current per coil, $I_{RF} = 7.5\text{A}$, $\nu_{rf} = 13.56\text{MHz}$)

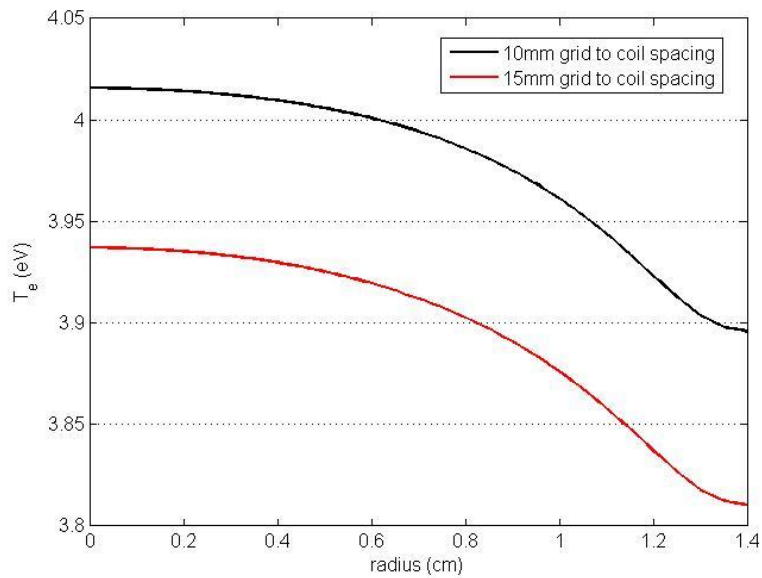


Figure 6.55. Comparison of electron temperature along grid boundary for a discharge with a 10mm grid-to-coil spacing and a 15mm grid-to-coil spacing.,
 (neutral pressure $P_n = 20\text{mTorr}$, current per coil, $I_{RF} = 7.5\text{A}$, $\nu_{rf} = 13.56\text{MHz}$)

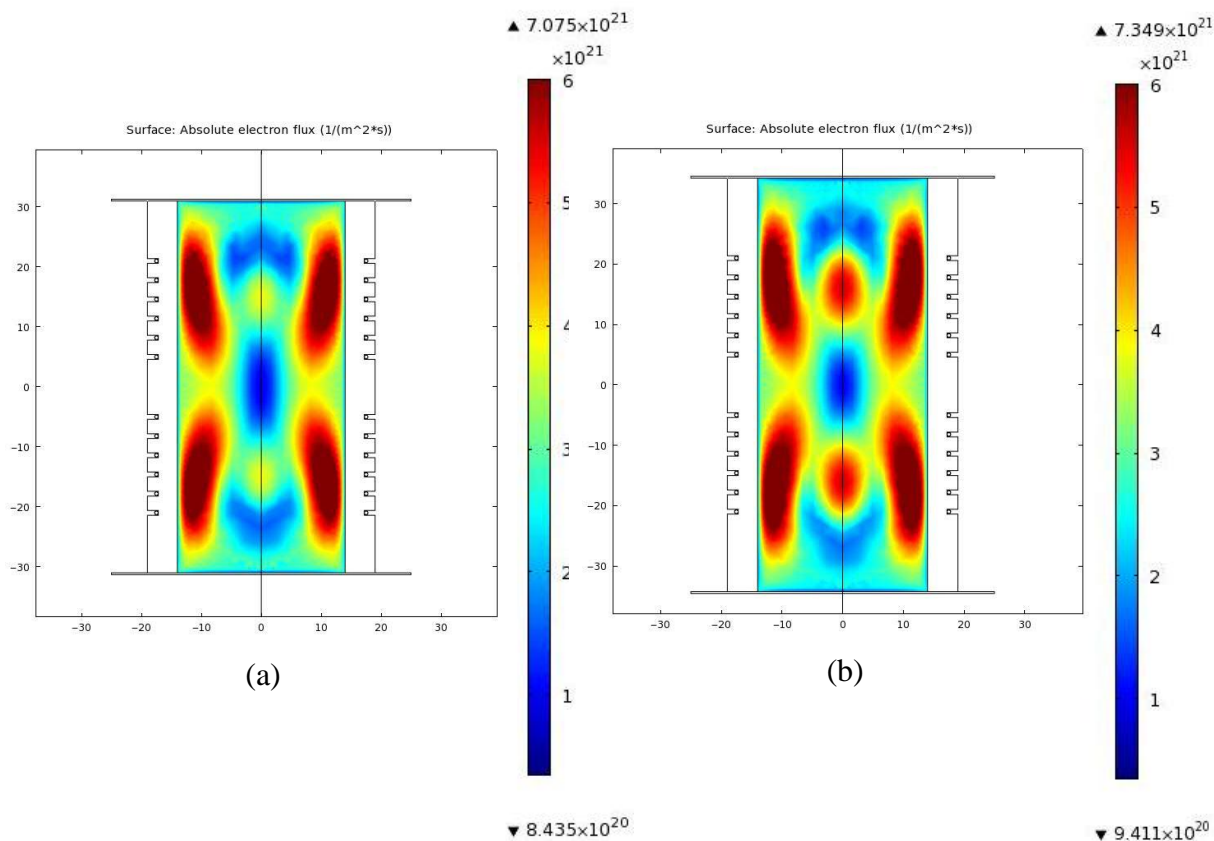


Figure 6.56. Electron flux for a xenon discharge with a grid to coil spacing of (a) 10mm and (b) 15mm. (*neutral pressure $P_n = 20\text{mTorr}$, current per coil, $I_{RF} = 7.5\text{A}$, $\nu_{rf} = 13.56\text{MHz}$*)

It might also be expected that discharge efficiency could be improved by gas injection into the regions where electron flux and temperature are greatest, as was partially demonstrated for the RIT-2.5 thruster [93]. As can be seen from Figures 6.52 and 6.56, electron temperature and electron flux are greatest directly underneath the coils; if it were possible to radially inject gas more uniformly along the length of the discharge chamber underneath the coils, this may improve efficiency to some degree compared to the annular gas distributor employed for the MiDGIT breadboard which was located in-between the induction coils.

The discharge chamber length could also be reduced, in order to reduce wall losses, by decreasing the separation of the induction coils. Ideally the adjacent coils would be located as close as possible to each other but mutual coupling between the coils, which may particularly affect differential operation of the thruster, might limit this distance. An optimal coil separation might be expected to minimize power losses and reduce any noise or instabilities that may result from close proximity of the two coils; this would be important to investigate and characterize during any future testing activities on the MiDGIT thruster.

6.3 SUMMARY OF DIFFERENTIAL THRUST CONTROL

Differential thrust control by variation of the accelerator grid voltage on each end of the MiDGIT thruster was not found to provide a suitable thrust range for fine thrust control. For the operating conditions of the preliminary tests, a net thrust between approximately $4\mu\text{N}$ - $25\mu\text{N}$ was achieved for an applied voltage range between -75V to -325V . As previously mentioned, high negative accelerator grid potentials are undesirable due to increased sputtering of the accelerator grid by CEX ions and should be kept in the region -100V [93]. The accelerator grid potential must also be kept more negative than the electron backstreaming limit; the predicted electron backstreaming limit for the MiDGIT breadboard grids was determined to be -84.4V at a beam potential of 950V , with measurements in approximate agreement with this value. At a beam potential of 1300V , the predicted electron backstreaming limit is approximately -115V . These points restrict the range over which the accelerator grid voltage should ideally be varied. Though differential control by variation of the accelerator grid voltage may not prove a means to achieve the thrust range required for fine thrust control alone, the results do indicate that very fine thrust resolution could be achieved by this method.

The two main control parameters for RF ion thrusters are the propellant mass flow rate and RF power. Differential thrust by variation of the RF power delivered to each end of the MiDGIT thruster was therefore investigated by use of two induction coils. Each induction coil could typically be driven by a separate RF amplifier and matching circuit with an RF attenuator in line to control the power delivered to each coil independently. However, only a single RF signal generator and amplifier were available during testing of prototype and breadboard models of the MiDGIT thruster; therefore, variation of the RF power to each coil was achieved by use of an antenna matching unit in between each coil and the RF amplifier, connected by a BNC T-piece connector, in order to vary the match to each coil and consequently, the power delivered to the coil.

Demonstration of differential control by adjustment of the variable tuning capacitor on the transmitter side of one of the antenna matching units was conducted using the MiDGIT prototype thruster operating with beam and accelerator grid potentials of $950\text{V}/-95\text{V}$ respectively. Rogowski coils provided an estimate of the RF current in each induction coil during the tests. The results suggested that a maximum net thrust of $\sim 115\mu\text{N}$ could be achieved when varying the tuning capacitor through its full range, with an estimated variation of approximately 2.7A (rms) current in the coil connected to the AMU being adjusted. The current in the opposite coil (with fixed settings on its matching unit) was observed to vary by approximately 0.8A (in an opposite manner) due to coupling across the T-piece connector.

The equivalent specific impulse at a net thrust of $115\mu\text{N}$ was $\sim 58\text{s}$ due to the high flow rate required for stable, dual ion beam extraction from the MiDGIT prototype thruster within the EP1 vacuum chamber. The smallest (net) thrust step that could be achieved by manual variation of the control dial for the capacitor was $\sim 4\mu\text{N}$; a much finer thrust resolution would be expected for finer control of the variable capacitors. Discharge diagnostics by use of triple Langmuir probes of the MiDGIT prototype thruster for similar settings but slightly lower coil currents (equivalently power levels) indicated that plasma density was of the order $2 \times 10^{17} \text{ m}^{-3}$ and electron temperature $\sim 3.5\text{eV}$. Axial measurements indicated that plasma density was higher underneath the coil with greater current, as would be expected.

Differential beam tests by variation of the AMUs were also performed on the MiDGIT breadboard thruster within the LEEP-1 loadlock chamber at the QinetiQ LEEP facilities, with a single T5 hollow cathode neutralizer providing neutralization. The MiDGIT breadboard thruster was expected to demonstrate better performance than the prototype thruster, which was apparent by the reduced flow rates compared to the prototype operated in the EP1 chamber. The breadboard thruster was operated at a frequency of 5.25MHz and flow rate of 0.058 mgs^{-1} with beam and accelerator grid potentials of $995\text{V}/-95\text{V}$. Beam profiles were obtained on one end of the thruster as verification of the electrical thrust. These were in good agreement at high beam currents but agreed only to within 80%-90% at relatively low beam currents. The beam profiles indicated that CEX collisions had an effect on the beam at low beam currents, and therefore the discrepancy may be the result of highly divergent CEX ions not being detected by the beam probe swept between $\pm 45^\circ$. A net thrust out of both ends was achieved, with a maximum of $\sim 125\mu\text{N}$ and equivalent specific impulse of $\sim 220\text{s}$. The thrust profiles during the tests indicated that thrust levels down to $1\mu\text{N}$, and even less, could possibly be maintained if the thruster is thermally stabilized. Thrust resolution was not characterized quantitatively but will be dependent on the resolution of the RF generator circuit (including variable RF attenuator). Performance of the MiDGIT breadboard thruster during initial differential operation is summarized in Table 6-6.

	MiDGIT breadboard (Differential)	RIT-4/7	Fine Thrust Requirement
Thrust range	< 1 μ N - 125 μ N [†]	10 μ N – 200 μ N	< 1 μ N - 150 μ N
Specific impulse	< 5s - 220s [^] (~70s @ 40 μ N)	3850s @ 250 μ N	>90s @ 12 μ N
Specific Power	> 300 W/mN [*]	-	< 50 W/mN
Flow rate	0.058 mgs ⁻¹	< 0.008 mgs ⁻¹	
Discharge power (P_{fw})	25W – 36.4W ^ᵈ	-	
Mass utilization efficiency	24% - 32% ^ᵈ	25% - 50%	
Electrical efficiency	26% - 31% ^ᵈ	<50%	
Minimum Discharge Loss	2217 eV/ion ^ᵈ	-	
Operating frequency	5.25 MHz	1 MHz	
Grid apertures (per grid set)	55	7	
Beam potential	995V	1100V to 1600V	
Accelerator potential	-95V	-100V to -200V	

† Net thrust

[^] Determined from net thrust and total flow rate

^{*} Determined from net thrust and total power for the two beams and coils

^ᵈ Values incorporate total beam current, total discharge power and total beam power where appropriate.

Table 6-5. Summary of initial performance demonstrated during differential operation of the MiDGIT breadboard thruster (*neglecting neutralizer power and flow rate*). (Performance data for the RIT-4/7 thruster is provided as a comparison ^[41]).

As can be seen, though the concept of a differential ion thruster permits a wide throttling range with the possibility of very fine thrust resolution, the extraction of two ion beams to achieve very low thrust levels will make such a thruster very inefficient compared to any single-ended ion thruster that can achieve the same thrust range (though a similar thrust range to that demonstrated by the MiDGIT has not currently been demonstrated by a single configuration of a single-ended ion thruster so far). Optimization of the geometry of the discharge chamber and induction coils and optimization of the RF generator will be particularly important to the performance of the MiDGIT thruster during differential operation.

Chapter Seven

7. Conclusion

Propulsion systems capable of providing low but highly accurate thrust levels in the sub- μN to mN throttling range will be an enabling technology for complex formation flying missions. Currently, propulsion systems baselined for these missions often comprise cold gas thrusters to provide coarse attitude control at mN level and miniature electric propulsion thrusters to provide precision control at low μN level [12]. An all-electric propulsion system would be attractive for a large number of missions due to the mass savings that could be achieved through the use of high specific impulse thrusters and the reduction of propellant tanks, pipework and valves. A need for a precision, low thrust, miniature electric propulsion device with a wide throttling range therefore exists.

The concept of a *differential* gridded ion thruster was initially proposed by the Ion Propulsion Group of QinetiQ to address this requirement. It was proposed that an unprecedented throttling range and thrust resolution could be achieved through differential control of opposing ion beams, enabling very small net offsets in thrust to be achieved. Also, single ion beam operation, as for conventional gridded ion thrusters, would permit mN thrust levels to be achieved with high specific impulse. A differential ion thruster utilizing a common radio frequency inductive plasma discharge from which two ion beams could be extracted was selected by QinetiQ to meet this objective. The extraction and control of two independent ion beams from a gridded ion thruster has never previously been reported.

The work presented in this thesis contributed to the design of prototype and breadboard models of the proposed Miniaturised Differential Gridded Ion Thruster (MiDGIT) and provides the first study and characterisation of such a configuration of miniature gridded ion thruster. This chapter summarizes the main results and conclusions of the work, highlighting the significance of the work with regards to assessment of the MiDGIT thruster as a viable micropropulsion option for missions requiring precision attitude control.

7.1 PRELIMINARY PERFORMANCE OF THE MIDGIT THRUSTER

Test campaigns were performed on prototype and breadboard models of the MiDGIT thruster in order to provide a proof-of-concept for a twin-ended differential ion thruster, to investigate design issues and to demonstrate preliminary performance. The MiDGIT thruster was designed with the intention of achieving precise μN thrust levels through differential operation and higher mN thrust levels, with high specific impulse, through single-end operation required for coarse thrust control.

7.1.1 Coarse Thrust Control

A detailed characterisation of the MiDGIT breadboard thruster configured for single-end operation was performed in collaboration between the author and QinetiQ at the QinetiQ Large European Electric Propulsion Facilities to determine baseline performance with regard to coarse thrust control requirements. Data was obtained to determine thrust range, specific impulse, specific power and beam divergence. The breadboard thruster incorporated a simple ceramic shutter plate inserted across the diameter of the discharge chamber to restrict neutral flow to one half of the thruster in order to achieve high specific impulse.

Single-end (SE) operation of the MiDGIT breadboard thruster has initially demonstrated thrust levels between $200\mu\text{N}$ - $500\mu\text{N}$ and specific impulse of 400s - 1100s using beam and accelerator grid voltages of 950V / -95V respectively. Beam profiles were obtained by use of a single screened faraday cup probe in order to provide verification of the measured electrical thrust and to determine a thrust correction factor to account for losses due to beam divergence. No correction for doubly-charged ions was applied as the amount was assumed to be negligible; the ratio of doubly-charged to singly-charged ions is typically $<1\%$ within RF ion thrusters [40]. The extracted ion beams were observed to be affected by CEX interactions at low beam currents due to the high background pressure ($\sim 10^{-4}$ mbar) during the tests performed within the QinetiQ LEEP-1 loadlock chamber. Beam divergence was estimated to be of the order 13° from the measured beam profiles. Additional tests that were performed solely by QinetiQ at a later stage in the test campaign within the LEEP-3 vacuum facility in order to reduce background pressure to 2.1×10^{-5} mbar, demonstrated that maximum thrust, achieved prior to the onset of direct ion impingement on the accelerator grid, could be increased to $\sim 780\mu\text{N}$ by increasing the beam voltage to 1300V [100]. Step wise thrust variation was also demonstrated by QinetiQ [88]. Thrust resolution was observed to be of the order of $25\mu\text{N}$ worst-case, limited by the 0.1dB resolution of the signal generator.

7.1.2 Fine Thrust Control

Tests were performed on both the prototype and breadboard models of the MiDGIT thruster configured for differential operation to provide a proof-of-concept for dual ion beam extraction and to investigate differential control methods for achieving the thrust requirements specified for fine thrust control.

It was originally proposed by QinetiQ that very fine control of the ion beam current could be achieved by fine adjustment of the accelerator grid voltage, and therefore, the low and precise thrust requirements for fine thrust control could be achieved by varying the accelerator grid voltage on either end of the thruster to create a net imbalance in thrust.

Tests were performed on the MiDGIT breadboard thruster within the QinetiQ LEEP-1 loadlock by the author and QinetiQ regarding differential ion beam control by variation of the accelerator grid potential. Beam profiles indicated that independent control of the ion beams was possible by separately varying the accelerator grid potential on either end of the thruster. In general, a positive increase in screen grid current and accelerator grid current with increasingly negative accelerator grid potential was observed for the grid set being varied. Beam profiles displayed some de-focussing of the extracted ion beam with increasingly negative V_{ACC} . The results support the theory that the plasma sheath upstream of the screen grid apertures becomes more convex with increasingly negative V_{ACC} , as observed in the simulations of Zhong et al [71]. For the operating conditions of the tests performed, a net thrust between approximately $4\mu\text{N}$ - $25\mu\text{N}$ was achieved for an applied voltage range between -75V to -325V . High negative accelerator grid potentials should ideally be avoided to reduce sputtering of the accelerator grid by CEX ions, particularly so for missions with a high total impulse requirement of several 1000Ns . The accelerator grid potential is also limited by the electron backstreaming limit; therefore, the range over which the accelerator grid voltage can ideally be varied is restricted. The results of these tests indicate that the full thrust range of $1\mu\text{N}$ - $150\mu\text{N}$ specified for fine thrust control can not be achieved by variation of the accelerator grid potentials; however they do indicate that very fine thrust resolution can be achieved, as originally proposed.

It was suggested during the course of this work that differential thrust control could also be achieved by varying the RF power delivered to each end of the thruster to create a higher plasma density on one end of the discharge, and ultimately, a greater thrust out of that end (extracted ion current being dependent on ion density and electron temperature at the sheath

edge upstream of the extraction grids through the Bohm current). Differential thrust by variation of the RF power delivered to each end of the MiDGIT thruster was therefore investigated by use of two induction coils. Only a single RF signal generator and amplifier were available during the test campaigns; variation of the RF power to each coil was therefore achieved by use of an antenna matching unit inserted in-between each coil and the RF amplifier, connected by a BNC T-piece connector, in order to vary the match to each coil and consequently the power delivered to each of the coils.

Demonstration of differential control by adjustment of the variable tuning capacitor on the transmitter side of one of the antenna matching units was conducted by the author within the EP1 vacuum chamber at Southampton using the MiDGIT prototype thruster. Rogowski coils were used to provide an estimate of the current within each of the induction coils. An estimated net thrust up to $\sim 115\mu\text{N}$ (determined from the grid currents) could be achieved when varying the tuning capacitor through its full setting range. The equivalent specific impulse at a net thrust of $115\mu\text{N}$ was $\sim 58\text{s}$ due to the high flow rate found to be required for stable, dual ion beam extraction within the EP1 vacuum chamber. The smallest (net) thrust step that could be achieved by manual variation of the control dial for the tuning capacitor was $\sim 4\mu\text{N}$; a much finer thrust resolution would be expected for finer control of the variable capacitors of the antenna matching units. Triple Langmuir probes were also used to perform discharge diagnostics of the MiDGIT prototype thruster, with axial measurements indicating that plasma density can be increased on one end of the discharge chamber by increasing the RF current in the induction coil on that end with respect to the other coil. Plasma density and electron temperature were measured to be of the order $2 \times 10^{17} \text{ m}^{-3}$ and 3.5eV respectively, as might be expected for a 3cm diameter RF ion thruster [24, 25].

Differential beam tests by variation of the capacitor settings on the antenna matching units were also performed on the MiDGIT breadboard thruster within the LEEP-1 loadlock chamber by the author and QinetiQ, with the breadboard thruster expected to provide better performance than that demonstrated by the prototype thruster. The breadboard thruster was operated at a frequency of 5.25MHz and flow rate of 0.058 mgs^{-1} , with beam and accelerator grid potentials of $995\text{V}/-95\text{V}$. Beam profiles were obtained on one end of the thruster as verification of the electrical thrust. These were in good agreement at high beam currents but agreed to within only 80%-90% at relatively low beam currents. The beam profiles indicated that CEX collisions had an effect on the beam at low beam currents, and therefore the discrepancy may be the result of highly divergent CEX ions not being detected by the beam probe swept between $\pm 45^\circ$. A maximum net thrust of $\sim 125\mu\text{N}$ and equivalent specific impulse

of ~220s were achieved indicating that the full thrust range up to 150 μ N should be possible for fine thrust control. The thrust profiles also indicated that thrust down to 1 μ N, and even less, could possibly be maintained if the thruster is thermally stabilized. Further steady-state thrust data would be required to better assess the minimum thrust level.

7.1.3 General Observations

Discharge ignition was achieved during the test campaigns on the MiDGIT prototype and breadboard thrusters by use of filament cathodes and also by a T5 hollow cathode neutralizer. The neutral pressure required for ignition was estimated to be in the region 5-6mTorr based on the observed flow rates for both single-end and differential operation (with background pressure $\sim 10^{-4}$ mbar). RF power required for ignition during differential operation was approximately twice that required for SE operation, as might be expected due to the two matching units and induction coils presenting twice the power losses. Ignition at slightly lower flow rates might be achieved within a higher vacuum environment which might facilitate a greater conductance of electrons from the cathode to the discharge chamber. Ignition was observed to be difficult after prolonged operation of the thruster as a result of heating of the inductions coils increasing coil resistance. Thermal effects were also observed to particularly influence thrust level during differential operation; closed loop control by a PID beam current controller, as applied for the RIT thrusters, would be important for future tests to achieve steady state thrust.

Self-ignition was observed during testing of the MiDGIT prototype thruster within the EP1 chamber, expected to be due to the higher operating pressure required for the prototype thruster within this chamber compared to tests performed at the QinetiQ LEEP facilities. Self-ignition at high discharge pressures would be useful in terms of response time of a thruster but would have implications on propellant requirements unless very short pressure impulses can be applied.

Discrepancies were observed between the different mass flow controllers employed during characterisation of the two ends of the MiDGIT breadboard thruster, leading to a slight difference in performance between the two ends. This highlights the importance of reliable and accurate flow control systems for electric propulsion thrusters, as the performance and specific impulse of a thruster can be severely impacted.

7.2 SUITABILITY AS A PRECISION MICROTHRUSTER

A summary of the performance of the MiDGIT breadboard thruster is provided in Table 7-1, along with performance data for competing microthruster technologies and requirements for coarse thrust and fine thrust control.

Electrical efficiency and mass utilization efficiency for the MiDGIT breadboard thruster was found to be low compared to similar miniature RF ion thrusters. Significant improvements to electrical efficiency can be expected by operating the MiDGIT thruster with an optimized RF supply located directly next to the thruster; the development programme of the MiDGIT thruster unfortunately did not allow for the additional development of a dedicated, vacuum compatible RF generator. The design of the induction coil should also be improved to minimize coil resistance.

Although a reasonable thrust range was achieved for both single-end and differential modes of the MiDGIT breadboard thruster, it can be seen that the current configuration of the thruster is unable to meet the propulsion requirements specified. Poor power coupling to the plasma led to specific power being considerably high even for SE operation. An increase of up to 50% in coupling efficiency would be required to reduce power levels in order to meet the requirement of 50W/mN during SE operation. Increased power coupling may also permit reductions in propellant flow rate and the possibility of lowering the minimum thrust level. Maximum thrust level could be increased by either operating the thruster at higher beam voltages than 1300V or increasing the number of grid apertures, although these would impact the minimum thrust level achievable. Discharge losses could be reduced by possibly moving to a conical shaped discharge chamber for each end of the MiDGIT thruster. A semi-spherical discharge chamber has been identified by Closs [67] to be the optimal geometry for a single-ended RF ion thruster and implementation of such a geometry for the RIT-2.5 thruster was found to provide a 15%-25% increase in electrical efficiency [93].

Differential control by variation of the RF power delivered to the induction coils on each end of the MiDGIT thruster has been identified to provide a means for achieving the full thrust range specified for fine thrust control. The extraction of two ion beams to achieve very low thrust levels however leads to specific impulse being very low and specific power very high compared to other microthrusters that can achieve the same thrust levels (as can be seen in Table 7-1 by comparison of the MiDGIT with the RIT and FEEP thrusters). The use of a single thruster which can provide both coarse and precision thrust capability over a wide throttling range however, may provide overall system mass savings and increased redundancy compared to a

	MiDGIT †	RIT-4/7 †	RIT-2.5/37 †	FEEP	Requirement
Thrust range (Coarse)	200 μ N - 780 μ N	10 μ N – 200 μ N	50 μ N - 575 μ N	0.25 μ N - >450 μ N	150 μ N - >1mN
Thrust range (Fine)	< 1 μ N - 125 μ N				<1 μ N – 150 μ N
Specific impulse (Coarse)	500s – 1100s	3850s @ 250 μ N	363s – 2861s	4000s – 8000s	>1500s @ 1mN
Specific impulse (Fine)	< 5s – 220s (~70s @ 40μN)				>90s @ 12 μ N
Thrust Resolution	4 μ N - 25 μ N	0.44 μ N	-	<0.5 μ N	<0.5 μ N
Specific Power (Coarse)	> 55 W/mN	-	> 59.8 W/mN	< 80 W/mN	<50W/mN
Specific Power (Fine)	> 300 W/mN	-			
Mass utilization efficiency	< 30%	< 50%	< 50%	-	
Electrical efficiency	< 35%	<50%	<50%	-	
Propellant	Xenon	Xenon	Xenon	Indium	
TRL *	4	4	4	-	

† Neglecting neutralizer power and flow rate

* Technology Readiness Level

Table 7-1 – Comparison of the performance of the MiDGIT breadboard thruster against competing microthrusters [27, 41, 93, 114]

similar system utilizing single-ended RF ion thrusters, provided that power requirements for the MiDGIT system can be accommodated. The use of xenon as a propellant also alleviates concerns over contamination of optical and other spacecraft components, which is a disadvantage for FEEP thrusters.

Thrust resolution was not characterized quantitatively in great detail during differential operation of the MiDGIT breadboard thruster but results of the differential tests regarding variation of the accelerator grid voltage suggest that this method in combination with differential control via the RF power could provide a means for very precise thrust control over the full thrust range specified for fine thrust control, possibly even providing sub- μN resolution. Variation of both the accelerator grid voltage and RF power during differential operation of the thruster however would require greater complexity in the thruster control algorithms.

In order for the MiDGIT thruster to be a viable option as a microthruster considering current technologies, it will be important to maximize mass utilization efficiency and electrical efficiency as far as possible, particularly so regarding differential operation. It is therefore proposed that optimization of the geometry of the discharge chamber and the induction coils and optimization of the RF generator will be essential undertakings for any future engineering model.

7.3 SIGNIFICANCE OF THE WORK

The extraction and independent control of two ion beams from a gridded ion thruster has never previously been reported. This work has confirmed:

- 1 Two stable ion beams can be extracted simultaneously from a common inductive plasma discharge.
- 2 The extracted ion beams can be controlled to produce a net offset in thrust.
- 3 The feasibility of single ion beam operation by use of a gating mechanism across the discharge chamber of the thruster.

Two control methods were identified which permit differential control of the ion beams. The method initially proposed by QinetiQ by variation of the accelerator grid potential has been confirmed to provide very small thrust changes as expected, but testing indicated that it will not be able to achieve the full thrust range specified for fine thrust control. Results of the tests performed regarding variation of the accelerator grid potential provide support to the theory that the plasma sheath upstream of the screen grid apertures becomes more convex

with increasingly negative accelerator grid potential, as observed in the simulations of Zhong et al. [71].

This work has also demonstrated that differential ion beam control can be achieved by varying the RF power delivered to each end of the discharge by varying the relative current in two adjacent induction coils. Triple Langmuir probe measurements have provided the first discharge diagnostics of such a configuration of thruster and indicate that plasma density can indeed be controlled on each end by this method.

A 2D cylindrical axisymmetric discharge model developed using the plasma simulation module of COMSOL Multiphysics has demonstrated the principles by which inductive coupling can control the plasma density in the MiDGIT thruster and has provided an insight into the effect of varying the relative current in two induction coils on a plasma discharge common to both coils.

RF power to each of the coils of the MiDGIT thruster would ideally be controlled by two independent RF generator circuits, each incorporating a RF power attenuator. Such a set up was not available during the test campaigns on the MiDGIT thruster but differential control was demonstrated using a single RF signal generator and RF amplifier connected to two matching units. Measurements conducted by the author have shown that adjustment of the variable tuning capacitor on the transmitter side of one of the antenna matching units can provide a suitable variation in beam current on each end of the thruster to provide a net thrust range of the order required for fine thrust control.

Ultimately the work presented in this thesis has contributed to the MiDGIT thruster achieving a Technology Readiness Level of 4 [115].

7.4 RECOMMENDATIONS AND FUTURE WORK

Limitations to the performance of RF ion thrusters exist due to the focusing range of the ion extraction grids and the optimal transfer of power to sustain the discharge against losses. As stated previously, the efficiency of the MiDGIT thruster must be maximized in order for it to be a viable option as a microthruster. Particularly, the electrical efficiency must be significantly improved. It is recommended that the following work must be undertaken if the MiDGIT concept is to be developed further:

- Develop a dedicated, vacuum compatible RF generator to minimize power losses and identify the optimal operating frequency for the thruster. (*This work showed that the MiDGIT thruster can be operated at the same frequency during both single-end and differential operation and therefore only a fixed-frequency source should be required*).
- Identify the optimal geometry for the discharge chamber to minimize surface losses.
- Optimize the geometry of the extraction grids to maximize ion transparency but minimize neutral transparency. A third grid may be required, as has been identified by the University of Giessen for the RIT microthrusters [93].
- Optimize the design of the induction coils to minimize coil resistance.
- Investigate the optimal design for gas injection, which may provide some improvement to discharge efficiency through injection of gas into regions where electron temperature and flux are greatest.
- Ultimately, and most importantly, conduct direct thrust measurements in order to verify net thrust produced during differential operation.

Spatial mapping of plasma parameters for the MiDGIT thruster would assist the suggested work and also provide input to grid optimization studies. An accurate 2D, or even 3D, discharge model would be an extremely useful tool for optimizing the discharge chamber. The fluid model developed in this work is not strictly valid for the conditions of the MiDGIT thruster and two of the main limitations of the model (as stated in Appendix B) are that capacitive coupling was not included and that neutral density was assumed uniform meaning the effect of neutral injection into the discharge chamber on plasma distribution could not be assessed. It is recommended that a PIC-MCC (or PIC-DSMC) model or a hybrid model combining fluid assumptions and PIC-MCC should be developed to capture non-local electron kinetic effects. It may be particularly interesting to model the discharge region between the coils to determine the effect of coil separation and field geometry on the discharge.

Background pressure was observed to be high during the tests performed on the MiDGIT thruster within the QinetiQ LEEP-1 loadlock chamber and the EP1 vacuum chamber at Southampton. Charge-exchange interactions were observed to have an effect on the extracted ion beams and the accelerator grid currents were relatively high, of the order 5% of the beam current. Operation of the MiDGIT thruster within a higher vacuum environment will be essential for any future performance or lifetime testing of an engineering model. Three important factors to characterize will be thruster self-ignition at high neutral pressure, noise levels (and any instabilities) and thruster resolution.

Appendix A

A. Triple Langmuir Probe Theory

A.1 LANGMUIR PROBES

Langmuir probes were first introduced in 1926 by Mott Smith and Langmuir as an early diagnostic tool for measuring plasma properties [57]. They are relatively simple devices generally consisting of an exposed wire inserted into a plasma, to which a variable bias is applied in order to draw a current. Application of appropriate theories regarding electron and ion current collection enables estimates for plasma density, electron temperature, plasma potential and floating potential to be extracted from the current-voltage characteristic of the probe. Interpretation of the characteristic is often problematic however, and as Langmuir probes are intrusive to the plasma, consideration must be given to the design and operation of the probes to minimise probe induced perturbations. Numerous reviews on Langmuir probes and associated issues can be found by Chen [58], Hutchinson [56], Huddleston [55] and Merlino [101].

An example of a typical Langmuir probe I-V characteristic is given in Figure A.1. The ion current collected by the probe is typically displayed as negative and electron current as positive.

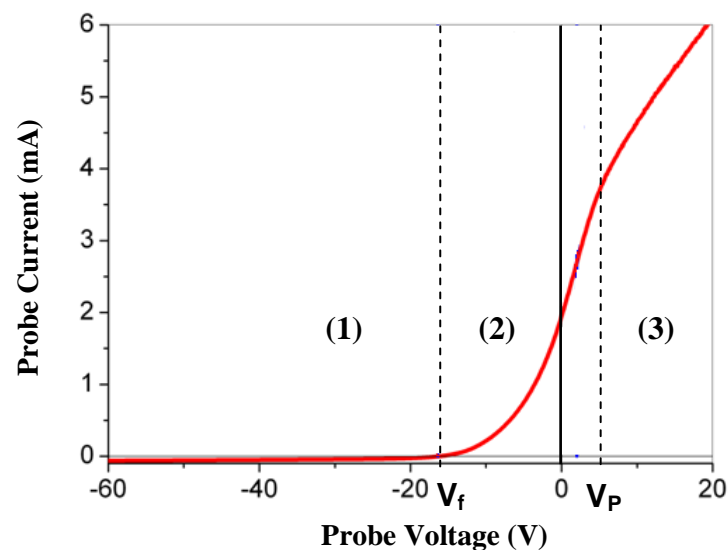


Figure A.1. A typical I-V trace for a Langmuir probe.

Three distinct regions are apparent:

1) Ion saturation region

When the probe is biased sufficiently negative with respect to the plasma, only ions are collected and a positive space-charge sheath forms around the probe to screen the bulk plasma from the effect of the localized potential. The linear region of the probe characteristic at negative potentials is termed the ion saturation region. The probe current measured in this region is not constant as might be expected, but the magnitude of the current increases as the probe voltage becomes increasingly negative. This is a result of sheath effects.

The thickness of the sheath surrounding the probe can be approximated by the following equation considering the Child-Langmuir law:

$$s = \frac{\sqrt{2}}{3} \lambda_{ds} \left(\frac{2eV_{sh}}{kT_e} \right)^{3/4} \tag{A.1}$$

where V_{sh} represents the potential difference across the sheath and λ_{ds} is the electron Debye length evaluated from the plasma density at the sheath edge [46]. As the potential across the sheath increases, the sheath thickness increases resulting in a larger surface area for the sheath boundary and therefore, larger collection area for ions. The magnitude of the probe current can therefore be observed to increase as the difference between the probe voltage and plasma potential increases.

2) Transition region

As the probe voltage is increased to more positive potentials, high energy electrons begin to be collected by the probe as these electrons are able to overcome the Coulomb barrier and the probe current starts to deviate from linearity. At the point where the net current to the probe is zero, equal amounts of ions and electrons are collected. The potential at this point is termed the floating potential V_f . Further increase to the probe voltage above the floating potential results in more electrons being collected by the probe and the low-energy ions to be repelled. The region of the I-V characteristic displaying an exponential relation is termed the transition region and represents the range of potentials over which both ion and electron currents are collected by the probe.

3) Electron saturation region

When the probe potential reaches the plasma potential, no electric field exists to accelerate charged particles to the probe; therefore, the total current collected by the probe at this point is that due to the random thermal fluxes of ions and electrons only. As the probe voltage is increased above the plasma potential, all of the low energy ions are repelled and only electrons are collected. This region is termed the electron saturation region and an electron sheath forms. Again, the probe current is not constant in this region but displays a positive gradient on the I-V characteristic due to the sheath expanding as the probe voltage is increased. An ideal Langmuir probe characteristic should display a distinct ‘knee’ in the I-V curve at the plasma potential.

A.1.1 Analysis of the I-V Characteristic

In order to extract estimates of plasma parameters from the I-V characteristic of a Langmuir probe, the ion and electron components of the probe current must be separated. The simplest and crudest method often employed is to fit a straight line to the linear section of the characteristic in the ion saturation region; the ion saturation current is then taken as the probe current measured at the point where the current departs from linearity, which can then be subtracted from the total probe current to give electron current. Alternatively, the linear fit over the ion saturation region can be extrapolated to the transition region and then subtracted from the total probe current to give electron current [46].

A.1.1.1 Electron Temperature

Provided electrons are Maxwellian, the Boltzmann relation states that the electron density in the vicinity of the probe will vary exponentially with the potential across the sheath according to:

$$n_s = n_{e0} \exp\left(\frac{e(V_p - V_{Lp})}{kT_e}\right) \tag{A.2}$$

where n_{e0} is the electron density at the plasma-sheath boundary, and the probe and plasma potentials are given by V_{Lp} and V_p respectively [46].

The electron current diffusing to the probe with a surface area A_p is given by:

$$I_e = \frac{1}{4} en_s \bar{u}_e A_p \quad (\text{A.3})$$

where the mean electron velocity is:

$$\bar{u}_e = \left(\frac{8kT_e}{\pi m_e} \right)^{1/2} \quad (\text{A.4})$$

The electron current can therefore be written in terms of the bulk plasma density and probe voltage as:

$$I_e = en_{e0} A_p \left(\frac{kT_e}{2\pi m_e} \right)^{1/2} \exp\left(\frac{e(V_p - V_{Lp})}{kT_e} \right) \quad (\text{A.5})$$

with the electron saturation current defined to be:

$$I_{es} = en_{e0} A_p \left(\frac{kT_e}{2\pi m_e} \right)^{1/2} \quad (\text{A.6})$$

The electron current within the transition region should therefore be linear if plotted on a semi-log plot against probe voltage. An estimate of the electron temperature can then be obtained from the gradient of the linear region according to:

$$\frac{d(\ln I_e)}{dV_{Lp}} = \frac{e}{kT_e} \quad (\text{A.7})$$

A.1.1.2 Plasma Potential

The plasma potential is identified by the inflection point in the I-V characteristic where the gradient of the curve changes between the transition and electron saturation regions. Plasma potential can be determined from the maxima of the first derivative of the electron current (I'_e) or the zero of the second derivative of electron current (I''_e).

Alternatively, plasma potential can also be approximated from the floating potential and the estimated electron temperature according to:

$$V_f - V_p = \frac{kT_e}{2e} \left[\ln \left(2\pi \frac{m_e}{M_i} \right) - 1 \right] \quad (\text{A.8})$$

For xenon, this equation reduces to:

$$V_p = V_f + 5.77 \left(\frac{kT_e}{e} \right) \quad (\text{A.9})$$

A.1.1.3 Plasma Density

The electron saturation current is taken as the electron current measured at the plasma potential, from which an estimate of electron density can be made:

$$n_{e0} = \frac{I_{es}}{eA_p} \left(\frac{2\pi m_e}{kT_e} \right)^{1/2} \quad (\text{A.10})$$

Sheath expansion, collisions within the sheath, magnetic fields, plasma oscillations and even averaging in the data acquisition process all influence the profile of the measured probe current, which can lead to a rounding of the ‘knee’ in the I-V characteristic [46, 56]. Sharp, well defined inflection points are only normally obtained for low pressure, low density, unmagnetized DC plasma discharges [86]. Estimates of plasma density obtained from the electron saturation current can therefore have relatively large associated uncertainties. It is often advised that more accurate estimates of the plasma density can be obtained from measurements of the ion saturation current assuming quasineutrality [58].

The ion flux at the sheath boundary is given by:

$$\Gamma_i = n_s u \quad (\text{A.11})$$

The Bohm criterion states that in order for a stable and monotonically decreasing sheath potential to form, the ions must fall through a potential in the plasma of at least $(T_e/2)$ volts before entering the sheath, in order for the ions to enter the sheath with a velocity of at least:

$$u_B = \left(\frac{kT_e}{M_i} \right)^{1/2} \quad (\text{A.12})$$

which is termed the Bohm velocity [46]. The plasma produces the required potential drop across a region which is known as the *presheath* in order to accelerate the ions. Quasineutrality is assumed to hold within the presheath [46].

Assuming electrons are Maxwellian, so that electron density is approximated by the Boltzmann relation given in Equation A.2, and that the plasma is quasineutral, the ion saturation current can be given by:

$$I_{is} = en_{e0}A_p \exp\left(-\frac{e}{kT_e} \left(\frac{kT_e}{2e}\right)\right) \left(\frac{kT_e}{M_i}\right)^{1/2} \quad (\text{A.13})$$

which reduces to:

$$I_{is} = 0.61en_{e0}A_p \left(\frac{kT_e}{M_i}\right)^{1/2} \quad (\text{A.14})$$

This current defined in equation A.14 is also referred to as the Bohm current [46]. Measurement of the ion saturation current and knowledge of T_e then provides an estimate for ion density (or electron density assuming quasineutrality).

The above equation for the Bohm current to the probe is only valid for collisionless, planar sheaths however. A generalised form of the Bohm current for cylindrical Langmuir probes is given by:

$$I_{is} = \alpha en_{e0}A_p \left(\frac{kT_e}{M_i}\right)^{1/2} \quad (\text{A.15})$$

where the parameter α varies with the ratio of probe radius to Debye length ($\xi = r_p/\lambda_d$), with the Debye length being a measure of the sheath thickness [58].

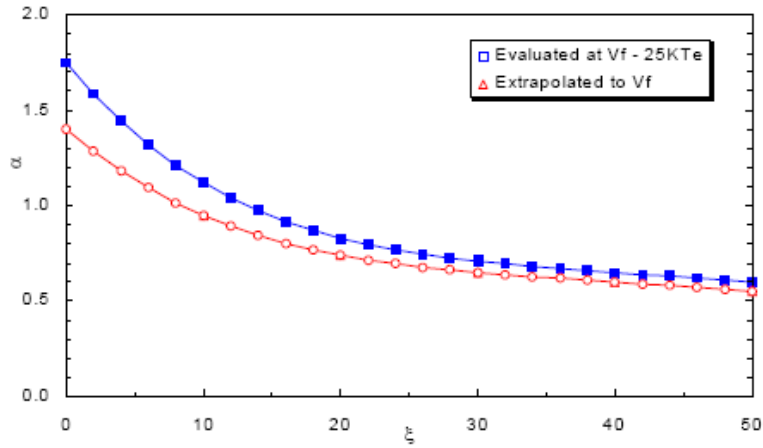


Figure A.2. Values for parameter α used to determine Bohm current to a cylindrical Langmuir probe^[58].

As briefly mentioned, and is apparent from Figure A.2, the nature of the sheath will affect the ion current collected by the probe. The sheath can be defined to be; *collisional*, if the mean free paths for ion-ion (λ_{ii}), ion-electron (λ_{ie}) and ion-neutral (λ_{in}) collisions are less than the Debye length (λ_d); *collisionless*, if the mean free paths are larger than the Debye length λ_d ; *thick*, if the Debye length is much greater than the probe radius; *thin*, if the Debye length is much smaller than the probe radius. Current collection by Langmuir probes can therefore be classified into four regimes, as summarised in Table A-1.

	Thick Sheath	Thin Sheath
Collisional	$\lambda_{ii}, \lambda_{ie} < \lambda_d, r_p \ll \lambda_d$	$\lambda_{ii}, \lambda_{ie} < \lambda_d, r_p \gg \lambda_d$
Collisionless	$\lambda_{ii}, \lambda_{ie} > \lambda_d, r_p \ll \lambda_d$	$\lambda_{ii}, \lambda_{ie} > \lambda_d, r_p \gg \lambda_d$

Table A-1. Conditions defining four regimes of current collection by Langmuir probes.

Appropriate theories accounting for collisional or collisionless sheaths and other effects must be applied in order to gain reliable and accurate estimates of plasma density from measured ion current. The three main theories describing ion current collection by Langmuir probes, which all assume collisionless sheaths, are Orbital Motion Limited (OML) theory, Allen-Boyd-Reynolds (ABR) theory and Bernstein-Rabinowitz-Laframboise (BRL) theory (listed in Table A-2) [55, 58]. A complete treatment of ion current collection including collisions is

very complex and involves the numerical solution of Poisson's equation. Kinetic treatments accounting for collisions have been developed by Su and Lam [102], Godyak and Sternberg [103] and Riemann [104], though these are very complicated to apply.

Of the three collisionless theories, OML theory first proposed by Langmuir and further developed by Laframboise, is the simplest. A collisionless, thick sheath is assumed so that a particle's total energy and momentum are conserved. The OML theory accounts for the orbital motion of ions, since ions entering the sheath from relatively large distances will have large angular momentum, and therefore, on approaching the probe may orbit around it and not be collected.

The equation derived for ion current by OML theory is of the form:

$$I_i = A_p j_r \left[\frac{2}{\sqrt{\pi}} \phi^{1/2} + e^\phi \left(1 - \text{erf} \left(\phi^{1/2} \right) \right) \right] \quad (\text{A.16})$$

where j_r is the random thermal ion current to the probe and $\phi = (-eV/kT_i)$. As $T_i \rightarrow 0$, then $(1/\phi) \ll 1$ and a limiting value of the ion current can be determined. For cylindrical Langmuir probes, the ion current given by OML theory reduces to:

$$I_i \xrightarrow{T_i \rightarrow 0} A_p n_i e \frac{\sqrt{2}}{\pi} \left(\frac{e(V_p - V_{Lp})}{M_i} \right)^{1/2} \quad (\text{A.17})$$

which is independent of T_i and predicts that a plot of I^2 against V_{Lp} should be linear. A linear least-squares fit of $I^2 - V_{Lp}$ can therefore provide a means of determining plasma density [56, 58].

The assumption of a large sheath and neglect of collisions in the derivation of OML theory implies that it should only be valid for very low density plasma. The ABR theory accounts for finite sized (thin) sheaths, so should be valid for analysing higher density plasmas than OML, but assumes $T_i = 0$ so that angular momentum is neglected and only radial ion motion is considered. The BRL theory was the first theory to be developed that accounts for both finite sized sheaths and angular momentum. Solutions for ion current by the ABR and BRL theories however are relatively complicated compared to OML theory. Even following parameterization of the ABR and BRL functions by Chen [86], analysis of Langmuir probe data by the ABR and BRL theories requires considerable processing. OML theory provides a

much simpler and quicker method for determining ion saturation current, and consequently ion density.

	OML	ABR	BRL
Sheath	Collisionless, thick	Collisionless, thin	Collisionless, thin
Ion motion	orbital	radial motion	orbital
Valid range $\xi = r_p/\lambda_d$	< 3	> 100	-

Table A-2. Summary of assumptions and validity of the three main theories for ion current collection by Langmuir probes.

Comparison of the OML, ABR and BRL theories against microwave interferometry measurements was conducted by Chen to investigate the regimes of validity for the three theories [105]. The plasma densities inferred from the Langmuir probe I-V characteristics were found to disagree by a factor larger than 3 in some cases [105]. Generally, it was observed that the ABR theory underestimated ion density compared to the microwave interferometry measurements, while the BRL theory overestimated it. The OML theory was also found to overestimate the ion density at low pressures but was in close agreement with the microwave interferometry measurements at high pressure (in the region of 10mTorr) [105]. Langmuir probe characteristics of partially ionized RF plasmas have often displayed an $I^2 - V$ relation in the ion saturation region of the probe characteristic and have therefore been fitted well by OML theory, despite plasma density being $>10^{15} \text{ m}^{-3}$ [86]. The geometric mean of the plasma density determined by the ABR and BRL theories was found to agree best with the measurements obtained by microwave interferometry [86]. Similar results to these have also been observed in other studies; the ABR theory typically yielded plasma density values lower than OML theory, while the BRL theory yielded higher densities than OML theory [86, 105].

The ABR theory neglects orbital motion of the ions and is therefore expected to predict higher ion currents to the probe than actual, which would lead to the ion density being underestimated from measurements, as observed. It has been suggested by Chen that the discrepancy between the OML and BRL theories (which do account for ion angular momentum) with the microwave interferometry measurements is due to charge-exchange

(CEX) collisions in partially ionized plasmas [86, 105]. Charge exchange collisions occurring within the sheath, even within the presheath, will destroy the angular momentum of an ion, after which the ion will be accelerated radially to the probe. The ion current predicted by the OML or BRL theories would therefore be lower than actual, and so, plasma density overestimated [86]. However, Monte Carlo simulations by Trunec, Španěl and Smith [106] to investigate the effect of CEX collisions on ion current found that the discrepancy between the simulation and OML theory decreased to zero as plasma density increased from 10^{13} m^{-3} to 10^{16} m^{-3} for a fixed probe radius and probe potential. This was attributed to the sheath thickness decreasing with increasing density, leading to less CEX collisions occurring within the sheath. Similar results were observed by Pletnev and Laframboise during Monte Carlo simulations of N_2 plasma [107].

The range of validity of the collisionless probe theories, OML, ABR and BRL, can be given in terms of $\xi = r_p/\lambda_d$ (as summarised in Table A-2). The three theories are inadequate for providing accurate estimates of the plasma density in the range $3 < \xi < 100$; estimates by the individual theories can be in error by a factor of 2 over this range but the geometric mean between the ABR and BRL theories does provide a good estimate [86]. For $\xi < 3$, the OML theory can be used to good accuracy though is theoretically only valid for $\xi < 1$, while for $\xi > 100$, ABR theory provides reasonable estimates of plasma density [86]. For very large values of ξ the Bohm current can simply be used.

In summary, it has been found that OML theory fits experimental data well in a range of density and collisionality regimes typical of inductive plasma sources [105]. Correct sizing and design of Langmuir probes should allow estimates of plasma density to be determined using OML theory to within reasonable accuracy, in conditions beyond the theoretical limit of validity of the OML theory.

A.1.2 Complications of Langmuir Probe Measurements in RF Plasmas

Analysis of Langmuir probe characteristics is far more complicated for RF plasmas than for DC plasma discharges. Oscillation of the plasma potential in RF discharges leads to the I-V characteristic being distorted, as can be seen in Figure A.3 [46]. As the plasma potential oscillates, the ‘knee’ of the characteristic (which indicates the point where $V_p = V_{Lp}$) will also oscillate in time. As the voltage sweep of the probe is performed over a much longer time

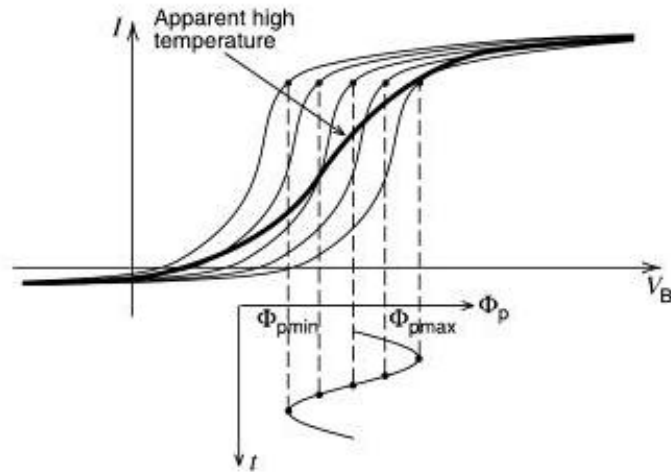


Figure A.3. Instantaneous probe characteristic in a plasma with an oscillating potential ^[46].
(The slope of the time-averaged characteristic (bold) can be seen to be lowered leading to the electron temperature being overestimated).

period than the RF oscillation period, the time-averaged I-V characteristic recorded by the probe will therefore not be the same as the instantaneous I-V characteristic. The effect on the

I-V characteristic is that the curve is made wider; the floating potential becomes shifted to lower values and the slope of the curve in the transition region is lowered leading to the electron temperature being overestimated [46].

The effects of RF on Langmuir probes must normally be compensated to provide sensible data on plasma properties. In general, there are two techniques for RF compensation, *active* and *passive* compensation [59, 86]. Active compensation involves biasing the probe with an additional RF signal (sometimes tapped directly from the RF source) where the amplitude and phase of the signal are varied to achieve a maximum value of the floating potential and minimum value of electron temperature. Passive compensation involves placing a tuned RF filter (inductor and capacitor in parallel) or a RF choke (a self-resonant inductor) close to the probe tip which presents a large impedance to the RF signal. It is commonly found that the RF signal contains a large component at the second harmonic and therefore, two sets of RF filters connected in series are often used; one which is resonant at the fundamental frequency and one at the second harmonic. A large compensating electrode is also frequently connected between the probe tip and RF filters via a capacitor to collect enough charge to ensure that $V_p - V_{Lp}$ remains constant [108].

Studies by Oksuz, Soberón and Ellingboe [59] and Sudit and Chen [110] however have shown that good estimates of electron temperature can still be obtained by partially compensated probes (where the probe does not follow the RF oscillations precisely) and even uncompensated probes in the presence of moderate sinusoidal plasma oscillations [59]. Compensated probes must be used for capacitive (RF) discharges as large sheath potential oscillations occur in these discharges, but partially compensated and uncompensated probes may still be suitable for determining electron temperature in inductive plasma discharges. Also, measurements by Tuszewski and Tobin [109] demonstrated that uncompensated Langmuir probes yielded reasonable estimates of ion density, to within 50% of microwave interferometry measurements, within a high density inductive discharge ($\sim 10^{17} \text{ m}^{-3}$). Therefore, unless highly accurate estimates of plasma parameters are of interest, simple uncompensated Langmuir probes can often be used to investigate inductive plasma discharges, removing the need to design and construct filters.

A.2 TRIPLE LANGMUIR PROBES

Another diagnostic technique beneficial for investigating RF plasmas involves the use of three Langmuir probes configured in such a way as to provide instantaneous and simultaneous measurements of electron temperature, plasma density and floating potential (from which plasma potential can also be inferred). The *triple Langmuir probe* (TLP), first proposed by Chen and Sekiguchi [85], essentially comprises three equally sized wires inserted into a plasma in close proximity to one another. A fixed bias is applied between two of the probes, while the third is left floating. The electrical configuration of a triple Langmuir probe is displayed schematically in Figure A.4. If the applied potential is at least $2kT_e/e$ volts, the negatively biased probe will draw a current equal to the ion saturation current, while the positively biased probe will draw an equal electron current. For this to occur, the two probes will adopt a potential that is near the floating potential, measured by the third probe [55, 58]. Simultaneous measurement of the collected current and the potentials of the probes essentially provide three points on the Langmuir probe I-V characteristic. Application of appropriate theory then enables values for electron temperature and plasma density to be evaluated [85, 99]. The TLP technique has advantages in that all potentials remain near the floating potential so that large electron saturation currents are not drawn from the plasma which could perturb the plasma or damage the probe, and that the probes do not need to be swept in voltage meaning that virtually instantaneous measurements can be made. Provided that the wires are separated by a few Debye lengths so that the sheaths surrounding each probe do not interact with one another, but the probes are close enough so that large gradients in the plasma

do not exist across the probes, the triple Langmuir probe will also be insensitive to plasma oscillations as each probe will experience the perturbation simultaneously.

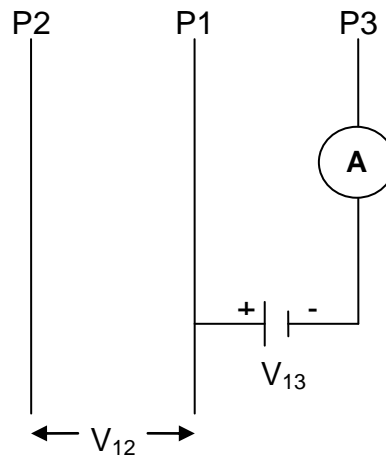


Figure A.4. Triple Langmuir probe circuit for direct-display of electron temperature and density.

The triple Langmuir probe is therefore an attractive diagnostic tool for various time-dependent plasmas and plasma processes, as it offers a more simplified diagnostic technique compared to the single Langmuir probe. Measurements can be obtained with a much greater time resolution, though at the cost of spatial resolution compared to a single probe.

A.2.1 Triple Langmuir Probe Theory

The theory behind triple Langmuir probes is derived under a number of assumptions:

- Quasineutrality holds within the plasma up to the plasma-sheath boundary.
- The electron energy distribution in the plasma is Maxwellian.
- The probes are operated in the collisionless, thin sheath regime so that the collection area can be considered to be equal to the exposed surface area of the probe.
- The probes are separated by a distance greater than the sheath thickness so that the probes do not interact.

The total current to each of the probes defined in Figure A.4 can then be written as:

$$-I_1 = -I_{es} \exp\left(\frac{e(V_p - V_1)}{kT_e}\right) + I_{is}(V_1) \quad (\text{A.18})$$

$$I_2 = -I_{es} \exp\left(\frac{e(V_p - V_2)}{kT_e}\right) + I_{is}(V_2) \quad (\text{A.19})$$

$$I_3 = -I_{es} \exp\left(\frac{e(V_p - V_3)}{kT_e}\right) + I_{is}(V_3) \quad (\text{A.20})$$

where probe 1 is positively biased, probe 3 is negatively biased and probe 2 is floating. If the variation in ion saturation current with probe voltage is assumed to be negligible compared to the variation in electron current and that the surface area of each probe is the same, then $I_{is}(V_1) = I_{is}(V_2) = I_{is}(V_3) = I_{is}(V)$. The ratio of $(I_1 + I_2)$ and $(I_1 + I_3)$ will then reduce to:

$$\frac{(I_1 + I_2)}{(I_1 + I_3)} = \frac{1 - \exp\left(\frac{eV_{d2}}{kT_e}\right)}{1 - \exp\left(\frac{eV_{d3}}{kT_e}\right)} \quad (\text{A.21})$$

where $(V_{d2} = V_2 - V_1)$ and $(V_{d3} = V_3 - V_1)$ [85]. Though the assumption that the ion saturation current collected by each probe is the same despite the probes being biased to different potentials is not strictly valid, it provides a means to make the above simplification from which an estimate of electron temperature can be extracted. Since probe 2 is floating, the condition $I_2 = 0$ is imposed. Also, $I_1 = I_3$ by Kirchoff's law. Equation A.21 then becomes:

$$\frac{1}{2} = \frac{1 - \exp\left(\frac{eV_{d2}}{kT_e}\right)}{1 - \exp\left(\frac{eV_{d3}}{kT_e}\right)} \quad (\text{A.22})$$

which can be solved to find T_e . A further simplification can also be made, as the fixed bias V_{d3} is typically required to be several times T_e (volts) to ensure the negatively biased probe is within the ion saturation region; therefore, $(1 - \exp(eV_{d3}/kT_e)) \rightarrow 1$ and the electron temperature in eV can be determined directly from the floating potential and the potential of the positively biased probe according to:

$$T_e \text{ [eV]} = \frac{V_{d2}}{\ln 2} \quad (\text{A.23})$$

Though equations A.22 and A.23 provide a very fast and simple method of determining electron temperature, the electron temperature tends to be overestimated due to the simplifying assumptions involved [85, 99].

Once an estimate of electron temperature has been obtained however, an approximate estimate of the plasma density can be evaluated from the measured probe current assuming the current to be equal to the Bohm current. For cylindrical probes, the plasma density will be given by:

$$n_{e0} = \frac{I_{is}}{\alpha e A_p \exp\left(\frac{kT_e}{M_i}\right)^{1/2}} \quad (\text{A.24})$$

where the parameter α can be taken from Chen [58].

More accurate solutions for electron temperature and plasma density have been derived by Kamitsuma, Chen and Chang [99] to account for variation of the ion saturation current with plasma potential, and also finite ion temperature as previous corrections performed by Chen were only conducted for the zero ion temperature limit for cylindrical probes [85]. The equations derived by Kamitsuma, Chen and Chang were developed from OML theory under collisionless, thin sheath conditions [99].

The expression for determining electron temperature given by Kamitsuma, Chen and Chang is:

$$\frac{1}{2} = \frac{1 - \exp(-\phi_{d2}) + M_1(\phi)}{1 - \exp(-\phi_{d3}) + M_2(\phi)} \quad (\text{A.25})$$

where the correction terms are:

$$M_1(\phi) = \left[1 - \left(1 - \frac{K\phi_{d2}}{\epsilon + K\phi_f} \right)^{1/2} \right] \exp(-\phi_{d2}) \quad (\text{A.26})$$

$$M_2(\phi) = \left[\left(1 - \frac{K(\phi_{d2} - \phi_{d3})}{\epsilon + K\phi_f} \right)^{1/2} - \left(1 - \frac{K\phi_{d2}}{\epsilon + K\phi_f} \right)^{1/2} \right] \exp(-\phi_{d2}) \quad (\text{A.27})$$

and $\phi = (eV/kT_e)$, $\epsilon = (T_i/T_e)$, $K = (4/\pi)$.

The effect of ion temperature on the determination of T_e was found to be negligible for cylindrical probes. The maximum error on T_e for assuming a temperature ratio of $\epsilon = 0.1$ was found to be $\sim 5\%$ for cylindrical probes for all plasma cases investigated by Kamitsuma, Chen and Chang [99].

The expression for plasma density is given as:

$$n_{e0} = \frac{I}{aK^{1/2}} f(\phi_{d2}) \frac{1}{eA_p} \left(\frac{2\pi m_e}{kT_e} \right)^{1/2} \quad (\text{A.28})$$

where $a = (m_e/M_i)^{1/2}$. The function $f(\phi_{d2})$ can be taken from Kamitsuma knowing the measured potential ϕ_{d2} for a given $(\epsilon/K + \phi_f)$, as displayed in Figure A.5.

The effect of ion temperature on the estimate of plasma density was found to be more significant than on electron temperature, but still considered to be negligible. The maximum error on n_{e0} was approximately 7% for cylindrical probes [99].

Comparison of single and triple Langmuir probe measurements by Kamitsuma in low density plasma ($\sim 10^{12} \text{ m}^{-3}$) also found that for small potentials applied between the biased probes, electron temperature agreed to within 2%, though increased with bias potential, up to a maximum of 14% in their experiments. Estimates of plasma density were found to agree to within a factor of 2 for small bias potentials [99].

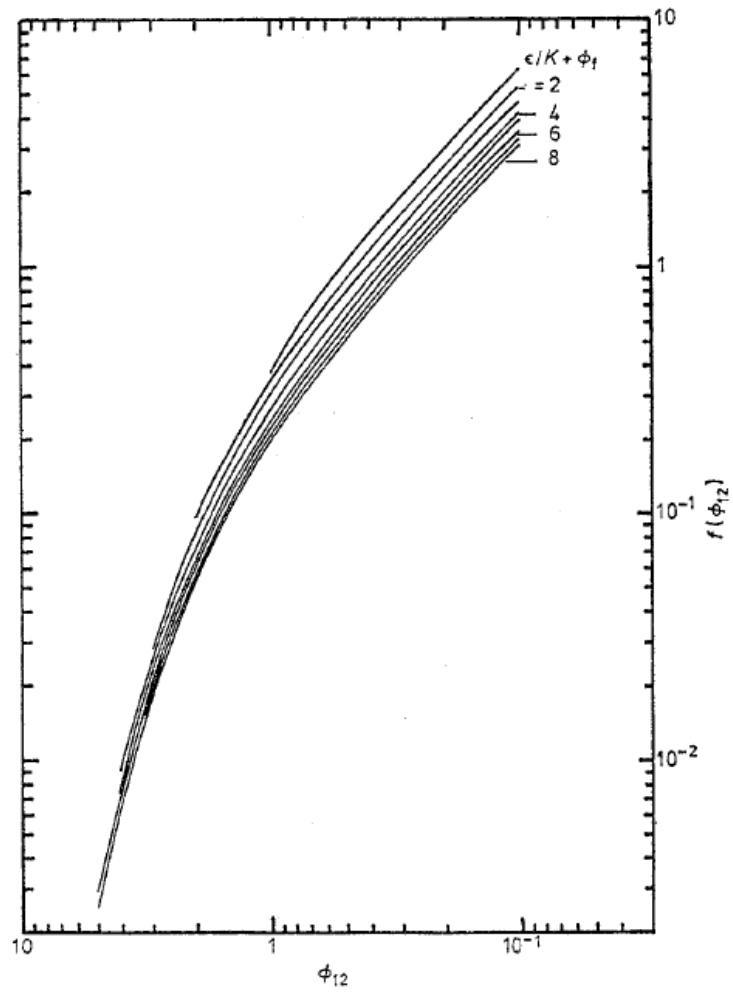


Figure A.5. Function $f(\phi_{12})$ for a cylindrical Langmuir probe for various $(e/K + \phi_f)$.

Appendix B

B. Discharge Model

A 2D cylindrical axisymmetric model of an inductive discharge was developed based on the geometry of the MiDGIT thruster using the FEA software package COMSOL Multiphysics. A brief outline of the model is provided in this appendix.

The COMSOL Multiphysics software provides a plasma simulation module that couples a two-term Boltzmann equation solver with reduced Maxwell field equations for modelling low temperature plasmas. The ICP interface automatically solves a series of coupled partial differential equations for:

- The electron density
- The mean electron energy
- The plasma potential
- The electric field due to induction currents

The induction currents are solved in the frequency domain while all other variables are solved in the time domain [94]. The electron density and mean electron energy are calculated by solving a pair of drift-diffusion equations. Electron diffusivity and electron mobility are calculated from the reduced electron mobility entered as an input. Rate coefficients for collisions between plasma species are calculated from cross section data imported into the model. Detailed information on all equations used by the software and relevant theory can be found in [94].

B.1 GENERAL ASSUMPTIONS

The following assumptions are imposed on the discharge model developed with the plasma module of COMSOL Multiphysics:

- 1) The electron energy distribution function is assumed to be Maxwellian. Initial estimates of the mean electron temperature and density are required at the start of the simulation.

- 2) Quasineutrality holds throughout the plasma domain; this is imposed by forcing $n_e = n_i$.
- 3) Neutral density is uniform throughout the plasma domain; the density is calculated from the neutral pressure and temperature entered as inputs to the model.
- 4) The helical induction coil can be approximated as separate circular rings lumped together as a single current source. Such an assumption has been shown to have little influence on a similar ICP discharge model by Tsay [25].

The limitations of the model are:

- 1) Capacitive coupling to the plasma is neglected; the discharge is considered a purely inductive discharge. Full treatments of inductively coupled plasmas including both inductive and capacitive coupling are very challenging.
- 2) The pre-sheath is in principle resolved but the software is not capable of fully resolving the plasma sheath in an ICP.
- 3) The neutral density is assumed to be uniform; therefore, the effect of neutral injection into the discharge chamber on plasma distribution is ignored.

B.2 GENERAL DESCRIPTION

A xenon inductive discharge is modeled with geometry based on the MiDGIT breadboard thruster configured for differential operation. The discharge chamber is defined to be a cylindrical alumina tube with an internal diameter of 14mm. Two 6 turn helical copper coils are modeled by defining individual circular rings for each turn of each coil. The coil turns are then lumped together to define the domains Coil 1 and Coil 2. The end plates at each end of the discharge chamber are specified to be graphite to represent the extraction grids of the thruster. The basic geometry of the 2D axisymmetric model is shown in Figure B.1.

Material properties are defined from the Materials Library of COMSOL Multiphysics. A current is specified for each coil by entering a value for two variables defined to be I_{c1} and I_{c2} . The ‘*single turn coil domain*’ feature of the ICP interface automatically constrains the integral of the current density over the coil domain to be the specified current. The RF current in the induction coil induces an azimuthal current in the plasma, which in turn induces a current back in the coil. COMSOL Multiphysics provides a fully self-consistent model that is able to capture this two-way coupling between the coil and plasma.

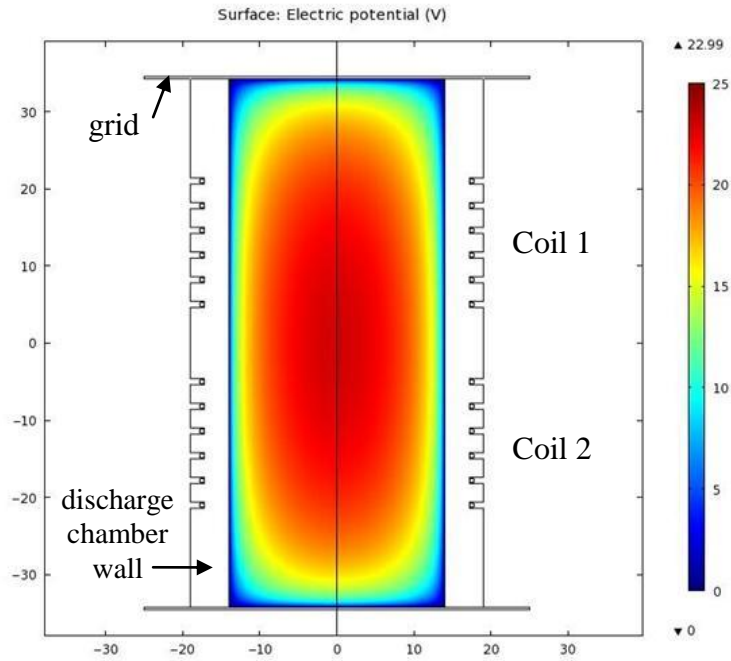


Figure B.1. Plot of plasma potential showing geometry of 2D axisymmetric discharge model.

A fine free-triangular mesh is applied to the simulation domain. A boundary layer mesh is defined along the inner walls of the discharge chamber and internal surface of the end plates (grids) in order to capture the separation of space charge between the electrons and ions close to the walls. An extra fine mesh is applied in the coil domains, which increases exponentially from the edge of the coil to centre, to capture the skin effect.

A xenon plasma is modeled including excitation of the ground state of xenon. The four plasma species are specified as e, Xe, Xe*, Xe⁺. Cross section data are imported as text files; these are taken from [111-113] and are given in the following section in the format required by COMSOL Multiphysics. Recombination and de-excitation at the walls are included by defining the surface reactions Xe⁺ + e → Xe and Xe* → Xe. Convergence of the model is defined by observing steady-state outputs, as shown for electron temperature in Figure B.2.

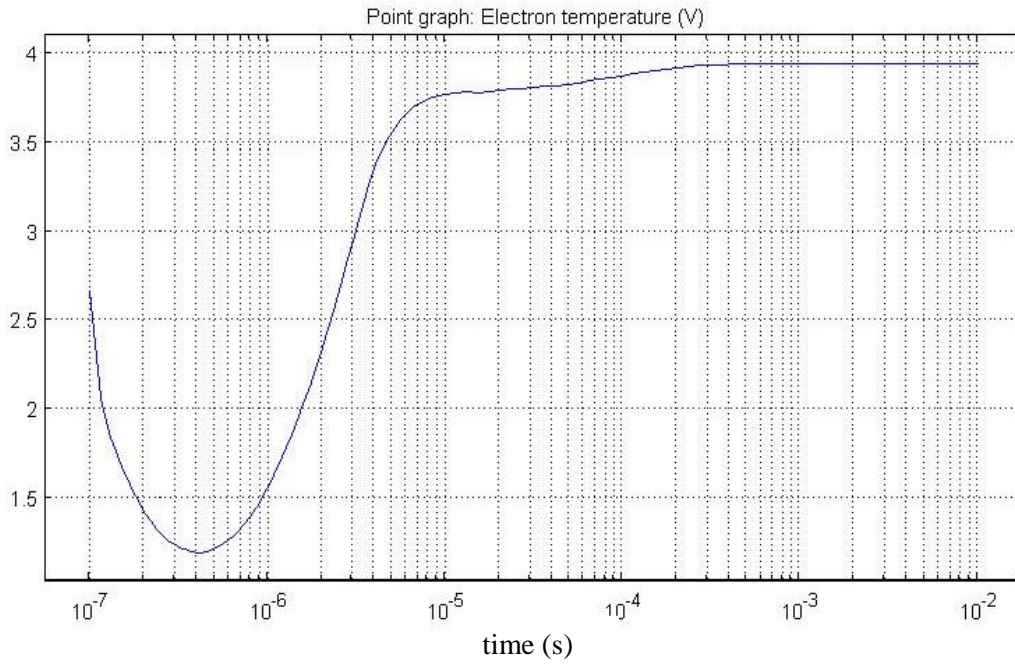


Figure B.2. Plot of electron temperature with time showing convergence.

B.3 CROSS SECTION DATA

ELASTIC
 e+Xe=>e+Xe
 4.178E-06
 1. 1.

0.0000E+00	178.0000E-20	0.7000E+00	1.360000E-20	0.1500E+02	10.20000E-20
0.1000E-02	175.0000E-20	0.1000E+01	2.480000E-20	0.1700E+02	8.300000E-20
0.2000E-02	170.0000E-20	0.1200E+01	3.350000E-20	0.2000E+02	7.000000E-20
0.3000E-02	160.0000E-20	0.1300E+01	3.900000E-20	0.2500E+02	5.900000E-20
0.5000E-02	144.0000E-20	0.1500E+01	5.000000E-20	0.3000E+02	5.100000E-20
0.7000E-02	130.0000E-20	0.1700E+01	6.300000E-20	0.4000E+02	4.300000E-20
0.8500E-02	123.0000E-20	0.1900E+01	7.500000E-20	0.5000E+02	3.600000E-20
0.1000E-01	116.0000E-20	0.2100E+01	9.100000E-20	0.6000E+02	3.200000E-20
0.1500E-01	103.0000E-20	0.2200E+01	9.900000E-20	0.7500E+02	2.750000E-20
0.2000E-01	80.00000E-20	0.2500E+01	12.50000E-20	0.1000E+03	2.350000E-20
0.3000E-01	61.00000E-20	0.2800E+01	15.00000E-20	0.1500E+03	1.900000E-20
0.4000E-01	48.00000E-20	0.3000E+01	17.00000E-20	0.2000E+03	1.600000E-20
0.5000E-01	39.50000E-20	0.3300E+01	18.90000E-20	0.3000E+03	1.300000E-20
0.7000E-01	29.00000E-20	0.3600E+01	21.30000E-20	0.5000E+03	0.970000E-20
0.1000E+00	20.20000E-20	0.4000E+01	24.80000E-20	0.7000E+03	0.780000E-20
0.1500E+00	13.00000E-20	0.4500E+01	27.60000E-20	0.1000E+04	0.580000E-20
0.2000E+00	8.400000E-20	0.5000E+01	30.80000E-20	0.1500E+04	0.370000E-20
0.2500E+00	5.350000E-20	0.6000E+01	30.50000E-20	0.2000E+04	0.250000E-20
0.3000E+00	3.150000E-20	0.7000E+01	28.00000E-20	0.3000E+04	0.150000E-20
0.3500E+00	2.100000E-20	0.8000E+01	23.50000E-20	0.5000E+04	0.073000E-20
0.4000E+00	1.750000E-20	0.1000E+02	16.00000E-20	0.7000E+04	0.045000E-20
0.5000E+00	1.380000E-20	0.1200E+02	13.00000E-20	0.1000E+05	0.027000E-20

IONIZATION

e+Xe=>2e+Xe+

12.13

1. 1.

0.0000E+00	0.0000E+00
12.1000E+00	0.0000E+00
12.5000E+00	0.1100E-20
13.0000E+00	0.2560E-20
15.0000E+00	0.9100E-20
17.0000E+00	1.5300E-20
20.0000E+00	2.2800E-20
24.0000E+00	3.1000E-20
30.0000E+00	3.8500E-20
35.0000E+00	4.1000E-20
40.0000E+00	4.4800E-20
50.0000E+00	4.8400E-20
60.0000E+00	5.0300E-20
75.0000E+00	5.2000E-20
100.000E+00	5.3800E-20
150.000E+00	5.2000E-20
200.000E+00	4.6000E-20
300.000E+00	3.9000E-20
500.000E+00	2.9000E-20
700.000E+00	2.4000E-20
1000.00E+00	1.8800E-20
1500.00E+00	1.2500E-20
2000.00E+00	0.9400E-20
3000.00E+00	0.6300E-20
5000.00E+00	0.3800E-20
7000.00E+00	0.2700E-20
10000.0E+00	0.1900E-20
15000.0E+00	0.1250E-20

EXCITATION

e+Xe=>e+Xes

8.32 4.5 1

1. 1.

0.0000E+00	0.0000E+00
8.32000E+00	0.0000E+00
9.00000E+00	0.0915E-20
9.20000E+00	0.1300E-20
9.32000E+00	0.1330E-20
9.41000E+00	0.1310E-20
9.52000E+00	0.1260E-20
9.64000E+00	0.1340E-20
12.0000E+00	0.3750E-20
15.0000E+00	0.7500E-20
17.5000E+00	0.9000E-20
20.0000E+00	0.8000E-20
22.5000E+00	0.6000E-20
25.0000E+00	0.4000E-20
28.0000E+00	0.3200E-20
32.0000E+00	0.3000E-20
35.0000E+00	0.3200E-20
40.0000E+00	0.3200E-20
45.0000E+00	0.3200E-20
50.0000E+00	0.3300E-20
70.0000E+00	0.3500E-20
100.000E+00	0.3700E-20
150.000E+00	0.3000E-20
500.000E+00	0.2000E-20
1000.00E+00	0.1000E-20
3000.00E+00	0.0330E-20
10000.0E+00	0.0100E-20

References

- [1] Kaltenecker, L., Fridlund, M., “The Darwin mission: Search for extra-solar planets,” *Advances in Space Research*, Vol. 36, 2005, pp. 1114-1122.
- [2] Hough, J., Robertson, D., Ward, H. and McNamara, P., “LISA – The Interferometer,” *Advances in Space Research*, Vol. 32, No. 7, 2003, pp. 1247-1250.
- [3] Parmar, A. N. et al, “Studying the evolution of the hot universe with the X-ray evolving universe spectroscopy mission - XEUS,” *Advances in Space Research*, Vol. 34, No. 12, 2004, pp. 2623-2627.
- [4] Polzin, K. A., Chouerie, E. Y., Gurfil, P. and Kasdin, N. J., “Plasma Propulsion Options for Multiple Terrestrial Planet Finder Architectures”, *Journal of Spacecraft and Rockets*, Vol. 39, No. 3, 2002, pp. 347-356.
- [5] Reichbach, J., *Micropropulsion System Selection for Precision Formation Flying Satellites*, Thesis for Master of Science, Massachusetts Institute of Technology (2001).
- [6] Gonzalez, J., Saccoccia, G. and Serafini, L., “Electric Propulsion for ESA Science and Earth Observation Missions”, 3rd International Conference on Spacecraft Propulsion, Cannes, October 2000.
- [7] Micci, M. and Ketsdever, A., *Micropropulsion for Small Spacecraft*, Progress in Astronautics and Aeronautics, Vol. 187, AIAA Reston, VA (2000).
- [8] Mueller, J., “Thruster Options for Microspacecraft: A Review and Evaluation of State-of-the-Art and Emerging Technologies”, *Micropropulsion for Small Spacecraft*, Progress in Astronautics and Aeronautics, Vol. 187, edited by M. Micci and A. Ketsdever, AIAA Reston, VA (2000), Chap 3.
- [9] Brown, C. D., *Spacecraft Propulsion*, American Institute of Aeronautics and Astronautics Inc., Washington, 1996.
- [10] London, A. P., *A Systems Study of Propulsion Technologies for Orbit and Attitude Control of Spacecraft*, Thesis for Master of Science, Massachusetts Institute of Technology (1996).
- [11] de Groot, W. A., “Propulsion Options for Primary Thrust and Attitude Control of Microspacecraft”, NASA CR 98-206608, COSPAR Colloquium on Scientific Microsatellites, Dec. 1997.
- [12] Kilter, M. and Karlsson, A., “Micropropulsion Technologies for the European High-Precision Formation Flying Interferometer Darwin”, 4th International Spacecraft Propulsion Conference, Sardinia, Italy, June 2004.
- [13] MicroNewton Proportional Thruster VP03, Product Data Sheet, Marotta UK Ltd. http://www.ampacispcheltenham.eu/docs/VP03_marotta.pdf (last accessed Sept 2010).
- [14] Rathakrishnan, E., *Applied Gas Dynamics*, John Wiley & Sons, Singapore, 2010.

- [15] Sutton, G. and Biblarz, O., *Rocket Propulsion Elements*, 7th edition, John Wiley and Sons, New York, 2001.
- [16] Jahn, R. G., *Physics of Electric Propulsion*, Dover Publications, 2006.
- [17] Killinger, R., Kukies, R., Surauer, M., Tomasetto, A. and van Holtz, L., “Artemis Orbit Raising In-Flight Experience with Ion Propulsion”, *Acta Astronautica*, Volume 53, Issues 4-10, 2003, pp. 607-621.
- [18] Brophy, J. R., Marcucci, M. G., Ganapathi, G. B., Garner, C. E., Henry, M. D., Nakazono, B. and Noon, D., “The Ion Propulsion System for DAWN”, **AIAA 2003-4542**, (2003)
- [19] Edwards, C. H., Wallace, N. C., Tato., C. and van Put, P., “The T5 Ion Propulsion Assembly for Drag Compensation on GOCE”, in Proc. 2nd Int. GOCE User Workshop ‘GOCE: The Geoid and Oceanography’, ESA-ESRIN, Frascati, Italy, 8-10 march 2004 (ESA SP-569, June 2004).
- [20] Rudwan, I. M., Wallace, N. C., Coletti, M. and Gabriel, S. B., “Emitter Depletion Measurement and Modeling in the T5 and T6 Kaufman-type Ion Thrusters”, 30th International Electric Propulsion Conference, **IEPC-2007-256**, (2007)
- [21] Killenger, R., Bassner, H., Muller, J. and Kukies, R., “Status of the RIT_XT High Performance RF-Ion Thruster Development”, 3rd International Conference on Spacecraft Propulsion, Cannes, 2000.
- [22] Patterson, M. J., Foster, J. E., Haag, T. W., Rawlin, V. K. and Soulas, G. C., “NEXT: NASA’s Evolutionary Xenon Thruster”, 38th *AIAA/ASME/SAE/ASEE Joint Propulsion Conference and Exhibit* **AIAA 2002-3832** (2002).
- [23] Wirz, R. E., *Discharge Plasma Processes of Ring-Cusp Ion Thrusters*, Thesis submitted for the degree of Doctor of Philosophy, California Institute of Technology (2005).
- [24] Tsay, M., *Numerical Modeling of a Radio-frequency Micro Ion Thruster*, Thesis for Master of Science, Massachusetts Institute of Technology (2006).
- [25] Tsay, M., *Two Dimensional Numerical Modeling of Radio Frequency Ion Engine Discharge*, Thesis submitted for the degree of Doctor of Philosophy, Massachusetts Institute of Technology (2010).
- [26] Loeb, H., Schartner, W., Feili, D. and Meyer, B., “Development of RIT Microthrusters”, 55th International Astronautical Congress, **IAC-04-S.4.04** (2004)
- [27] Feili, D., Loeb, W., Schartner, H., Weis, St., Kirmse, D., Meyer, M., Killinger, R. and Mueller, H., “Performance mapping of new μ N-RITs at Giessen”, 29th International Electric Propulsion Conference, **IEPC-2005-252** (2005)
- [28] Paita, L., Ceccanti, F., Spurio, M., Cesari, U., Priami, L., Nania, F., Rossodivita, A. and Andrenucci, M., “Alta’s FT-150 FEEP Microthruster: Development and Qualification Status”, 31st International Electric Propulsion Conference, **IEPC-2009-186** (2009)

- [29] Tajmar, M., Genovese, A. and Steiger, W., “Indium Field Emission Electric Propulsion Microthruster Experimental Characterization”, *Journal of Propulsion and Power*, Vol. 20, No. 2, 2004, pp 211-218.
- [30] Sanders, B., Van Vliet, L., Tata Nardini, F., Gronland, T., Rangsten, P., Shea, H., Noca, M., Visee, R., Monna, B., Stark, J., Bult, A. and Maria Di Cara, D., “Development of MEMS based Electric Propulsion”, Space Propulsion Conference 2010, San Sebastian, Spain, May 2010.
- [31] Hruby, V., Gamero-Castano, M., Falkos, P. and Shenoy, S., “Micro Newton Colloid Thruster System Development”, 27th International Electric Propulsion Conference, **IEPC-01-281** (2001).
- [32] Schilling, J., *Development of the Two-Stage Micro Pulsed Plasma Thruster*, Thesis submitted for the degree of Doctor of Philosophy, University of Southern California, May 2007.
- [33] Cassady, R. J., Hoskins, W. A., Campbell, M. and Rayburn, C., “A Micro Pulsed Plasma Thruster (PPT) for the Dawgstar Spacecraft”, in Proc. of the 2000 IEEE Aerospace Conference, Big Sky, Montana (2000).
- [34] Manente, M., Walker, M., Carlsson, J., Bramanti, C., Rocca, S., Curreli, D., Guclu, Y. and Pavarin, D., “Feasibility Study of a Low Power Helicon Thruster”, 5th International Spacecraft Propulsion Conference, Crete, Greece (2008)
- [35] Tajmar, M., Scharlemann, C. A., “Micropropulsion Developments at AIT”, in Proc. of the International Astronautical Congress, Daejon, South Korea, **IAC-09.C4.8.5** (2009).
- [36] Micro Pulsed Plasma Thrusters, Product Data Sheet, Busek Co. Inc. <http://www.busek.com/downloads/MicroPPT.pdf> (last accessed Sept 2010).
- [37] Coletti, M., Guarducci, F. and Gabriel, S., “A micro-PPT for Cubesat application: Design and preliminary experimental results”, *Acta Astronautica*, article-in-press, 2011.
- [38] Ceccanti, F., Marcuccio, S. and Andrenucci, M., “FEPP Thruster Survivability in the LEO Atomic Oxygen Environment”, 27th International Electric Propulsion Conference, **IEPC-01-295** (2001).
- [39] Yashko, G. J. and Hastings, D. E., “Analysis of Thruster Requirements and Capabilities for Local Satellite Clusters”, 10th Annual AIAA/USU Conference on Small Satellites, Utah (1996).
- [40] Leiter, H., Killinger, R., Boss, M., Braeg, M., Gollor, M., Weis, S., Feili, D., Tartz, M., Neumann, H., Haderspek, J., Bock, D. and Maria Di Cara, D., “RIT- μ X – The New Modular High Precision Micro Ion Propulsion System”, 30th International Electric Propulsion Conference, **IEPC-2007-209** (2007)
- [41] Feili, D., Di Cara, D.M., Leiter, H.J., Del Amo, J.G., Loeb, H.W., Weis, S., Kirmse, D., Frigot, P.E., Orlandi, M., Muller, H. and Meyer, B.K., “The micro-N RIT-4 ion engine: a first step towards a European mini-ion engine system development”, 30th International Electric Propulsion Conference, **IEPC-2007-218** (2007)

- [42] Jameson, P., “Requirements Assessment for Mini Ion Engines”, QinetiQ/S&DU/Space/CR0700280 (2007)
- [43] Jameson, P., “Mini Ion Engine,” QinetiQ/S&DU/Space/Bid/0601744 (2006)
- [44] Loeb, H., Schartner, K., Meyer, B., Feili, D., Weis, St. and Kirmse, D., “Forty Years of Giessen EP-Activities and the Recent RIT-Microthruster Development”, 29th International Electric Propulsion Conference, **IEPC-2005-031** (2005)
- [45] Hittorf, W., *Wiedmann Ann. D. Physik*, Vol. 21, 1884, pp. 90.
- [46] Lieberman, M. A. and Lichtenberg, J. A., *Principles of Plasma Discharges and Materials Processing*, John Wiley & Sons, New York, 1994.
- [47] Goebel, D. M. and Katz, I., *Fundamentals of Electric Propulsion: Ion and Hall Thrusters*, John Wiley and Sons, New Jersey, 2008.
- [48] Vasilescu G., *Electronic Noise and Interfering Signals*, Springer Berlin Heidelberg, New York, 2005.
- [49] Seo, S.H., Chung, C.W. and Chang, H.Y., “Review of heating mechanism in inductively coupled plasma”, *Surface and Coatings Technology*, Vol. 131, 2000, pp 1-11.
- [50] Godyak, V., “Plasma phenomena in inductive discharges”, *Plasma Phys. Control Fusion*, **45** (2003) A399-A424.
- [51] Kim, H. C., Iza, F., Yang, S. S., Radmilovic-Radjenovic, M. and Lee, J. K., “Particle and fluid simulations of low temperature plasma discharges: benchmarks and kinetic effects”, *J. Phys. D: Appl. Phys.*, **38** (2005) R283-R301.
- [52] Tyshetskiy, Y. O., Smolyakov, A. I. and Godyak, V. A., “ Electron heating reduction in inductively coupled plasma at conditions of the anomalous skin effect”, 29th International Conference on Plasma Science, Banff, Canada, 2002.
- [53] Gudmundsson, and Lieberman, M. A., “Magnetic induction and plasma impedance in a cylindrical inductive discharge,” *Plasma Sources Science and Technology* Vol. 6, 1997, pp. 540-550.
- [54] Kortshagen, U., Gibson, N.D. and Lawler, J.E., “On the E-H mode transition in RF inductive discharges” *J. Phys. D: Appl. Phys.*, Vol. 29, 1996, pp. 1224-1236.
- [55] Huddlestone, R.H. and Leonard, S.L., *Plasma Diagnostic Techniques*, Academic Press Inc., New York, 1965.
- [56] Hutchinson, H.I., *Principles of Plasma Diagnostics*, Cambridge University Press, New York, 2002.
- [57] Mott Smith, H. M. and Smith, I., “The Theory of Collectors in Gaseous Discharges” *Phys. Rev.*, Vol. 28 (4), 1926, pp. 727-763.
- [58] Chen, F., “Langmuir Probe Diagnostics”, *Mini-Course on Plasma Diagnostic Techniques, IEEE-ICOPS meeting*, Korea, June 2006.

- [59] Oksuz, L., Soberon, F. and Ellinboe, A. R., “Analysis of uncompensated langmuir probe characteristics in radio frequency discharges revisited” *J. Appl. Phys.*, Vol. 99 (2006).
- [60] Klik, M., Rehak, W. and Kammeyer, M., “Plasma Diagnostics in RF Discharges Using Nonlinear and Resonance Effects”, *Jpn. J. Appl. Phys.*, Vol. 36, 1997, pp 4625-4631.
- [61] Walker, D. N., Fernsler, R. F., Blackwell, D. D. and Amatucci, W. E., “Using rf impedance probe measurements to determine plasma potential and the electron energy distribution”, *Phys. Plasmas*, **17**, 113503 (2010).
- [62] Argüeso, M., Robles, G. and Sanz, J., “Measurement of high frequency currents with a Rogowski coil”, 9th Spanish Portuguese Congress on Electrical Engineering, Marbella, 2005.
- [63] Ray, W. F., “Wide bandwidth Rogowski current transducers, Part I. The Rogowski coil”, *EPE Journal*, Vol. 3, (1993).
- [64] Capacci, M., and Noci, G., “New ion source design for ion propulsion application”, *Review of Scientific Instruments*, Vol. 69, No. 2, 1998, pp. 788-790
- [65] Mistoco, V., Trudel, T., Bilen, S. and Micci, M., “Vacuum Testing of the Miniature Radio-Frequency Ion Thruster”, 29th International Electric Propulsion Conference, **IEPC-2005-265** (2005)
- [66] Mistoco, V. F. and Bilen, S. G., “Numerical Modeling of a Miniature Radio Frequency Ion Thruster”, 44th AIAA/ASME/SAE/ASEE Joint Propulsion Conference and Exhibit, **AIAA 2008-5194** (2008).
- [67] Closs, M. F., *Numerical Modelling and Optimisation of Radio-Frequency Ion Thrusters*, Herbert Utz Verlag GmbH, Germany, 2002.
- [68] Groh, K. H., Loeb, H., “State-of-the-Art Radio Frequency Ion Thrusters,” *Journal of Propulsion and Power*, Vol. 7, No. 4, 1991, pp. 573-579.
- [69] Bird, G. A., *Molecular Gas Dynamics and the Direct Simulation of Gas Flows*, Oxford University Press, New York, 1994.
- [70] Bassner, H., Killinger, R., Leiter, H. and Muller, J., “Development Steps of the RF-Ion Thrusters RIT”, 27th International Electric Propulsion Conference, **IEPC-01-105** (2001)
- [71] Zhong, L., Liu, Y., Wen, Z. and Ren, J., “Numerical Simulation of Ion Extraction Through Ion Thruster Optics”, *Plasma Science and Technology*, Vol. 12, No. 1, 2010.
- [72] Lenz, B., Schweitzer, M. and Loeb, H., “Improved RF-Coupling Methods for RIT-Engines”, 14th International Electric Propulsion Conference, **AIAA-1979-2057** (1979)
- [73] Brophy, J. R., Katz, I., Polk, J. E. and Anderson, J. R., “Numerical Simulations of Ion Thruster Accelerator Grid Erosion”, 38th AIAA/ASME/SAE/ASEE Joint Propulsion Conference and Exhibit **AIAA 2002-4261** (2002).

- [74] Loeb, H., Trojan, F., Bussweller, K. and Lang, H., "Development of the Radio Frequency Microthruster RIT 4", 9th *AIAA/ASME/SAE/ASEE Joint Propulsion Conference and Exhibit*, **AIAA-1972-473** (1972)
- [75] Caro, I., Ahedo, E., Guraya, C., Landaberea, A. and Marcos, J., "High Performance Ceramic Discharge Chambers", 57th International Astronautical Congress, **IAC-06-C4.P.4.12** (2006)
- [76] Iwata, T. and Takegahara, H., "Effects of Discharge Chamber Configuration on RF Plasma Properties", **IEPC-97-142** (1997).
- [77] Collingwood, C. M., Gabriel, S.B., Corbett, M. H., Wallace, N. C. and Jameson, P., "Investigation of neutral flow through an annular gas distributor for a novel micro-ion thruster", 5th International Space Propulsion Conference, Crete, May 2008.
- [78] 75A250A 75W RF amplifier, Product Data Sheet REV09050, Amplifier Research, <http://www.arww-rfmicro.com/post/75A250A.PDF> (last accessed April 2011).
- [79] Aera FC-D980 Digital Mass Flow Controllers, Product Brochure, Advanced Energy (Hitachi Metals Ltd.)
- [80] Mundy, D. H., Fearn, D. G. and Bond, R. A., "The Influence of Charge Exchange Ions on the Beam Divergence of an Ion Thruster", 27th International Electric Propulsion Conference, **IEPC-01-111** (2001)
- [81] Ion Beam Neutralization, Technical Note KRI-02, Kaufman and Robinson Inc. <http://www.4waveinc.com/TN02.pdf> (last accessed August 2010).
- [82] Smart-Trak 2 Series 100 Mass Flow Meters and Controllers Instruction Manual, Sierra Instruments Inc, (last accessed August 2010). http://www.sierrainstruments.com/products/userfiles/file/manuals/im_100st2_c2.pdf
- [83] Ding, Z. F., Yuan, G. Y., Gao, W. and Sun, J. C., "Effects of impedance matching network on the discharge mode transitions in a radio-frequency inductively coupled plasma", *Physics of Plasmas*, **15**, 063506 (2008).
- [84] Godyak, V.A., Piejak, R.B., and Alexandrovich, B.M., "Measurements of electron energy distribution in low pressure RF discharges," *Plasma Sources Science and Technology*, Vol. 1, 1992, pp. 36-58.
- [85] Chen, S. and Sekiguchi, T., "Instantaneous Direct-Display System of Plasma Parameters by Means of Triple Probe", *J. Appl. Phys*, 36(8), 1965.
- [86] Chen, F. F., "Langmuir probe analysis for high density plasmas", *Phys. Plasmas*, **8**, 3029 (2001)
- [87] Mueller, J., Marresse, C., Ziemer, J., Green, A., Yang, E.H., Mojarradi, M., Johnson, T., White, V., Bame, D., Wirz, R., Tajmar, M., Schein, J., Reinicke, R. and Hruby, V., "JPL Micro-Thrust Propulsion Activities", 38th *AIAA/ASME/SAE/ASEE Joint Propulsion Conference and Exhibit* **AIAA 2002-5714** (2002).
- [88] Corbett, M., "Breadboard Miniaturised Gridded Ion Thruster Test Report," QinetiQ/IS/Aero/TSTR0801908 (2008).

- [89] Biagioni, L., Kim, V., Nicolini, D., Semekin, A. V. And Wallace, N. C., “Basic Issues in Electric Propulsion Testing and the Need for International Standards”, 28th International Electric Propulsion Conference, **IEPC-03-230** (2003).
- [90] Brown, D. L. And Gallimore, A. D., “Faraday Probe Analysis, Part 2: Evaluation of Facility Effects on Ion Migration in a Hall Thruster Plume”, *Review of Scientific Instruments*, Preprint (2010).
- [91] Randolph, T., Kim, V., Kaufman, H., Kozubsky, K., Zhurin, V. and Day, M., “Facility Effects on Stationary Plasma Thruster Testing” 23rd International Electric Propulsion Conference, **IEPC-93-93**, (1993)
- [92] Synder, J. S., Goebel, D. M., Hofer, R. R., Polk, J. E., Wallace, N. C. and Simpson, H., “Performance Evaluation of the T6 Ion Engine”, 46th AIAA/ASME/SAE/ASEE Joint Propulsion Conference and Exhibit **AIAA 2010-7114** (2010).
- [93] Feili, D., Lotz, B., Bonnet, St., Meyer, B. K., Loeb, H. W. and Puetmann, N., “ μ NRIT-2.5 – A New Optimized Microthruster of Giessen University”, 31st International Electric Propulsion Conference, **IEPC-2009-174** (2009)
- [94] COMSOL Multiphysics Plasma Module User’s Guide, COMSOL Inc. (2010)
- [95] Birdsall, C. K. and Langdon, A. B., *Plasma Physics via Computer Simulation*, Institute of Physics Publishing, London, 1991.
- [96] Fridman, A. A. and Kennedy, L. A., *Plasma Physics and Engineering*, 2nd edition, CRC Press Inc, 2011.
- [97] Carmen, R. J. and Mildren, R. P., “Electron energy distribution functions for modelling the plasma kinetics in dielectric barrier discharges”, *J. Phys. D: Appl. Phys.*, **33** (2000).
- [98] Lin, D. (2010). Personal communication, COMSOL Multiphysics Ltd, UK..
- [99] Kamitsuma, M., Chen, S. L. and Chang, J. S., “The theory of the instantaneous triple-probe method for direct-display of plasma parameters in low-density collisionless plasmas”, *J. Phys. D: Appl. Phys.*, Vol. 10, 1977.
- [100] Corbett, M., “Engineering Model Miniaturised Differential Gridded Ion Thruster Design Report”, QinetiQ/IS/Aero/SSDD0802762 (2008).
- [101] Merlino, R. L., “Understanding Langmuir probe current-voltage characteristics”, *Am. J. Phys.*, **75** (12), 2007.
- [102] Su, C. H. and Lam, S. H., “Continuum Theory of Spherical Electrostatic Probes”, *Phys. Fluids*, **6**, 1479 (1963)
- [103] Godyak, V. A. and Sternberg, N., “Dynamic model of the electrode sheaths in symmetrically driven rf discharges”, *Phys. Rev. A*, **42**, 2299 (1990)
- [104] Riemann, K-U., “The influence of collisions on the plasma sheath transition”, *Phys. Plasmas*, **4**, 4158 (1997)
- [105] Chen, F. F., “Langmuir probes in RF plasma: surprising validity of OML theory”, *Plasma Sources Sci. Technol.*, **18**, 2009.

- [106] Trunec, D., Spanel, P. and Smith, D., *Contrib. Plasma Phys.*, **35**, 1995, pp. 203-212.
- [107] Pletnev, V. and Laframboise, J. G., “Current collection by a cylindrical probe in a partly ionized, collisional plasma”, *Phys. Plasmas*, **13** (2006).
- [108] Ghosh, S. N., Dhungel, S.K., Yoo, J., Gowtham, M., Yi, J., and Bora, D., “Study of high-density helicon plasma generation and measurement of the plasma parameters using a frequency compensated langmuir probe” *J. Korean Phys Soc.*, 48 (5), 2006, pp. 908-913.
- [109] Tuszewski, M. and Tobin, J. A., “The accuracy of Langmuir probe ion density measurements in low frequency RF discharges”, *Plasma Sources Sci. Technol.*, **5**, 1996, pp 640-647.
- [110] Sudit, I. D. and Chen, F. F., “RF compensated probes for high density discharges”, *Plasma Sources Sci. Technol.*, **3**, 162, 1994.
- [111] Koizumi, T., Shirakawa, E. and Ogawa, I., “Momentum Transfer Cross Sections for Low Energy Electrons in Krypton and Xenon from Characteristic Energies”, *J. Phys. B: At. Mol. Phys.*, Vol. 19 (1986), 2331-2342.
- [112] Hayashi, M., “Determination of Electron-Xenon Total Excitation Cross Sections, from Threshold to 100eV, from Experimental Values of Townsends’s”, *J. Phys. D: Appl. Phys.*, Vol. 16 (1983), pp 581-589.
- [113] Frost, L. S. and Phelps, A. V., “Momentum Transfer Cross Sections for Slow Electrons in He, Ar, Kr and Xe from Transport Coefficients”, *Phys. Rev.*, Vol. 136, No. 6A , 1964, pp A1538-A1545.
- [114] Tajmar, M., Vasiljevich, I., Plesescu, F., Grienauer, W., Buldrini, N., Betto, M. and Gonzalez del Amo, J., “Development of a Porous Tungsten mN-FEEP Thruster”, Space Propulsion Conference 2010, San Sebastian, Spain, May 2010.
- [115] Technology Readiness Levels Handbook for Space Applications (TEC-SHS/5551/MG/ap), Issue 1, Rev. 6, European Space Agency (2008).
- [116] Leiter, H., “Development and Qualification of a Miniaturised Ion Engine System RIT- μ X for High Precision Orbital Manoeuvres”, presentation presented at the Space Propulsion Conference 2010, San Sebastian, Spain, May 2010.